
End-to-end cluster cosmology: Constraining cosmological parameters with X-ray selected galaxy clusters

Jethro Venn Ridl



München 2017

End-to-end cluster cosmology: Constraining cosmological parameters with X-ray selected galaxy clusters

Jethro Venn Ridl

Dissertation
an der Fakultät für Physik
der Ludwig-Maximilians-Universität
München

vorgelegt von
Jethro Venn Ridl
aus Durban, Südafrika

München, den 12. Mai 2017

Erstgutachter: Prof. Dr. Kirpal Nandra

Zweitgutachter: Prof. Dr. Joseph Mohr

Tag der mündlichen Prüfung: 20. June 2017

*For my mom.
My rock.*

Contents

Zusammenfassung	xxiii
Abstract	xxv
1 Introduction	1
1.1 Preface	1
1.2 Cosmological context	3
1.2.1 Basics of General Relativity	3
1.2.2 The cosmological principle	4
1.2.3 The Expanding Universe	10
1.2.4 The growth of structure	12
1.3 Clusters of galaxies	22
1.3.1 X-ray Properties of Clusters	22
1.3.2 Optical properties of Clusters	29
1.3.3 The Sunyaev-Zel'dovich effect	35
1.3.4 Diffuse radio emission in clusters	36
1.3.5 Shedding light on dark matter	37
1.4 Galaxy clusters as probes of cosmology	42
1.4.1 Galaxy cluster number counts	42
1.4.2 Clustering of clusters	47
1.4.3 Baryon fraction measurements	47
1.4.4 Using clusters as standard candles	48
1.4.5 Sources of systematic error	49
2 GROND observations and data reduction	51
2.1 The XCLASS/GROND observing program	52
2.2 Overview of GROND technicalities	53
2.3 Operation of GROND	57
2.4 Data reduction and image combination	58
2.4.1 Bias and dark subtraction	58
2.4.2 Flat-fielding	59
2.4.3 Fringing	60
2.5 Coaddition of images and sky subtraction	60

2.6	Astrometry	61
2.6.1	Pipeline recovered astrometry	61
2.6.2	Refinement with SCAMP	61
2.7	Source detection and PSF modelling	62
2.8	Photometric calibration	62
2.9	Data quality control	63
2.10	Summary of the X-CLASS/GROND observing campaign	71
3	The X-CLASS/GROND catalogue	73
3.1	Introduction	73
3.2	The XMM Cluster Archive Super Survey	75
3.2.1	Selection of XMM pointings and cluster detection	75
3.2.2	Catalogue construction and selection of the cosmological sub-sample	76
3.3	Redshift measurements	77
3.3.1	Archival redshifts	77
3.3.2	The GROND cluster photometric redshift tool	78
3.3.3	Application to GROND	81
3.3.4	Unconfirmed clusters	84
3.3.5	Comparison between GROND and archival redshifts	84
3.4	Characterisation of X-ray properties	86
3.4.1	Growth curve analysis	86
3.4.2	Energy conversion factors	86
3.4.3	Physical parameter measurements	87
3.4.4	Errors on X-ray derived properties	88
3.5	Results	89
3.5.1	Spatial distribution of clusters	89
3.5.2	Redshift distribution of clusters	89
3.5.3	X-ray properties of X-CLASS	91
3.5.4	The X-CLASS/GROND cluster catalogue	96
3.6	Discussion	96
3.6.1	Comparison of X-ray measurements with other XMM surveys	96
3.6.2	Nearby groups	98
3.6.3	Distant clusters	98
3.6.4	X-ray luminous clusters	99
3.7	Conclusions	99
4	Cosmological analysis of the X-CLASS/GROND catalogue	101
4.1	Current status of cluster cosmology	101
4.2	The z-CR-HR method	111
4.3	Modelling the z-CR-HR distribution	112
4.3.1	The halo mass function	112
4.3.2	Scaling relations	113
4.3.3	Instrumental model for XMM-Newton	114

4.3.4	The effect of varying cosmological parameters and scaling relations	115
4.3.5	Accounting for pointed observations of known clusters	118
4.3.6	Selection function	121
4.3.7	The effects of measurement errors	123
4.4	Parameter estimation	125
4.4.1	Cash likelihood	125
4.4.2	Markov Chain Monte Carlo sampling	126
4.5	Verification and testing	131
4.5.1	Mock creation	131
4.5.2	Testing the MCMC algorithm on mocks	132
4.6	Cosmological analysis of the X-CLASS/GROND catalogue	135
4.6.1	Consistency test with the full X-CLASS C1 ⁺ sample	135
4.6.2	Analysis of the X-CLASS/GROND sample	136
4.6.3	Looking forward	141
4.6.4	Summary and conclusions	143
5	Concluding remarks	145
5.1	Summary and conclusions	145
5.2	Future prospects	150
A	The X-CLASS/GROND catalogue	153
	Bibliography	167
	Acknowledgements	179

List of Figures

1.1	<i>Left</i> : The original Hubble diagram (with the incorrect unit on the velocity axis which should be in km s^{-1}) from 1929 showing the radial velocity of galaxies as a function of their distance. It is relatively easy to measure the velocity of galaxies from the Doppler shift in their spectral lines. Measuring the distance however is somewhat more challenging. Hubble significantly underestimated the distances to the galaxies and thus obtained an extremely high value for the Hubble constant. <i>Right</i> : A more recent Hubble diagram, taken from Jha (2002) which measured the distances to galaxies by using supernova. This allowed for the Hubble expansion to be proved at much greater distances. The small red square in the bottom-left corner is the region covered by the original Hubble diagram.	11
1.2	Observations of the Universe (left; SDSS) and simulations (right; Millennium) of structure formation history of the Universe show that the Universe is indeed largely inhomogeneous, with a high amount of structure present even on very large scales. Both of these images highlight the filamentary nature of structure in the Universe, forming what we call the Cosmic Web. Galaxy clusters typically appear at nodes in this web-like structure and we see that the bulk of the volume of the Universe lies in vast, under-dense regions called voids. Image credit: M. Blanton and the Sloan Digital Sky Survey; Springel et al. (2005)	13
1.3	The mass function derived from the <i>Magneticum</i> simulations over a variety of redshifts intervals. The mass function was measured by extracting halos from N-body simulations consisting purely of dark matter (DMonly) and also from hydrodynamical simulations featuring baryons as well (Hydro). The mass function is measured over a variety of redshift slices and it is clear that the later in time the more massive halos have formed. The lines here are the best-fitting functions for the mass function. Image taken from Bocquet et al. (2016)	21

- 1.4 Wavelet filtered XMM-Newton (M1+M2+PN) image, ObsID: 0555020201_20ks. Red boxes show the locations of two serendipitously detected clusters, X-CLASS 2305 ($z = 0.62$) and X-CLASS 2304 (distant candidate; see discussion in Section 3.6.3) along with the GROND *gri* image where the cyan contours represent the X-ray distribution. The PI target, RBS 1055 is located near the centre of the pointing. For comparison, a point source is indicated by the dashed-green circle. 23
- 1.5 *Left*: The expected unabsorbed X-ray emission spectrum for three galaxy clusters with temperatures of $T=1$ keV (black), 3 keV (red) and 9 keV (green). The dominant component is the continuum emission from thermal bremsstrahlung. We see that the emission continues to higher photon energy (and therefore frequencies) for hotter clusters. Also included in this plot are radiation from atomic transitions and recombination which present as line features. Clearly, these are more important for the 1 keV cluster. *Right*: The unabsorbed spectrum of a $T = 3$ keV cluster (black) and as it would be observed taking photo-absorption into account with hydrogen column densities of $3 \times 10^{20} \text{ cm}^{-2}$ (red) and 10^{21} cm^{-2} (green). We see a cutoff in the spectrum at lower energies. Images courtesy of Schneider (2006). . . . 25
- 1.6 *Left*: A map of the temperature of the galaxy cluster A1795 observed with Chandra which allows us to accurately measure any substructure present in clusters due to the high angular resolution of the telescope. Clearly, the gas temperature is not uniform throughout the cluster and the cluster core appears cooler than its outskirts. *Right*: A deep Chandra image of the Perseus cluster. By using sophisticated filtering techniques, which are able to remove the continuous X-ray emission, one can reveal the hugely detailed substructure present in galaxy clusters caused by interaction with a central AGN, gas sloshing and cooling flows, amongst other phenomena. Image credit: Hofmann et al. (2016); Sanders et al. (2016). 28
- 1.7 Two typical galaxy clusters X-CLASS 2122 at a redshift $z = 0.37$ (left) and X-CLASS 1858 with redshift $z = 0.60$ (right) observed with GROND on the MPG/ESO 2.2m telescope at La Silla. Clusters are easily identified in optical imaging surveys as over-densities in the galaxy distribution. In the left panel, cluster members appear as yellowish sources with a clear BCG at the centre of the image and an interesting linear configuration of four galaxies just above it. In the right panel, which is a more distant cluster, the cluster members are red and considerably fainter than in the left image. 30
- 1.8 The Coma cluster is a nearby, massive cluster that has been extensively studied. A spectroscopic survey along with a morphological study of its cluster members leads to the interesting result that passive, elliptical galaxies tend to lie almost exclusively in a narrow, red band in the colour-magnitude space in the plot on the right. Spiral galaxies on the other hand tend to be much bluer than their elliptical counterparts. Image credit: Dean Rowe; Bower et al. (1998) 33

- 1.9 When CMB photons pass through ICM of a galaxy cluster, the inverse-Compton scattering process shifts them to higher frequencies. We thus see that below the characteristic frequency of 217 Ghz, there is a decrement in the CMB (cold spot) whereas above this frequency there is an increment (hot spot). It is thus perhaps easier to detect clusters in the low frequency bands where they would not be easily confused with radio-emitting galaxies, which would appear as extended hot-spots in both passbands above and below 217 Ghz. Image credit: [Carlstrom, Holder & Reese \(2002\)](#) 35
- 1.10 AGN are incredibly powerful sources of energy and they produce large-scale radio-loud jets which interact with the surround ICM, displacing gas and creating large bubbles. This incredible composite image displaying the inner 700kpc of the galaxy cluster MS 0735 in optical data (white) from the Hubble Space Telescope I-band, X-rays (blue) from Chandra and radio observations (red) from the Very Large Array (VLA), highlights to interplay between the various components of a galaxy cluster. Despite originating from a single black hole at the centre of the BCG, the radio jets powered by the central AGN displace the cluster gas on large scales, impacted the environment many kiloparsecs from their origin. Combining data from multiple datasets allows us to better understand cluster physics. Image from [McNamara et al. \(2009\)](#) 38
- 1.11 Examples of two types of radio emission associated with galaxy clusters. In both images we clearly see the extended nature of this emission. *Left*: A smoothed ROSAT (red) image of Abell 3527-bis, one of the first galaxy clusters detected initially through its radio emission from a 1 Mpc long radio relic shown by the blue contours obtained from 323 Mhz data from the GMRT. It's name is acquired due to its close proximity to Abell 3527 and is one of the least massive clusters to host a relic. It was originally detected as a point source by ROSAT and was by chance observed with GROND on the MPG 2.2m telescope at La Silla as a part of a program following up such sources. I performed the data analysis of the GROND data, providing the confirmation that this was indeed a cluster (cluster members indicated by white crosses). Image from [de Gasperin et al. \(2016\)](#). *Right*: Radio emission (white contours) from an ATCA 1.867 GHz of the radio halo Planck cluster PLCK G285.0-23.7 overplotted on a smoothed XMM image in the [0.3-2.0] keV energy band. Image from [Martinez Aviles et al. \(2016\)](#). 39

- 1.12 The Bullet cluster (1E 0657-558) provides an excellent example of the power of gravitational lensing. Shown here are optical data from HST (yellow), X-rays (red) from Chandra and the dark matter distribution obtained from the gravitational lensing analysis. The clear offset between the X-ray and dark matter peaks has been hailed as ‘a smoking gun’ for dark matter since there is currently no prominent gravitational theory which could describe the gravitational lensing features in the regions that the dark matter is postulated to inhabit. Verlinde however, thinks that his emergent gravity theory (Verlinde 2016) will be able to account for these observations without the need for dark matter. Image Credit: X-ray: NASA/CXC/CfA/ M.Markevitch et al.; Lensing Map: NASA/STScI; ESO WFI; Magellan/U.Arizona/ D.Clowe et al. Optical: NASA/STScI; Magellan/U.Arizona/D.Clowe et al. 41
- 1.13 The number of galaxy clusters as a function of redshift depends on the parameters of the background cosmology. The top panel here illustrates the total number of clusters with $M > 10^{12.5} h M_{\odot}$ per square degree on the sky for a fiducial cosmology with $\Omega_M = 0.24$ and $\sigma_8 = 0.88$ along with the result of varying each of these parameters. The bottom panel depicts the number of clusters detected per square degree for a hypothetical XMM survey with a depth of 10 ks taking selection effects into account. 43
- 1.14 The two rows of images show three redshift snapshots of a simulated region containing two million particles with side of $250 h^{-1}$ Mpc and a depth of $75 h^{-1}$ Mpc. The upper panel is representative of a realistic (according to most observations) flat, low-density model with a matter density $\Omega_M = 0.3$ and cosmological constant $\Omega_{\Lambda} = 0.7$. The bottom panel depicts an Einstein-de Sitter universe with $\Omega_M = 1$. The amplitude of the power spectrum is normalised in both cases to match the number density of clusters at low redshifts and the yellow circles highlight the positions of galaxy clusters that would have a temperature $k_B T > 3$ keV. As one goes to higher redshifts it is plainly apparent that one observes a significantly different number of clusters at earlier times in each of the simulations, highlighting the power of the evolution of cluster number counts for constraining cosmological parameters. Image from Borgani & Guzzo (2001). 44
- 1.15 This images illustrates the sensitivity of the cluster mass function to the background cosmological model. The left panel shows the mass function measured from a sample of galaxy clusters split between low redshifts (black) and high redshifts (blue), along with a theoretical mass function at two redshifts $z = 0$ and $z = 0.55$ derived from the best-fit cosmology obtained from this sample (with $\Omega_M = 0.25$ and $\Omega_{\Lambda} = 0.75$. In the panel on the right, the data points and theoretical models are computed with a different cosmological model (with $\Omega_{\Lambda} = 0$). When the model is normalised so that the the low redshift mass function matches the local abundance, the predicted number density of clusters with $z > 0.55$ disagrees strongly with the data, providing an independent confirmation that $\Omega_{\Lambda} \neq 0$ 46

2.1	The efficiency of GROND (solid) and for comparison, SDSS (dotted) filters is shown as a function of wavelength. The narrow width of the GROND <i>i</i> -band compared to SDSS is clearly visible. Also plotted is an arbitrarily scaled spectral energy distribution (SED) of a early type galaxy at redshift $z = 0.6$. The 4000Å break, the key feature used for determination of the redshift of the cluster is marked with a star.	54
2.2	Three dimensional structure of the components making up the GROND optical and near-IR arms. The most important individual components are labelled. Image courtesy of Greiner et al. 2008.	55
2.3	Layout of the GROND optics show a slice through the optical arm (top) the near-IR arm (bottom). Image courtesy of Greiner et al. 2008.	56
2.4	The evolution of the GROND photometric zeropoints in each of the optical bands (<i>g</i> : blue, <i>r</i> : green, <i>i</i> : red, <i>z</i> : magenta) over the course of the observing period from ESO periods 91 (starting April 2013) to 96 (ending February 2016). Each point represents the median zeropoint correction for a given observing night, measured from all fields overlapping with the SDSS footprint and after taking into account corrections for atmosphere extinction and differing exposure times. The top panel indicates the zeropoint correction and the bottom panel a measure of the RMS scatter across all measured fields on a given night.	64
2.5	The upper panels describe the distributions of the measured seeing and the lower panels describe the 10σ point-source limiting magnitudes for 8min4TD (blue) and 20min4TD (red) for each of the <i>g</i> , <i>r</i> , <i>i</i> , <i>z</i> -bands. The median values are indicated by the vertical dashed lines.	65
2.6	This compilation shows X-CLASS 2162 ($z_{spec} = 0.12$, $z_{phot} = 0.12$).	67
2.7	X-CLASS 40 ($z_{spec} = 0.33$, $z_{phot} = 0.32$).	68
2.8	X-CLASS 459 ($z_{spec} = 0.55$, $z_{phot} = 0.54$).	69
2.9	X-CLASS 505 ($z_{spec} = 0.79$, $z_{phot} = 0.81$).	70
3.1	The expected colour-evolution of the cluster red sequence as a function of redshift for the three colours considered in the determination of photometric redshifts, i.e. $g - r$, $r - i$, $i - z$	79

- 3.2 ‘Likelihood’ distributions of three galaxy clusters are shown in the upper panels. *Left*: X-CLASS 459, with a spectroscopic redshift $z = 0.55$. *Middle*: X-CLASS 228 with a spectroscopic redshift $z = 0.83$ *Right*: X-CLASS 430 with spectroscopic redshift $z = 0.58$. The dotted lines are the ‘likelihood’ distributions for the individual galaxies in the field, calculated from Equation 3.3 and the black dashed is the β -model weighted sum of the individual galaxies. The lower panel shows the number of galaxies contributing to likelihood at each redshift. The solid magenta curve in the upper panel is the final ‘likelihood’ given in Equation 3.3. The solid-red vertical lines indicate the redshift of the cluster obtained from the archival redshift search which, in the left and centre cases, overlap with the redshift determined after visually inspecting these curves as described in Section 3.3.3. The dashed-red vertical line shows the redshift determined from the GROND observation, which is slightly different from the spectroscopic redshift of the cluster. 82
- 3.3 Comparison of GROND photometric redshift with 76 of the spectroscopic redshifts with $z < 0.85$ obtained from the literature as discussed in Section 3.3.1. The grey shaded region is bounded by the lines $z \pm 0.02(1 + z)$, indicating the typical error of our measurements. 85
- 3.4 Distribution of clusters across the sky. X-CLASS clusters presented in this sample are described by coloured circles. The colour of the marker indicates the redshift on the cluster and size is proportional to the X-ray luminosity. The X-CLASS clusters further north than the limits of this survey are indicated by green x’s and candidate clusters from a new processing of XMM data up to January 2012 are indicated by black +’s. The solid blue line shows the declination above which we do not observe and the red curves show Galactic latitudes $b = \pm 20^\circ$. Coordinates are given in the Equatorial J2000 system. 90
- 3.5 Distribution of X-CLASS clusters redshifts: GROND photometric redshifts for all clusters in the southern X-CLASS cosmological sample (solid-blue) and the spectroscopically confirmed subsample (dashed-red). 92
- 3.6 *Left*: The distribution of X-ray luminosity as a function of redshift for X-CLASS clusters. *Right*: The number density of X-CLASS clusters as a function of X-ray luminosities with redshift are indicated by the colour map, smoothed with a Gaussian filter. The contours indicate the expected distribution from the eROSITA 4 year all-sky survey under the assumptions discussed in the text and the grey +’s represent the ROSAT selected MCXC meta-catalogue (Piffaretti et al. 2011). 93
- 3.7 Distribution of X-ray luminosities as a function of redshift for X-CLASS clusters compared to the XCS-DR1 and XXL-100 catalogues. The XCS and XXL catalogues have been binned by to redshift slices of width $z = 0.1$ and the error bars represent the respective scatter about the median luminosity of each bin. 94

- 3.8 The number of clusters as a function of bolometric luminosity for the X-CLASS sample presented in this thesis (solid blue line), compared with the distributions of the XCS-DR1 (black, dashed-dot) and XXL-100 (red, dashed) samples respectively. 95
- 3.9 Comparison of X-CLASS bolometric [0.05-100 keV] X-ray luminosities within r_{500} of the cluster centre (left) and the X-ray temperatures(right) with the same quantities from the XCS and XXL catalogues. 97
- 4.1 Constraints on various cosmological parameters coming from analyses based purely on clusters, and with combining with external datasets. The dark/light shading represent the 68.3% and 95.4% confidence regions. *Left*: Constraints on Ω_M and σ_8 from these papers by Mantz et al. (2008, 2010, 2015) showing the improvements achieved by increasing the accuracy of the calibration of the absolute mass scale and the associated scaling relations. *Right*: Constraints on w and Ω_M from various datasets along with the combination of all of them, highlighting the power of utilising multiple, independent datasets when trying to constrain cosmological parameters. Images courtesy of [Mantz et al. \(2015\)](#). 106
- 4.2 The impact of varying cosmological parameters on the number of clusters detected of a given redshift, count rate and hardness ratio. The contour levels contain 30 and 90 percent of the clusters. Illustrated here are a fiducial WMAP9+XXL cosmology (dashed-black) and the effect of varying Ω_M (top), σ_8 (middle) and w_0 (bottom) represented by the solid-red curves. The numbers at the bottom of the panels indicate the expected number of clusters in that redshift interval for each of the fiducial (black) and modified (red) models. 117
- 4.3 The impact of varying the normalisation, slope and evolution of the $L - T$ relation as parameterised in Equation 4.5 with $T_{pivot} = 4$ keV, on the number of clusters detected of a given redshift, count rate and hardness ratio. The contour levels contain 30 and 90 percent of the clusters. Illustrated here are a fiducial WMAP9+XXL cosmology (dashed-black) and the effect of varying C_{LT} , α_{LT} and γ_{LT} (solid-red). The number at the bottom of the panels indicate the expected number of clusters in that redshift interval. . . 119
- 4.4 The impact of varying the normalisation, slope and evolution of the $M - T$ relation as parameterised in Equation 4.4 with $T_{pivot} = 4$ keV, on the number of clusters detected of a given redshift, count rate and hardness ratio. The contour levels contain 30 and 90 percent of the clusters. Illustrated here are a fiducial WMAP9+XXL cosmology (dashed-black) and the effect of varying C_{MT} , α_{MT} and γ_{MT} (solid-red). The number at the bottom of the panels indicate the expected number of clusters in that redshift interval. . . 120

- 4.5 *Top*: The bias factor in three redshift intervals as a function of CR arising due to the presence of pointed observations in the sample. The values here take the sensitivity and area weighted ratio between the number of clusters in the inner and outer populations into account. *Bottom*: The effect that the bias has on the recovered CR-HR distribution for each redshift interval. The main impact is simply one of increasing the number of clusters expected, particularly at high redshifts, where we also notice a broadening of the distribution towards higher CR. This makes sense as these would be massive, high redshift clusters, which are currently objects attracting a lot of attention from astronomers studying them across the electromagnetic spectrum. 122
- 4.6 The effect of implementing two different selection functions. The dashed-black curves show the 30 and 90 percent contours for a selection function based on a maximum XMM off-axis position of 13' while the solid-red curves represent a selection function where the maximum off-axis position is 10'. It is important to recall here that the CR and HR measurements of all clusters are corrected for vignetting effects and for the aperture in which they are measured. 124
- 4.7 The impact of uncertainties in the measurement in CR and HR. The introduction of measurement errors induces a significant smoothing of the resultant CR-HR distributions. As expected, the total number of clusters remains almost identical. 125
- 4.8 An illustration of the 'stretch' move. Here, the blue circles and red squares represent two population ensembles of walkers as implemented by `emcee`. A walker from the first population X_k is moved to a new position Y , which lies along the straight line connecting X_k and X_j , a randomly selected walker from the second population represented by blue circles, i.e., $Y = X_j + Z[X_k - X_j]$. In principle, Z can be either greater or less than one and so it is also possible that X_k moves towards X_j . Once all walkers in the population of red squares have been stepped forward, the blue circles are evolved based on their new positions. 130
- 4.9 An illustration of the walkers making up the ensemble in a MCMC run with `emcee` when fitting Ω_M and σ_8 . The three colour-coded walkers, start their journeys at the points marked by the large squares. Small squares indicated the position of the walker at each successive step and the large stars mark the position of the walkers after 50 (left), 250, (middle) and at the end of the run after some 850 steps (right). We see that although the walkers have not ended up at the same location, they have ended up with similar sampling distributions, each representative of the posterior distribution of the parameters in question 131

- 4.10 The distribution of ‘fake’ clusters drawn from a model z -CR-HR diagram for a 10,000 square degree survey (*left*) and a 100 square degree survey (*right*). The contours are drawn from the model distribution and represent the expect 10, 68 and 95 percent enclosing regions. 132
- 4.11 The recovered posterior distributions for a run of the MCMC code on a mock catalogue. The green contours indicate the case where redshift information was not considered. The overlaid-black contours represent the distribution recovered when binning clusters by redshift into 3 bins ($0.05 \leq z < 0.32$, $0.32 \leq z < 0.53$ and $0.53 \leq z < 1.32$). The input values are indicated by the red lines. Most parameters show minor improvements with this binning scheme however, clear improvements are already seen in the constraints on Ω_M and γ_{LT} 134
- 4.12 *Left*: The black contours indicate the 68 and 95 percent confidence intervals derived from the output MCMC chains of C12, making use of the entire X-CLASS C1⁺ cosmological sample of 347 galaxy clusters. The green, filled regions indicate the sample confidence intervals derived from the analysis presented in this thesis. We notice a very good agreement between the best-fit values with the new confidence intervals overlapping completely with those of C12, although with considerably smaller scatter. *Right*: The predicted distribution of clusters with CR-HR derived and the total number of clusters expected from the C12 (black) best-fit parameters and those derived from our analysis (green). We notice the good agreement of both sets of parameters with the number of clusters, shown for each set of parameters in the bottom right and left respectively. 137
- 4.13 The recovered posterior distributions based on an MCMC analysis of the inner (left) and full (right) surveys. The results obtained in our analysis are shown has the green contours and the results of C12 are indicated by the black contours. We see no significant difference between the results obtained for the two surveys although there is tension between both surveys and the results obtained by both C12 and our analysis of that sample. The tension is slightly smaller for the inner survey, which could be explained by the greater similarity between this data that of C12. The most significant tension comes from constraints for σ_8 and γ_{MT} . These two parameters are highly degenerate with each other. This is because a high value for σ_8 causes the number of clusters forming in the Universe to be greater, particularly at high redshifts. This necessitates a high value of γ_{MT} as it reduces the number of objects that fall into the range of detection dictated by the selection function. This is illustrated in Figures 4.2 and 4.4. 139

-
- 4.14 *Left*: The constraints obtain by combining the redshift selection $0.1 < z < 0.81$ with the bias model used by C12 and in our analysis of their sample. These constraints are not in tension with the results based on the previous sample, providing an indication that there might be an issue with the bias modelling for the more recent work. *Right*: The bias factor for a variety of surveys. Shown here are the bias factor from C12, and for the X-CLASS/GROND sample containing the entire sample and only those with $0.1 < z < 0.81$; and for both the inner and full surveys. I highlight the high-CR regions where all subsequent samples have considerably lower bias values than the C12 values. 140
- 4.15 The recovered posterior distributions based on an MCMC analysis of the inner (left) and full (right) surveys when including information about the cluster redshifts. Both the inner and full surveys display similar levels on tension with the previous analyses. 142

List of Tables

2.1	Total exposure times of the predefined GROND observing blocks in the optical (<i>griz</i>) and near-IR (<i>JHK</i>) channels used in this study. Execution times are approximate and include telescope slewing.	58
2.2	The median seeing and 10σ -limiting magnitude in each of the four optical channels and for each of the chosen observing blocks. The limiting magnitudes are determined by the magnitude at which the signal-to-noise for an extended source reaches 10.	63
2.3	Table summary of the GROND observing campaign at the ESO/MPG-2.2m telescope relevant to the sample presented in this paper. The first column lists the standard run identifiers as referenced in the ESO archive database. The number of allocated nights takes into account target of opportunity (ToO) and technical overheads. These nights were also shared with separate programs to followup distant clusters as well as clusters from the updated X-ray processing, which are not included in this paper. The number of targets indicates the successful observations of XCLASS sources acquired during this period. The attachments between sources and observing runs is available through the L4SDataBase (http://xmm-1ss.in2p3.fr:8080/14sdb/). . .	72
3.1	Average errors induced by offsetting the X-ray count-rate and redshift of the clusters and adjusting the scaling relations by their respective scatter and their effect on the bolometric luminosity and temperature obtained from the iterative method. The totals are calculated by adding the individual errors in quadrature.	89
3.2	The bias and standard deviation of a comparison with other XMM cluster surveys.	98
4.1	The results obtained by Clerc et al. (2012b) compared to the results obtained for the MCMC analysis performed for this thesis. Values quoted are the median values of the MCMC chains and the errors are such that they contain 68 percent of the samples obtained by the MCMC algorithm.	136
A.1	The X-CLASS/GROND catalogue.	154

Zusammenfassung

Der XMM Cluster Archive Super Survey (X-CLASS) ist eine Sammlung von 845, zufällig, anhand deren Röntgenstrahlung ausgewählten Galaxienhaufen, basierend auf 2774 *XMM-Newton* Archiv-Beobachtungen und bedeckt etwa 90 Grad^2 des Himmels über dem Galaktischen Breitengrad ($|b| > 20^\circ$). Das primäre Ziel dieser Arbeit war es, eine kosmologische Analyse auf der Grundlage dieser Sammlung an Haufen durchzuführen. Bevor dies geschehen konnte, war es notwendig, eine gut ausgewählte und charakterisierte Sammlung von Haufen zu erstellen. Da ich neben den Einschränkungen kosmologischer Parameter wie Ω_M und σ_8 interessiert war die Evolution der Haufen-Skalierungsbeziehungen zu studieren, war es zuerst notwendig photometrische Rotverschiebungen für die Galaxienhaufen zu erhalten. Zu diesem Zweck wurden photometrische Rotverschiebungsmessungen einer Untergruppe von 265 dieser Haufen, mit dem höchstem Signal/Rauschen Verhältnis im Röntgen und Deklination $\delta < +20^\circ$ durchgeführt. Diese Beobachtungen wurden mit GROND, einem siebenkanaligen (*grizJHK*) gleichzeitig Bildgebendem Instrument des MPG 2.2 m Teleskops am ESO La Silla Observatorium durchgeführt. Ich entwickelte eine neue Technik, die auf der Farb-Rotverschiebungs Relation der Rot-Sequenz der Galaxien in den Haufen basiert, die mit Informationen aus der Messung der Röntgenstrahlen erweitert wurde um photometrische Rotverschiebungen für diese Sammlung der Haufen zu liefern. Ich konnte am Ende photometrische Rotverschiebungen für 232 Haufen bestimmen und eine mediane Rotverschiebung von $z = 0.39$, mit einer Genauigkeit von $\Delta z = 0.02(1 + z)$, im Vergleich zu Messungen von 76 spektroskopisch bestätigten Haufen. Ich berechnete auch Röntgen-Luminositäten für die gesamte Sammlung an Haufen und fand eine mittlere bolometrische Helligkeit von $7.2 \times 10^{43} \text{ erg s}^{-1}$ und eine mediane Temperatur von 2.9 keV. Ich verglich diese Ergebnisse mit den XMM-XCS- und XMM-XXL-Ergebnissen und fand eine gute Übereinstimmung mit beiden Proben. Mit den photometrischen Rotverschiebungen in der Hand habe ich eine kosmologische Analyse der X-CLASS/GROND Probe mit der z-CR-HR Methode durchgeführt. Meine Ergebnisse zeigen Abweichungen zu den jüngsten kosmologischen Analysen, die auf verschiedenen anderen Studien wie des CMB, der BAO und SN1a basieren, aber ich habe mögliche Ursachen für diese und skizziere Lösungsansätze, die diese Probleme in Zukunft lösen sollten.

Abstract

The XMM Cluster Archive Super Survey (X-CLASS) is a serendipitously-detected X-ray-selected sample of 845 galaxy clusters based on 2774 XMM archival observations and covering approximately 90 deg^2 spread across the high-Galactic latitude ($|b| > 20^\circ$) sky. The primary goal of this thesis was to perform a cosmological analysis based on this cluster survey. Before this could be done it was necessary to produce a well-selected, and characterised sample of clusters. Since along with constraining cosmological parameters such as Ω_M and σ_8 , I was interested in studying the evolution of the cluster scaling relations it was necessary to first obtain photometric redshifts for this sample. To this end a photometric redshift followup of a high signal-to-noise subset of 265 of these clusters with declination $\delta < +20^\circ$ was undertaken. These observations were performed with GROND, a seven channel (*grizJHK*) simultaneous imager on the MPG 2.2m telescope at the ESO La Silla Observatory. I developed a new technique based on the red sequence colour-redshift relation, enhanced with information coming from the X-ray detection to provide photometric redshifts for this sample. I was able to determine photometric redshifts for 232 clusters, finding a median redshift of $z = 0.39$ with an accuracy of $\Delta z = 0.02(1+z)$ when compared to a sample of 76 spectroscopically confirmed clusters. I also computed X-ray luminosities for the entire sample and found a median bolometric luminosity of $7.2 \times 10^{43} \text{ erg s}^{-1}$ and a median temperature 2.9 keV. I compared these results to the XMM-XCS and XMM-XXL surveys, finding good agreement with both samples. With the photometric redshifts in hand, I undertook a cosmological analysis of the X-CLASS/GROND sample with the z-CR-HR method. My results are found to be in tension with the most recent cosmological analyses based on various other probes such as the CMB, BAO and SN1a, but I have identified probable causes for this and outlined prospective solutions which should resolve these issues in the future.

Chapter 1

Introduction

1.1 Preface

One of the primary goals of modern astronomy is to further our understanding of cosmology and the parameters that dictate the expansion and structure formation histories of the Universe. As the most massive collapsed structures in the Universe, galaxy clusters provide a powerful probe of the distribution of matter throughout the cosmos and by studying them over a wide range of redshifts we can infer a great deal about the underlying cosmological model. Galaxy clusters are observable over a wide range of the electromagnetic spectrum extending from radio waves to gamma rays and this makes them interesting objects of study in their own right. At X-ray wavelengths, clusters appear as luminous, spatially extended sources due to thermal bremsstrahlung emission from the hot gas which makes up the intra-cluster medium (ICM). Further, they are the most luminous and numerous class of extended sources in X-rays and this makes the selection of clusters at these wavelengths relatively straightforward compared to other wavelengths. In the optical and near-infrared bands, clusters appear as over-densities in the galaxy distribution and are characterised by a sequence of red, early-type galaxies (known as the red sequence) which can also be used to constrain their redshifts. At sub-millimeter wavelengths, clusters are detected through the characteristic signature that they imprint onto the cosmic microwave background through inverse-Compton scattering in a process known as the Sunyaev-Zel'dovich effect. When galaxy clusters merge with one another, tremendous amounts of energy are liberated causing the acceleration of particles to relativistic velocities. We detect this through synchrotron radiation at radio-wavelengths where clusters are observed as extended sources due to the presence of a radio halo, or identified from the presence of large-scale radio relics.

In my thesis, I have conducted a study of an X-ray selected sample of galaxy clusters drawn from the XMM Cluster Archive Super Survey (X-CLASS). The main goal was to use this sample to constrain cosmological parameters. Before this could be accomplished, an extensive optical and near-infrared followup campaign was undertaken, to observe 265 galaxy clusters so that their photometric redshifts could be derived. With these redshifts

in hand, we are then able to probe cosmological parameters along with the evolution of the scaling relations between their total mass and X-ray observables, namely, luminosity and temperature. We performed these observations with the Gamma-Ray Burst Optical and Near-infrared Detector (GROND), and this was the first study of this kind to be completed with this instrument. I thus had to extend the previously existing data reduction pipeline and tailor it for use on galaxy clusters. I then developed my own method for the determination of cluster photometric redshifts, taking advantage of the unique technical capabilities of GROND and its simultaneous imaging in seven channels. I was able to obtain photometric redshifts for 232 clusters in the redshift range $0.01 < z < 0.8$ and to identify a further 24 sources as possible distant candidates. I used these redshifts to derive X-ray temperatures and luminosities for the clusters in this sample and compared these measurements to previously existing XMM surveys of similar depths and areas.

I proceeded with a cosmological analysis of the X-CLASS/GROND cluster catalogue. I was able to verify the cosmological tools that are used for this study by re-deriving the constraints of Clerc et al. (2012b). The constraints that were obtained for the X-CLASS/GROND sample however are in tension with these previous results, as well as those derived from various cosmic microwave background (CMB), baryonic acoustic oscillations (BAO) and type 1a supernovae (SN1a). I identified probable causes for this tension and highlight ways in which these results can be improved.

The remainder of this thesis is structured as follows. In Chapter 1, I present an overview of the currently accepted cosmological model, Λ CDM, i.e. a universe whose energy density is dominated by a cosmological constant Λ and cold dark matter. I introduced the theory of structure formation and present the derivations of the halo mass function following the prescription of Press & Schechter. I introduced cluster observations covering radio, sub-millimeter, optical and X-ray wavelengths and show how one can use clusters to derive robust constraints on the parameters describing the background cosmological model.

In Chapter 2, I detail the extensive optical and near-IR followup program to observe X-CLASS galaxy clusters with GROND along with the data reduction techniques and in Chapter 3, I use the GROND data to obtain photometric redshifts for this sample. In addition to this I characterise the sample in terms of its X-ray properties, namely the bolometric luminosity and temperature. The bulk of these two chapters appear in a publication, Ridl et al. 2017, published by the Monthly Notices of the Royal Society.

In Chapter 4, I give an overview of the current status of cluster cosmology and present the cosmological analysis that was performed with the X-CLASS/GROND cluster catalogue using the z-CR-HR method.

Finally, I conclude my thesis in Chapter 5, with a short summary and outline my future prospects based on both the X-CLASS/GROND catalogue and looking further ahead to eROSITA.

1.2 Cosmological context

Modern cosmology is built on two major pillars. The first of these is general relativity (GR), Einstein's theory of gravity in which the space-time structure of the Universe is determined by how matter or energy is distributed across it. The second of these pillars is the cosmological principle: the hypothesis that on large enough scales, the Universe can be considered to be homogeneous and isotropic. By the end of this chapter, we will see that together, these foundations lead to a cosmology that is wholly described by the curvature of the Universe and the scale factor, which describes how the length scales of the Universe evolves.

1.2.1 Basics of General Relativity

In Newtonian physics, physical processes act in a flat, infinite and eternal space in which time flows uniformly and independently. The framework of General Relativity (GR) however is such that space-time is treated as a single four-dimensional manifold with properties such as curvature that are influenced by dynamical processes and energy densities. In essence, GR is a geometric theory describing the force of gravity, and it is the most widely accepted gravitational theory in modern physics, astrophysics and cosmology. Some of the great triumphs of GR include the successful predication the offset of stars behind the sun due to the gravitational lensing effect by Eddington in 1919, solving the problem of the precession of the orbit of Mercury; and most recently the confirmation of Einstein's prediction of gravitational waves by LIGO. In this section I will present a brief overview of the mathematical formalism of general relativity.

The curvature of space-time is directly related to the stress-energy of any matter or radiation that is present and a system of partial differential equations known as the Einstein Field Equations specifies this relation. To start with, we first define the metric and the length of a infinitesimal line element. The metric contains all the information relating to the geometry of the space in which we are working; in our case a four-dimensional space-time with three spatial dimensions and one of time and the line element is expressed in terms of it. In a general space-time, the line element ds is given by,

$$ds^2 = g_{\mu\nu} dx^\mu dx^\nu, \quad (1.1)$$

where $g_{\mu\nu}$ is the symmetric 4×4 metric tensor and x^μ are the general space-time coordinates.

A description of a curved space-time involves at least the second derivatives of the metric $g_{\mu\nu}$. The curvature is best described in terms of the fourth-rank Riemann tensor

$$R^\alpha_{\mu\beta\nu} = \frac{\partial \Gamma^\alpha_{\mu\nu}}{\partial x^\beta} - \frac{\partial \Gamma^\alpha_{\mu\beta}}{\partial x^\nu} + \Gamma^\alpha_{\beta\rho} \Gamma^\rho_{\mu\nu} - \Gamma^\alpha_{\nu\rho} \Gamma^\rho_{\mu\beta}, \quad (1.2)$$

where the Greek-letter indices run over the time and space dimensions of a four-dimensional space-time and $\Gamma^\alpha_{\mu\nu}$ is the affine connection which connects vectors in nearby tangent spaces.

Another useful tool in the description of the curvature is the second-rank Ricci tensor $R_{\mu\nu}$ which is obtained by contracting the Riemann tensor of the first and third indices,

$$R_{\mu\nu} = R_{\mu\alpha\nu}^{\alpha} = g_{\alpha\sigma}g^{\sigma\beta}R_{\mu\beta\nu}^{\alpha}. \quad (1.3)$$

Lastly, we can sum over the indices of the Ricci tensor to get the Ricci scalar

$$R = R_{\mu}^{\mu} = g^{\mu\nu}R_{\mu\nu}. \quad (1.4)$$

From here we are in a position to define the Einstein tensor $G_{\mu\nu}$ as

$$G_{\mu\nu} = R_{\mu\nu} - \frac{1}{2}g_{\mu\nu}R. \quad (1.5)$$

An important property of the Einstein tensor, which as we will see later implies that energy and momentum are conserved, is that its divergence vanishes, i.e.

$$\nabla_{\mu}G^{\mu\nu} = 0, \quad (1.6)$$

where ∇_{μ} is the covariant derivative and is defined for an arbitrary tensor V^{ν} as,

$$\nabla_{\mu}V^{\nu} = \partial_{\mu}V^{\nu} + \Gamma_{\mu\sigma}^{\nu}V^{\sigma}. \quad (1.7)$$

In GR, gravity is described purely as a geometric property of the space-time. We now turn our eye to the distribution of matter throughout the Universe, the energy and momentum of which controls the curvature of space-time and thus according to GR is the source of gravity. The curvature of the Universe and the energy and momentum of matter, represented by the so-called stress-energy tensor $T_{\mu\nu}$, are related via the Einstein field equations,

$$G_{\mu\nu} = R_{\mu\nu} - \frac{1}{2}g_{\mu\nu}R = 8\pi GT_{\mu\nu}. \quad (1.8)$$

From this and due to Equation 1.6

$$\nabla_{\mu}T_{\mu\nu} = 0, \quad (1.9)$$

which implies the conservation of energy and momentum.

1.2.2 The cosmological principle

The second pillar on which our modern theory of cosmology is built is the idea that the Universe can be considered to be spatially homogeneous and isotropic i.e., that there are no preferred locations in the Universe. This is the cosmological principle and given the current state of observations, it appears to be reasonable. The cosmological principle implies that all points in the Universe should be equivalent and that our location on Earth, or at any other position, should be typical and fundamentally indistinguishable from every other point.

The cosmological principle implies that one can imagine a fundamental observer situated at each location in space who perceives the Universe to be isotropic. Such a fundamental observer would thus define the ‘cosmological frame of rest’ for each location. For such a comoving observer i.e. one with $dx^i = 0$, the line element from Equation 1.1 reduces to,

$$ds^2 = g_{00}dt^2, \quad (1.10)$$

implying that $g_{00} = c^2$. From the isotropy requirements of the cosmological principle, all non-diagonal elements g_{0i} are equal to zero and so the line element becomes

$$ds^2 = c^2dt^2 + g_{ij}dx^i dx^j. \quad (1.11)$$

Note that the Greek letters μ and ν which run over 0,1,2,3 have been replaced by the Latin i and j which run over 1,2,3. Thus we see that for a curved four-dimensional space-time, the line element takes the form,

$$ds^2 = c^2dt^2 - dl^2, \quad (1.12)$$

where dl^2 is the three-dimensional spacial distance for a uniformly evolving hypersurface. These three dimensional hypersurfaces are symmetric and, making use of the spherical symmetry implied by isotropy to express dl in spherical polar coordinates, the four dimensional line element can be written as,

$$ds^2 = c^2dt^2 - a^2(t) \left[\frac{dr^2}{1 - Kr^2} + r^2 d\theta^2 + r^2 \sin^2 \theta d\phi^2 \right], \quad (1.13)$$

where $a(t)$ is the scale factor of the universe, K is the curvature parameter which can take the values 1, 0 or -1 and r is a dimensionless comoving coordinate. This is the Robertson-Walker metric. The scale factor which appears naturally in the equations, is a quantity of crucial importance to cosmology as it measures the universal expansion rate. It depends only on time and acts only on the spatial part of the metric, thus showing how the physical separation between two points changes with time. From this metric, we can see that a universe which is homogeneous and isotropic at a given time will remain so indefinitely. Further, a galaxy situated at some position in the universe will remain at the same point since it is only the scale of spatial distances which changes and thus all spacial displacements will remain zero. The metric equation is thus reduced to

$$ds^2 = c^2 dt^2. \quad (1.14)$$

Such an expanding frame is known as a comoving frame. An observer at rest in this frame is considered to be a fundamental observer and a universe which appears to be homogeneous to such an observer must be isotropic. Conversely, an observer moving with a relative motion will not observe isotropy. We can thus define a new set of coordinates in the preferred comoving frame. ¹ We define the radial coordinate in the comoving frame

¹One should note here that a fundamental observer might not necessarily see all objects radially receding due to the peculiar velocities in other directions. For example, the Andromeda galaxy is currently moving towards our Milky Way and these two galaxies will eventually merge to form a new, larger galaxy.

χ by,

$$d\chi = \frac{dr}{\sqrt{1 - Kr^2}}. \quad (1.15)$$

Combining Equations 1.13 and 1.15, we arrive at an alternative form of the Robertson-Walker metric,

$$ds^2 = cdt^2 + a^2(t) [d\chi^2 + f_K^2(\chi)(d\theta^2 + \sin^2\theta d\phi^2)], \quad (1.16)$$

where

$$f_K(\chi) \equiv \begin{cases} \sin \chi & K = 1 \\ \chi & K = 0 \\ \sinh \chi & K = -1 \end{cases} \quad (1.17)$$

We see here that depending on the value of the curvature parameter K , we can define three particular geometrical representations of the space-time. When $K > 0$, the space-time is a three-sphere embedded into a four-dimensional hyperspace and we call this a closed universe. When $K = 0$, we obtain the Euclidean geometry which represents a flat universe. Finally, when $K < 0$, the space-time has a hyperbolic geometry, represented by a saddle-shaped geometry and this defines an open universe. All observational evidence available at present is consistent with the case that our Universe has the geometry of the second case and that we live in a flat universe.

Suppose now that non-relativistic matter was continuously distributed as an ideal fluid throughout the Universe. We can then conveniently describe the energy density, pressure and shear of the fluid by the stress-energy tensor $T_{\mu\nu}$ which takes the form

$$T_{\mu\nu} = (p + \rho)U_\mu U_\nu - pg_{\mu\nu}, \quad (1.18)$$

where the energy density is given by ρ , the pressure by P and U_μ is the four-velocity of the fluid. Once again, our work is simplified by the assumptions of homogeneity and isotropy as peculiar motion is forbidden and the only component of the four-velocity allowed is the time component. This means that the stress-energy tensor can be written as a diagonal tensor with values $(-\rho, p, p, p)$.

Combining the Robertson-Walker metric with the Einstein field equations and the stress-energy tensor, and breaking them into time and space components we arrive at the dynamical equations,

$$\left(\frac{\dot{a}}{a}\right) = \frac{8\pi G}{3}\rho - \frac{K}{a^2}, \quad (1.19)$$

$$\frac{\ddot{a}}{a} = -\frac{4\pi G}{3}(\rho + 3p), \quad (1.20)$$

the first of which is known as the Friedmann equation. This equation describes the expansion rate of the Universe and the left-hand side can be replaced with the Hubble parameter $H(t)$. The value of the Hubble parameter at current times is defined to be $H_0 = H(t_0)$, and

is referred to as the Hubble constant while the scale factor at current times is normalised for the sake of simplicity to $a_0 = a(t_0) = 1$. With these definitions in hand and making use of the Friedmann equation, we see that the curvature of space is determined by the energy content of the universe. The universe will only be flat, i.e. $K = 0$, when the energy density is equal to a certain critical density,

$$\rho_c = \frac{3H_0^2}{8\pi G} = 1.878 \times 10^{-26} h^2 \text{kg m}^{-3}, \quad (1.21)$$

where $h \equiv H_0/(100 \text{km s}^{-1} \text{Mpc}^{-1})$. The actual energy density of the Universe is made up of a variety of components e.g. matter, radiation and dark energy. Using ρ_c one defines a density parameter in terms of the critical density for each component i ,

$$\Omega_i \equiv \frac{\rho_{i,0}}{\rho_c} = \frac{8\pi G}{3H_0^2} \rho_{i,0}, \quad (1.22)$$

and the corresponding parameter for the curvature,

$$\Omega_K = -\frac{K}{H_0^2}. \quad (1.23)$$

Combining the above Equations 1.19 and 1.20 we are able to derive the adiabatic equation,

$$\dot{\rho} + 3\frac{\dot{a}}{a}(\rho + p), \quad (1.24)$$

which shows that energy is conserved as expected. This represents the first law of thermodynamics with the absence of a heat-flow, which would violate the conditions of homogeneity and isotropy. The density appearing in the Friedmann equation is made up of various components, each with their own respective equation of state. For most applications in cosmology we are interested in barotropic fluids, for which $p = w\rho$ and the speed of sound $c_s^2 = dp/d\rho$ is constant. Inserting this form for the equation of state into Equation 1.24 and integrating we see that the density must scale as,

$$\rho \propto a^{-3(1+w)}. \quad (1.25)$$

Using this, we obtain an equation for the time variation of the scale factor,

$$\dot{a}^2 = H_0^2 \left[\sum_{i=0}^N \Omega_i a^{-(1+3w_i)} + \Omega_K \right], \quad (1.26)$$

and thus, assuming a flat universe we obtain

$$a(t) \propto t^{\frac{2}{3(1+w)}}. \quad (1.27)$$

Matter

Current observational constraints on the amount of matter the Universe put an estimate on the matter density of $\Omega_m \simeq 0.3$. Estimates of the amount of baryonic matter in the Universe, derived from calculations from the theory of Big Bang Nucleosynthesis and from the observed abundances of light elements show that the density of baryons is around $\Omega_b \simeq 0.04$. This means that most of the matter density of the Universe is not actually baryonic in nature. Various other sources of evidence coming from galaxy rotation curves, gravitational lensing and the cosmic microwave background indicate the presence of a different type of matter which seems to only interact gravitationally. This is called dark matter and although its direct detection in a laboratory has been illusive, we can already infer a few details about its properties from existing observations. For now we assume that dark matter is pressureless, i.e its equation of state parameter is $w_m = 0$. Using this in the energy conservation equation we obtain the scaling of the density parameter with the scale factor,

$$\rho_m \propto a^{-3}. \quad (1.28)$$

This is somewhat intuitive, as we see that the density goes just with the volume of the universe. Further, we can substitute this dependence into Equation 1.27 and taking a flat, matter dominated universe ($\Omega_K = 0; \Omega_m = 1$), we see that the scale factor goes as,

$$a(t) \propto t^{2/3}. \quad (1.29)$$

This particular solution to the Friedmann equations is called the Einstein-de Sitter universe and we will use it later when we describe the growth of density perturbations, leading to the formation of structures in the Universe.

Radiation

Another important component of the Universe, particularly at early times in its evolutionary history is radiation. Although it is perhaps not obvious, radiation behaves as a fluid with an equation of state parameter $w_r = 1/3$. Following the procedure described in the case of matter, this implies that $\rho \propto a^{-4}$. So we see that compared to the evolution of the matter density, there is an extra factor a^{-1} . This extra factor arises due to the change in wavelength of the radiation as the universe evolves. The bulk of the radiation in the Universe is in the form of CMB photons and we can estimate the energy density of radiation from the temperature of the CMB. The photon density is then,

$$\rho_{CMB} = \frac{\pi^2 k_B^4}{15 \hbar c^3} T_{CMB}^4 = 4.5 \times 10^{-31} \text{kg m}^{-3}, \quad (1.30)$$

where k_B is the Boltzmann constant. Dividing this by the critical density of the Universe we arrive at the conclusion that $\Omega_{CMB} = 2.4 \times 10^{-5} h^{-2}$. The radiation content of the Universe is not made up only of photons. Neutrinos, of which there are three known species, contribute a similar amount to the radiation budget. Compared to the matter

density at current times, the contribution from radiation to the total energy density is negligible and we can therefore ignore it. At early times in the Universe, due to the scaling of radiation with a^{-4} , radiation would have dominated the energy density over matter. We can derive the evolution of the scale factor at such times, assuming a flat universe, leading to,

$$a \propto t^{1/2}. \quad (1.31)$$

This period is referred to as the epoch of radiation domination and the Universe expanded more slowly during this era.

Dark energy and the cosmological constant

In the 1990's two independent teams (Riess et al. 1998; Perlmutter et al. 1999) studying distant supernova came to the shocking conclusion that instead of the rate of expansion of the Universe slowing down as expected, it was in fact accelerating. This strange feature of our Universe is now attributed to dark energy, a fluid which according to Equation 1.20 must have equation of state parameter $w_{DE} < -1/3$. It thus has a negative pressure and violates the strong energy condition which stipulates that

$$\rho + p \geq 0 \quad \text{and} \quad \rho + 3p \geq 0. \quad (1.32)$$

When Friedmann first used the Einstein field equations in a cosmological sense he found that they naturally described dynamic universes. Einstein however was a believer in a static and infinite universe and, in what he would later go on to describe as the ‘greatest blunder’ of his lifetime, modified the field equations to include a constant term to counteract the force of gravity. He thus missed the opportunity to predict the expansion of the Universe before it was confirmed observationally. Such a universe is inherently very unstable, as a minor deviation from equality would result in the universe either collapsing or expanding. For Einstein’s static universe, the field equations then became,

$$G_{\mu\nu} - \Lambda g_{\mu\nu} = 8\pi G T_{\mu\nu}, \quad (1.33)$$

where the constant Λ is now known as the cosmological constant and forms a crucial part of the standard model of cosmology. The Friedmann equations are thus also modified due to the introduction of Λ and become,

$$\left(\frac{\dot{a}}{a}\right) = \frac{8\pi G}{3}\rho - \frac{K}{a^2} + \frac{\Lambda}{3}, \quad (1.34)$$

$$\frac{\ddot{a}}{a} = -\frac{4\pi G}{3}(\rho + 3p) + \frac{\Lambda}{3}. \quad (1.35)$$

From these equations one can describe a static universe (which was later ruled out by observations; see Section 1.2.3). If however, $\Lambda > 0$, one can obtain $\ddot{a} > 0$, corresponding to the accelerated state that our Universe is currently experiencing. The energy associated with a cosmological constant is indistinguishable from the effect of a vacuum energy despite

the very different nature of these phenomena. We thus do not attempt to distinguish them here and simply write the dark energy equation of state parameter as $w_{DE} = -1$. According to the Equation 1.25 the energy density of such a fluid remains constant with time and as the universe expands. This means that even if its initial energy density is very small, it will eventually dominate the matter and radiation components in an eternally expanding universe. The scale factor then evolves as,

$$a(t) \propto e^{H_0 t}, \quad (1.36)$$

and so we see that a dark energy dominated universe expands exponentially. This solution is referred to as a de Sitter universe.

Cosmic evolution

We can now write the former equations in terms of the the dimensionless energy components,

$$\Omega_m \equiv \frac{\rho_m}{\rho_{cr}}; \quad \Omega_r \equiv \frac{\rho_r}{\rho_{cr}}; \quad \Omega_{DE} \equiv \frac{\rho_\Lambda}{\rho_{cr}} = \frac{\Lambda c^2}{3H^2}, \quad (1.37)$$

with any energy density excess is attributed to a curvature term such that

$$\Omega_K = 1 - \Omega_m - \Omega_r - \Omega_\Lambda, \quad (1.38)$$

We can then re-write the Friedmann equation as

$$H^2(a) = H_0^2 [\Omega_m a^{-3} + \Omega_{DE} a^{-4} + \Omega_{DE} a^{-3(w+1)} + \Omega_K a^{-2}]. \quad (1.39)$$

Finally we want to define the cosmic evolution function $E(a)$, the function for which the expansion history of the Universe, $H(a)$, can be expressed in terms of its current value H_0 so that $H^2(a) = H_0^2 E^2(a)$, as

$$E^2(a) = \Omega_m a^{-3} + \Omega_{DE} a^{-4} + \Omega_{DE} a^{-3(w+1)} + \Omega_K a^{-2}. \quad (1.40)$$

This equation nicely illustrates how the importance of each parameter on the expansion of the Universe changes with time. We see that at early times, the radiation term is the most dominant component and this is followed by a period of matter domination. Modern experimental results indicate the we presently live in a period post-matter domination and the current universe is dominated by dark energy or the cosmological constant.

1.2.3 The Expanding Universe

Hubble's Law

In 1929, Hubble measured the distances to a number galaxies by observing Cepheid variable stars hosted by them with the 100-inch Hooker Telescope. He combined these measurements with data of their speed of approach or recession, provided by Slipher, to produce a

plot of speed against distance (as seen in Figure 1.1. In one of the most important pieces of observational evidence in cosmology he noticed that all, except for the closest galaxies, were moving away from us. Further, he found that the greater the distance, the greater the apparent speed of recession:

$$\mathbf{v} = H_0 \mathbf{r}, \quad (1.41)$$

where \mathbf{v} and \mathbf{r} are the speed of recession and distance to the galaxy respectively. This is now known as Hubble's law and H_0 is called the Hubble parameter. The interpretation of this is that the Universe is expanding which, as we showed earlier, is a natural property of cosmological world models.

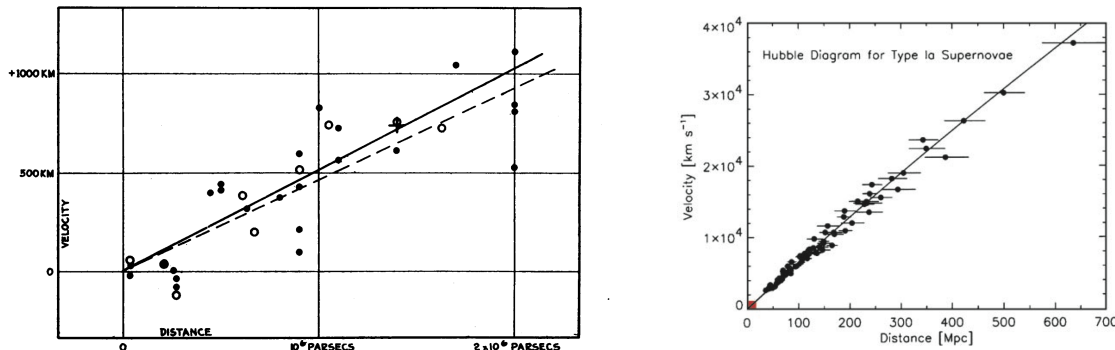


Figure 1.1: *Left*: The original Hubble diagram (with the incorrect unit on the velocity axis which should be in km s^{-1}) from 1929 showing the radial velocity of galaxies as a function of their distance. It is relatively easy to measure the velocity of galaxies from the Doppler shift in their spectral lines. Measuring the distance however is somewhat more challenging. Hubble significantly underestimated the distances to the galaxies and thus obtained an extremely high value for the Hubble constant. *Right*: A more recent Hubble diagram, taken from [Jha \(2002\)](#) which measured the distances to galaxies by using supernova. This allowed for the Hubble expansion to be proved at much greater distances. The small red square in the bottom-left corner is the region covered by the original Hubble diagram.

Although it is true that we observe all galaxies receding from us as if we were at the centre of the Universe, the same is true for any other observer elsewhere in the Universe. This leads us to conclude that at some point in the distant past, everything in the Universe was much closer together. Extrapolating back to very-early times in the history of the Universe we arrive at the conclusion that the Universe must have been in an incredibly hot and dense state which then underwent a period of rapid outwards expansion. This is known as the Big Bang and forms the basis of the prevailing model for our cosmological origins: Big Bang Cosmology.

Redshift

When performing observations of astrophysical sources such as stars or galaxies, one notices that the light they emit has an emission spectrum with very sharp spectral lines. Also, hot radiation traveling through cooler matter in stellar atmospheres excites the atoms and is absorbed at well defined wavelengths which results in very clear characteristic dark absorption lines in the measured spectrum. By studying how these spectral lines are Doppler shifted as a result of the expansion of the Universe it is possible to define a useful measure of the distance to the light emitting object. Consider radiation emitted by stars and distant galaxies with wavelength $\lambda_{rest} = c/v_{rest}$ at time t in the reference frame of the star or galaxy. The cosmological expansion of the Universe causes the wavelength to be stretched to λ_{obs} when observed by an observer on the Earth. The shift in the spectrum is in the red direction so $\lambda_{obs} > \lambda_{rest}$ and we thus call this measure the redshift

$$z = \frac{\lambda_{obs} - \lambda_{rest}}{\lambda_{rest}}. \quad (1.42)$$

The ratio of the wavelengths actually measured by the observer on Earth would then be

$$1 + z = \frac{\lambda_{obs}}{\lambda_{rest}} = \frac{1}{a(t)}. \quad (1.43)$$

It is important here to note that the cosmological redshift is caused by the expansion of the Universe i.e., only the increase in the scale factor $a(t)$ with t , and not the peculiar velocities of the receding objects. It is however possible in the case of nearby stars and galaxies to observe a kinematic effect which can be larger than the cosmological expansion rate on those scales. This may result in a Doppler redshift or a Doppler blueshift for a receding or approaching source respectively such as for the Andromeda galaxy.

1.2.4 The growth of structure

Up until this point I have set the framework for a universe which is both homogeneous and isotropic. However, one does not have to look very closely at the Universe to see that this is clearly not the case. We observe structure throughout the cosmos in the form of stars, galaxies and galaxy clusters and even on very much larger scales e.g., in the galaxy distribution observed by SDSS (see Figure 1.2). The filamentary structure that we observe today has evolved from small perturbations in the early Universe under the influence of gravity until they eventually collapse to form virialised objects. As time progresses, it is possible to form ever larger structures and as the largest and most recently virialised objects to form, galaxy clusters play an important role in our understanding of the physics involved. They also mark the transition region between linear and non-linear gravitational dynamics. Further their distribution both spatially and in mass can tell us a great deal about the underlying cosmological model. We study the physics behind the growth of structure over cosmic time through large N-body simulations that trace the matter distribution of the Universe from when it was randomly distributed across the early Universe and evolving it to

the point where we see structure on large scales as we observe today. Figure 1.2 shows how the galaxy distribution through the Universe, as observed by the Sloan Digital Sky Survey (Eisenstein et al. 2011) exhibits a large degree of structure, even on very large scales. This notion is also supported by massive N-body simulations such as the Millennium simulation Springel et al. (2005) support this view.

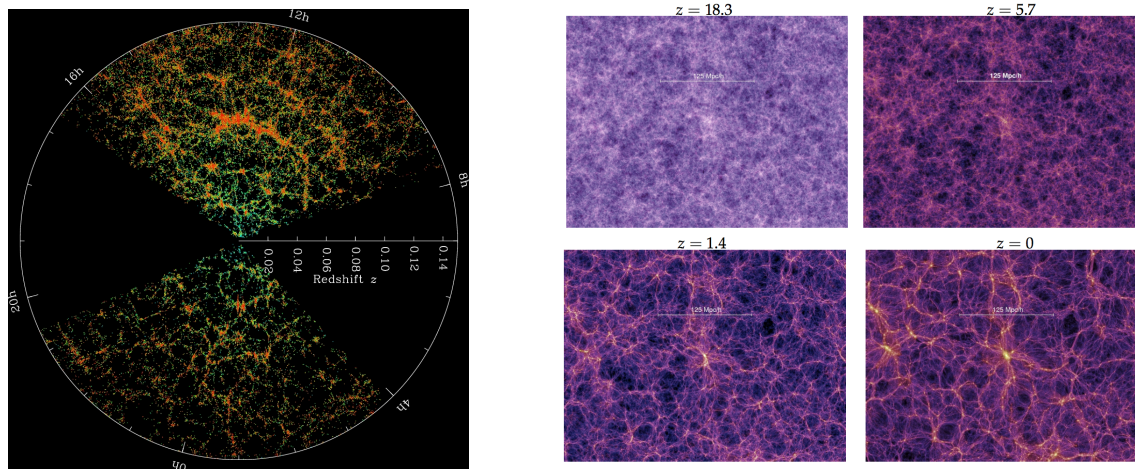


Figure 1.2: Observations of the Universe (left; SDSS) and simulations (right; Millennium) of structure formation history of the Universe show that the Universe is indeed largely inhomogeneous, with a high amount of structure present even on very large scales. Both of these images highlight the filamentary nature of structure in the Universe, forming what we call the Cosmic Web. Galaxy clusters typically appear at nodes in this web-like structure and we see that the bulk of the volume of the Universe lies in vast, under-dense regions called voids. Image credit: M. Blanton and the Sloan Digital Sky Survey; Springel et al. (2005)

Linear theory

To begin with our study of how structures form and grow, we first define the dimensionless density contrast as

$$\delta(\mathbf{x}) = \frac{\rho(\mathbf{x}) - \bar{\rho}}{\bar{\rho}}, \quad (1.44)$$

where $\rho(\mathbf{x})$ is the matter density field as a function of position \mathbf{x} and $\bar{\rho}$ is its average value computed over a large, representative volume of the Universe. The growth of structure can be considered in the framework of Newtonian gravity since the effects of space-time curvature only need to be accounted for on very large scales, comparable to the Hubble radius. The standard Newtonian equations for the evolution of the density due to gravity can be extended to include the scale factor, making them to be appropriate for the treatment of

our expanding Universe. The equations are then,

$$\dot{\delta} + \frac{1}{a} \nabla \cdot [(1 + \delta)\mathbf{u}] = 0; \quad \text{continuity equation,} \quad (1.45)$$

$$\dot{\mathbf{u}} + H\mathbf{u} + \frac{\mathbf{u} \cdot \nabla \mathbf{u}}{a} = -\frac{1}{a} \left[\frac{\nabla p}{\rho} - \nabla \Phi \right]; \quad \text{Euler equation,} \quad (1.46)$$

$$\nabla^2 \Phi = 4\pi G \bar{\rho} a^2 \delta; \quad \text{Poisson equation.} \quad (1.47)$$

The continuity equation states that mass is always conserved, the Euler equation formulates the relation between the acceleration of an element in the fluid and the gravitational attraction and finally the Poisson equation specifies the Newtonian nature of gravity. When dealing with small perturbations and low peculiar velocities, these equations can be linearised. Neglecting second order terms in δ and \mathbf{u} , differentiating the continuity equation with respect to time and substituting in the Euler and Poisson equations we arrive at the second order differential equation for the density contrast. This equation describes the Jeans instability and is given as,

$$\ddot{\delta} + 2H\dot{\delta} = \frac{\nabla^2 p}{a^2 \rho} + 4\pi G \bar{\rho} \delta, \quad (1.48)$$

where the term $2H\dot{\delta}$ expresses the effect of the expanding background in suppressing the growth of perturbations and is called the Hubble drag. Assuming that the matter content of the Universe is dominated by dark matter, a pressureless self-gravitating fluid, the first term on the right of Equation 1.48 vanishes and the equation is then independent of any spatial derivatives. Since none of the coefficients depend on position we can find a solution of the form,

$$\delta(\mathbf{x}, t) = \tilde{\delta}(\mathbf{x})D(t). \quad (1.49)$$

The differential equation above has two linearly independent solutions, one of which increases while the other decreases with time. Since after some time, the decreasing solution becomes irrelevant, we consider only the increasing solution which we denote $D_+(t)$ (called the *growth factor*) and the density contrast becomes,

$$\delta(\mathbf{x}, t) = \delta_+(\mathbf{x})D_+(t) + \delta_-(\mathbf{x})D_-(t). \quad (1.50)$$

This solution shows us that the spatial shape of the fluctuations does not change with time and that they are frozen in comoving coordinates. It is only the amplitude, or growth factor, that increases. For arbitrary values of the density parameter, the growth factor takes the form,

$$D_+(a) \propto \frac{H}{H_0} \int_0^a \frac{da'}{[a'E(a')]^3} = \frac{H(t)}{H_0} \int_0^a \frac{da'}{(\Omega_m a'^{-1} + \Omega_r a'^{-2} + \Omega_\Lambda a'^2)^{3/2}}, \quad (1.51)$$

where we have used the cosmic evolution function given in Equation 1.40 and assumed a flat universe with a cosmological constant. From this and normalising the growth factor

so that $D_+(t_0) = 1$, we would expect that $\delta_+(\mathbf{x})$ would still represent the distribution of density fluctuations of the Universe at the present, provided the evolution remains linear. This is however not the case as the fluctuations become large enough that the condition $|\delta| \ll 1$ breaks down and we need to include the terms that were neglected here. To study this non-linear regime of structure formation we rely on numerical procedures and N-body simulations. We can however find useful, explicit solutions to the above mentioned linear equations, one of which we considered earlier: an Einstein-de Sitter universe with $\Omega_m = 1$ and $\Omega_\Lambda = 0$. Previously, we saw that for this model, $a(t) \propto t^{2/3}$ and so, for the growing mode, we arrive at the solution,

$$D_+(t) \propto t^{2/3} = a(t), \quad (1.52)$$

and see that the growth factor is just equal to the scale factor. The solution for the decreasing mode can be found similarly as $D_-(t) = t^{-1}$ but as mentioned earlier, this mode decays rapidly and becomes unimportant and it does not have a large influence on the evolution of the perturbations.

Non-linear growth and spherical collapse

The linear perturbation theory that we have described has a rather limited range in which it can be applied. The evolution of galaxy clusters, the focus of this thesis, for instance cannot be treated within the linear regime. Typically, extensions to the linear theory involving higher order terms of δ and $|\mathbf{u}|$ require significant amounts of mathematical effort to obtain solutions. There are however some interesting cases for which analytical solutions representing the mass distribution of the Universe can be found.

The particular case for which we can find an analytical solution is that of a spherical perturbation with a uniform density. In such a case, we can treat each individual perturbation as a homogeneous universe of its own and its evolution can be computed based on its local density parameters. Even though this model is based on very restrictive assumptions, it is useful for describing the processes involved in the formation and evolution of virialized dark matter halos, which are a good representation of galaxy clusters.

To proceed, we consider a spherical perturbation and for the sake of simplicity, assume that the background is described by an Einstein-de Sitter model. The density parameter which characterises this perturbation, denoted by $\Omega_p(t)$, is then initially,

$$\Omega_p(t_i) = \frac{\rho(t_i)(1 + \delta_i)}{\rho_c(t_i)} = \Omega(t_i)(1 + \delta_i), \quad (1.53)$$

where $\rho(t)$ and $\Omega(t)$ refer to the background. The expansion of the perturbation is then,

$$\left(\frac{\dot{a}}{a_i}\right)^2 = H_i^2 \left[\Omega_p(t_i) \frac{a_0}{a} + 1 - \Omega_p(t_i) \right]. \quad (1.54)$$

Structure will form if the perturbation stops expanding with the background due to its gravity and turns around to start collapsing on itself. The condition which ensures this is

$\Omega_p(t_i) > 1$. The density of the perturbation at the time it turns around t_m is

$$\rho_p(t_m) = \rho_c(t_i)\Omega_p(t_i) \left[\frac{\Omega_p(t_i) - 1}{\Omega_p(t_i)} \right]^3. \quad (1.55)$$

and writing the Hubble parameter with the perturbation H_i , we see that the time it takes to reach its maximum size before beginning to collapse is,

$$t_m = \frac{\pi}{2H_i} \frac{\Omega_p(t_i)}{[\Omega_p(t_i) - 1]^{3/2}} = \left[\frac{3\pi}{32G\rho_p(t_m)} \right]. \quad (1.56)$$

At this time, the density of the background is

$$\rho(t_m) = \frac{1}{6\pi G t_m^2}. \quad (1.57)$$

We thus obtain the value for the perturbation overdensity in terms of the ratio between the density of the perturbation and the density of the background,

$$\delta_+(t_m) = \frac{\rho_p(t_m)}{\rho(t_m)} - 1 = \left(\frac{3\pi}{4} \right)^2 - 1 \approx 4.6. \quad (1.58)$$

Extrapolating in the linear theory on the other hand would have yielded $\delta_+(t_m) \approx 1.07$, which clearly demonstrates that the linear theory underestimates the overdensities at turnaround.

One would expect that once the perturbation starts to collapse, it would, after a time $2t_m$ have collapsed to a single point with an infinite density. This only happens if the system remains perfectly symmetric and pressure effects are ignored, which due to the presence of baryons, one cannot do for the real Universe. In real halos, minor departures from the spherical symmetry will introduce the formation of shocks and pressure gradients which will heat the material in the perturbation. At some point, the perturbation will end up in a state of equilibrium. In other words, the structure is virialized.

The virial theorem gives us the relation between kinetic and potential energy ($E_{\text{kinetic}} = -E_{\text{potential}}/2$) and assuming that at t_m all of the energy was in the form of potential energy, we get,

$$E = E_{\text{potential}} = -\frac{3}{5} \frac{GM^2}{R_m}, \quad (1.59)$$

where R_m is the radius of the perturbation at the turnaround time t_m . Further, from the virial theorem, we have the total energy of a virialized system,

$$E_{\text{virial}} = -\frac{1}{2} \frac{3GM^2}{5R_{\text{virial}}}, \quad (1.60)$$

and so we see that $R_{\text{virial}} = R_{\text{max}}/2$ and $\rho_p(t_{\text{virial}}) = 8\rho_p(t_{\text{max}})$. Assuming that the background model is still described by an Einstein-de Sitter model and noting that the volume

is 1/8 of its value at t_{max} , the ratio between the density of the perturbation and that of the background is,

$$\Delta_c = \frac{\rho_p(t_c)}{\rho(t_c)} \approx 180, \quad (1.61)$$

which corresponds to an extrapolated linear perturbation of $\delta_c = 1.68$. This last value is important when attempting to find theoretical estimates of the halo mass function, which will be discussed later. The value $\Delta_c \approx 180$ is the reason we typically define R_{200} , the radius at which the average density is 200 times the critical density, as the cluster radius. A typical virialized halo with a final radius of $1.5h_{70}^{-1}$ Mpc originates from a region with an initial size of $10h_{70}^{-1}$ Mpc, approximately 6 times larger.

Statistics of density perturbations

A useful way of thinking about cosmological perturbations is to consider them as a superposition of plane waves. While these perturbations are still evolving linearly, the plane waves evolve independently. We thus expect that the final structure that is formed will depend on the initial mass and length scales of the fluctuations and how each of these different scales have grown relative to one another. This provides a better description of the matter distribution than if one were to divide the Universe into independently evolving volume elements because once the gravitational forces become strong enough, neighbouring cells affect the evolution of each other.

In order to treat the perturbations as plane waves we must, instead of working in real space, perform our calculations in Fourier space. To do this, we consider a volume V e.g., a cube with a side length L which is very much larger than the maximum scale at which there is structure in the perturbations. In this case, V can be thought of as a representative realisation of the Universe. The density contrast can be expressed as a Fourier series,

$$\delta(\mathbf{x}) = \sum_{\mathbf{k}} \delta_{\mathbf{k}} \exp(i\mathbf{k} \cdot \mathbf{x}) = \sum_{\mathbf{k}} \delta_{\mathbf{k}}^* \exp(-i\mathbf{k} \cdot \mathbf{x}). \quad (1.62)$$

Assuming that the boundary conditions at each surface of the cube are periodic, the wavevector \mathbf{k} has components,

$$k_i = n_i \frac{2\pi}{L}; \quad n_i \in \mathbb{Z}; \quad i = x, y, z. \quad (1.63)$$

The density contrast expressed by its Fourier transform, is then given by

$$\delta_{\mathbf{k}} = \frac{1}{V} \int d\mathbf{x} \delta(\mathbf{x}) \exp(-i\mathbf{k} \cdot \mathbf{x}). \quad (1.64)$$

Assuming we had chosen a different volume V' , the Fourier series of the perturbations enclosed would be represented by different coefficients $\delta_{\mathbf{k}}$. We can thus break the universe up into an ensemble of volumes, each representing a realisation of a universe itself. The mean value of the perturbations in all realisations is equal to zero by definition but its variance

on the other hand is not. Assuming that the density field is statistically homogenous and isotropic we see that the variance is,

$$\sigma^2 \equiv \langle \delta^2 \rangle = \frac{1}{V} \sum_{\mathbf{k}} \delta_k^2 \rightarrow \frac{1}{2\pi^2} \int_0^\infty P(k) k^2 dk, \quad (1.65)$$

where we have taken the limit $V \rightarrow \infty$ and we have simply defined $\delta_k^2 \equiv P(k)$ in this limit.

The quantity $P(k)$ is called the power spectrum and it has no dependence on the direction of \mathbf{k} but only on $k = |\mathbf{k}|$. The variance thus does not depend on spatial position and so contains no information about the spatial structure of the perturbations, but since the perturbations evolve, it does depend on time. The power spectrum of the density fluctuations then depends only on the modulus of the wave-vector, and it describes the level of structure as a function of the length-scale i.e. the larger the value for $P(k)$ the higher the amplitude of the fluctuations with a length-scale of $2\pi/k$.

The typical form the power spectrum takes is

$$P(k) = Ak^{n_s}. \quad (1.66)$$

This form is predicted by single-field inflation models where n_s is called the spectral index. The most constraining results obtained for the spectral index of our Universe come from the Planck Collaboration who found a value of $n_s = 0.9603 \pm 0.0073$ (Planck Collaboration XVI et al. 2014).

The overall shape of the power spectrum can be derived theoretically but its normalisation must be determined empirically. We can do this by filtering the density fluctuations on an appropriate scale that is sufficiently large that linear theory remains valid but small enough that one can still observe large amounts of structure. We thus perform a statistical evaluation of the fluctuation field after applying some kind of spatial filter function to give a resolution scale R . The mean mass inside a sphere with radius R is given by

$$\langle M \rangle = \frac{4}{3} \langle \rho \rangle R^3, \quad (1.67)$$

and then taking the average over all spatial volumes, the mass variance inside this volume is

$$\sigma_M^2 = \frac{\langle \delta M^2 \rangle}{\langle M^2 \rangle} = \frac{1}{2\pi^2} \int_0^\infty P(k) W^2(kR) k^2 dk \quad (1.68)$$

where we have used the Fourier decomposition of the density perturbations given in Equation 1.64, the expression for the variance in Equation 1.65 and the function $W(kr)$ is a window function given by

$$W(kr) = \frac{3(\sin kR - kR \cos kR)}{(kR)^3}. \quad (1.69)$$

Spatial filtering such as this is equivalent to taking a convolution of the density field with a function W_R . A good choice for the filtering scale that we can use to derive the

normalisation of the power spectrum is $R = 8 h^{-1}$ Mpc. This value was initially chosen because the variance of galaxy counts in spatial bins of this size is similar to the mean value. This corresponds well to the value of $10h^{-1}$ Mpc that we derived earlier for the scale from which clusters collapse and the mass scale at these filtering lengths is $M \sim 5 \times 10^{14} M_{\odot}$. We refer to the normalisation of the power spectrum on this length scale of $R = 8 h^{-1}$ Mpc as σ_8 and it strongly influences the number of galaxy clusters that form in the Universe.

The halo mass function

The mass function (MF), defined as the number density of virialized halos of a given mass at a given redshift, depends strongly on cosmological parameters such as Ω_m and σ_8 and is defined by the relation,

$$dN = n(M)dM. \quad (1.70)$$

This means that counting the number of galaxy clusters we observe and measuring their masses and redshifts can tell us a great deal about the underlying cosmology. Here we derive the MF as was first described by Press & Schechter, and we will see later that this observable property of the Universe provides a useful tool in cosmological analyses.

In the current cosmological paradigm of Λ CDM, galaxies and large scale structure are built up hierarchically with the smallest structures such as stars and galaxies forming first and clumping together to form the largest structures such as galaxy clusters at later times. If we assume that the primordial density perturbations were Gaussian in nature, then their phases are random and the probability that at some point the linearly-evolved density field δ_M exceeds the critical density contrast δ_c is,

$$\mathcal{P}_{>\delta_c}(\delta_M) = \frac{1}{\sqrt{2\pi\sigma_M^2}} \int_{\delta_c}^{\infty} \exp\left(-\frac{\delta_M^2}{2\sigma_M^2}\right) d\delta_M, \quad (1.71)$$

where the density field has been filtered on a spatial scale R , (corresponding to a mass M) and σ_M is as expressed in Equation 1.68. In the Press-Schechter formalism, this probability describes the mass fraction of collapsed objects with mass greater than M , $F(> M)$. In this assumption however, the *cloud-in-cloud problem* arises and this equation predicts that only half of the Universe is a part of a system of any mass. This problem originates from incorrectly accounting for regions which are under-dense. Considering an object that has $\delta > \delta_c$ when filtered at a scale R , one would expect that this object would correspond to a system with mass greater than $M(R)$. Equation 1.71 has no problem dealing with this. For an object with a lower density $\delta < \delta_c$ however, there is a possibility that this object would have $\delta > \delta_c$ at a later stage when the field is filtered with $R' > R$. Such an object should then also be included as a system with mass greater than M . This is neglected in this formalism and thus Equation 1.71 underestimates $F(> M)$ by a factor of 1/2. In the Press-Schechter analysis, it is therefore necessary to multiply throughout by a factor 2. The result of this is that we find that the number density of collapsed objects with masses

in the range $M \rightarrow M + dM$ is given by

$$n(M, t)dM = 2 \frac{\rho_m}{M} \left| \frac{d\mathcal{P}_{>\delta_c}}{d\sigma_M} \right| \left| \frac{d\sigma_M}{dM} \right| dM, \quad (1.72)$$

$$= \sqrt{\frac{2}{\pi}} \frac{\rho_m}{M^2} \frac{\delta_c}{\sigma_M} \exp\left(-\frac{\delta_c^2}{2\sigma_M^2}\right) \left| \frac{d \ln \sigma_M}{d \ln M} \right| dM. \quad (1.73)$$

The Press-Schechter formalism presented here is based on a number of strong assumptions and simplifications. Included among these are that structures form from the collapse of spherically symmetric regions with no substructures; the choice of the filter function $W(kr)$; and that the *cloud-in-cloud* problem is solved by the ‘fudge-factor’ of two. Given the simplicity of this model, it may be surprising how accurately this method is able to describe the observed abundance of halos. In cosmological studies however, the mass function used is typically calibrated through large numerical simulations. These simulations still rely on the Press-Schechter approach but the parameters are derived from the simulations themselves e.g., Tinker et al. (2008a); Bocquet et al. (2016). The cosmological parameters enter the mass function through σ_M which depends on the cosmological density parameters and the power spectrum. When studying the mass function of galaxy clusters, which are the most massive collapsed objects, we are probing the exponential tail and so the MF is very sensitive to the cosmological parameters. Thus a reliable sample of massive clusters enables one to place stringent constraints on the cosmological parameters.

Due to the limitations of the Press-Schechter formalism, universal functions that can accurately describe simulation results have been sought after. One common functional form is given by Tinker et al. (2008) and the mass function can be recast as

$$\frac{dn}{dM} = f(\sigma) \frac{\bar{\rho}_m}{M} \frac{d \ln \sigma^{-1}}{dM}. \quad (1.74)$$

Here the function $f(\sigma)$ is not expected to vary much with redshift, is only weakly dependent on the cosmology, and is parametrised as,

$$f(\sigma) = A \left[\left(\frac{\sigma}{b} \right)^{-a} + 1 \right] \exp\left(-\frac{c}{\sigma^2}\right), \quad (1.75)$$

and σ is as given in Equation 1.68. The parameter A gives the amplitude of the mass function, a and b determine the slope and amplitude of the low-mass power law respectively and c sets the scale at which the number of halos of a given mass decreases exponentially. These parameters need to be calibrated by simulations.

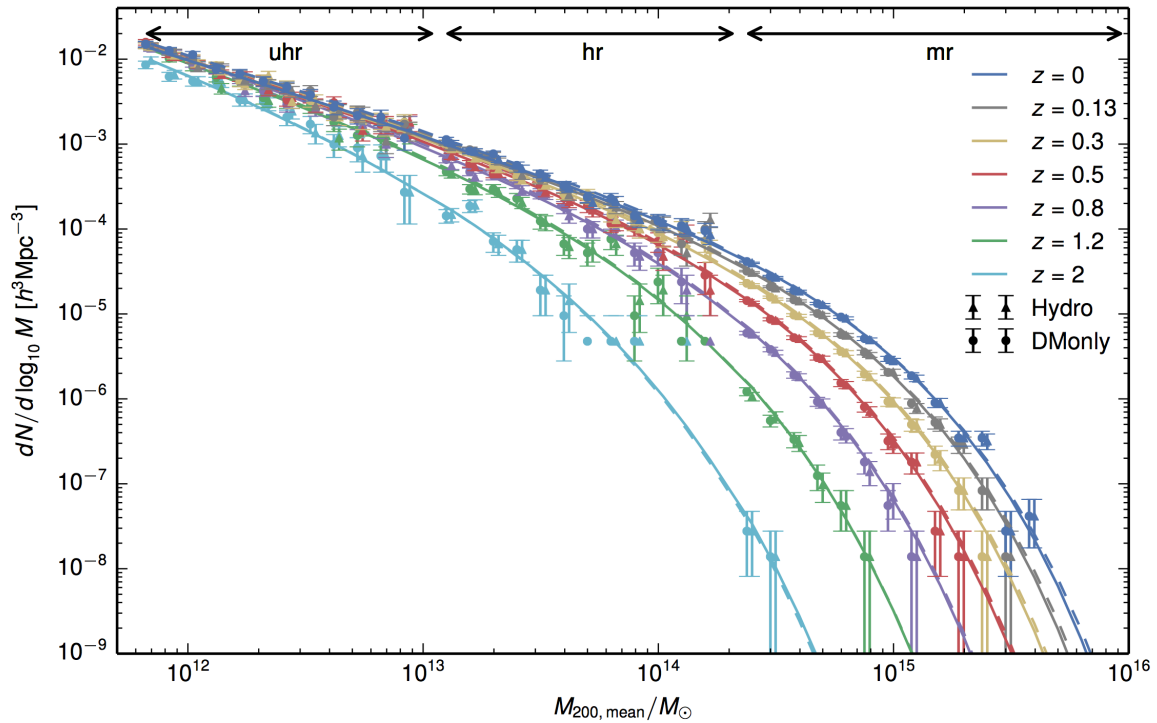


Figure 1.3: The mass function derived from the *Magneticum* simulations over a variety of redshifts intervals. The mass function was measured by extracting halos from N-body simulations consisting purely of dark matter (DMonly) and also from hydrodynamical simulations featuring baryons as well (Hydro). The mass function is measured over a variety of redshift slices and it is clear that the later in time the more massive halos have formed. The lines here are the best-fitting functions for the mass function. Image taken from [Bocquet et al. \(2016\)](#).

1.3 Clusters of galaxies

The multi-component nature of galaxy clusters marks them as ideal candidates for multi-wavelength studies and observations. The bulk of the mass contained in clusters is in the form of dark matter which, although not yet directly observed, can be measured through its distorting effect on distant background galaxies through gravitational lensing. The mass of dark matter in a cluster can also be inferred through the velocity dispersion of cluster member galaxies or, assuming hydrostatic equilibrium, through measurement of the hot gas that makes up the intracluster medium. Most of the baryonic component of galaxy clusters is in the form of an extremely hot ($\sim 10^7$ K) diffuse gas which is detected either directly through its X-ray emission or indirectly via its impact on the Cosmic Microwave Background through the Sunyaev-Zel'dovich (SZ) effect. The merging of galaxy clusters is an incredibly energetic process that can cause the acceleration of electrons to relativistic speeds. This causes them to emit synchrotron radiation which can be observed at radio wavelengths. Thus, observations of clusters over a wide range of wavelengths from radio-waves to gamma-rays are necessary to highlight the variety of cluster components and properties.

When constructing catalogues of galaxy clusters there are a number of factors which need to be taken into account. Some of the requirements are the angular scale, sensitivity of the survey and the redshift range to be examined. Further, the catalogue should not miss any clusters (completeness) and not contain any spuriously detected sources (purity). For cosmological purposes, it is also crucially important to have a complete knowledge of the selection function in terms of the position, redshift and the observable being used for the selection. For an analysis of the cluster mass function one should also ensure that the observable properties correlate strongly with the cluster mass.

In this section we discuss the physics of the various components and properties of galaxy clusters that are accessible at various wavelengths, as well as how cluster catalogues are constructed taking advantage of their respective observable quantities.

1.3.1 X-ray Properties of Clusters

The X-ray emission of massive galaxy clusters was first detected by the UHURU X-ray satellite in the 1970s (E. Kellogg, H. Gursky, H. Tananbaum 1972; Forman et al. 1978). Since then, the field of X-ray astronomy has undergone massive advancements as both the X-ray optics and detectors have improved. ROSAT (Trümper 1993) was able to detect the X-ray emission of lower mass systems across the entire extragalactic sky and later, XMM (Barré, Nye & Janin 1999) and Chandra (Weisskopf et al. 2000) spent a significant amount of their time observing galaxy clusters. Observations of galaxy clusters and using them to derive strict constraints on cosmological parameters are a key objective of eROSITA (Merloni et al. 2012). Figure 1.4 illustrates a wavelet-filtered XMM image containing 2 detected clusters and GROND *gri* three-colour images of the cluster positions overlaid.

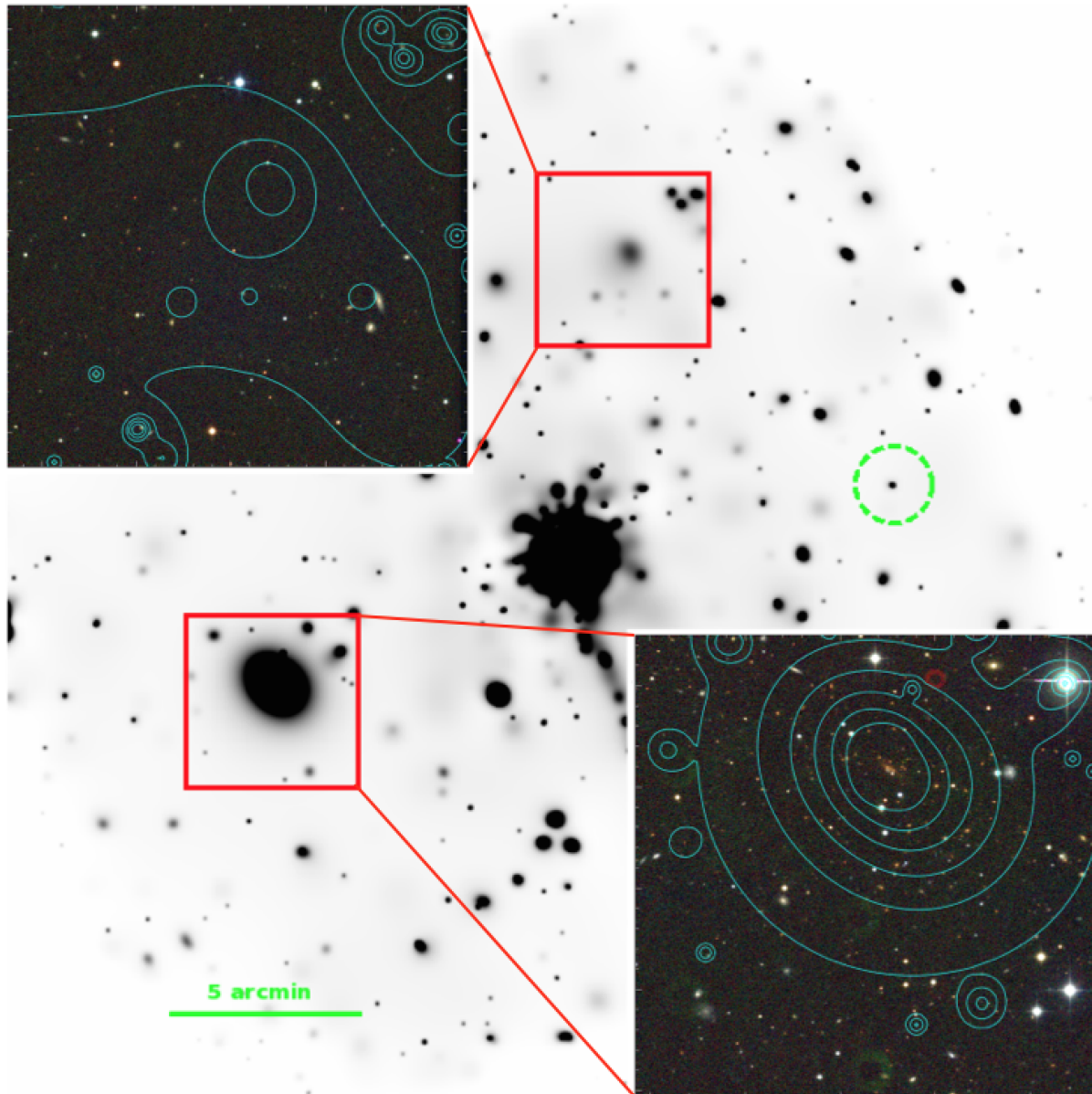


Figure 1.4: Wavelet filtered XMM-Newton (M1+M2+PN) image, ObsID: 0555020201.20ks. Red boxes show the locations of two serendipitously detected clusters, X-CLASS 2305 ($z = 0.62$) and X-CLASS 2304 (distant candidate; see discussion in Section 3.6.3) along with the GROND *gri* image where the cyan contours represent the X-ray distribution. The PI target, RBS 1055 is located near the centre of the pointing. For comparison, a point source is indicated by the dashed-green circle.

Mechanisms of emission

Galaxy clusters are among the brightest extragalactic X-ray sources, with AGN being the only known objects that are significantly brighter. Clusters are usually differentiated from AGN in data due to the extended nature of their emission, as opposed to the point-like nature of AGN. The typical X-ray luminosity of galaxy clusters is $L_X \sim 10^{43} - 10^{45} \text{ erg s}^{-1}$ and extends over regions of up to 1 Mpc, and in extreme cases even larger. Here I summarise two main mechanisms responsible for the X-ray emission originating in clusters namely, thermal bremsstrahlung and line emission.

Thermal bremsstrahlung

The majority of the baryonic component of the Universe is in the form of diffuse intergalactic gas. In clusters, this gas becomes gravitationally compressed, greatly increasing its density and temperature, leading to the emission of a large amount of X-rays. The bulk of this emission comes from thermal bremsstrahlung. In this process a free electron interacts with a positively charged ion in the intra-cluster medium (ICM), causing it to be accelerated. In order to obey the laws of conservation of momentum and energy, a photon must be emitted. The energy of these interactions is such that the photon emitted has an energy that lies in the X-ray part of the electromagnetic spectrum. The temperature of the gas can be computed from the spectral shape of the emission and it is typically found to be in the range $T \sim 10^7 - 10^8 \text{ K}$, which translates to about $k_B T \sim 1 - 10 \text{ keV}$.

The thermal bremsstrahlung has an emissivity that is proportional to the square of the gas density and is described by the equation,

$$\epsilon_\nu^{brems} \propto n_e n_i g^{brems}(\nu, T) T^{-1/2} \exp\left(-\frac{h\nu}{k_B T}\right), \quad (1.76)$$

where n_e and n_i are the number density of electron and ions (typically hydrogen). The factor $g(\nu, T) \sim 1 + \log(k_B T/h\nu)$ is a quantum mechanical correction factor called the Gaunt factor and is of order 1. The ICM typically behaves as a fully ionised plasma and thus the electron and ion number densities are approximately equal. As indicated by Figure 1.5, we see that for $h\nu \ll k_B T$ the bremsstrahlung spectrum is roughly constant whereas it experiences a step exponential cutoff when $h\nu \geq k_B T$ and the cutoff point on the temperature, i.e. for cooler clusters, the drop off starts at lower ν .

One can also determine the bolometric emissivity by integrating over all frequencies,

$$\epsilon_{bol}^{brems} = \int_0^\infty d\nu \epsilon_\nu^{brems} \propto \sqrt{\frac{T}{1\text{keV}}} \left(\frac{n_e}{10^{-3}\text{cm}^{-3}}\right)^2 \text{ ergs}^{-1}\text{cm}^{-3}, \quad (1.77)$$

where we have assumed a thermal plasma with solar metallicity. We see here that the emissivity is proportional to the square of the density which means we see more emission at the cluster centre than in the outskirts.

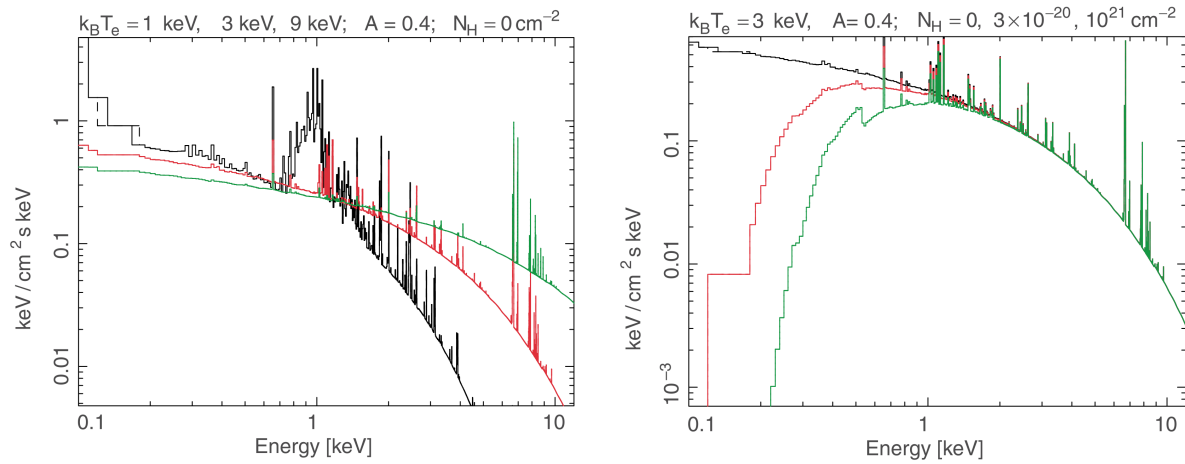


Figure 1.5: *Left*: The expected unabsorbed X-ray emission spectrum for three galaxy clusters with temperatures of $T=1$ keV (black), 3 keV (red) and 9 keV (green). The dominant component is the continuum emission from thermal bremsstrahlung. We see that the emission continues to higher photon energy (and therefore frequencies) for hotter clusters. Also included in this plot are radiation from atomic transitions and recombination which present as line features. Clearly, these are more important for the 1 keV cluster. *Right*: The unabsorbed spectrum of a $T = 3$ keV cluster (black) and as it would be observed taking photo-absorption into account with hydrogen column densities of $3 \times 10^{20} \text{ cm}^{-2}$ (red) and 10^{21} cm^{-2} (green). We see a cutoff in the spectrum at lower energies. Images courtesy of Schneider (2006).

Line emission

In addition to the thermal bremsstrahlung, the X-ray spectrum of clusters also contains significant line emission. The most prominent line comes from iron ions with just a single electron. Generally speaking, the hotter a gas is, the more its atoms are completely ionised and thus the line emission is weaker. So, for clusters with high temperatures ($k_B T \sim 10$ keV), the contribution from line emission is small but for clusters with low temperatures ($k_B T \lesssim 2$ keV), the total emission can be dominated by line emission from a variety of highly ionised atoms as illustrated in Figure 1.5. Apart from iron, other important line features originate from the ions of O, Mg, Si, S, Ar, Ca, and Ne. The specific emissivity for ions with an ionization potential χ_i of state i has the form,

$$\epsilon_\nu^{line} \propto \frac{g^{line}(\nu, T)}{T^{3/2}} \exp\left(-\frac{h\nu - \chi_i}{k_B T}\right). \quad (1.78)$$

Morphology of the X-ray emission

Based on the morphology of the gas distribution of a cluster, inferred from its X-ray emission one can classify a cluster as being either relaxed or disturbed. Relaxed clusters typically exhibit smooth X-ray contours with a peak centred on or near to a bright galaxy which is itself at the centre of the galaxy distribution and the surface brightness decreasing outwardly. These types of clusters typically have high X-ray luminosities and temperatures. Disturbed clusters display greater levels of irregularity and substructure and are normally indicative of on-going merger processes.

Hydrostatic equilibrium and the β -model

For relaxed clusters we can infer the total dynamical mass under the assumption of hydrostatic equilibrium. The assumption of hydrostatic equilibrium is motivated by considering the speed of sound of the gas in the cluster,

$$c_s \approx \sqrt{\frac{P}{\rho_{gas}}} = \sqrt{\frac{k_B T}{\mu m_p}} \sim 1000 \text{ km s}^{-1}, \quad (1.79)$$

where P is the pressure of the gas and ρ_{gas} is its density. This gives a crossing time for sound waves in a cluster of $\sim 7 \times 10^8$ yr which is far shorter than the age of a cluster which is itself approximated by the age of the Universe. Therefore, there is enough time for the smoothing out of any deviations from pressure equilibrium. The assumption of hydrostatic equilibrium thus appears to be reasonable.

Making the further assumption of spherical symmetry and relating the pressure to the gravitational potential, we obtain the total mass M (DM+baryons) enclosed by a radius r ,

$$M(r) = -\frac{r k_B T}{G \mu m_p} \left(\frac{d \ln n}{d \ln r} + \frac{d \ln T}{d \ln r} \right). \quad (1.80)$$

In order to make use of this relation however, one must first obtain accurate measurements of the gas mass and temperature. These are determined from the X-ray luminosity and the detected spectrum which of course, can only be observed in projection. The surface brightness profile at a position $\mathbf{x} = (r, \mathbf{R})$ on the sky is obtained by integrating the emissivity at each point along the line of sight giving,

$$S_X(\mathbf{R}) = -\frac{1}{4\pi} \int d\nu w(\nu) \int dr \frac{\epsilon_\nu^{brems}}{(1+z)^3}, \quad (1.81)$$

from which we can determine the density and temperature (from spectral fitting) by de-projection. This resulting profile is typically averaged in concentric annuli and a theoretical model is fit to it. One of the models which is often used to fit X-ray profiles of clusters is the β -model. This model is based not only on the assumption that the temperature of the gas is the same throughout the cluster but further that the underlying dark matter profile is also described by an isothermal distribution, such that $\rho_{gas}(r) \propto [\rho_{tot}]^\beta$, where β depends on the dynamical temperature and the gas temperature. Since the distribution of the intracluster medium is typically described by a King model (King 1966), we obtain a density profile for the gas of,

$$\rho_{gas}(r) = \rho_{gas,0} \left[1 + \left(\frac{r}{r_c} \right)^2 \right]^{\frac{3\beta}{2}}, \quad (1.82)$$

where r_c is called the core radius and determines the characteristic X-ray extent of the source. Typically clusters are found to have values for $r_c \sim 0.1 - 0.3 h^{-1} \text{Mpc}$ and index $\beta \sim 2/3$.

Departures from equilibrium

Obtaining accurate temperatures for clusters is often a rather difficult task. Since these measurements are emission-weighted, they are dominated by central regions of the cluster which have the highest density. One often notices that the central regions are cooler than the outskirts and as such we could end up underestimating the average temperature of the cluster. Another difficulty in earlier times was that X-ray telescopes such as ROSAT were mostly sensitive at low ($\lesssim 2.5 \text{keV}$) energies where the spectral form of ϵ_ν^{brems} is nearly flat (see Figure 1.5) and so measurements of temperature were difficult. By taking advantage of their superior angular and spectral resolution and range, Chandra and XMM-Newton allowed for the detection of temperature gradients and inhomogeneities in the ICM showing that it is not actually isothermal. Some examples of these departures from equilibrium are shown in Figure 1.6. By obtaining deep observations of galaxy clusters with Chandra, it is possible to identify large amounts of substructure even on very small scales relative to the total extent of the cluster. Hofmann et al. (2016) studied the thermodynamic perturbations in the X-ray halos of 33 massive clusters (an example is given in the left panel of 1.6). By making use of a gradient filtering edge detection method Sanders et al. (2016) was able

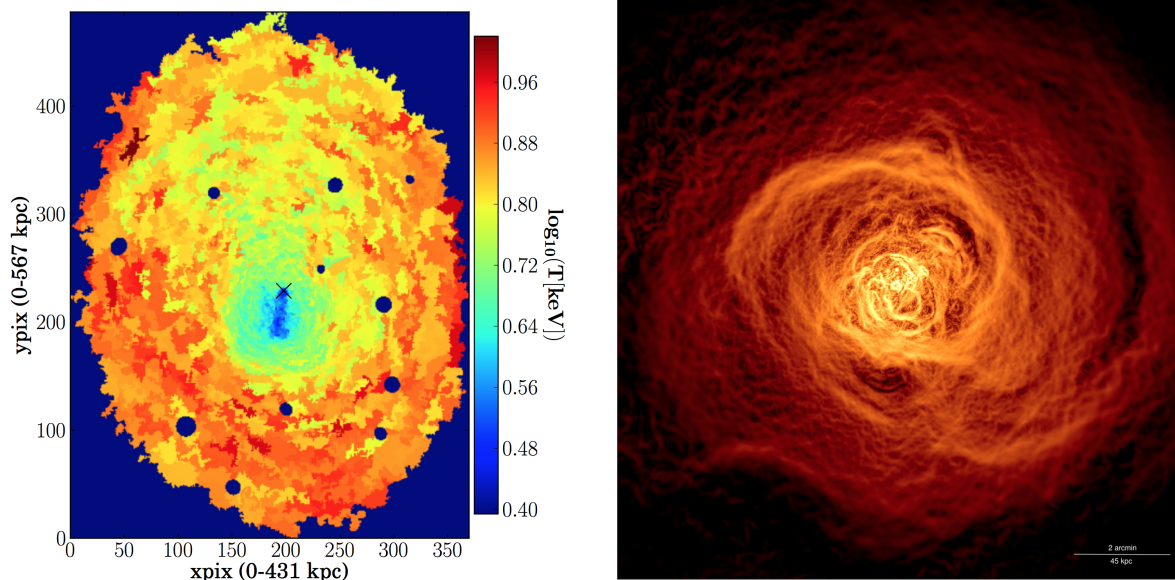


Figure 1.6: *Left*: A map of the temperature of the galaxy cluster A1795 observed with Chandra which allows us to accurately measure any substructure present in clusters due to the high angular resolution of the telescope. Clearly, the gas temperature is not uniform throughout the cluster and the cluster core appears cooler than its outskirts. *Right*: A deep Chandra image of the Perseus cluster. By using sophisticated filtering techniques, which are able to remove the continuous X-ray emission, one can reveal the hugely detailed substructure present in galaxy clusters caused by interaction with a central AGN, gas sloshing and cooling flows, amongst other phenomena. Image credit: [Hofmann et al. \(2016\)](#); [Sanders et al. \(2016\)](#).

to obtain spectacular images of the Perseus cluster (right panel of 1.6) and M87, and a merging system, A3667 uncovering many intricate features in the X-ray emission such as X-ray cavities and AGN feedback.

X-ray surveys

Galaxy clusters are typically easy to detect and identify at X-ray wavelengths and as we have seen, X-ray observations of clusters provide a number of important observable quantities that can be strongly correlated to the cluster mass, such as temperature and luminosity. This correlation is seen to extend across the entire flux and redshift ranges of interest to cluster surveys. In addition to this, the peaked nature of their emission coming from its dependence on the square of the density means that projection effects are unlikely to be significant. It is thus possible to create very pure and complete samples of clusters by selecting them based on their X-ray emission.

Although the first X-ray detections of clusters were made in the 1970s with the UHURU X-ray satellite ([E. Kellogg, H. Gursky, H. Tananbaum 1972](#)), it would take until the early

1990s for the first cosmological cluster catalogues to be formed based on data from the Ariel V (McHardy et al. 1981) and HEAO-1 (Wood et al. 1984) all-sky surveys and from pointed observations with the Einstein Observatory and EXOSAT (Branduardi-Raymont et al. 1985). Some of the highlights of this early work included evidence for the evolution of the X-ray luminosity function and a number of pioneering cosmological analyses. The launch of ROSAT heralded a new era for X-ray cluster astronomy and consisted of both an all-sky survey followed by a number of years of pointed observations. This, coupled with the large field-of-view of ROSAT (2° in diameter) provided a large area of deep observations from which clusters can be serendipitously detected. A number of cluster catalogues have been created based on a wide variety of selection criteria and these have been combined to form the MCXC meta-catalogue (Piffaretti et al. 2011), containing 1743 clusters. The main samples included in the MCXC are, NORAS, REFLEX, BCS, SGP, NEP, MACS and CIZA, which are all based on the ROSAT All-Sky Survey (RASS); and 160SD, 400SD, SHARC, WARP and EMSS, which are serendipitous surveys. Although the serendipitous surveys cover far smaller regions than the RASS, they reach an order of magnitude or more fainter in flux.

With the launch of XMM-Newton and Chandra within a few months of each other in 1999, we have been able to probe the distribution of clusters at much higher angular resolution and to much fainter fluxes. In addition to providing deep followup of ROSAT detected clusters, some of the prominent surveys include medium-field observations with XMM e.g. XMM-LSS (Pierre et al. 2007; Pacaud et al. 2007; Clerc et al. 2014), XMM-XXL (Pierre et al. 2016; Pacaud et al. 2016) and XMM-BCS (Šuhada et al. 2012b) and narrow surveys such as the COSMOS field with Chandra (Scoville et al. 2007) or XMM (Finoguenov et al. 2006). Additionally, the vast number of PI observations with XMM and Chandra provides an abundance of exploitable data in which serendipitous cluster searches can be performed with Chandra (ChAMP, Barkhouse et al. 2006) and with XMM e.g. XCS (Romer et al. 2001; Lloyd-Davies et al. 2011a; Mehrrens et al. 2012) and X-CLASS (Clerc et al. 2012b; Sadibekova et al. 2014, Ridl et al. 2017).

In the near future, with eROSITA (currently scheduled for early 2018), X-ray cluster cosmology will once again enter a new era as the number of X-ray detected clusters will drastically improve from relatively small samples of a few hundreds to an expected catalogue of $\sim 100,000$ clusters. eROSITA will perform a four-year all-sky survey (with eight full scans of the sky) followed by a series of pointed observations.

1.3.2 Optical properties of Clusters

Although they only make up a small part of the mass budget of galaxy clusters, stars dominate the emission spectrum at optical and near-infrared wavelengths. The emission at these wavelengths is mostly concentrated in member galaxies but is also detected as a part of the more diffuse intra-cluster light. Here we discuss the basic properties of the cluster member galaxies.



Figure 1.7: Two typical galaxy clusters X-CLASS 2122 at a redshift $z = 0.37$ (left) and X-CLASS 1858 with redshift $z = 0.60$ (right) observed with GROND on the MPG/ESO 2.2m telescope at La Silla. Clusters are easily identified in optical imaging surveys as overdensities in the galaxy distribution. In the left panel, cluster members appear as yellowish sources with a clear BCG at the centre of the image and an interesting linear configuration of four galaxies just above it. In the right panel, which is a more distant cluster, the cluster members are red and considerably fainter than in the left image.

Optical morphology

As seen in Figure 1.7, observations of clusters show an over-density of galaxies relative to the background source density. The shape of these over-densities can provide important information relating to the dynamical state of the cluster. In addition to this, if the galaxies are distributed in a similar manner to the dark matter in the halo, we can infer the distribution of the otherwise, directly unobservable dark matter.

The radial number density of galaxies within clusters is normally well described by,

$$n(r) \propto \frac{1}{r^\gamma (r + r_s)^{3-\gamma}}, \quad (1.83)$$

where r_s is a characteristic scale radius (typically $\sim 20\%$ of the cluster radius) and γ gives the slope of the inner profile (typically ~ 1). Most regular clusters exhibit a galaxy distribution which is peaked towards the centre and decreases towards the cluster outskirts.

The luminosity function of cluster galaxies

One of the best observational tests for theories of galaxy formation and evolution is provided by the galaxy luminosity function (LF). Clusters allow for the probing of this function with a large number of galaxies all at the same redshift. A primary objective of the study of the luminosity function is to make a comparison between its form in over-dense regions, such as clusters and in less dense environments, such as for field galaxies. This can provide insights into the environmental impact on the global statistical properties of galaxies (Popesso et al. 2005).

The LF gives the number distribution of galaxy luminosities i.e. the $N(L)dL$ is the number of galaxies with a luminosity in the range L to $L + dL$. The form of the luminosity function was given by Schechter (1976) as

$$n(L)dL = N^*(L/L^*)^{-\alpha} \exp(L/L^*)d(L/L^*), \quad (1.84)$$

where α is the slope of the function at small L and L^* is a characteristic luminosity above which the distribution decreases exponentially. Interestingly, there seems to be no obvious reason why such a simple relation as the one above should so accurately describe the luminosity distribution of galaxies so well. Further, there is a difference between the observed LF's of cluster and field galaxies and the simplicity of the total luminosity function is largely coincidental and cannot be easily modelled.

Galaxy colours and the cluster red sequence

The classification of galaxies by their morphology, as given by the traditional Hubble classification scheme, can be both difficult to quantify and rather subjective. This is because the morphology is often determined by visual inspection e.g. the Galaxy Zoo program (Lintott et al. 2008), where members of the public have classified over a million galaxies. There have also been attempts to perform this classification automatically and

using machine learning algorithms e.g., [Banerji et al. \(2010\)](#) but even these methods have difficulties for surveys with insufficient angular resolution to allow for the fitting of surface brightness profiles. However, we can also learn about the morphological classification of a galaxy based on its colour because we expect that early-type (E and S0) galaxies are redder compared to late-type (spiral) galaxies. Colours are far easier to measure than morphology and so provide a useful way for studying the formation and evolutionary history of galaxies in clusters.

The distribution of galaxies on the absolute magnitude-colour plane, measured for a large number of galaxies with SDSS photometry and spectroscopy is unambiguously bimodal over a wide range in absolute magnitude ([Baldry et al. 2004](#); [Martinez, O’Mill & Lambas 2006](#)). This bimodality reflects that there are two main classes of galaxies. The first of these is early-type galaxies which typically have old stellar populations and so are red. The second class is late-type galaxies which are likely to be in a phase of star formation and so contain more massive bluer stars. Of course, this simple explanation is not perfect as it is possible to have completely quenched disk galaxy which appears red or an elliptical which is blue due to a period of star formation in its recent past. Dust obscuration can also affect the galaxy colour making its classification even more challenging. Typically, the bright end of the luminosity function is dominated by red galaxies while the blue galaxies are more prominent at the faint end. Further, it appears that both of these populations show respectively redder galaxies at the bright end which probably indicates that the stellar populations of more luminous galaxies are older and more metal rich.

This bimodality holds true for clusters of galaxies as well ([Visvanathan & Sandage 1977](#); [Sandage & Visvanathan 1978](#)). Clusters are normally rich in early-type galaxies and the fraction of E and S0 galaxies relative to late-types is around $\sim 80\%$ in regular clusters and $\sim 50\%$ in irregular clusters. This is compared to the field galaxies of which only $\sim 30\%$ are late-types. Apart from the differences in colour by galaxy type, one normally sees more massive, red galaxies concentrated at the centre of clusters. This gives an indication that environmental effects play an important role in galaxy formation and that some mechanism in galaxy clusters is acting to quench star formation in its member galaxies. At present, it is not yet clear what are the most dominant processes.

One of the most notable features of cluster galaxy populations is provided by the red sequence which has been shown to extend over 8 magnitudes in the Coma and Virgo clusters at $z = 0.1$ ([Bower, Lucey & Ellis 1992](#)). It has further been shown that not only is the relationship tight within individual clusters, but it is also remarkably homogeneous across all clusters at the same redshift, extending to clusters at redshifts above to $z \sim 1$ ([Mei et al. 2006](#)) and has even been observed in very young clusters found around bright radio emitting galaxies at high redshifts ([Kodama et al. 2007](#)). The implication of this universality with redshift indicates that the stellar populations of these galaxies formed in the very early Universe with a burst of near-instantaneous star-formation followed by a passive evolution thereafter. This means that their luminosities only evolve due to the ageing of already existing stars. Since blue stars are hotter and more luminous, they burn out on much shorter scales than the smaller, cooler red stars and so we are left mostly with a population of small, red stars in these galaxies.

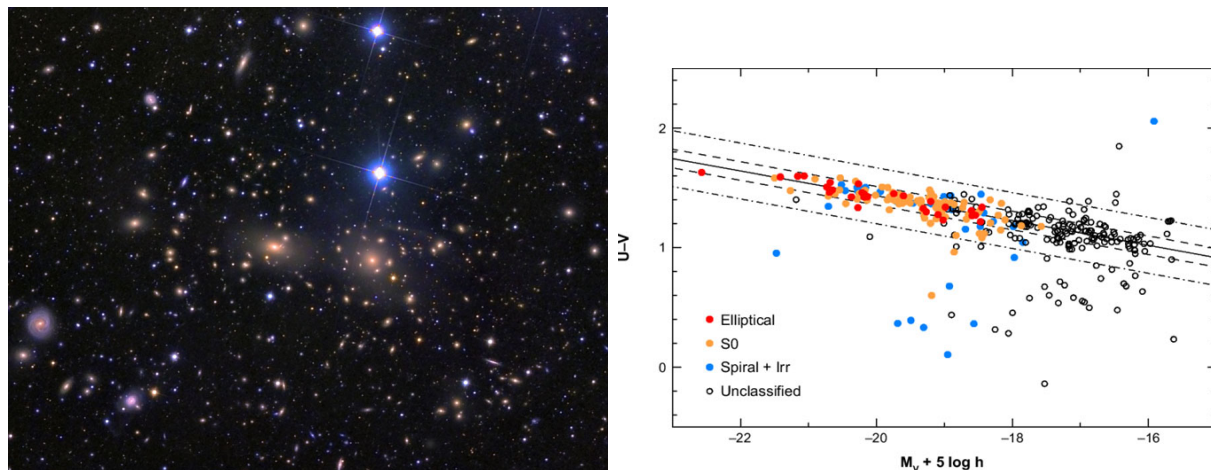


Figure 1.8: The Coma cluster is a nearby, massive cluster that has been extensively studied. A spectroscopic survey along with a morphological study of its cluster members leads to the interesting result that passive, elliptical galaxies tend to lie almost exclusively in a narrow, red band in the colour-magnitude space in the plot on the right. Spiral galaxies on the other hand tend to be much bluer than their elliptical counterparts. Image credit: Dean Rowe; [Bower et al. \(1998\)](#)

The red sequence on the colour-magnitude relation can typically be fit by a linear relationship which is parametrised by its normalisation, slope and the intrinsic scatter around it. The normalisation is given by the colour at the location of galaxies with luminosity L^* . The slope of the red sequence rises towards higher luminosities and this is attributed to increasing metallicities for brighter galaxies. The slope arises from the fact that larger, more luminous galaxies live in deeper gravitational potential wells and are thus more efficient at containing supernova driven winds that would otherwise have ejected metals from the galaxy. The small intrinsic scatter ~ 0.05 tells us that the galaxies should have fairly similar star formation histories and that the period over which stars were formed should have been a small fraction of the age of the galaxies. The scatter of the red sequence remains small even as redshift increases despite the expectation that we should see more star formation and hence bluer galaxies at high redshift ([Mei et al. 2009](#)). That we don't observe this, tells us that the formation redshift of these galaxies can be estimated as $z_f \gtrsim 3$ which provides strong constraints for evolutionary models. The red sequence is an important feature that can be used in the detection and redshift characterisation of clusters. We discuss this more in Chapter 3 where we use the red sequence to obtain photometric redshifts for a sample of X-ray selected galaxies.

Optical surveys

Galaxy clusters are named for the fact that they can be identified as an over-density in the galaxy distribution. Since galaxies emit most of their light in the optical and near-infrared passbands, it is logical that we can use the concentration of galaxies to detect

clusters. Indeed, this is how the first cluster catalogues were created by Abell in 1958 based on the visual inspection of photographic plates from the Palomar Observatory Sky Survey (Abell 1958). Abell also measured distances to the clusters he detected based on the magnitude of the tenth brightest galaxy, which he assumed to be a standard candle. Fortunately, we no longer need to rely on manually detecting clusters visually and a variety of sophisticated methods for the detection of galaxy clusters from optical imaging surveys have been developed (Koester et al. 2007; Rykoff et al. 2014; Wen & Han 2015). These methods also automatically provide an estimate of the photometric redshift based on the galaxy colours.

Galaxy cluster catalogues derived from optical imaging typically result in much larger catalogues than those existing for X-ray selected samples. This is due to the relative ease of detecting galaxies and we are able to detect clusters with lower masses, even pushing to the galaxy group scale. This ease of detection comes with the caveat that probing the low mass regime of clusters means that catalogues are more susceptible to projection effects due to the steepness of the cluster mass function: there is simply a higher probability to have more than one over-density of a given mass along a single line-of-sight.

Since Abell’s catalogue, there have been a large number of cluster surveys performed at optical wavelengths and a complete summary of all of them would be too exhaustive to list here. Instead we will focus on a few catalogues derived from imaging data from the Sloan Digital Sky Survey (SDSS) on the 2.5m telescope at the Apache Point Observatory which saw first light in 1998. Since the inner regions of clusters are dominated by red sequence galaxies, one can effectively reduce the contamination from projection effects simply by only selecting galaxies of a given colour when searching for over-densities in the galaxy distribution. Since the main feature in red sequence galaxies is the 4000 Å break, which is thus redshifted to higher wavelengths for more distant galaxies, multi-colour photometry is needed to track it as we search at higher redshifts. This is enabled by the 5-band u, g, r, i, z photometry of the SDSS. Some of the notable cluster catalogues derived from SDSS data are the MaxBCG catalogue (Koester et al. 2007), which also uses the fact that clusters typically have a large, red brightest cluster galaxy (BCG) at the centre, and contains some 13,823 clusters. The WHL catalogue (Wen, Han & Liu 2012; Wen & Han 2015) includes a Gaussian mixture modelling to the MaxBCG algorithm and contains 132,684 clusters. Finally, redMaPPer (Rykoff et al. 2014), a cluster search based on an optical richness estimator, contains $\sim 25,000$ clusters and has made good progress in limiting the scatter on the recovered richness.

One of the biggest challenges in the cosmological analysis of optical cluster catalogues is the definition of tightly fitting mass proxies that have a well understood scatter across the entire mass and redshift ranges of interest. They are also affected by the fact the clusters typically lie at nodes of the cosmic web and thus filamentary structures feeding into them can have a large impact on the recovered observable mass proxies and redshift estimates. The modelling of these effects continues to be a challenge and is the limiting factor of cosmological analyses with such samples.

1.3.3 The Sunyaev-Zel'dovich effect

As we discussed in Section 1.3.1 galaxy clusters contain most of their baryonic mass in the form of a hot, diffuse gas. Apart from its X-ray emission, this gas has a secondary effect on CMB photons that are streaming through it from the surface of last scattering. These photons interact with the gas via inverse-Compton scattering and are up-scattered in energy and thus have a shorter wavelength. This imprints a characteristic feature into the CMB power spectrum at very small scales and is also directly detectable in images of clusters in the 0.1-10 mm passbands. The scattering takes place around a frequency of $\nu = 217$ GHz and we thus expect to see a deficit of photons at lower frequencies, characterised by a dark spot on an image of the CMB and an increment at higher frequencies which we observe as a bright spot. The spectral shape of the SZ effect is illustrated in Figure 1.9.

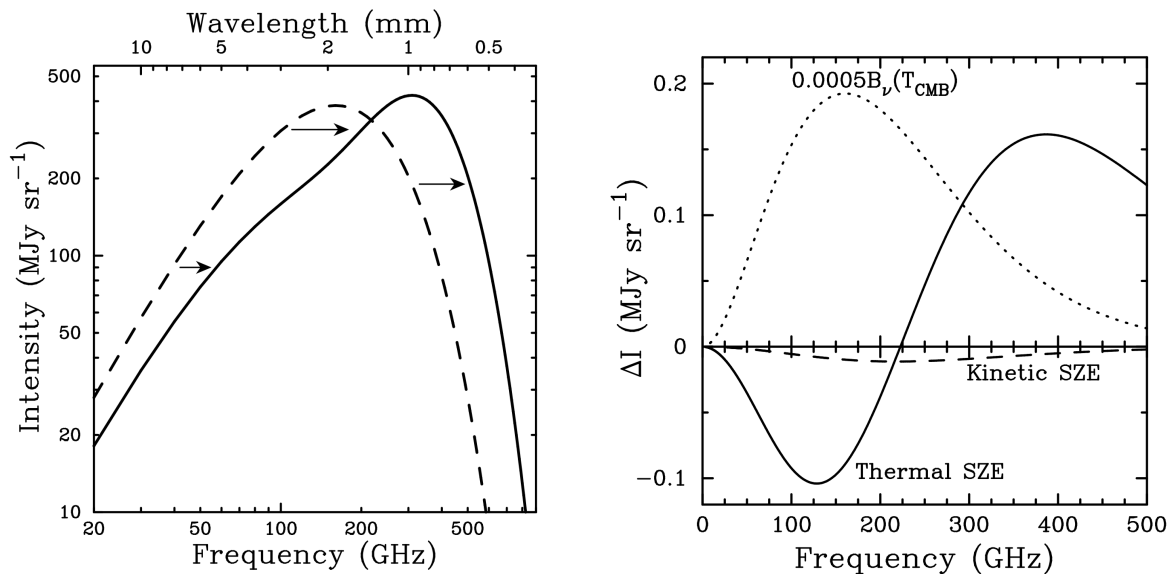


Figure 1.9: When CMB photons pass through ICM of a galaxy cluster, the inverse-Compton scattering process shifts them to higher frequencies. We thus see that below the characteristic frequency of 217 GHz, there is a decrement in the CMB (cold spot) whereas above this frequency there is an increment (hot spot). It is thus perhaps easier to detect clusters in the low frequency bands where they would not be easily confused with radio-emitting galaxies, which would appear as extended hot-spots in both passbands above and below 217 GHz. Image credit: [Carlstrom, Holder & Reese \(2002\)](#)

The strength of the SZ signal is characterised by the Compton parameter y , defined as,

$$y = \int \frac{k_B T_e}{m_e c^2} \sigma_T n_e dr, \quad (1.85)$$

where m_e , T_e and n_e are the electron mass, temperature and density respectively, σ_T is the Thomson scattering cross-section and the integral runs along the line of sight. A measure

of the total SZ signal is then obtained by integrating over the angular size of the cluster so that,

$$Y_{SZ} = \int y d\Omega. \quad (1.86)$$

This quantity is an important observable because it is a powerful proxy for the cluster mass along with correlating strongly with the gas mass and temperature obtained from X-ray observations.

A secondary component of the SZ effect is a result of the peculiar motion of the cluster and hence the gas in the intracluster medium relative to the CMB. This effect is about 20 times smaller than the thermal-SZ effect discussed above (as seen in Figure 1.9) and is commonly referred to as the kinetic-SZ (kSZ) effect or the Ostriker-Vishniac effect. The first statistical detection of this effect was made by combining data from the Atacama Cosmology Telescope with spectroscopy from the Baryon Oscillation Spectroscopic Survey (BOSS), and measuring the mean pair-wise momentum of clusters (Hand et al. 2012). The weakness of this signal means that it is difficult to detect for individual clusters but recently Sayers et al. (2013) and Adam et al. (2017) have detected the kSZ effect in the direction of the massive cluster MACS J0717.5+3745 with Bolocam and NIKA data respectively.

SZ surveys

The biggest advantage to using the SZ effect for detecting clusters is that unlike optical and X-ray measurements, it is unaffected by surface brightness dimming as the distance increases. We can thus detect clusters independently of their redshift and thus probe the cluster mass function up to very high redshifts. The SZ effect also provides a good proxy for the total mass of the cluster.

The history of using SZ selected galaxy clusters for cosmology does not extend very far to the past. The first catalogues for cosmological purposes were produced by ground based observatories: the Atacama Cosmology Telescope (ACT, Swetz et al. 2011) containing 91 clusters (Sehgal et al. 2011; Hasselfield et al. 2013); and the South Pole Telescope (SPT, Carlstrom et al. 2011) containing 677 cluster candidates (Vanderlinde et al. 2010; Reichardt et al. 2013; de Haan et al. 2016). The Planck satellite scanned the entire CMB sky and detected 1,653 clusters and cluster candidates (Planck Collaboration XXVII et al. 2016). Some of the challenges for performing cosmological analyses with SZ selected samples include the fact the one typically has to work in a fairly low signal-to-noise regime; the calibration of the mass proxies; and the understanding of how radio and infrared sources contaminate the SZ signal.

1.3.4 Diffuse radio emission in clusters

Many clusters of galaxies are also observed to emit radiation at radio wavelengths. One fairly straightforward explanation for part of this radio emission is that it is generated by individual galaxies and radio-loud AGN. Often, this emission extends far beyond the optical region of the galaxy and one thus expects that these radio emitting regions should

interact with the ICM. We see this notably in the centre of many clusters where radio jets from central galaxies expand outwards creating cavities in the X-ray emission. An example of this is given in Figure 1.10 where multi-wavelength data extending from the radio-waves to X-rays shows how the highly energetic processes in small regions at the centre of a galaxy cluster can affect the environment on the largest cluster scales.

Another, more complicated type of source presents itself through extended diffuse regions of radio emission. The regions are not associated with a particular galaxy and are attributed to the ICM. When galaxy clusters merge, huge amounts of energy ($\sim 10^{64}$ erg) are released on time-scales of 1-2 Gyr (Hoefl & Bruggen 2007). These mergers thus generate large-scale shock waves in the ICM and observations of radio synchrotron emission indicates that as these shocks travel through the ICM they interact with its constituent electrons accelerating them to be ultra-relativistic ($\gamma \sim 10^3 - 10^4$) cosmic rays. We observe these large-scale shocks as extended radio sources and they reveal that the ICM contains both a thermal plasma and non-thermal components.

Extended radio emission associated with the ICM have been observed over a range of cluster masses, evolutionary states and locations in the cluster. Depending on their location in the cluster and polarisation, these diffuse sources are classified differently either as relics, halos, or mini-halos. Typically, halos are found at the centres of merging clusters and are extended over large areas $\gtrsim 1$ Mpc. They usually display a fairly regular shape and are not expected to be strongly polarised. Relics are normally located towards the outer regions of both relaxed and disturbed clusters and are strongly polarised. They are often associated with shock fronts in the ICM and give evidence in support of the existence of μG -level magnetic fields in the cluster outskirts (Eckert et al. 2016). Mini-halos on the other hand, are usually observed at the centres of relaxed cool-core clusters and usually surround a powerful radio galaxy. They are considerably smaller in area than halos and relics and their emission is attributed to relativistic particles and magnetic fields which are strongly mixed with the thermal ICM gas. Figure 1.11 illustrates a few examples of extended radio emission. An excellent review of the radio emission from clusters can be found in Ferretti et al. (2012)

1.3.5 Shedding light on dark matter

The bulk of the mass of a galaxy cluster is in the form of dark matter. Most models for dark matter require that it interacts only gravitationally and has a very low self-interaction cross-section with upper limits coming from observations of the Bullet cluster.

One of the most powerful ways in which this dark matter can be mapped is through the gravitational lensing effect. Gravitational lensing is predicted by general relativity and is built on the principle that when light passes by a massive and dense object, its path is deflected by the gravitational potential. Since galaxy clusters are the most massive collapsed structures in the Universe, they are a good place to look for evidence of lensing. The lensing effect is purely gravitational and is thus independent of the type of matter causing it. The effect of lensing on background sources is one of magnification and distortion. This means that clusters can act as gigantic cosmic telescopes and provide a powerful probe

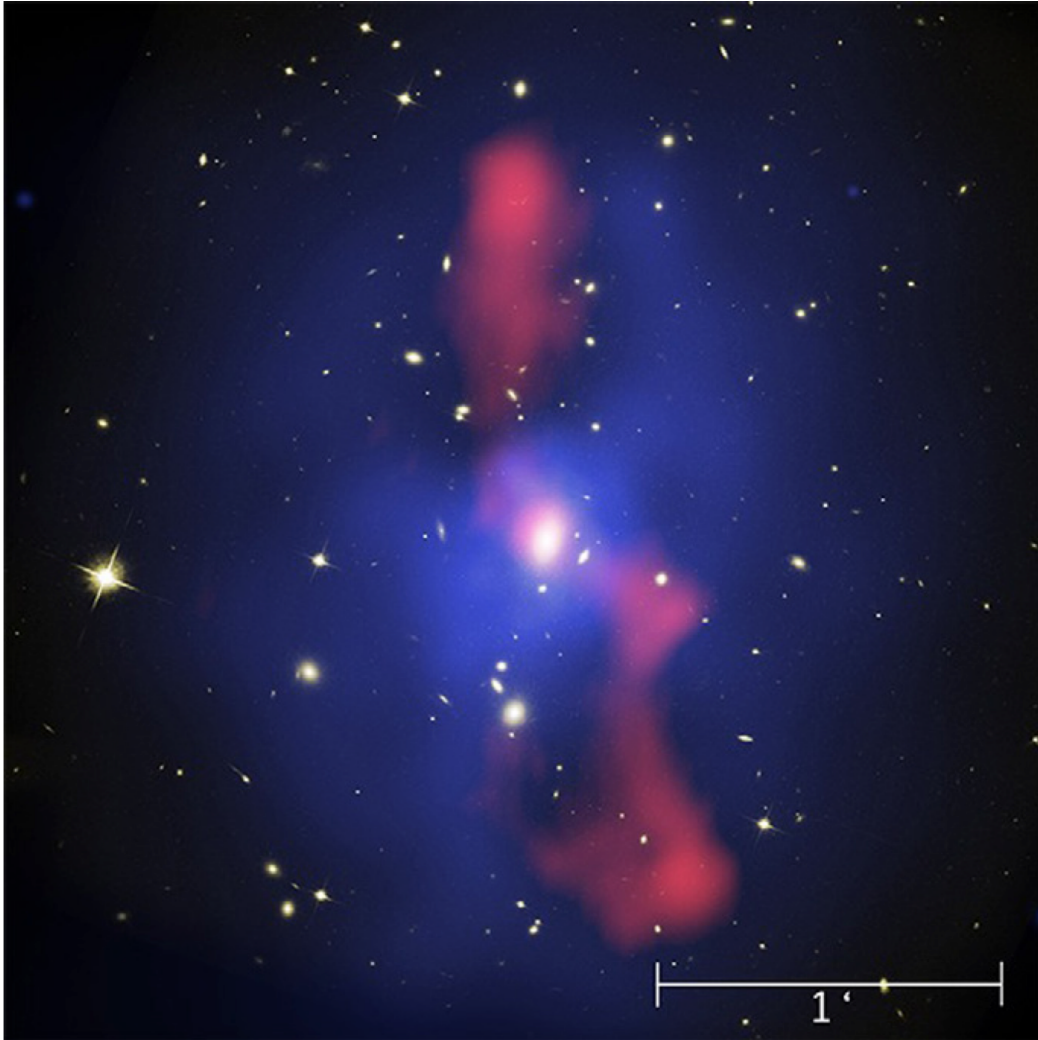


Figure 1.10: AGN are incredibly powerful sources of energy and they produce large-scale radio-loud jets which interact with the surround ICM, displacing gas and creating large bubbles. This incredible composite image displaying the inner 700kpc of the galaxy cluster MS 0735 in optical data (white) from the Hubble Space Telescope I-band, X-rays (blue) from Chandra and radio observations (red) from the Very Large Array (VLA), highlights to interplay between the various components of a galaxy cluster. Despite originating from a single black hole at the centre of the BCG, the radio jets powered by the central AGN displace the cluster gas on large scales, impacted the environment many kiloparsecs from their origin. Combining data from multiple datasets allows us to better understand cluster physics. Image from [McNamara et al. \(2009\)](#)

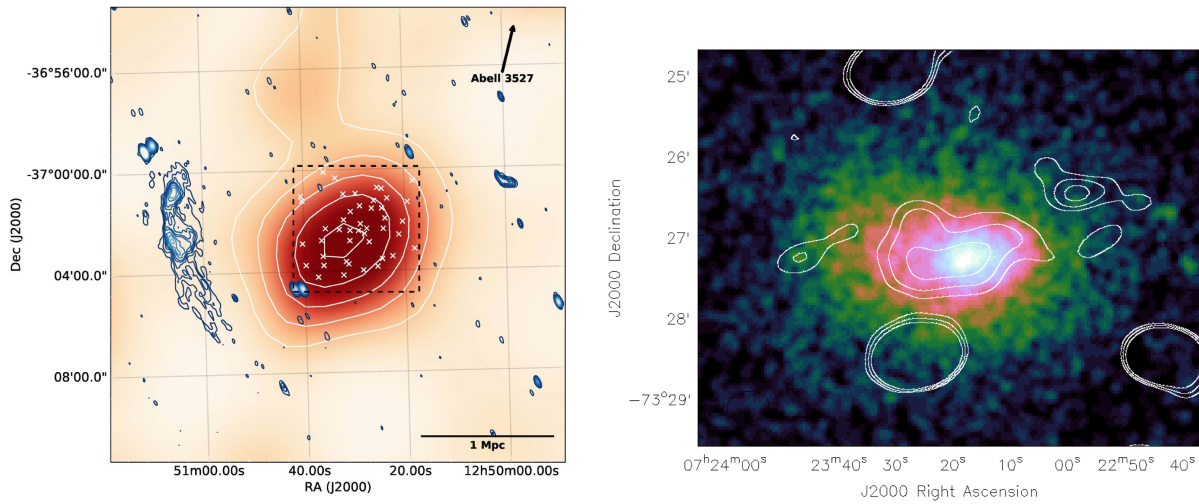


Figure 1.11: Examples of two types of radio emission associated with galaxy clusters. In both images we clearly see the extended nature of this emission. *Left*: A smoothed ROSAT (red) image of Abell 3527-bis, one of the first galaxy clusters detected initially through its radio emission from a 1 Mpc long radio relic shown by the blue contours obtained from 323 Mhz data from the GMRT. It's name is acquired due to its close proximity to Abell 3527 and is one of the least massive clusters to host a relic. It was originally detected as a point source by ROSAT and was by chance observed with GROND on the MPG 2.2m telescope at La Silla as a part of a program following up such sources. I performed the data analysis of the GROND data, providing the confirmation that this was indeed a cluster (cluster members indicated by white crosses). Image from [de Gasperin et al. \(2016\)](#). *Right*: Radio emission (white contours) from an ATCA 1.867 GHz of the radio halo Planck cluster PLCK G285.0-23.7 overplotted on a smoothed XMM image in the [0.3-2.0] keV energy band. Image from [Martinez Aviles et al. \(2016\)](#).

of the very early Universe by magnifying distant galaxies. The secondary effect, that of distortion causes background sources to be elongated in a particular direction and we can observe these sources as strong lensing arcs.

The above mentioned examples are all incidences of ‘strong’ lensing. In actual fact, the majority of background sources are only marginally distorted and the change in shape is not measurable in individual galaxies since the galaxies themselves are intrinsically elliptical. It is impossible to distinguish between the intrinsic ellipticity and that imparted by the lensing distortion. Instead, one needs to average over the ellipticity of all background galaxies and since we expect them to be randomly oriented, any favoured ellipticity is an indication of gravitational lensing. This is known as the weak lensing regime.

Importantly, gravitational lensing provides us with a completely independent method of measuring galaxy cluster masses. Hydrostatic mass estimates based on measurements of the ICM come with the caveat that they require that the cluster is in hydrostatic equilibrium. In clusters undergoing mergers or displaying significant amounts of substructure this assumption breaks down and this introduces a bias to the total masses derived for these clusters. At present, gravitational lensing measurements provide the most accurate tool for the calibration of scaling relations in order to convert X-ray and SZ observable quantities into masses. Without accurately calibrated masses, it is not possible to use clusters to obtain precise estimates of cosmological parameters.



Figure 1.12: The Bullet cluster (1E 0657-558) provides an excellent example of the power of gravitational lensing. Shown here are optical data from HST (yellow), X-rays (red) from Chandra and the dark matter distribution obtained from the gravitational lensing analysis. The clear offset between the X-ray and dark matter peaks has been hailed as ‘a smoking gun’ for dark matter since there is currently no prominent gravitational theory which could describe the gravitational lensing features in the regions that the dark matter is postulated to inhabit. Verlinde however, thinks that his emergent gravity theory (Verlinde 2016) will be able to account for these observations without the need for dark matter. Image Credit: X-ray: NASA/CXC/CfA/ M.Markevitch et al.; Lensing Map: NASA/STScI; ESO WFI; Magellan/U.Arizona/ D.Clowe et al. Optical: NASA/STScI; Magellan/U.Arizona/D.Clowe et al.

1.4 Galaxy clusters as probes of cosmology

1.4.1 Galaxy cluster number counts

The number density of galaxy clusters as a function of redshift depends on a variety of cosmological parameters. Thus, simply counting the number of clusters over a range of redshifts will enable us to place constraints on these parameters. In Figure 1.13 I highlight the effect that changing two key parameters Ω_M and σ_8 has on the expected number density of clusters. When counting galaxy clusters, great care must be taken to ensure that the selection function is precisely known as this has a strong influence on the number of detected clusters. The lower panel of Figure 1.13 shows how the selection function of for a hypothetical XMM survey to a depth of 10 ks would affect the number density of clusters. In these figures, we see that an increase in either Ω_M or σ_8 will increase the number density of clusters at all redshifts. Through the use of simulations Borgani & Guzzo (2001) illustrated how for a fixed number density of clusters in the local Universe, we can infer the parameters of the background cosmology by looking at the evolution of the number counts with redshift. In Figure 1.14 we see that in an Einstein-de Sitter universe with $\Omega_M = 1$ the onset of structure formation needs to happen far later in the history of the Universe to be consistent with local number counts compared to a Λ CDM universe with $\Omega_\Lambda = 0.7$ and $\Omega_M = 0.3$. Thus, by counting clusters at high redshifts we will be able to distinguish between these two models.

As shown in Section 1.2.4 the halo mass function depends strongly on a variety of cosmological parameters. Since clusters are roughly defined as having masses greater than $10^{14}M_\odot$, the mass function for galaxy clusters is representative only of the high mass end of the halo mass function. The initial perturbations from which clusters collapse typically have the comoving scale of $\sim 10h^{-1}$ Mpc, a scale on which the Universe is dominated by gravitational effects and the dynamics take place in the linear or only weakly non-linear regime. It is thus clear that the value of σ_8 will strongly affect the number of clusters that form in the Universe. We can use clusters to probe the steepest part of the halo mass function (which is also the most sensitive to cosmology) with the caveat that we must assume that in massive clusters, baryonic effects do not significantly modify the mass function and we can treat clusters as pure dark matter halos. More recent calibrations of the mass function have been performed taking baryons into account by making use of hydrodynamical simulations e.g. Bocquet (2015) who calibrated the mass function with the Magneticum simulation (Dolag et al., in prep).

Perhaps the most simple way in which one derives limits on cosmological parameters is to simply search for the most massive (and thus easiest to detect) clusters at high redshifts. In this way we compare the likelihood of such massive clusters existing early in the universe for a given cosmological model. Due to the inherently low number of clusters involved in such a study, each cluster must be very well measured in all of its parameters to obtain an accurate cluster mass. It is also possible that our Universe is not a perfectly representative realisation of the cosmological parameters and thus the small number statistics could easily

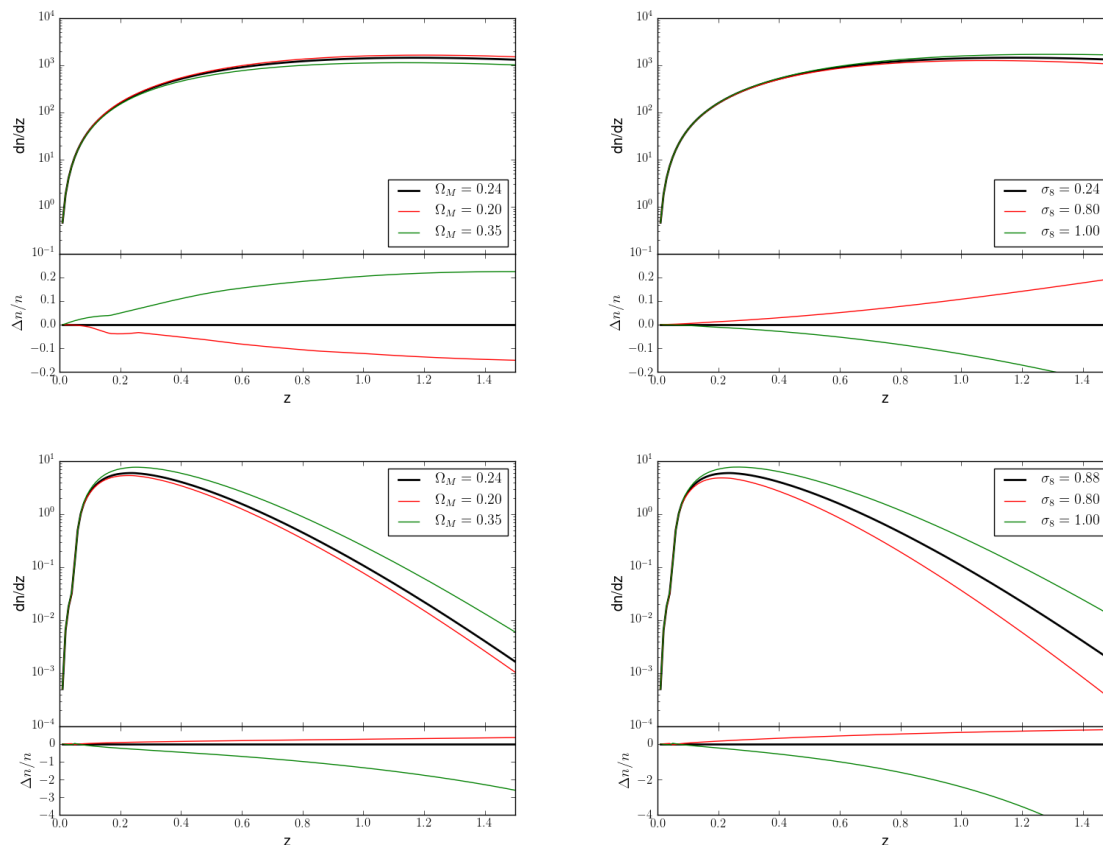


Figure 1.13: The number of galaxy clusters as a function of redshift depends on the parameters of the background cosmology. The top panel here illustrates the total number of clusters with $M > 10^{12.5} h M_\odot$ per square degree on the sky for a fiducial cosmology with $\Omega_M = 0.24$ and $\sigma_8 = 0.88$ along with the result of varying each of these parameters. The bottom panel depicts the number of clusters detected per square degree for a hypothetical XMM survey with a depth of 10 ks taking selection effects into account.

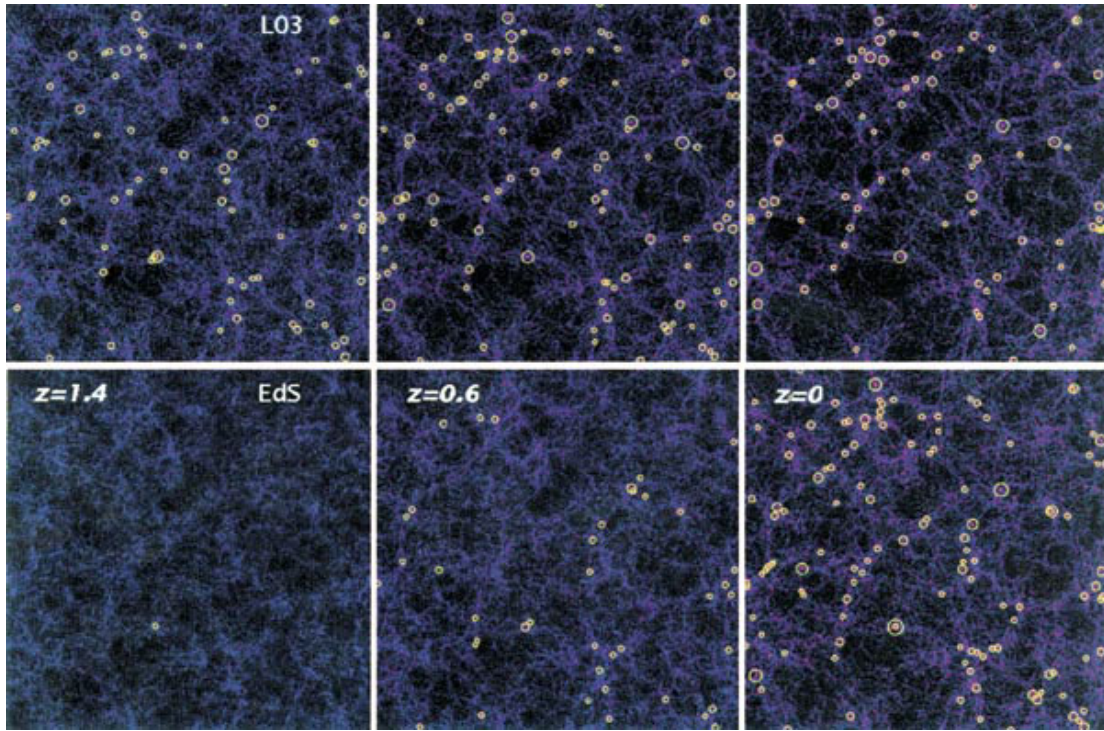


Figure 1.14: The two rows of images show three redshift snapshots of a simulated region containing two million particles with side of $250 h^{-1}$ Mpc and a depth of $75 h^{-1}$ Mpc. The upper panel is representative of a realistic (according to most observations) flat, low-density model with a matter density $\Omega_M = 0.3$ and cosmological constant $\Omega_\Lambda = 0.7$. The bottom panel depicts an Einstein-de Sitter universe with $\Omega_M = 1$. The amplitude of the power spectrum is normalised in both cases to match the number density of clusters at low redshifts and the yellow circles highlight the positions of galaxy clusters that would have a temperature $k_B T > 3$ keV. As one goes to higher redshifts it is plainly apparent that one observes a significantly different number of clusters at earlier times in each of the simulations, highlighting the power of the evolution of cluster number counts for constraining cosmological parameters. Image from [Borgani & Guzzo \(2001\)](#).

lead to a strong bias in the recovered cosmology.

In the local Universe, the most prominent cosmological parameters affecting the theoretical mass function are Ω_M and σ_8 . These parameters can thus be well constrained given a large sample of low redshift clusters spanning a wide range of masses. These measurements are however degenerate, i.e., a higher Ω_M can be compensated for by a lower σ_8 . By looking at how the mass function evolves with redshift however, one can place constraints on the variation of dark energy parameters and study the evolution of the cluster scaling relations. It is therefore better to use large samples of clusters spanning a wide range of masses and redshifts.

In a perfect situation where we are able to precisely measure cluster masses and redshifts, for a large enough survey one could simply count the number of clusters as either a function of their mass or redshift and compare it to that expected for a given set of cosmological parameters,

$$\bar{n}_{ai} \equiv \frac{\Delta\Omega}{4\pi} \int_{z_i}^{z_{i+1}} dz \frac{dV}{dz} \int_{M_a}^{M_{a+1}} d \ln M \frac{dn}{d \ln M}, \quad (1.87)$$

where $\Delta\Omega$ is a solid angle area of the sky, and the subscripts a and i indicate the respective mass and redshift bins. In order to use this expression in a likelihood analysis however, a number of modifications need to be made. One of these is the requirement of transforming from masses to the actual signal used for cluster detection and characterisation. Also, errors in the number statistics arising from incompleteness and impurity need to be accounted for along with the inclusion of error measurements on any parameters that are used.

Apart from the theoretical halo mass function being modified by a change of cosmological parameters, the masses of individual clusters is also affected. The mass function changes because the predicted growth of structure is different whereas the cluster masses change because they are measured by making use of a different distance-redshift relation. This is illustrated nicely in Figure 1.15, taken from [Vikhlinin et al. \(2009b\)](#).

We know that measuring cluster masses is a non-trivial exercise and dependent on a variety of the multi-wavelength properties of clusters as we discussed earlier. The most well utilised tracers of the dark matter component of clusters are currently gravitational lensing and the velocity dispersion of cluster members. Gravitational lensing is typically thought to provide unbiased and reliable mass estimates with the limitation that it is a projected mass that will therefore includes all structures along the line of sight. It is also very observationally intensive as either space-based observations with HST (e.g., [Jauzac et al. 2015](#)) or ground-based observations (e.g., with VLT/MUSE, [Richard et al. 2014](#)) performed under excellent conditions are required. Further, the brightness of galaxies decreases with redshift and gravitational lensing requires a large number of background galaxies to precisely reconstruct the mass distribution ([Limousin et al. 2007](#); [Jauzac et al. 2014](#)). This means that measuring masses of high redshift clusters requires a significant time investment. Velocity dispersion methods (e.g., [Zwicky 1937](#); [L. Danese, Zotti & di Tullio 1980](#); [Bocquet et al. 2015](#); [Clerc et al. 2016](#)) rely on the assumption that the galaxies trace the dark matter distribution and require intensive observational programs to obtain a sufficient number of galaxies with measured velocities.

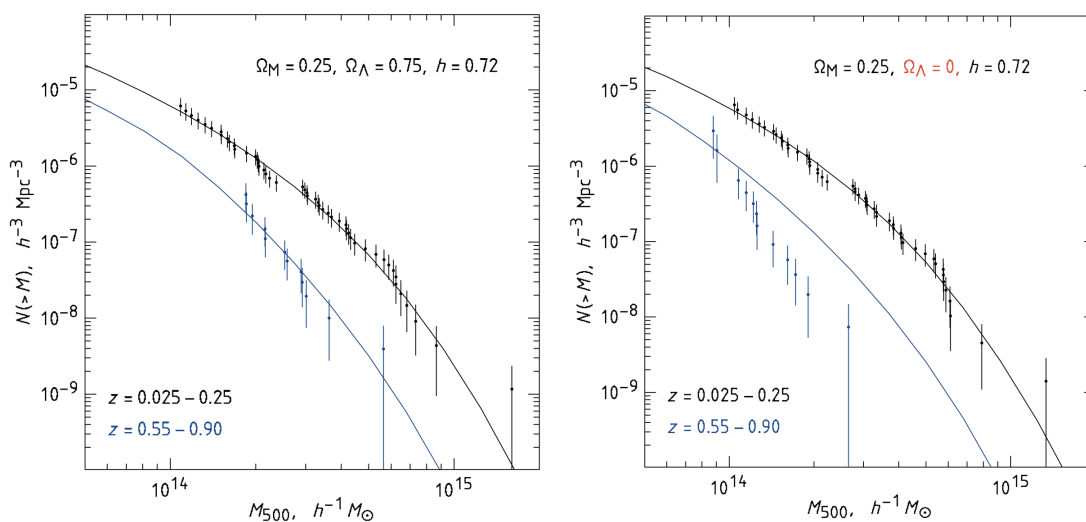


Figure 1.15: This images illustrates the sensitivity of the cluster mass function to the background cosmological model. The left panel shows the mass function measured from a sample of galaxy clusters split between low redshifts (black) and high redshifts (blue), along with a theoretical mass function at two redshifts $z = 0$ and $z = 0.55$ derived from the best-fit cosmology obtained from this sample (with $\Omega_M = 0.25$ and $\Omega_\Lambda = 0.75$). In the panel on the right, the data points and theoretical models are computed with a different cosmological model (with $\Omega_\Lambda = 0$). When the model is normalised so that the the low redshift mass function matches the local abundance, the predicted number density of clusters with $z > 0.55$ disagrees strongly with the data, providing an independent confirmation that $\Omega_\Lambda \neq 0$.

A more efficient way for obtaining cluster masses comes from probing clusters over a range of wavelengths where good mass proxies are available. Examples of these include the SZ-decrement, X-ray emission or optical luminosity with redshifts derived from optical and near-IR photometric and spectroscopic surveys. Each of the mass proxies come with their own caveats though and there is no clear ‘best’ observable. For instance, mass measurements from X-ray observations are relatively strongly affected by the dynamical state of the cluster (Hofmann et al. 2016) compared with SZ measurements. X-ray measurements are also affected by redshift due to their dependence on the luminosity distance while by making use of the SZ effect, we can detect clusters independent of their redshift. The total number of galaxies in a cluster, or richness, is somewhat more scattered and less well constrained as a mass proxy than other observables and requires strong knowledge on the completeness limits of the survey as well as cluster members luminosity function (Rykoff et al. 2012).

All of these mass proxies depend only on the baryonic component of clusters and thus need to be calibrated against the total cluster mass. Currently, the most reliable cosmological constraints have come from constraining scaling relations between easily measured mass proxies such as X-ray luminosity or SZ decrement and total mass from gravitational lensing for small samples of clusters and then using these relations on large samples of clusters with readily available mass proxies (Mantz et al. 2015).

1.4.2 Clustering of clusters

One can also derive cosmological constraints by looking at how clusters are spatially distributed. The clustering of clusters sheds light on the high-peak, high-bias regime of the large-scale structure of the Universe. Analyses making use of this information complement more traditional cluster cosmological tests such as number counts and scaling relations and improves their constraining power by breaking calibration degeneracies. The amplitude and general shape of the cluster power spectrum depend strongly on Ω_M and σ_8 and one requires wide-angle contiguous surveys in order to reliably measure any clustering signal. This signal has been measured by a few groups, notably in the X-rays with the ROSAT All-sky survey with the REFLEX catalogue (Collins et al. 2000), the XXL collaboration with XMM-Newton Pacaud et al. (2016) and in optical surveys in the SDSS regions Mana et al. (2013). Future experiments such as eROSITA will perform these kinds of measurements on large catalogues of clusters with a total of 50,000 – 100,000 clusters with approximate redshifts required to achieve the scientific goals. This will provide one of the cleanest probes of dark energy to date.

1.4.3 Baryon fraction measurements

In Section 1.2.4 we described how clusters with virial radii of ~ 1.5 Mpc are formed due to the gravitational collapse of a comoving volume of ~ 10 Mpc. Since these are such large structures, one would anticipate that the clusters should have a somewhat universal baryon fraction, f_b , since the mixture of baryonic and dark matter wouldn’t be expected

to differ significantly from the cosmic average. This is in contrast to galaxies which are of a small enough size that their baryonic content can be significantly affected by phenomena such as supernova explosions or outflows associated with AGN amongst others. We can measure the cluster gas mass fraction with X-ray observations and the baryons in galaxies are well traced by their stars. Further, the cosmic baryon density is known from primordial nucleosynthesis models and we can thus obtain the total matter density via the relation,

$$\Omega_M = \frac{\Omega_b}{f_b}. \quad (1.88)$$

1.4.4 Using clusters as standard candles

The angular diameter distance of a cluster can be determined by measuring its apparent angular size on the sky (typically in arcminutes) and relating it to the knowledge of the actual physical radius of the cluster (in kpc). Once one has the angular diameter distance in hand, it can be related to the cosmological model and used to measure the Hubble constant through the relation

$$D_A(z) = \frac{1}{1+z} \frac{c}{H_0} \int_0^z \frac{dz'}{E(z')}. \quad (1.89)$$

In order to measure this we take advantage of the different dependences on the gas density of the measured X-ray and SZ signals. I briefly summarise the key points here but for more details about this method see [Carlstrom, Holder & Reese \(2002\)](#); [Bonamente et al. \(2006\)](#). This technique is possible because the SZ effect is a function of the integrated pressure and provides a measurement of the observed temperature decrement,

$$\Delta T_{CMB} \propto \int n_e T_e dl, \quad (1.90)$$

and the X-ray observation of the thermal gas gives the flux,

$$S_X \propto \int n_e^2 \Lambda_{ee} dl, \quad (1.91)$$

where Λ_{ee} is the X-ray cooling function, n_e and T_e are the electron density and temperature respectively, and the integration is along the line-of-sight. We can then explicitly introduce the angular diameter distance D_A through the relation $dl = D_A d\theta$, where θ is the line-of-sight angular size. We can then solve these equations simultaneously for D_A to give,

$$D_A \propto \frac{(\Delta T_{CMB})^2 \Lambda_{ee}}{S_X T_e^2}. \quad (1.92)$$

Combining this with a model of the density of the cluster gas allows for a direct measurement of the distance to the cluster once we have related the measured angular size in the plane of the sky and the size along the line-of-sight. These two sizes are equal if one

assumes a spherically symmetric cluster geometry. We can then combine the computed angular diameter distance with redshift of the cluster and the geometry of the universe allowing us to calculate the Hubble parameter as the normalisation of the theoretical angular diameter distance relation. So we see that by combining X-ray and SZ measurements we can use clusters as a ‘standard candle’ to measure the Hubble constant. There are a number of potential sources systematic error which must be mitigated including deviations from spherical symmetry, contamination by point sources and the absolute calibration of both the SZ and X-ray instruments. Further, the induced temperature decrement caused by the kSZ effect must also be taken into account.

1.4.5 Sources of systematic error

In the 1990s and 2000s much of the focus in cosmological studies with galaxy clusters revolved around improving on statistical errors by building ever larger and better selected samples of galaxy clusters. The work of [Vikhlinin et al. \(2009b\)](#) helped to drive cluster cosmology to a new era in which it is now limited by systematics and understanding their influence on the derived cosmological parameters. Further, gravitational lensing measurements now offer chance to accurately calibrate the mass to observable scaling relations, with a goal of reducing the uncertainty on this calibration to the 1 percent level in the coming years. Currently, gravitational lensing masses are only available for small subsets of clusters due to their high observational cost, with the best results currently coming from space-based observations.

In the near future however, it might be expected that the focus will shift again to the creation of vast cosmological samples of clusters with the advent of the next generation of all-sky surveys of eROSITA (in X-rays) and Euclid (in the optical and near-IR). Further in the future, one might expect that projects such as Athena will again cause a shift back to the systematically limited paradigm which currently dominates. A few sources of systematic error are summarised here.

Observational errors

One of the difficulties in determining accurate cluster masses comes from the fact that observable quantities can be difficult to measure or calibrate. The most obvious source of error comes from the process of data collection itself, where an electronic signal needs to be converted into some measure of the flux. The step of data analysis itself can also introduce some margins of error and different analyses of the same data can lead to different results if care is not taken. Another possible issue come from the intrinsic triaxiality of many clusters. For instance, measurements of a single component in a super-cluster environment would be strongly affected by the presence of other halos lying in the vicinity along the same line-of-sight. Since clusters are in general elliptical and not spherical, we have a higher chance to detect objects that have their major axis aligned with the line-of-sight, since most observable signals depend on the integrated matter distribution. Due to the collisional nature of the ICM however, the X-ray emission is typically more spherical than

the total matter distribution. Further sources of error could also come from problems with incorrectly identifying the cluster centre which would be an issue when fitting a density profile from which the mass is measured.

The matching of a detected cluster to its dark matter halo can also be challenging at times, in particular when trying to match identified sources from a variety catalogues (Sadibekova et al. 2014). The extended nature of clusters can result in a mismatch between catalogues particularly if there are multiple detected clusters in the same region. This is sensitive to the method used for detection and the mass of the clusters in question and is best measured against simulations of the sky.

Since a telescope harvests all photons independent of where they come from along the line-of-sight, extending all the way to the early Universe, there is a high probability that at some point there will be a chance alignment of clusters and disentangling the flux from these multiple sources can be a challenge. This effect is a smaller problem for X-ray detected samples of galaxy clusters, since the X-ray brightness profiles depend on the density, than for lensing and optically selected samples where the profiles in those passbands generally trace the flatter density distribution or SZ samples which depend on the electron pressure.

Selection effects

In any test of a cosmological nature, significant biases can be introduced by an incomplete knowledge of the selection effects in play when building a catalogue of objects. This holds true for cluster cosmology where the parameters of scaling relations between observables and cluster mass, e.g. luminosity-mass or temperature-mass, strongly influence both the amplitude and slope of the mass function recovered from the observables. These effects can be somewhat mitigated by survey self-calibration or through deep followup observations to calibrate the scaling relations.

In a X-ray flux-limited sample, there is a greater chance of detecting clusters with a higher luminosity. This is known as the Malmquist bias and the implication is that at lower luminosities, we only detect clusters that fall in the up-scattered part of the luminosity-mass ($L - M$) relation. Thus, in attempting to fit for the $L - M$ scaling relation one needs to take into account that the down-scattered part of the cluster distribution is missing from the sample. The underlying mass function also plays a role here due to its steepness. We thus expect to find more low mass clusters, which typically also have lower luminosities and fluxes and thus these clusters are most strongly affected by this selection effect. Fitting these relations thus requires very careful treatment. This problem can be further enhanced by measurement errors but for the current generation of X-ray experiments, the errors are typically smaller than the intrinsic scatter and so just obtaining deeper, more accurate observations is not helpful in mitigating this issue. This selection bias can also affect relationships between signals that were not used in the cluster detection process if there is a correlation between the observables. For instance, since the temperature and luminosity are correlated, the bias introduced through the $L - M$ would also strongly impact the temperature-mass $T - M$ relation.

Chapter 2

GROND observations and data reduction

One of the main goals of this PhD project was to provide photometric redshifts for X-ray selected galaxy clusters in order to perform a cosmological analysis. To achieve this, an extensive followup campaign with the **G**amma-**R**ay **B**urst **O**ptical and **N**ear-**I**nfrared **D**etector (GROND) (Greiner et al. 2008) on the MPG 2.2m telescope at the ESO La Silla Observatory was undertaken. The observations were performed over 6 observing periods (ESO periods P91-P96) and 77 nights between April 2013 and February 2016. The work presented in this chapter is based on Section 3 of Ridl et al. (2017).

This chapter is structured as follows. I begin with an overview of the X-CLASS/GROND observing program and follow this with an introduction to the GROND system and provide information on its technical specifications in Section 2.2. In Section 2.3, I discuss the operation of GROND and the choices that were made in terms of exposure times, telescope dither positions and data read-out modes. In Sections 2.4 - 2.6, I detail the data reduction procedures including bias and dark subtraction, flat-fielding, and astrometric calibration. These steps were all performed by taking advantage of the already existing GROND pipeline available at MPE (Küpcü Yoldaş et al. 2008; Krühler et al. 2008) and I created a scripting procedure to run this pipeline sequentially on all observations following each observing run. The developments introduced by me for the purposes of the work presented in this thesis focused primarily on photometric calibration. Since the GROND pipeline is optimised for performance on point sources, I developed my own photometry pipeline taking into account the extended nature of galaxies. Obtaining accurate photometric zeropoints was challenging and I developed a method to produce a master calibration for each observing night. These procedures are described in Section 2.8. I describe the data quality control in Section 2.9 and provide a summary of the observing program in Section 2.10.

2.1 The XCLASS/GROND observing program

The first proposal to follow up X-CLASS galaxy clusters was made by N. Clerc to begin observations in the ESO observing semester P91 (April 2013), with myself joining as a co-investigator for subsequent proposals. Initially the proposal was intended to include only those clusters without a redshift already existing in literature, which at the time totalled 160 galaxy clusters, and to obtain a photometric redshift by identifying the cluster red sequence. In P93, 80 clusters drawn from a processing of more recent XMM archival data (X-CLASS2) were added to this sample, and in P94 we decided to include all clusters with known redshifts from the initial X-CLASS catalogue. The purpose of adding the known-redshift clusters was to obtain a homogenous dataset for the entire X-CLASS catalogue in order to study the optical and near-IR properties of clusters, including the stellar mass, evolution of the red sequence and the cluster luminosity function. These observations would further serve as a sample on which to calibrate and test the methods and data analysis pipelines from which GROND photometric redshifts would be derived. In addition to this, we introduced the idea of performing short, ‘snap-shot’ observations for clusters under photometric conditions that were observed on non-photometric nights in order that they could be better calibrated. Further, in P93, we added a program to follow up follow up cluster candidates which we had identified as being potentially distant ($z > 0.9$) (PI: J. Ridl) with much deeper exposures than those from the nominal X-CLASS observations with the goal of extending X-CLASS photometric redshifts out to $z \sim 1.3$, a redshift range which would greatly enhance the constraining power of our cosmological analysis for dark energy parameters such as w . The analysis of X-CLASS 2 data, along with the distant clusters remain an outstanding task to be completed in the coming months.

Ultimately, the observing campaigns were distributed over 6 semesters (P91 through P96) starting April 2013 and ending in February 2016. Table 2.3 at the conclusion of this chapter provides a summary of the observing runs, grouped by blocks of contiguous nights. In this table, observing nights of various quality and outcome are listed, regardless of the weather or technical conditions on site.

The GROND observation proposals were designed in order to achieve complete follow-up of the selected samples. They took into account weather and technical time losses inherited from previous runs. Most of the observing runs were allocated during dark time, which was critical for ensuring deep g and r band images. Time requests were calculated by considering that without interruption of the observing sequences, up to 20 X-CLASS fields and a few standard stars fields can be imaged during a 10-hour night. Compensation time was granted to account for interruptions due to ToO (target of opportunity) or instrument shutdown, resulting in a number of observed nights typically greater than the number of allocated nights in a given period.

Over the six observing semesters, the most significant changes impacting the observing schedule were: (i) a failure in one of the two CCDs for each of the i - and z -bands channels during P91; (ii) a strong El Niño event in 2015 affecting notably the P94, P95 and P96 semester observations resulting in an increased number of time losses due to bad weather conditions (wind, humidity and clouds) ; (iii) recoating of the primary mirror (M1) in P95,

resulting in a net improvement of the sensitivity of the telescope.

In order to reach the depths and image quality required by the science objectives of the program, several targets were observed more than once and up to 8 times across the whole observing program. As described in Section 2.9, only the “best” calibrated observing sequence was kept for the photometric redshift analysis of this paper.

The target lists for each observing run were established on the basis of visual inspection of the 3-colour and single-filter images acquired during previous runs. Whenever a dataset did not comply to the quality standards of the project, we included the corresponding target in the pool of objects still requiring observations. These were assigned priorities using a combination of empirical grades based on the image quality, observing night quality, seeing and limiting magnitude (for those fields that could be photometrically calibrated).

Observers were provided with prioritized target lists, finding charts and observation blocks (OBs), those accessible from the observation management tool P2PP. Observers were encouraged to select targets at high elevation, still accommodating for the on-site real-time observing conditions (e.g. wind direction, atmospheric conditions, gamma-ray burst follow-up observations, etc.). At the end of each observing night a standardized log file was written, containing an entry for each OB that had been launched (time of observation, general conditions, comments).

A typical XCLASS/GROND observing night consists of: (i) afternoon instrument calibration and preparation of the telescope ; (ii) evening calibration (twilight flat fields) and standard fields acquisition ; (iii) series of science OB and standard fields acquisition and (iv) morning calibration (twilight flat fields, biases, darks, etc.). Target of opportunity observations occurring during (iii) have a different ESO run identifier to those listed in Table 2.3.

Finally, a typical XCLASS/GROND science OB acquisition consists in: (i) slewing the telescope to the target position ; (ii) selecting a guide star on the guiding camera ; (iii) launching the automated sequence of CCD/detectors integrations and readouts until completion of the observing block. Step (ii) has been the cause for repeated observations, due to the reduced availability of bright guide stars in the neighborhood of extragalactic science targets.

2.2 Overview of GROND technicalities

GROND is a 7-channel imager, allowing for simultaneous imaging in the Sloan g', r', i', z' and near-infrared JHK bands. It was primarily designed to provide rapid multi-wavelength observations of gamma-ray burst afterglows e.g. (Greiner et al. 2009, 2011, 2015). For the remainder of this work, GROND optical filters will be expressed as g, r, i and z .

Incoming light is split into different photometric bands by making use of dichroics and the design is such that the optical transmission functions are almost identical to those of the Sloan g', r', i', z' filter system. The optical filter system is shown in Figure 2.1. The exception to this is the i -band which, due to the overlap between the Sloan r', i', z' bands, is slightly narrower, in favour of standard-width r and z bands. Each of the optical CCDs

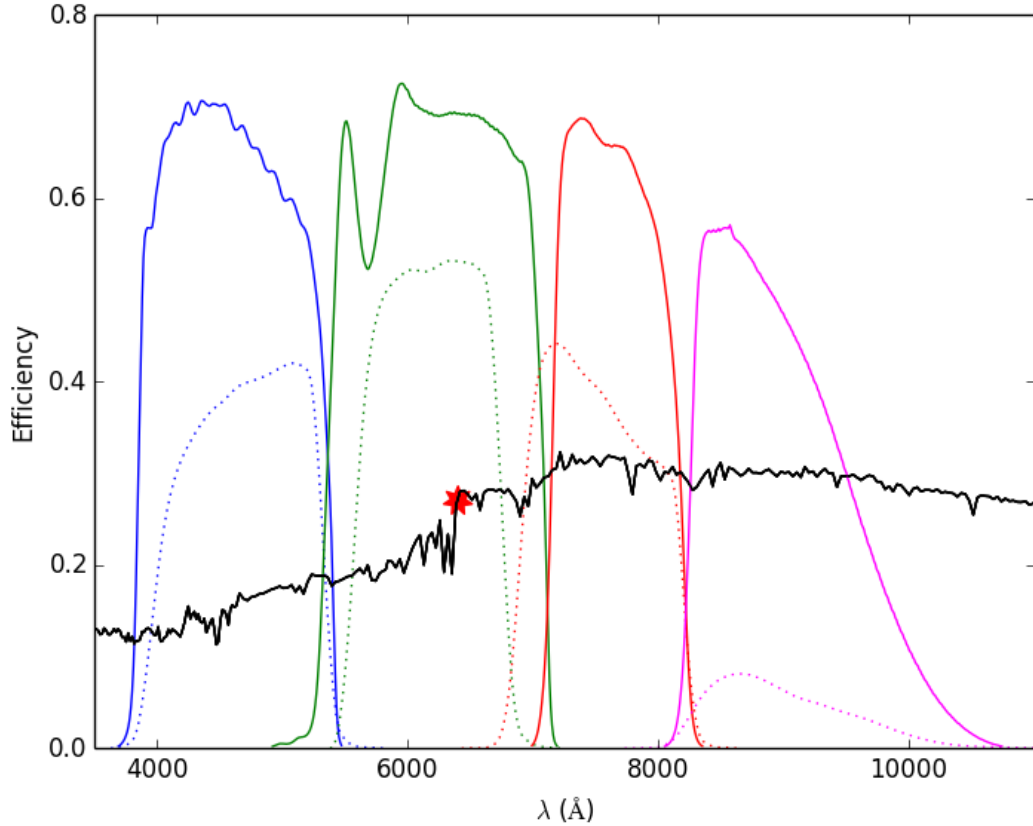


Figure 2.1: The efficiency of GROND (solid) and for comparison, SDSS (dotted) filters is shown as a function of wavelength. The narrow width of the GROND i -band compared to SDSS is clearly visible. Also plotted is an arbitrarily scaled spectral energy distribution (SED) of an early type galaxy at redshift $z = 0.6$. The 4000 Å break, the key feature used for determination of the redshift of the cluster is marked with a star.

provides a field-of-view of $5.4' \times 5.4'$ with a pixel scale of $0.158'' \text{ pixel}^{-1}$. The optical filter transmission curves are shown in Figure 2.1. The NIR part of GROND is a focal reducer system and provides a $10 \times 10 \text{ arcmin}^2$ field-of-view with a pixel scale of $0.60'' \text{ pixel}^{-1}$. The K channel additionally includes a flip mirror for dithering purposes. Schematic diagrams showing the layout of the GROND optics and detectors are given in Figures 2.2 and 2.3. For the remainder of this work we consider only the optical channels since they span the 4000 Å break, which is the most redshift-constraining feature for early-type galaxies, over the redshift range in which we are interested. A comprehensive description of the instrument is given in Greiner et al. (2008).

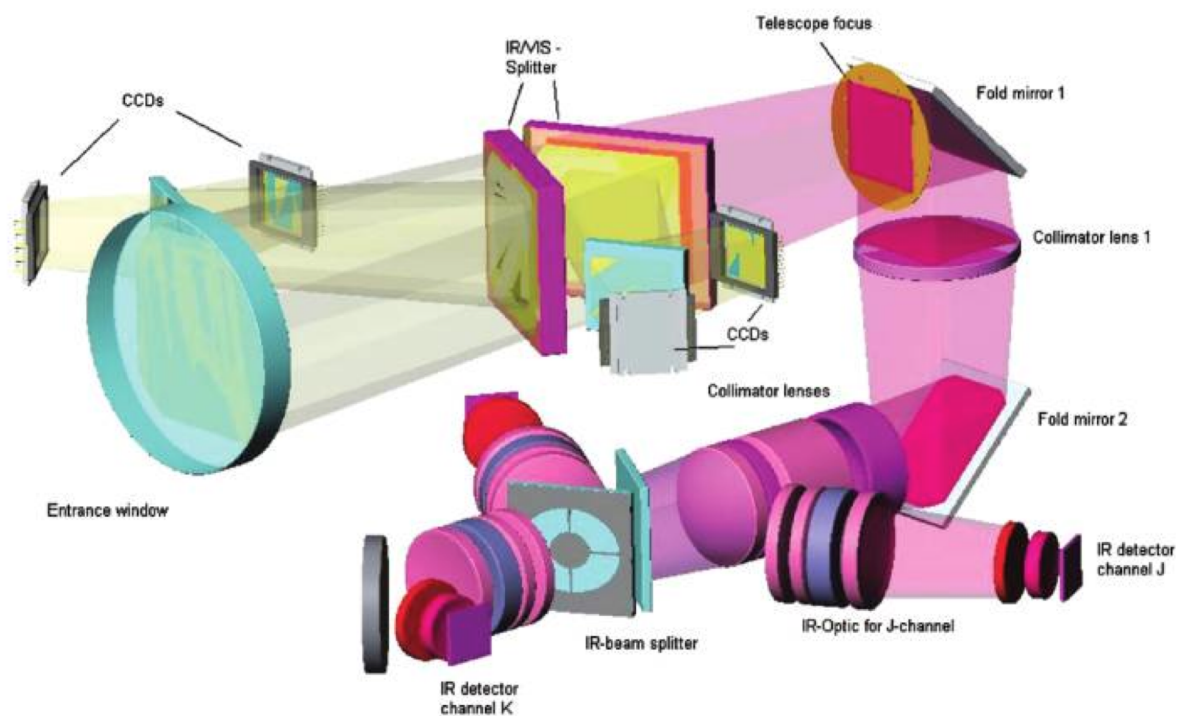
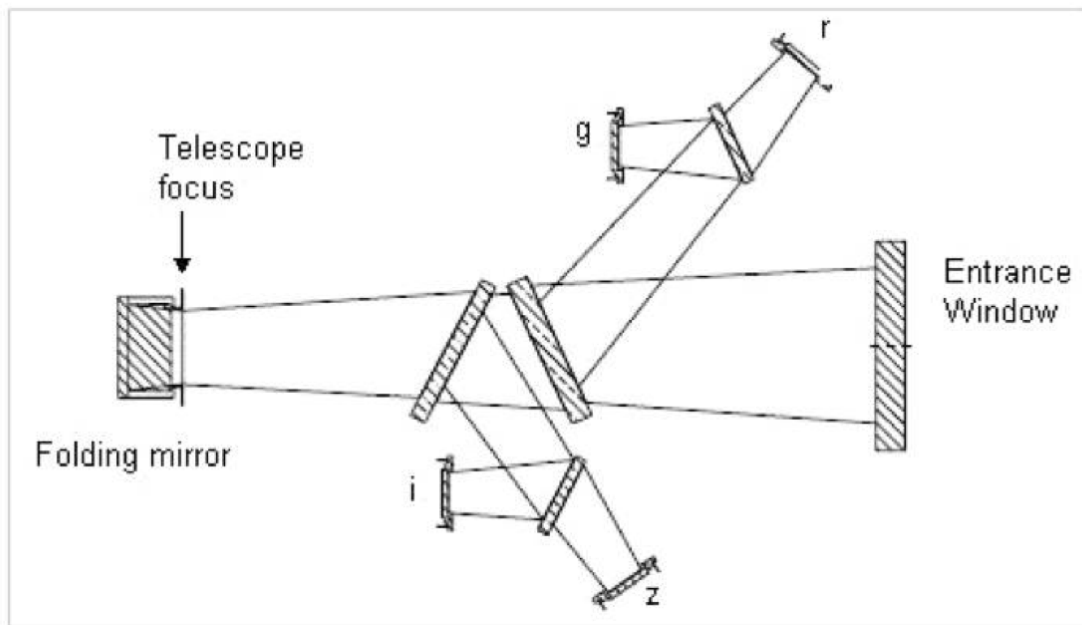
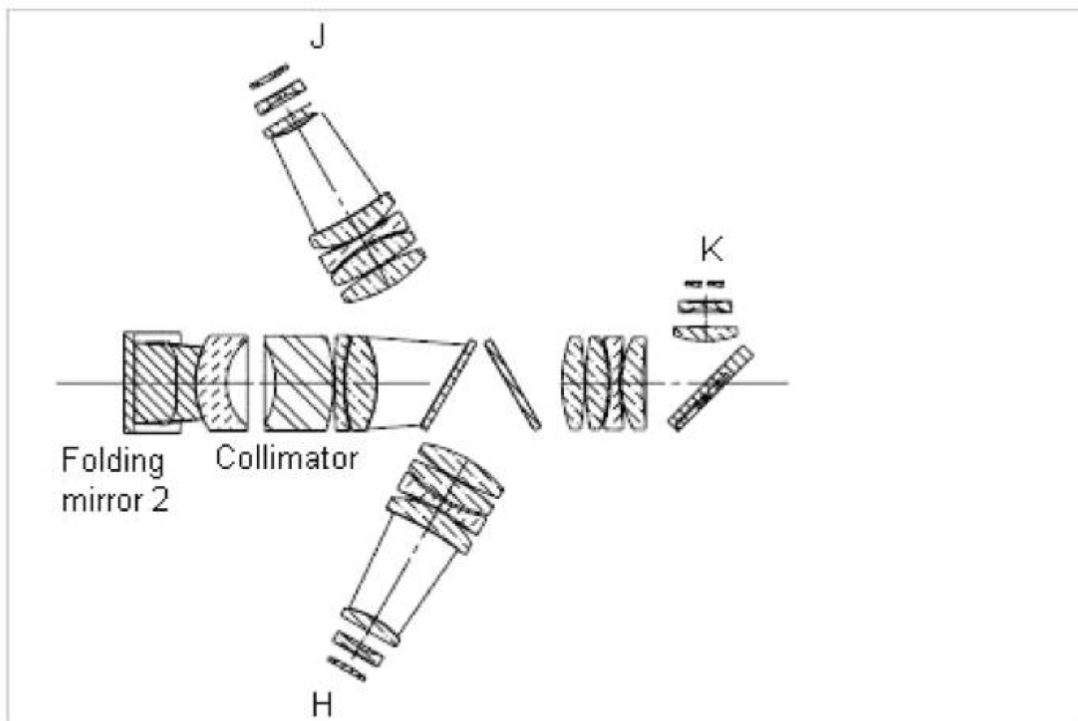


Figure 2.2: Three dimensional structure of the components making up the GROND optical and near-IR arms. The most important individual components are labelled. Image courtesy of Greiner et al. 2008.



Visual Optics System



IR Optics System

Figure 2.3: Layout of the GROND optics show a slice through the optical arm (top) the near-IR arm (bottom). Image courtesy of Greiner et al. 2008.

2.3 Operation of GROND

In operating a 7-channel simultaneous imager there are several observational constraints that need to be taken into account when preparing observation blocks. The optical and near-IR systems require a different number of exposures at each telescope dithering position and integration times for each of them should be set to optimise the exposure time also taking the differing read-out time of the detectors into account.

For GROND observations, the most important parameters to be taken into account are: the number of telescope dither positions (NTD); the number of telescope pointings (NTP); the number of exposures in the g and r -bands (NGR), and the number of exposures in the i and z -bands (NIZ), with the corresponding integration times (UITGR, UITGZ); the number of K mirror dither positions (NMD); the number of K mirror pointings (NMP); the number of JHK exposures in a single K mirror position (NINT); the number of stacked JHK exposures (NDIT); and the JHK integration time (DIT).

We determined that four telescope dithering positions with a single optical exposure at each would be sufficient for our observations and there are a number of predefined OB types, named for the total integration in the K -band namely 4-, 8-, 20-, 40-minute OBs which satisfy this constraint. Other commonly used observing blocks use six telescope dithering positions and in principle all of the parameters above can be freely set by an observer. The standard observing blocks however optimise the exposure times based on the differing readout speeds of the detectors and so using these OBs is advised. Two read-out modes for the optical CCDs are available namely ‘fast’ and ‘slow’. The exposure times for these OBs are given in Table 2.1.

Initial pathfinding observations indicated that sufficient depth is obtained for clusters of $z < 0.3$ and $z > 0.3$ (this classification was based on DSS imaging and is not always accurate; see Section 3.2 for more details) with the 8min4TD and 20min4TD OBs respectively. Standard fields used for photometric calibration are observed with 4min4TD OB. All observations were initially carried out in slow read-out mode until November 2015 when a technical issue necessitated a change to fast read-out mode with its somewhat higher read-out noise.

Practically all observations used in this project were performed in visitor mode, apart from 2 which were executed remotely by the GROND team from Garching. Prior to an observing run, all necessary OBs were loaded into the ESO P2PP software which allows for them to be directly pulled into the GROND observing environment sequentially and efficiently. Once an OB has been started, the telescope automatically slews to the position and then waits for input from an astronomer before starting to take exposures. The telescope is able to track the position on the sky automatically but inaccurately; it lags slightly behind and so sources can appear elongated. To get around this, it is necessary to adjust the position of the telescope every few seconds. The size of this adjustment is measured by observing a bright star with a separate camera, and ensuring that the star remains at the same position on the CCD of the guide camera. Finding an appropriately bright guide star was at times challenging, due to the extragalactic nature of our sources, and so the telescope occasionally had to be manually offset by up to $1.5'$ to bring a star into

Table 2.1: Total exposure times of the predefined GROND observing blocks in the optical (*griz*) and near-IR (*JHK*) channels used in this study. Execution times are approximate and include telescope slewing.

OB type	<i>griz</i> (s)	<i>JHK</i> (s)	Read-out	Execution time (min)
4min4TD	141.6	240	Slow	10
4min4TD	264.0	240	Fast	10
8min4TD	459.6	480	Slow	15
8min4TD	579.6	480	Fast	15
20min4TD	1476.0	1200	Slow	30
20min4TD	1596.0	1200	Fast	30

the field-of-view of the guide camera. We also frequently had problems with the guiding software which resulted in the guide star being lost and ruining the OB, which would then have to be repeated. This resulted in significant time losses.

Exposures from the observations are read-out immediately to a screen in the observing room and this allows for the measurement of the FWHM of stars which gives a more accurate account of the seeing than that available from the DIMM monitor at the observatory. A substantial number of observations were performed without the assistance of a telescope operator or support astronomer and this resulted in an incredibly rich experience of learning how to perform astronomical observations.

2.4 Data reduction and image combination

Preliminary reduction of the data was performed for each OB using the methods of Küpcü Yoldaş et al. (2008) and Krühler et al. (2008). This pipeline is based on the standard tools of *IRAF/PyRAF* and performs bias and dark current subtraction, flat-fielding and defringing along with providing astrometrised co-added images and a photometric measurements idealised for point sources for each channel.

2.4.1 Bias and dark subtraction

The first step in the data reduction process is the removal of electronic noise and dark currents. This is done by subtracting bias and dark frames from the raw images. Bias and dark frames were obtained using the standard calibration OB available at the telescope following each night of observations with ten bias frames followed by two dark frames of different integration times recorded sequentially. A bias frame is obtained by recording a zero second integration and gives the read-out noise of the CCDs. GROND has two

readout speeds for the optical CCDs with the fast readout mode having a considerably higher readout noise. Towards the end of 2015 however, a problem with one of the readout cables developed resulting in an increase in the readout noise, which affected the slow readout mode significantly. A decision was thus made to perform all following observations in fast readout mode. Biases for each readout mode were obtained for each calibration OB.

Even in the absence of illumination, a CCD will record a current due to the presence of thermal electrons. This is usually mitigated by cooling the CCDs to very low temperatures and the GROND optical CCDs are cooled to 165K, greatly reducing the amount of dark current. Dark frames are obtained by integrating for 600s with the shutter of the instrument closed. The dark current scales with integration time and it must thus be rescaled to the integration time of the respective science observation before it can be removed. Master bias and dark frames are produced by combining the individual exposures and these are then subtracted from the science observation under analysis.

2.4.2 Flat-fielding

The sensitivity of a CCD is not constant over the entire field of view. Different parts of the detector will record a different fluxes when exposed to the same source of light. This pixel-to-pixel variation is characterised by a flat-field observation i.e. an observation of a homogeneous light source, and it is a multiplicative effect. These observations are typically made either using a uniformly illuminated sheet on the inside wall of the telescope dome (dome-flat), by observing the sky while it is almost uniformly illuminated during morning or evening twilight (sky-flat) or by long exposures of the dark sky (super-flat). Each of these methods have advantages and disadvantages. The dome-flats can be convenient because they are performed with the dome closed and can be done during the day but it can be difficult to get a truly homogeneous field to observe. Also, the light source used to illuminate the flat field typically does not represent spectral energy distribution (SED) of the sky background or astronomical sources very well. Sky-flats on the other hand can be difficult to observe and must be performed at a very specific time (twilight) so that the sky is neither too bright, which would cause the CCDs to become saturated, or too dark, such that the signal is dominated by readout noise and poor statistics. This is particularly difficult for GROND since seven individual sky-flats must be measured simultaneously. The spectrum on the twilight sky however resembles the night sky much more closely than a lamp. Super-flats probably represent the most accurate method of compensating for the pixel-to-pixel variation but are observationally very expensive to obtain as they require long exposure of empty fields in the night sky; time which could be spent on science targets.

For this analysis we selected to use only sky-flats. These were observed whenever possible either in the evening before the start of observations or in the morning directly following the observations. It was not possible to have a sky-flat for every night due to weather and technical considerations but the GROND sky-flats have been shown to be consistent over a number of nights. For nights where no sky-flat was available, the next closest observation was taken. Evening sky-flats were typically started when the sun was roughly 4 degrees below the horizon. Past experience from observers indicates that a way

to ensure adequate illumination is to follow the real-time display of the J-band, set to 2 second exposures and to start the OB when this was flat and at a level of approximately 20,000 ADUs. Morning sky-flats were typically started when the sun was 9 degrees below the horizon. A database of flat fields is available on the control systems on the telescope and a field with a right ascension of 1-2 hours greater than the sidereal time at sunset on the given night was selected. Twelve exposures were then obtained the exposure times ranging from 6-40 seconds, increasing as the sky becomes darker. Great care was taken to ensure that all seven simultaneously observed sky-flats were suitably exposed and that the sky was bright enough to obtain a statistically robust flat-field without saturating the detectors.

The master bias and dark frames were subtracted from the individual exposures and these were then combined to create a master flat. The science frame was then divided by this master flat. The removal of the bias and dark current, and the correction for the pixel-to-pixel correction was performed using the IRAF tool `quadded.ccdproc`.

2.4.3 Fringing

As with many optical instruments, the CCDs of GROND exhibit fringing distortion caused by the interference of light within the CCD itself. This effect is strongest in the redder (i and z) bands and is neglected in the bluer (g and r) bands. The pattern of this distortion follows the slight variations in the thickness of the CCD and so it remains constant over time. It is possible to use a single, high signal-to-noise fringe map on all observations in a given filter with just the intensity of the pattern varying from frame to frame. The intensity of the fringes depends on the amount of light entering the CCD and scales with the exposure time. The fringing map must be carefully scaled to the correct intensity to match each of the individual frames before it can be accurately subtracted. All science observations making up this dataset comprise of four individual exposures in each of the optical bands and different telescope dithering positions. By median stacking these, one can obtain a master fringe map. The IRAF tool `rmfringe`, is utilised to subtract the fringe pattern by minimising the difference between the map and object frames. Here, one must be careful that any sources, bad pixels and cosmic ray hits are well masked.

2.5 Coaddition of images and sky subtraction

Once the individual exposures have been cleaned of the bias and dark currents, and corrected for the varying sensitivity across the field-of-view and fringing effects, they are combined to form a single image (coadd) for each filter using the IRAF tool `imcombine`. Astronomical sources are then masked out and the sky background is calculated and finally subtracted from each of the respective coadds.

2.6 Astrometry

Astrometry is the process of measuring precise positions of astronomical objects relative to a reference coordinate system. The pointing accuracy of the telescope varies over the course of a given night and thus, in order to know where exactly on the sky the telescope is pointed, it is necessary to compare the sources detected in an observation to a catalogue of known objects. The most commonly used catalogues for this purpose are the USNO and SDSS catalogues. The positional accuracy of sources in the SDSS is superior to the USNO but is limited to only the northern hemisphere. The lack of a comparable, publicly available survey in the south implies that for a large part of the fields observed from La Silla, in the southern hemisphere, must be matched to the USNO catalogues. In the future, the GAIA satellite will provide precision positional measurements of stars across the entire sky which will be incredibly useful for astrometric calibrations of future experiments.

2.6.1 Pipeline recovered astrometry

An astrometric solution was accomplished through the matching of stars in common with SDSS DR7 (Abazajian et al. 2009) when available or the USNO-A2.0 catalogue (Monet et al. 1998) where the observations fell outside the footprint of SDSS for the optical bands and the 2MASS catalogue (Skrutskie et al. 2006) for the near-IR bands and making use of the IRAF tool `xyxymatch`.

2.6.2 Refinement with SCAMP

In a number of cases, the standard GROND pipeline failed to find the correct astrometric solution. In order to find the correct solution, we used the publicly available code `SCAMP` (Bertin 2006). This code also allows for a mapping of the astrometric distortions across the field of view. A catalogue of objects is generated by a single pass of `SExtractor` on each of the *griz*-band images. The catalogue from the *r*-band is then matched to either the SDSS or USNO, depending on availability. This process generates a new FITS header which is used to resample the image to the new WCS solution using `SWARP`, a publicly available software for the resampling and coaddition of FITS images. A new reference catalogue is created by a second pass of `SExtractor` on this resampled *r*-band image. The astrometric solution was refined for all images, even those for which the pipeline produced a good result. The catalogues generated for the remaining (*giz*)-bands are then matched to this new *r*-band reference catalogue and resampled so that the pixel coordinates in each of the four channels are mapped to a common pixel grid with a scale of $0.158''\text{pixel}^{-1}$ with the use of `SWARP` (Bertin et al. 2002), a publicly available software that performs the resampling and co-addition of FITS images. This is necessary later on when calculating galaxy colours.

2.7 Source detection and PSF modelling

Source detection and photometric measurements were performed using `SExtractor` (Bertin & Arnouts 1996), operating dual-mode with a `SWARP` *riz*-coadd as the detection image. This forces the photometric measurements to be performed in the same extraction radius for each channel.

A general model for the PSF across the field-of-view was constructed from bright, unsaturated stars and making use of the publicly available software `PSFEx` (Bertin 2011), for which the various parameters were tuned to optimise the accuracy.

2.8 Photometric calibration

In this first step, the typical photometric zeropoints for each of the GROND channels were assumed, together with the necessary corrections for exposure time and atmospheric absorption, quantified by airmass. Where possible, the resulting photometric catalogue was cross-matched with SDSS DR7 photometric catalogue with a 1 arcsec matching radius, and non-saturated and unblended stars selected in order to calibrate the zeropoints. The final zeropoints in each channel were then determined by comparing PSF magnitudes (`MAG_PSF` from `SExtractor`) in the two catalogues with the SDSS photometry corrected using the conversion relations given at <http://www.mpe.mpg.de/~jcg/GROND/>.

Given that the majority of our sample lies to the south of the SDSS footprint, it was not possible to calibrate the individual zeropoints for each observation. For these fields we attempted to make use of stellar-locus regression methods to obtain a colour-colour calibration. In this method, it is assumed that stars follow a well defined locus in colour-colour space. Thus by comparing the colours of the stars in various colour combinations it is possible to calibrate the relative colours. This is however degenerate and it is not possible to directly obtain an absolute calibration for each band individually. If one is able to fix on the bands to a known catalogue (typically *J*-band from 2MASS), one can break the degeneracy and obtain the absolute zeropoints. This method was attempted but ultimately rejected due to a large number of fields not having enough stars to obtain statistically robust results in the individual fields.

Ultimately, it was decided that the most reliable way to achieve a homogeneous photometric calibration would be to determine a ‘master’ calibration for each observing night. This was accomplished by averaging the zeropoint corrections obtained from the comparison with SDSS for all possible fields, including science and standard star observations. The standard deviation σ of the zeropoints was also calculated and fields with zeropoints more than 3σ from the average were excluded and the average recalculated. Once this master calibration was in-hand, corrections for extinction due to airmass were applied to each observation independently. The master zeropoints for each observing night are displayed in Figure 2.4. This plot provides a useful indication of the photometric quality of each night, as discussed in Section 2.9. One of the reasons that we are able to use this method is unique to GROND, in that the imaging is performed simultaneous and this all

filter are observed with identical atmospheric conditions. This means that the atmospheric absorption affects observed magnitudes to a very similar degree in each band. So, while it is true that our calibration methods might not give the most accurate magnitudes in individual bands the colours that are derived are robust against an unstable atmosphere and still accurate enough to calculate photometric redshifts.

Corrections for Galactic extinction were then applied to the GROND object magnitudes based on the dust maps of [Schlegel, Finkbeiner & Davis \(1998\)](#), making use of the Python package `Astroquery`.

Star-galaxy separation was accomplished by selecting objects based on the `SExtractor` parameters `CLASS_STAR` and `SPREAD_MODEL` for the r -band and only objects with `FLAG = 0` in all bands included in the final catalogue. Kron magnitudes, `MAG_AUTO` were chosen for the total galaxy magnitudes and for the determination of galaxy colours. For galaxy magnitudes we also attempted to use the model fitting features of `SExtractor` (`MAG_MODEL` and `MAG_DETMODEL`) but ultimately achieved the most robust photometric redshifts when using the Kron magnitudes.

2.9 Data quality control

All observations were inspected visually in terms of the astrometric solution and photometric calibration. In cases where a single galaxy cluster was observed on more than one occasion, the best observation was selected based on seeing, background and limiting magnitude. The stability of the photometric zeropoint calibration for each particular night was also taken into account. The average data quality in terms of seeing and limiting magnitude is summarised in [Table 4.1](#) and [Figure 2.5](#).

Table 2.2: The median seeing and 10σ -limiting magnitude in each of the four optical channels and for each of the chosen observing blocks. The limiting magnitudes are determined by the magnitude at which the signal-to-noise for an extended source reaches 10.

Channel	Seeing [$''$]	8min4TD [mag AB]	20min4TD [mag AB]
g	1.28	22.59	23.44
r	1.06	22.38	23.15
i	1.04	21.52	22.25
z	1.00	21.07	21.84

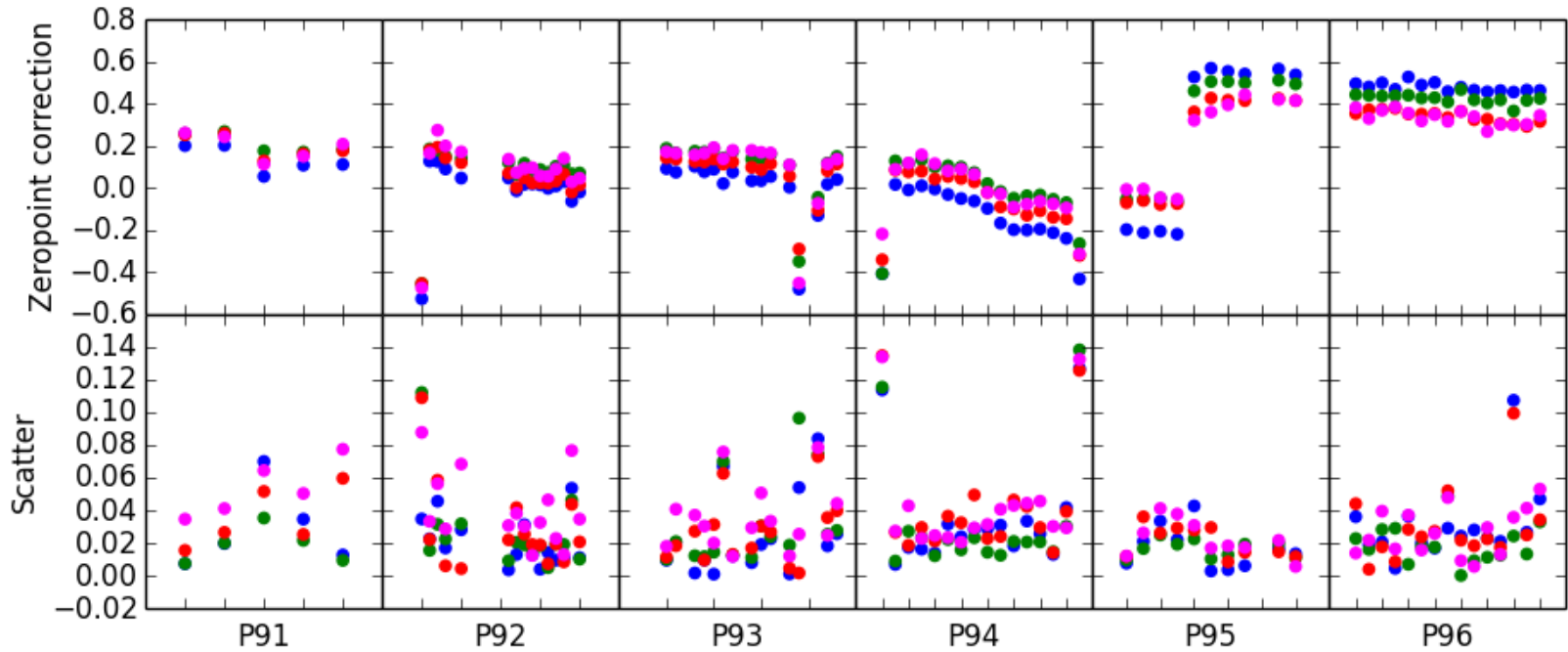


Figure 2.4: The evolution of the GROND photometric zeropoints in each of the optical bands (*g*: blue, *r*: green, *i*: red, *z*: magenta) over the course of the observing period from ESO periods 91 (starting April 2013) to 96 (ending February 2016). Each point represents the median zeropoint correction for a given observing night, measured from all fields overlapping with the SDSS footprint and after taking into account corrections for atmosphere extinction and differing exposure times. The top panel indicates the zeropoint correction and the bottom panel a measure of the RMS scatter across all measured fields on a given night.

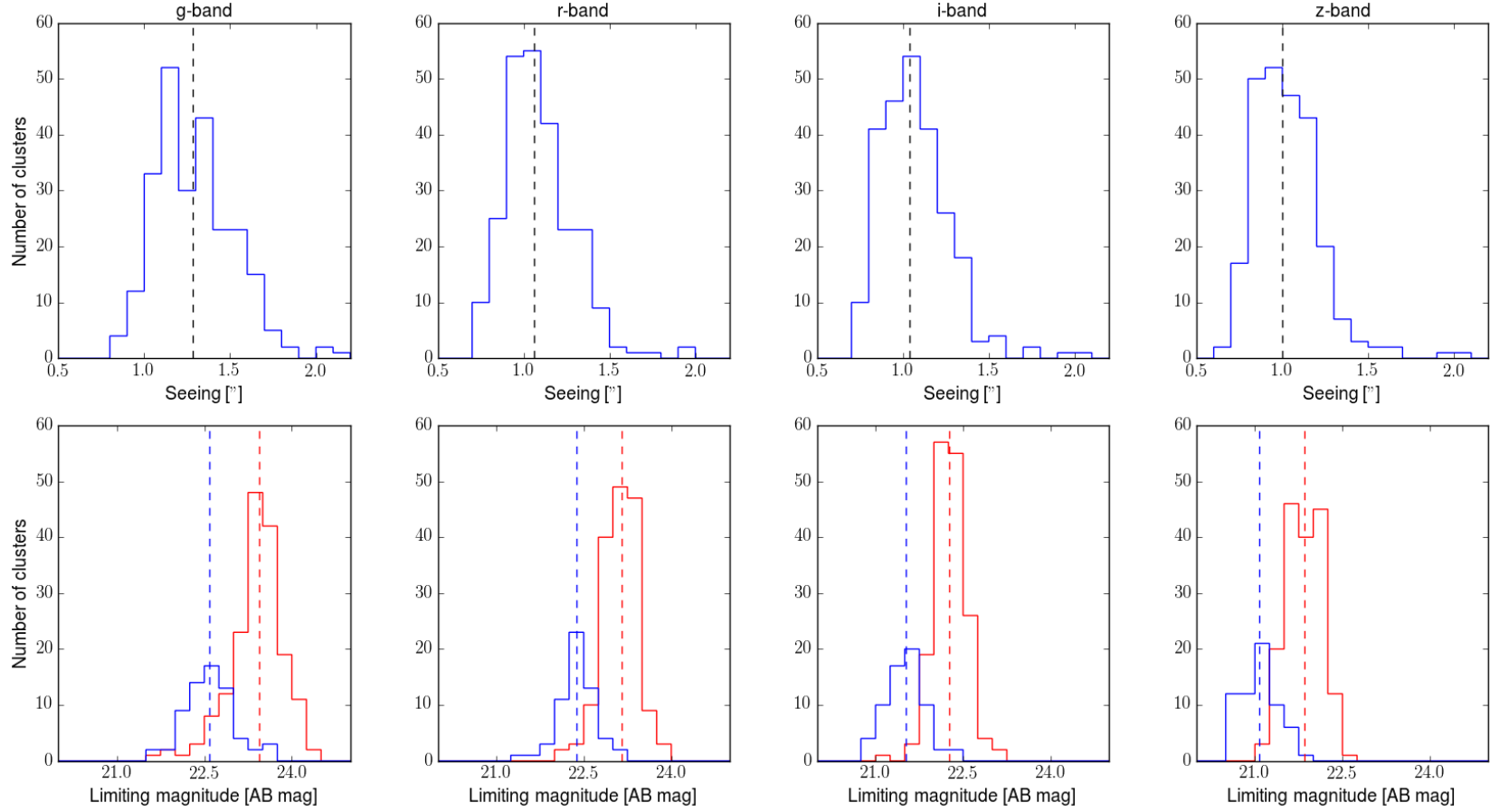


Figure 2.5: The upper panels describe the distributions of the measured seeing and the lower panels describe the 10σ point-source limiting magnitudes for 8min4TD (blue) and 20min4TD (red) for each of the *g*, *r*, *i*, *z*-bands. The median values are indicated by the vertical dashed lines.

It is interesting to note the evolution of the photometric zeropoints in each channel over the course of the observations, as illustrated in Figure 2.4. Over the first 4 ESO periods (actual dates of observations are given in Section 2.1) of observations (P91-P94) we notice a gradual decline in the zeropoints in all channels. This is predominantly due to the collection of dust and the gradual deterioration of the primary mirror of the telescope. During P95, the primary mirror was cleaned and recoated providing a large increase in the photometric depth of the instrument, most notably in the g -band where an improvement of 0.7 magnitudes is noted. Points significantly below the gradual trend in the zeropoint evolution and those where the scatter is higher than average give a good indication that the night was not photometric and that the calibration can not be trusted. Fields observed on these nights were typically reobserved on nights with higher photometric quality. A selection of $g'r'i'$ three-colour composite images for optically confirmed clusters over a range of redshifts are shown in Figures 2.6-2.9. All images are 4.5×4.5 arcmin and the cyan contours are drawn from the wavelet-filtered X-ray images in the [0.5-2] keV range.

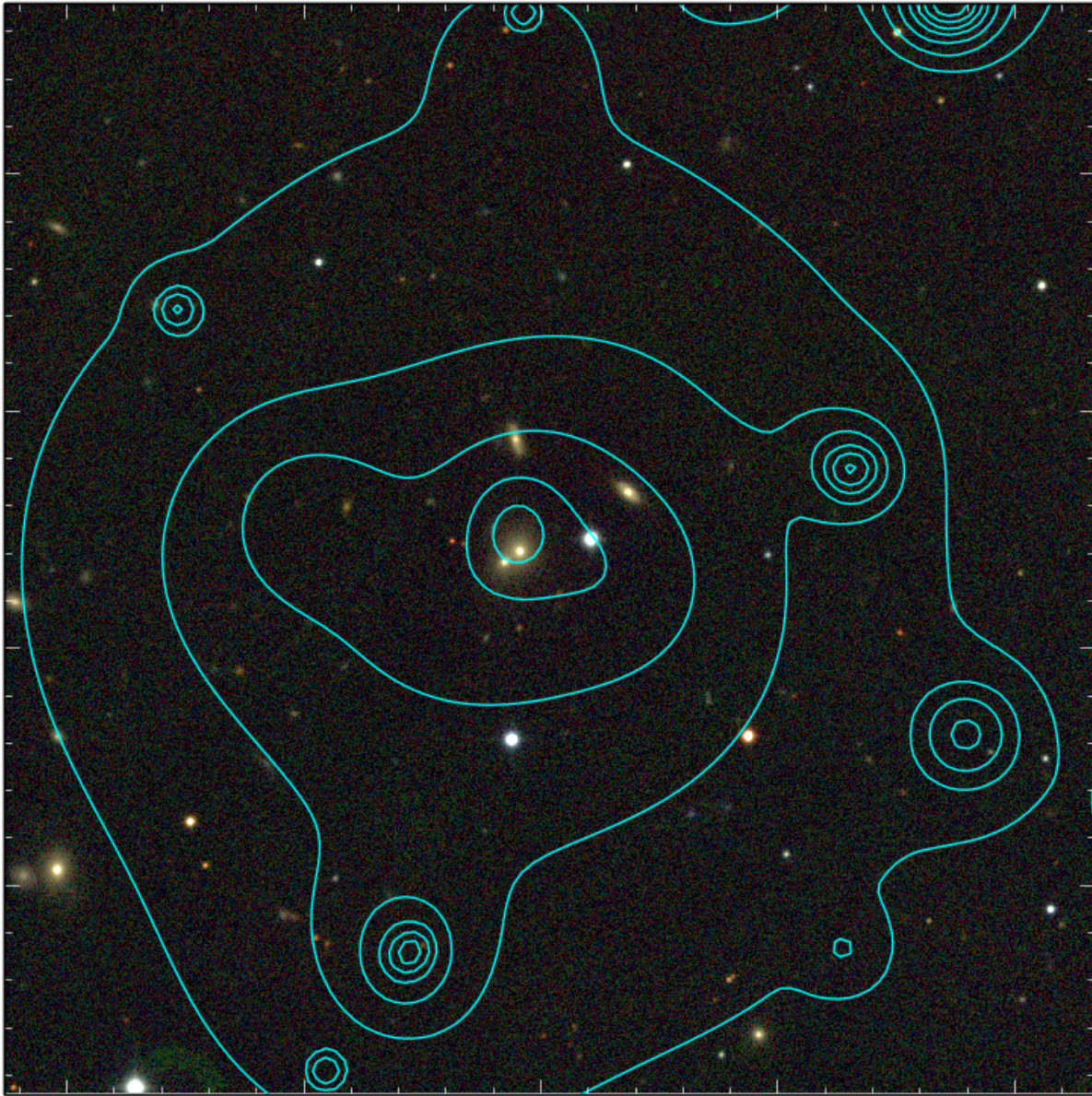


Figure 2.6: This compilation shows X-CLASS 2162 ($z_{spec} = 0.12$, $z_{phot} = 0.12$).

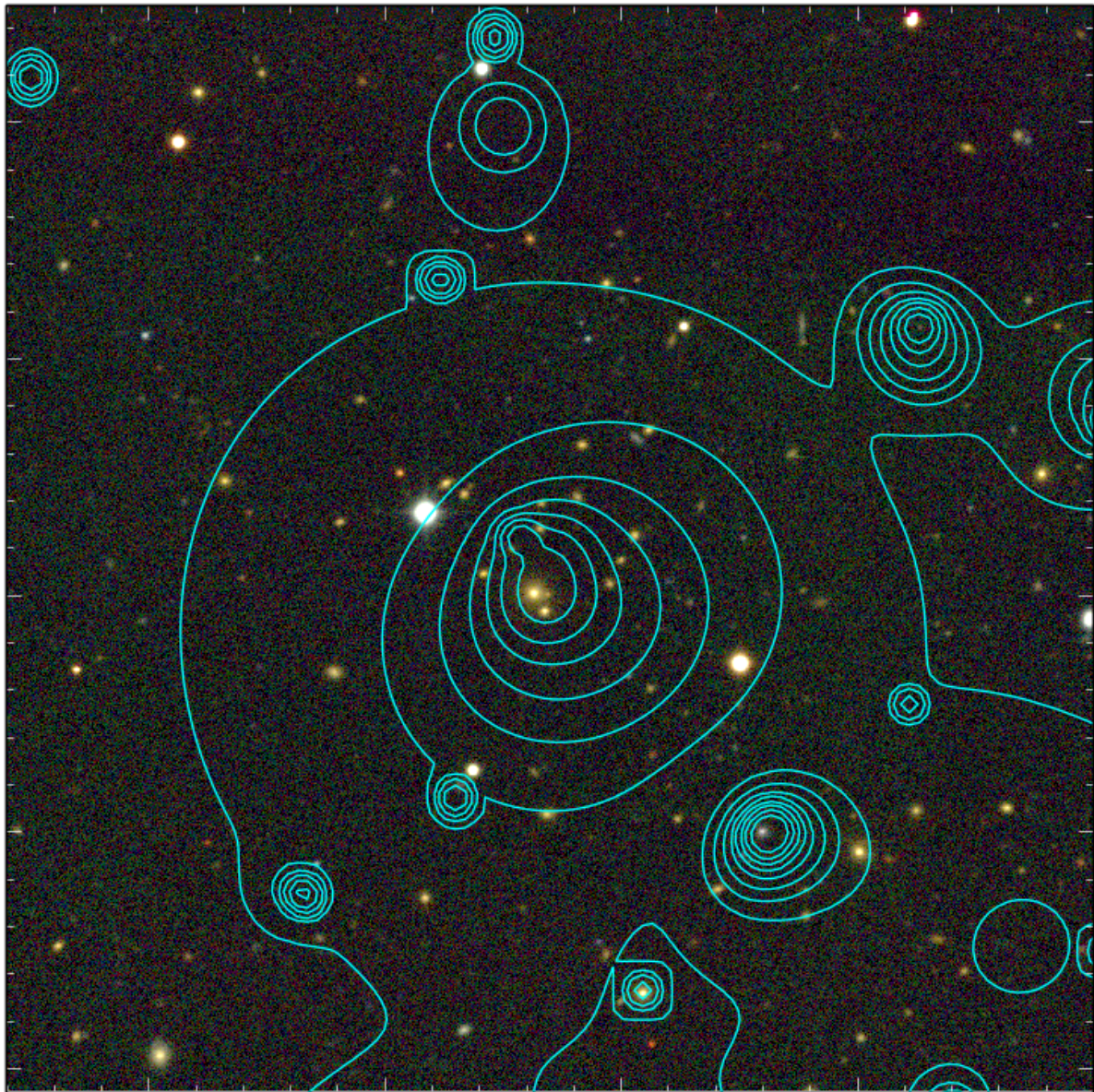


Figure 2.7: X-CLASS 40 ($z_{spec} = 0.33$, $z_{phot} = 0.32$).

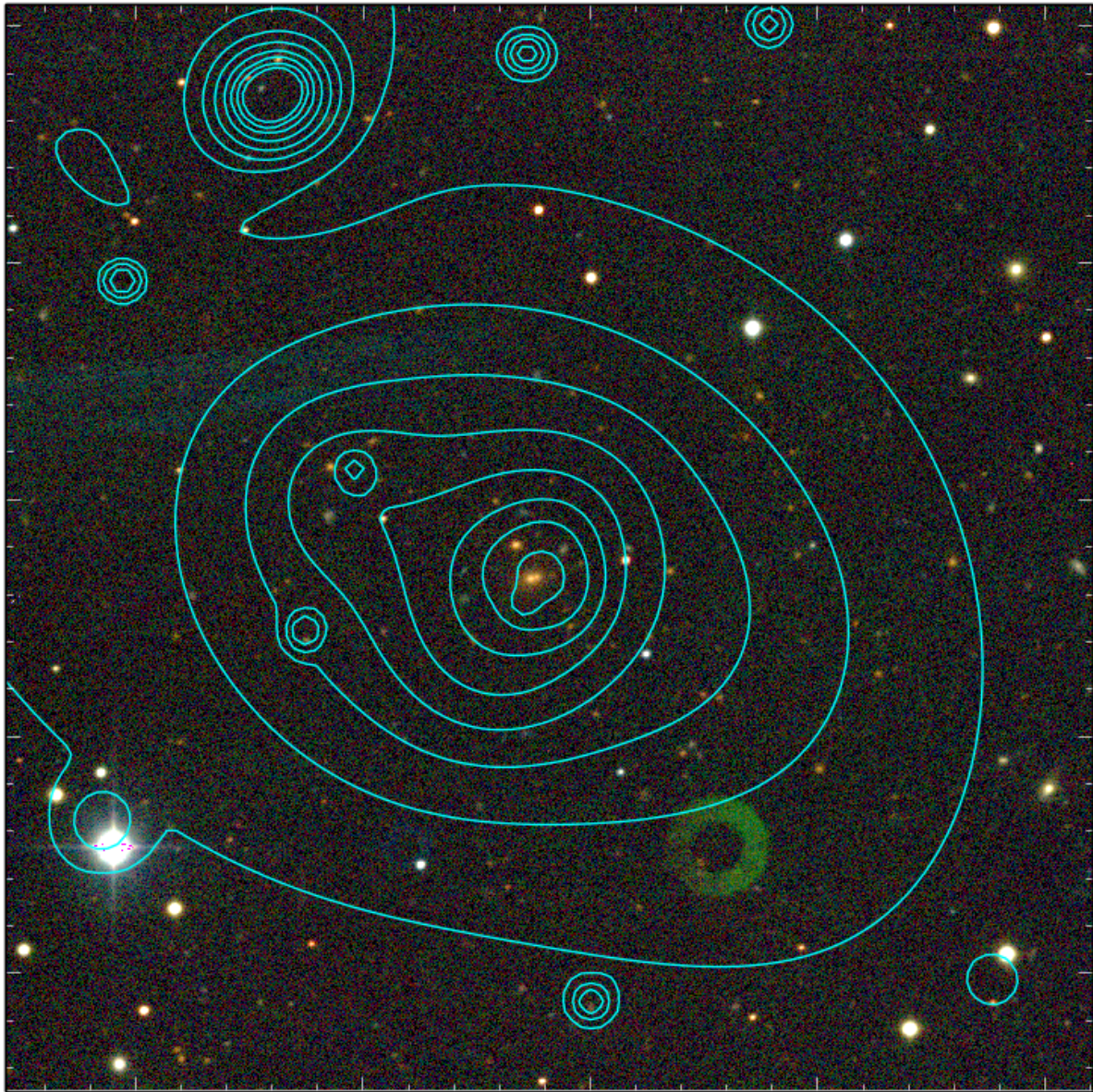


Figure 2.8: X-CLASS 459 ($z_{spec} = 0.55$, $z_{phot} = 0.54$).

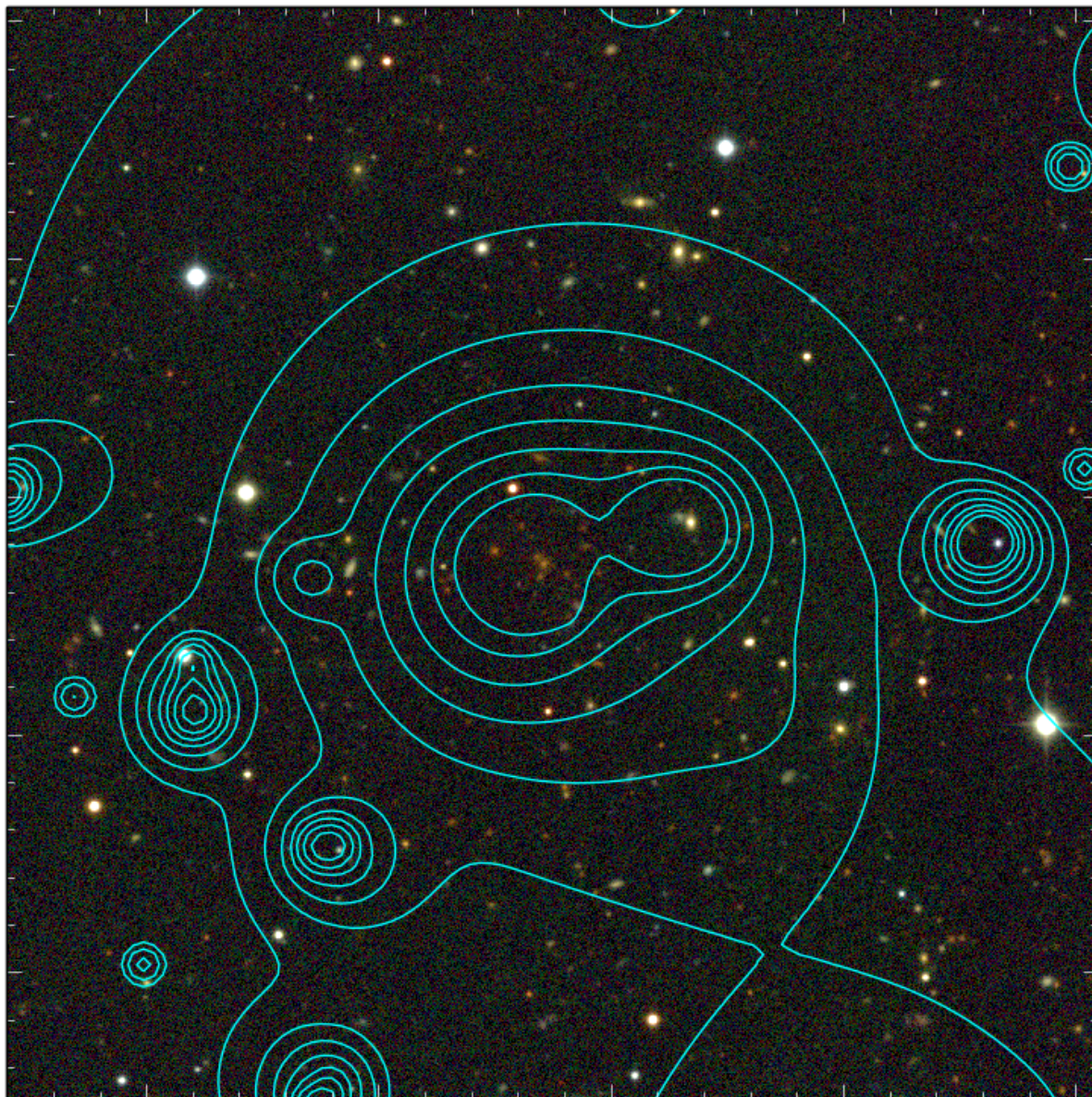


Figure 2.9: X-CLASS 505 ($z_{spec} = 0.79$, $z_{phot} = 0.81$).

2.10 Summary of the X-CLASS/GROND observing campaign

These observations provided an incredibly rich learning experience for me. I was able to learn a great deal about optical and near-IR observations, which I had no prior experience with. This lack of experience is evident when one considers the improved efficiency of observations as the campaign proceeded. Something that was lacking at the start of our observing campaign was a set of criteria to determine whether or not a particular observation was of a high enough quality and what level of photometric accuracy would be required to obtain good photometric redshifts. In order to quantify these requirements, I should have focussed sooner on a development of the photometric redshift pipelines, in parallel with the GROND observations and data reduction. This pipeline could have then been run first on SDSS data providing a nice extension to the X-CLASS/GROND program and could probably have produced an extra publication focusing purely on an X-CLASS/SDSS sample. By introducing random errors into the SDSS data, I also could have determined the level of accuracy needed from the GROND observations. Looking forward, these are factors which I will certainly prioritise before commencing an observational program.

A summary of the campaign to followup X-CLASS galaxy clusters is given in Table 2.3. The observations are grouped by blocks of continuous nights and ESO observing periods. In this table, observing nights of various quality and outcome are listed, regardless of the weather or technical conditions on site.

Table 2.3: Table summary of the GROND observing campaign at the ESO/MPG-2.2m telescope relevant to the sample presented in this paper. The first column lists the standard run identifiers as referenced in the ESO archive database. The number of allocated nights takes into account target of opportunity (ToO) and technical overheads. These nights were also shared with separate programs to followup distant clusters as well as clusters from the updated X-ray processing, which are not included in this paper. The number of targets indicates the successful observations of XCLASS sources acquired during this period. The attachments between sources and observing runs is available through the L4SDataBase (<http://xmm-lss.in2p3.fr:8080/l4sdb/>).

ESO Run ID	Alloc.	Observation period (UT date at night start)			N targets	Observers
091.A-9017(A)	8	2013	Apr	7, 8	14	N. Clerc
"		2013	Aug	23, 24, 25, 26, 29	4	M. L. Menzel
092.A-9023(A)	12	2013	Oct	1, 2, 3, 4	29	N. Clerc
"		2014	Jan	(fillers)	3	M. Salvato, F. Hofmann
"		2014	Feb	26, 27, 28	21	J. Ridl, H. Steinle
"		2014	Mar	1, 2, 3, 4, 5, 6, 7, 13	19	"
093.A-9018(A)	16	2014	Apr	28, 29	2	J. Ridl
"		2014	May	1, 2, 3, 4, 5	9	"
"		2014	June	1, 5	2	Remote observing
"		2014	Aug	24, 25, 26, 30, 31	9	M. Bernhardt, N. Clerc
"		2014	Sep	2, 3	7	"
094.A-9018(A)	12	2014	Oct	16, 17, 18, 19, 20, 21	44	H. Steinle, G. Vasilopoulos
"		2014	Nov	12, 13, 14	17	"
"		2015	Mar	11, 12, 13, 14, 15, 16, 17	27	H. Steinle, M. Salvato
095.A-9008(A)	14	2015	Apr	16, 17, 18, 19	10	J. Ridl
"		2015	Sep	9, 10, 11, 12, 13, 16, 17	14	N. Clerc
096.A-9011(A)	14	2015	Nov	14, 15, 17, 28, 29, 30	2	J. Ridl, T. Schweyer
"		2015	Dec	13, 14, 15, 16	1	P. Wiseman
"		2016	Feb	5, 6, 7, 8, 9, 10	16	T. Krühler

Chapter 3

The X-CLASS/GROND catalogue

This chapter is based on the work presented in [Ridl et al. \(2017\)](#) and is structured as follows. In Section 3.2, I present a summary of the XMM Cluster Archive Super Survey (X-CLASS) focusing on source detection and sample selection. The X-CLASS catalogue was originally presented by [Clerc et al. \(2012a\)](#) and this section is based on the results presented in that paper. The bulk of my contribution to the work presented in the remainder of this chapter was in the photometric redshift followup of this sample. The optical and near-infrared followup program with GROND was described in the previous chapter and I discuss the redshift determination of our clusters based on GROND photometry in Section 3.3. I was able to determine photometric redshifts for 232 out of 265 clusters, finding a median redshift of $z = 0.39$ with an accuracy of $\Delta z = 0.02(1 + z)$ when compared to a sample of 76 spectroscopically confirmed clusters. The matching of the X-ray detected sources to existing redshift information from literature was performed by a collaborator, Dr. Tatyana Sadibekova. The measurement of the X-ray properties of this sample, namely luminosity and temperature, is discussed in Section 3.4. I found a median X-ray bolometric luminosity of $7.2 \times 10^{43} \text{erg s}^{-1}$ and a median temperature 2.9 keV. The results and discussion of interesting cases are presented in Section 3.5 and Section 3.6 respectively.

3.1 Introduction

A significant goal of modern astronomy is to provide observations capable of testing the current cosmological paradigm, where the energy density of the Universe is dominated by the cosmological constant, Λ , and cold dark matter (Λ CDM). Since the number density of galaxy clusters as a function of mass and redshift depends strongly on various cosmological parameters such as Ω_M , σ_8 and the physical properties of dark energy, observations of clusters provide a powerful probe of the underlying cosmological model. The parameters Ω_M and σ_8 can be well constrained given a sufficiently large sample of low redshift clusters, spanning a wide range of masses. On the other hand, a sample spanning a wide range of masses and redshifts is necessary to place competitive constraints on evolutionary parameters such as the dark energy equation of state ([Vikhlinin et al. 2009b](#)). Such a

sample can also be used to study the evolution of various cluster scaling relations, such as the X-ray luminosity or temperature to total cluster mass ($L_X - M$ and $T_X - M$). Of crucial importance to any attempt to use clusters for cosmological studies is an intricate knowledge of the sample selection function and how it is related to the underlying cluster distribution, predicted by cosmological simulations. For a comprehensive review on clusters as cosmological probes, see [Allen, Evrard & Mantz \(2011\)](#) and the references therein.

The most obvious way in which galaxy clusters can be identified and selected is as an over-density in the spatial distribution of galaxies, particularly in optical and near-infrared (NIR) wavelengths (e.g. [Abell 1958](#); [Gladders & Yee 2000](#); [Rykoff et al. 2014](#)). Such samples are however difficult to characterise due to the lack of highly constrained scaling relations for moving from directly observable quantities, such as the cluster richness to the total halo mass. Further, they are generally more contaminated due to projection effects than other methods e.g. redMaPPer reports an incidence of contamination of $\sim 5\%$ ([Rykoff et al. 2014](#)). A significant advantage of optical/NIR cluster detection algorithms is that they typically produce an estimate of the cluster redshift, thanks to the well studied and constrained colour-redshift relation of passively evolving galaxies, which make up the cluster red sequence ([Baum 1959](#)).

The baryonic component of galaxy clusters typically takes the form of a hot intracluster gas which is detected either directly through its X-ray emission, or indirectly via the Sunyaev-Zel'dovich (SZ) decrement ([Sunyaev & Zeldovich 1970](#)). Methods taking advantage of this are less likely to be affected by projection effects but do not readily provide any redshift information in general. However, given a robust estimate of the redshift from followup optical observations, the intra-cluster gas provides a ready proxy of the total halo mass and is thus an excellent probe of the halo mass function.

It is thus clearly optimal to perform studies of galaxy clusters over a wide range of wavelengths to fully exploit all the available information. Many studies have followed this philosophy, whereby clusters are detected through their X-ray emission and then followed-up with ground or space-based optical and NIR observations to confirm the cluster candidate and to obtain the redshifts needed for their physical characterisation. Examples of these include wide-field surveys with ROSAT ([Vikhlinin et al. 1998](#); [Boehringer et al. 2000](#)), medium-field observations with XMM e.g. XMM-LSS ([Pierre et al. 2007](#); [Pacaud et al. 2007](#); [Clerc et al. 2014](#)), XMM-XXL ([Pierre et al. 2016](#); [Pacaud et al. 2016](#)) and XMM-BCS ([Šuhada et al. 2012a](#)) and narrow surveys such as the COSMOS field with Chandra ([Scoville et al. 2007](#)) or XMM ([Finoguenov et al. 2006](#)). Additionally, the vast number of PI observations with XMM and Chandra provides an abundance of exploitable data in which serendipitous cluster searches can be performed with Chandra (ChaMP, [Barkhouse et al. 2006](#)) and with XMM e.g. XCS ([Romer et al. 2001](#); [Lloyd-Davies et al. 2011b](#); [Mehrtens et al. 2012](#)) and X-CLASS ([Clerc et al. 2012b](#); [Sadibekova et al. 2014](#)). The sample presented in this thesis X-CLASS lies in the middle ground between the XCS and XXL surveys in that the pointings are distributed across the entire extragalactic sky and yet the detection of clusters take place on pointings with homogeneous exposure times.

A wide variety of techniques and methods have been used to identify cluster of galaxies in large, wide-area optical surveys, making use of various well known properties of clusters.

One of the well studied features of galaxy clusters that is commonly used for their detection is the presence of the cluster red-sequence which takes advantage of the colour-magnitude relation (CMR) of early-type galaxies due to the 4000 Å break in their rest frame, (e.g. Gladders & Yee 2000). The algorithm of maxBCG (Koester et al. 2007), also takes advantage of the existence of a unique brightest cluster galaxy (BCG) which lies on the red sequence. More recently, redMaPPer (Rykoff et al. 2014) and WHL (Wen, Han & Liu 2012; Wen & Han 2015) have provided optimised methods for the detection of optical clusters and accurate determination of the redshift and richness. For the photometric redshifts derived in this chapter I extend the red sequence method to take advantage of the prior knowledge that we obtain from the X-ray detection of the cluster, namely the position of the cluster centre and the extent of the X-ray emission.

Throughout, we assume a Λ CDM cosmological model relying on the parameters calculated by Hinshaw et al. (2013), in particular with $\Omega_M = 0.28$, $\Omega_\Lambda = 0.72$ and $H_0 = 70 \text{ km s}^{-1}\text{Mpc}^{-1}$.

3.2 The XMM Cluster Archive Super Survey

X-CLASS is a serendipitous search for galaxy clusters in archival observations from the XMM-Newton observatory, with the main objective of producing a well defined-cluster sample suitable for cosmological studies. The data were processed utilising the procedures of the XMM-LSS collaboration (Pacaud et al. 2006, Faccioli et al. in prep), and the construction of the X-CLASS catalogue is described in (Clerc et al. 2012b). We summarise the key points here.

3.2.1 Selection of XMM pointings and cluster detection

The following constraints were taken into account when selecting observations from the XMM Science Archive system from publicly available data, as of 26 May 2010, for analysis. In order to reduce the impact of galactic foregrounds, we selected only pointings centred at Galactic latitudes $|b| \geq 20 \text{ deg}$ and located (5 deg / 2 deg) from (Magellanic Clouds / M31). Further, we required that the exposure time (given by the duration in the XMM archive) was greater than 5 ks and that all three detectors (MOS1, MOS2 and PN) were in imaging mode, with at least one being in Full Frame mode.

Processing of data

The calibrated event lists are first filtered from proton and solar flares resulting in a *good time interval* (GTI) which is used to proceed with the analysis. The overall quality of each observation was then visually inspected and some observations discarded.

Since clusters detected with XMM exposure times of 10-20 ks form a highly relevant population for cosmological studies (Pierre et al. 2007, 2011) and the implementation of

a survey selection function is simplified when working with a survey consisting of homogeneous exposure times, new pointings are built from the original exposures so that each pointing is cut to either a 10 or 20 ks exposure time on the three detectors, after correcting for background flares. Once observations where one or more of the detectors had a GTI of less than 10 ks were removed, the total number of pointings from which sources are detected is 2409, giving a total exposure time of the survey of 24 Ms out of a possible 40 Ms of good-time-intervals (GTI) available.

X-ray source detection

The detection of sources is performed on a co-added image of the three EPIC detectors in the [0.5 - 2] keV range of each of the three EPIC detectors. The source extraction tool **SExtractor** (Bertin & Arnouts 1996) is run on a wavelet-filtered (`mr_filter`, Starck, Murtagh & Bijaoui 1998; Valtchanov, Pierre & Gastaud 2001), co-added image and only sources detected within 13 arcmin of the pointing centre are considered for further analysis. A maximum likelihood profile fitting procedure (XAMIN, Pacaud et al. 2006) further characterises the detected source as being either point-like or extended, i.e. a β -model convolved with the PSF. A set of parameters characterising each of the detected sources is also provided, including the angular extent (EXT), which defines the apparent core radius of the best fit β -model and the likelihood that the emission is extended (EXT_LIKE). Flux measurements are performed on the ‘full exposure’ pointings, after removing periods of high-background, containing the maximal available GTI for each observation, enhancing the signal-to-noise.

3.2.2 Catalogue construction and selection of the cosmological sub-sample

Following Pacaud et al. (2006) a catalogue is built by selecting extended sources within 13' of the centre of the parent pointing with $\text{EXT} > 5''$ and $\text{EXT_LIKE} > 33$. Such sources are denoted ‘C1’. This selection results in a low (< 5%) level of contamination by incorrectly classified point-sources. There are a variety of astronomical objects present in the observations and to accurately remove large nearby clusters, nearby galaxies, planets and unresolved double or saturated point-sources, human intervention is necessary. After removal of duplicate detections, all candidate clusters were screened by at least two independent astronomers based on optical data from the Digitized Sky Survey (DSS) POSS-II with the X-ray contours overlaid. Each astronomer awarded a ‘quality’ flag to the detection and a final decision was made by a moderator based upon the evaluators’ comments. In addition to a decision being made on the nature of the source, the DSS imaging was also used to give a rough estimate of the possible redshift range of the clusters, dividing them into categories of $0 < z < 0.3$ and $z > 0.3$. As of Aug. 2010, the catalogue contains 845 C1 clusters.

The cosmological sample

The primary goal of this study is to describe a catalogue for use in cosmological calculations, extending the previous CR-HR (*count rate - hardness ratio*) analysis with the addition of cluster redshift information i.e. z-CR-HR (Clerc et al. 2012a). For this purpose, a high signal-to-noise ratio subsample is selected according to the following criteria:

1. The data set was selected by removing pointings with high background; with one or more detectors not being in full frame mode; and those centred on luminous nearby clusters. This results in the total area surveyed for use in the cosmological fits of 1992 pointings.
2. A more pure sub-class of galaxy clusters with `EXT_LIKE` > 40, denoted by ‘C1+’ was selected and included in the catalogue.
3. A final cut was made in terms of the measured X-ray properties of the sources namely CR, as the count-rate measured in the [0.5-2] keV range and HR, the ratio between the [1-2] keV and [0.5-1] keV count-rates. We summarise these measurements in Section 3.4.1. Only clusters with $0.009 < \text{CR} < 0.5$ cts/s and $0.05 < \text{HR} < 2$ were included in the final cosmological subsample consisting of 461 clusters.

We account for the C1+ cluster selection by modelling the cluster population in the observable domain. Unobserved objects are filtered out by using the observable-based selection function derived from realistic XMM observations (see e.g. Pacaud et al. (2006) for the definition of C1, Clerc et al. (2012b) for the application to the CR-HR modelling, Pacaud et al. (2016) for the dn/dz modelling, Giles et al. (2016) for the modelling of the luminosity-temperature $L - T$ relation, and references therein).

The optical and near-IR followup of a Southern ($\delta < 20^\circ$) subset of 265 of these clusters, visible from the ESO La Silla observatory in Chile forms the basis of the rest of this chapter.

3.3 Redshift measurements

3.3.1 Archival redshifts

A comprehensive search for archival redshift information making use of the NED database was undertaken. Where counterparts to our clusters were found, a redshift was allocated to the cluster along with a flag indicating the redshift status. The criteria for each of these status flags are as follows:

1. *Confirmed*: Abell (Abell 1958), Planck (Planck Collaboration XXIX 2014; Planck Collaboration XXXII et al. 2015), SPT (Bleem et al. 2015), XCS-DR1 (Mehrtens et al. 2012) or other published clusters with spectroscopic redshifts are available; there are at least 3 similar spectroscopic redshifts within $3'$; or there is an obvious BCG with a spectroscopic redshift and many similar photometric redshifts within $3'$.

2. *Photometric*: There is a photometric redshift available for a cluster matched in the XCS-DR1 or elsewhere in literature; or the X-ray position is coincident with a redMaPPer candidate.
3. *Tentative*: There is at least 1, but fewer than 3 similar spectroscopic redshifts.

In total, we find that 88 clusters are already spectroscopically confirmed and a further 66 have a photometric redshift. We find that 25 clusters are allocated the redshift flag ‘tentative,’ but these should be treated with caution and the redshift should by no means be considered to be definitive.

3.3.2 The GROND cluster photometric redshift tool

Observing galaxy clusters with GROND in multiple bands simultaneously has several advantages, since a single pointing results in a multi-chromatic data set obtained under identical atmospheric conditions. This implies that non-photometric conditions have a minimised effect on galaxy colours compared to data taken under varying conditions. The relatively small field-of-view however does introduce some challenges to any attempt to determine cluster photometric redshifts for two main reasons. Firstly, as discussed in Section 2.8, it is difficult to obtain an absolute photometric zeropoint calibration due to the lack of stars present in extragalactic fields. Secondly, in most cases the entire field-of-view is taken up by the galaxy cluster itself and it is thus not feasible to obtain an estimate of the local background distribution of galaxies. This makes it difficult to perform an analysis similar to that of redMaPPer (Rykoff et al. 2014) or other similar techniques which require secure knowledge of the background galaxy distribution to which any over-densities can be compared. We thus developed our own algorithm to calculate cluster photometric redshifts based on the cluster red sequence colour-redshift technique with the addition of extra information obtained from the X-ray detection of the cluster.

Red sequence colour-redshift relation

In order to use this technique, one needs a well calibrated model of the colour-redshift relation for the cluster red sequence. The lack of spectroscopic coverage for this sample, and the general scarcity of large, wide area spectroscopic surveys, such as SDSS (which in any case is not deep enough for our purposes), in the Southern Hemisphere means that this relation could not be derived empirically for the GROND filter set. There are however a number of publicly available spectral energy distribution (SED) templates for early-type galaxies (Bruzual & Charlot 2003; Polletta et al. 2007; Maraston et al. 2009) which can be used to model the expected colour of the red sequence. We tested a variety of these models by comparing the templates (in the CFHTLS photometric system) with a combination of the XXL-100 brightest clusters (Pacaud et al. 2016) matched with photometric redshift catalogues for individual galaxies from Mirkazemi et al. (2015), using data from the CFHTLS wide-field surveys. We ultimately decided to use the SED of an early-type galaxy published by Polletta et al. (2007) and generated by the GRASIL code (Silva et al.

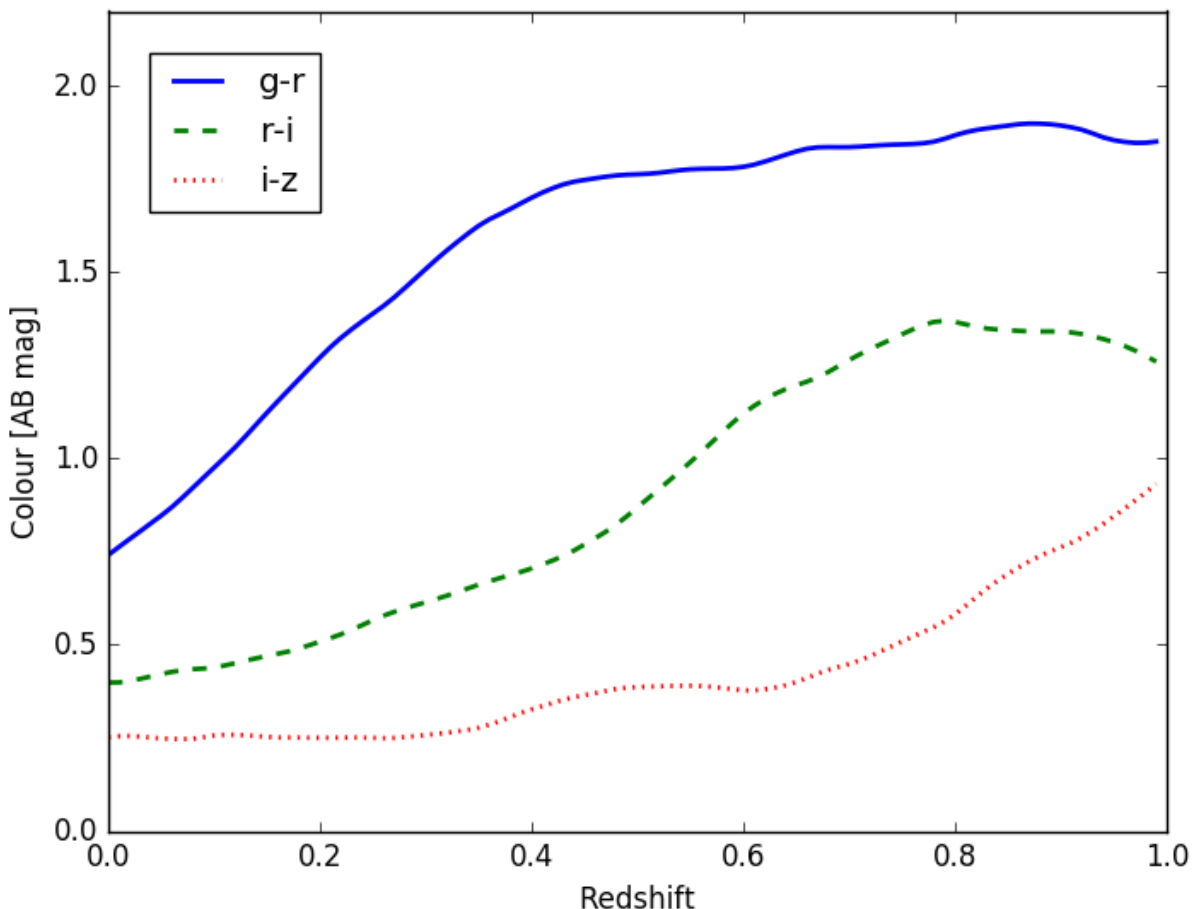


Figure 3.1: The expected colour-evolution of the cluster red sequence as a function of redshift for the three colours considered in the determination of photometric redshifts, i.e. $g - r$, $r - i$, $i - z$.

1998) as this provided the best fit to the CFHTLS photometry and the lowest bias and scatter in testing on a spectroscopically confirmed subset of clusters. The colour-redshift relation for these templates was computed by making use of LePhare (Ilbert et al. 2006; Arnouts et al. 1999) for the GROND filters in each of the g, r, i, z -bands respectively. The expected colours of a typical red sequence galaxy as a function of redshift are shown in Figure (3.1).

The photo-z algorithm

Taking advantage of information from the optical and X-ray observations, we built a ‘likelihood’ indicator for the redshift of galaxy clusters. This function is based on the optical colour of the detected galaxies along with the position and extent resulting from the X-ray detection of the clusters. We note that this is not a true likelihood estimator but rather an empirically derived indicator for the most likely redshift of the cluster.

1. For each galaxy in the field-of-view, we calculate the probability that it is an early-type galaxy at a given redshift by comparing the colour of the galaxy to that expected from the SED. We assume that the scatter around the colour of the red sequence follows a Gaussian distribution with a width of 0.05 in each colour and we include the error on the photometry. The probability as a function of redshift for an individual galaxy is calculated as in Equation (3.1) below:

$$p(z) = \prod_c \frac{1}{\sqrt{2\pi}\sigma_c} \exp \left[\frac{-(c_{gal} - c_{model})^2}{\sigma_c^2} \right], \quad (3.1)$$

where the product runs over all colour combinations $[g - r, r - i, i - z]$, $\sigma_c = \sqrt{0.05^2 + \sigma_{c,phot}^2}$, combines the width of the red sequence and the error on the photometry, c_{gal} is the measured galaxy colour, c_{model} is the expected colour from the colour-redshift relations given in Figure 3.1.

2. This probability is then weighted by the spatial position of the galaxy relative to the X-ray centre of the cluster and the extension as calculated by the X-ray detection pipeline to give the ‘likelihood’ that the given galaxy is a member of a cluster at that position and redshift. The selection of the X-ray centre as the cluster centre is well justified since the PSF of the XMM imaging ($\sim 15''$) is comparable to the typical size of a cluster core ($\sim 5\text{-}30''$). Experimentation with various weighting schemes and beta-model exponents lead to the choice of a beta-model profile and relevant parameters given by:

$$W(r) = \left[\frac{W_0}{1 + \left(\frac{r}{r_{ext}}\right)^2} \right]^{\frac{3}{2}}, \quad (3.2)$$

where W_0 is an arbitrary normalisation, set to unity, r is the angular distance between the galaxy and the X-ray centre of the cluster and r_{ext} is the angular X-ray extent, calculated from the X-ray detection pipeline.

3. This new ‘likelihood’ is then summed over all galaxies to obtain a total ‘likelihood’ distribution as a function of redshift for the entire cluster.
4. Additionally, the number of likely member galaxies, $N_{gal}(z)$, is calculated by selecting galaxies that have a ‘likelihood’ indicator of more than 80% of their peak value at each redshift and this distribution is combined with the ‘likelihood’ indicator of the cluster to give an over all redshift distribution.

The final redshift ‘likelihood’ indicator is then given by:

$$\mathcal{L}(z) = N_{gal}(z) \sum_{gal} W(r)p(z), \quad (3.3)$$

where $N_{gal}(z)$, $W(r)$ and $p(z)$ are as described above and the photometric redshift of the galaxy cluster is chosen such that $\mathcal{L}(z)$ is maximised.

3.3.3 Application to GROND

Galaxies are selected from SExtractor source catalogues as those with CLASS_STAR < 0.7 , r -band magnitude brighter than 24.0 and signal-to-noise in the aperture defined by MAG_AUTO greater than 5.0. We use this lower value of CLASS_STAR compared that used for the selection of stars for the astrometric calibration to reduce number of contaminating stars in our galaxy catalogues. For each of these galaxies a redshift range over which they could be possible cluster red sequence members is determined based on the criteria discussed in Section 3.3.3. The photometric redshift algorithm described previously is then run on each galaxy catalogue producing a ‘likelihood’ distribution with redshift. In instances where there is more than one observation of a given cluster, a photometric redshift is calculated for each observation. The ‘likelihood’ distributions are then compared and the best observation chosen, taking into account the ‘likelihood’ value, the FWHM seeing of the observation and the photometric calibration of the entire night on which the observation was performed. The position of the peak value of the ‘likelihood’ distribution is determined to be the redshift of the cluster. Examples of the ‘likelihood’ distributions computed by our code are given in Figure 3.2 for three cases.

Removal of contaminants

Initial testing of our method highlighted two classes of complications arising from either foreground or background contamination by galaxies not associated with cluster but along the same line of sight as the cluster centre. These contaminants are thus heavily weighted by the β -model of Equation 3.2. In order to mitigate these, we defined rules to remove possible contaminating galaxies which would otherwise strongly, and negatively affect our redshift calculations. These constraints were then used to pre-filter that galaxy catalogues before entering the photometric redshift algorithm.

The first class of impediments was the presence of distant, star-forming galaxies with similar apparent colours to a lower redshift early-type galaxy. To remove these, we selected galaxies based on the r -band magnitude-redshift relation. The magnitude, $m_*(z)$, was computed as a function of redshift using a Bruzual & Charlot (2003) stellar population model. This model was fixed to a single burst of star formation at $z = 3$, with solar metallicity and Salpeter initial mass function (Salpeter 1955), and evolved through redshift space by making use of the publicly available EzGal package (Mancone & Gonzalez 2012). Following the methodology of Rykoff et al. (2012) and Mirkazemi et al. (2015), $m_*(z)$ was normalised such that $m_{*,i}(z = 0.2) = 17.85$ in the SDSS filter system, corresponding to a galaxy with luminosity $L_* = 2.25 \times 10^{10} L_\odot$. Thus, any galaxy fainter than $m_{*,r}(z) + 2.5$ was excluded from the likelihood calculation.

The second class was due to galaxies that had a single colour agreeing well with that expected from the SED of an early-type galaxy while the other two colour constraints were only marginally met, implying that these were unlikely to actually be cluster red sequence members. These galaxies were eliminated by placing constraints on the colour allowed for the individual galaxies in multiple bands. In order to have sensitivity to the 4000Å break

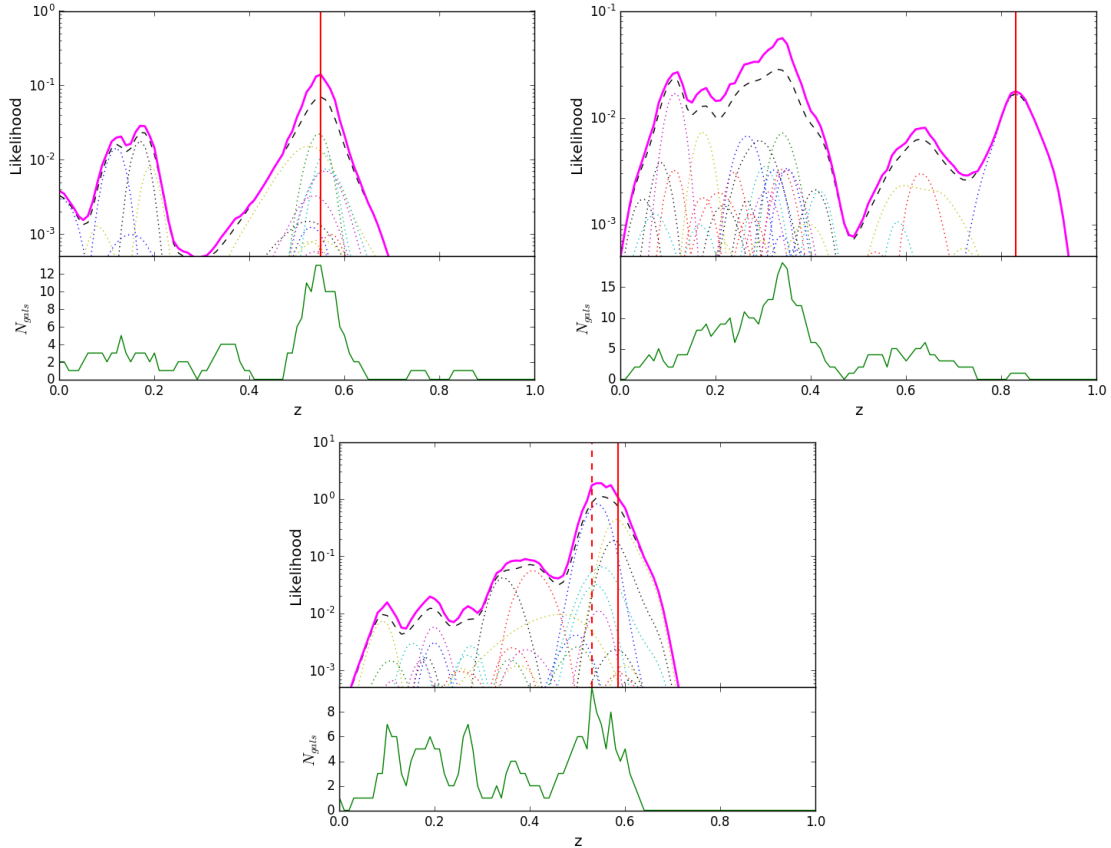


Figure 3.2: ‘Likelihood’ distributions of three galaxy clusters are shown in the upper panels. *Left*: X-CLASS 459, with a spectroscopic redshift $z = 0.55$. *Middle*: X-CLASS 228 with a spectroscopic redshift $z = 0.83$ *Right*: X-CLASS 430 with spectroscopic redshift $z = 0.58$. The dotted lines are the ‘likelihood’ distributions for the individual galaxies in the field, calculated from Equation 3.3 and the black dashed is the β -model weighted sum of the individual galaxies. The lower panel shows the number of galaxies contributing to likelihood at each redshift. The solid magenta curve in the upper panel is the final ‘likelihood’ given in Equation 3.3. The solid-red vertical lines indicate the redshift of the cluster obtained from the archival redshift search which, in the left and centre cases, overlap with the redshift determined after visually inspecting these curves as described in Section 3.3.3. The dashed-red vertical line shows the redshift determined from the GROND observation, which is slightly different from the spectroscopic redshift of the cluster.

over a wide range of redshifts and to enhance the robustness of the selection, possible member galaxies were constrained to be those with $g - i$ and $r - z$ colours consistent with those described in the previous section. This step was meant to eliminate only obvious contaminants and as such a broad range of allowed colours was chosen, so that only galaxies with a colour within 0.5 of that expected from the model were included in the redshift calculation.

Visual inspection of results

Since the number of clusters to be followed up is relatively small, and we are working with pointed observations, it is possible to visually inspect every cluster candidate. Once every cluster had a single redshift assigned to it, a visual inspection by three astronomers (J. Ridl, N. Clerc and J. Sanner) was performed. The results from running the photometric redshift algorithm, (see examples in Figure 3.2) are compared with three-colour (gri) images, and images in which the most likely redshift for individual galaxies, assuming them to be early-type galaxies, is over-plotted. We are thus able to check that the output photometric redshift of the photo- z algorithm matches what would be roughly expected by a human eye and obvious errors can be corrected. This happens most frequently for high-redshift clusters, where the number of cluster members detected is very low. It is thus far easier for the result to be contaminated by a foreground elliptical galaxy nearby in projection to the X-ray center. Additionally, some measurements were affected by a very bright, saturated star or a secondary reflection from a nearby bright star, close to the X-ray centre of the cluster which causes a large fraction of the cluster members to be excluded from the calculation.

This visual inspection procedure found that in 37 out of 265 cases the photometric redshift pipeline had selected an incorrect peak in the likelihood distribution, typically due to contamination by a foreground galaxy resulting in a significantly lower redshift being reported than that expected from the visual appearance of the apparent cluster members and their distribution. For these cases, the position of the peak was remeasured after removing the contaminating source. We also identify a subset of 19 clusters as being likely distant $z > 0.8$ candidates, which we discuss in Section 3.6.3. Any prior knowledge of the redshift of the clusters from the archival matching was hidden from the inspectors which is important for validating the visual inspection process over the entire sample.

The examples presented in Figure 3.2 illustrate three typical cases. For the first cluster, X-CLASS 459, there is a clearly defined peak which all three inspectors agreed was correct. It turns out to match the spectroscopic redshift of $z = 0.55$ (Barcons et al. 2007) in the literature to within $\delta z = 0.01$. The second example, X-CLASS 228, is one where all inspectors agreed that the most likely redshift of the cluster lies around the peak at $z \sim 0.8$. Initially, the photometric redshift algorithm determined the redshift to be $z = 0.34$. The visual inspection however revealed that this measurement was likely affected by the presence of a foreground cluster (X-CLASS 229) at a distance of $2'$ away. Visually, the mostly likely peak from the likelihood indicator appeared to be the one around $z \sim 0.8$ and the redshift was re-measured around this peak resulting in a redshift of $z = 0.83$,

in agreement with the redshift provided by the XMM Distant Cluster Project (XDCP [Nastasi et al. 2014](#)). The final example, X-CLASS 430, is a difficult case as two peaks appear nearby to one another in the likelihood distribution. In such cases we decide to trust the maximum likelihood peak as being the redshift of the cluster at $z = 0.53$ but for this example, when comparing to the spectroscopic redshift $z = 0.585$ [Guennou et al. \(2014\)](#), we find that the redshift has been underestimated and the higher peak should have been selected.

3.3.4 Unconfirmed clusters

Apart from the clusters identified as being distant candidates, we are further unable to confirm the redshift for 10 clusters for a variety of reasons. It was found to be impossible to observe X-CLASS 51 due to the presence of a very bright star in the GROND field-of-view. We were also unable to obtain an observation of sufficient quality for X-CLASS 2311 due to the lack of a usable guide star on which GROND could track. The X-ray detection of X-CLASS 560 is heavily contaminated by an AGN and no obvious red sequence of galaxies is seen in the GROND observation. We were unable to reach consensus as to whether or not this is a distant candidate. We were unable to obtain a redshift for X-CLASS 1400 as the only available observation took place on a night with an insufficiently good photometric calibration. We do however see a clear red sequence of galaxies and estimate the redshift visually to be $z \sim 0.7$. X-CLASS 1995 and 2002 are both affected by the presence of bright stars which prevent the recovery of the photometric redshift. For X-CLASS 996, 997, 998 and 2078 we are unable to obtain a suitable astrometric solution due to the lack of enough viable stars in the optical field-of-view of the observations.

3.3.5 Comparison between GROND and archival redshifts

In order to validate our photometric redshifts, we compare them with the sample of 76 spectroscopically confirmed galaxy clusters from various sources, as discussed in Section [3.3.1](#). We notice that the scatter around the one-to-one line in [Figure \(3.3\)](#) increases around a redshift of $z \sim 0.4$. This is due to the fact that the 4000 \AA break moves from the g to r -band filter, increasing the uncertainty in the colour-redshift relation at this point. We also note that our method is unable to compute reliable uncertainties for the photometric redshift determined from [Equation 3.3](#) and so we do not provide errors for individual cluster measurements. We are only able to give an indication of the average error for the entire sample. We find that our redshifts are accurate to $\Delta z = 0.02(1 + z)$. Practically all of the constraining power of z-CR-HR method, for which this sample has been assembled, is provided by binning clusters in redshift bins of $\Delta z = 0.1$ ([Clerc et al. 2012a](#)). Our redshifts are thus of a suitable quality in order to proceed with a cosmological analysis ([Ridl et al., in prep](#)).

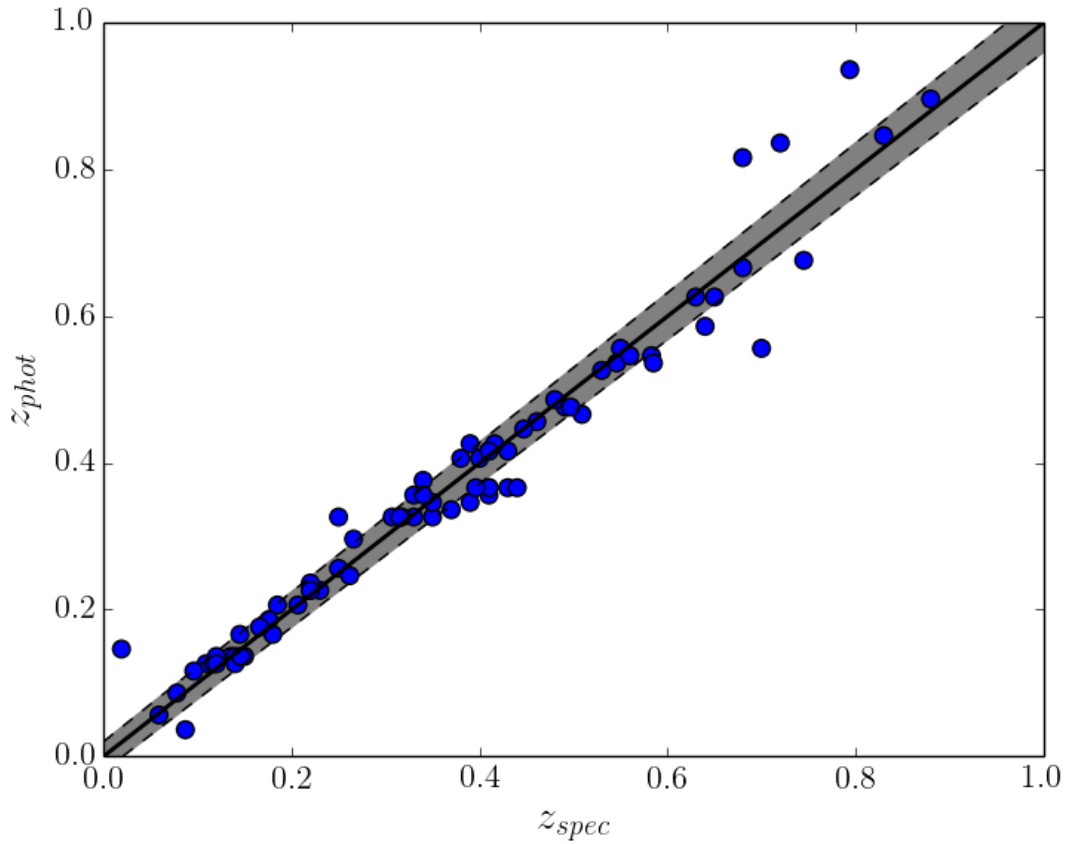


Figure 3.3: Comparison of GROND photometric redshift with 76 of the spectroscopic redshifts with $z < 0.85$ obtained from the literature as discussed in Section 3.3.1. The grey shaded region is bounded by the lines $z \pm 0.02(1+z)$, indicating the typical error of our measurements.

3.4 Characterisation of X-ray properties

3.4.1 Growth curve analysis

The first step in determining the X-ray properties of detected galaxy clusters is to measure the X-ray detector count-rate. For the sample presented in this thesis, count-rate measurements had already been performed in multiple bands as a function of radial distance from the X-ray defined centre of the cluster. A semi-iterative method is used to deal with sources that either occupy a large fraction of the detector or are heavily contaminated by point-sources such as AGN and allows for the manual redefinition of the cluster centre.

Count-rates, defined as the mean number of photons detected by the CCDs in one second, are measured in concentric annuli under the assumption that the source is spherically symmetric. This provides a straightforward way to correct for masked point sources, CCD gaps or detector borders, where part of the cluster lies outside the field-of-view of one of the cameras. These are then corrected for vignetting, and are thus equivalent to having the source positioned at the centre of the camera. The count-rates are always calculated on the full exposure of the given pointing, as opposed to the 10ks or 20ks subsets used for the source detection, ensuring a maximal signal-to-noise for each measurement. Each of the detectors is treated independently and the individual count-rates summed giving a total growth curve as a function of radius.

These measurements were validated through the use of simulated XMM observations of clusters and all count-rates were corrected for the fact that XMM observations are performed with the use of different filter (THIN1, MEDIUM or THICK) configurations at the discretion of the guest observer. For further details, see Section 2.4 of [Clerc et al. \(2012b\)](#).

3.4.2 Energy conversion factors

In order to convert the observable, count rate into flux it is necessary to determine an energy conversion factor (ECF). This was accomplished by selecting a set of 8 XMM observations spanning the 2000-2010 period, in order to test the long term variation of the ECF. These were used as representations of prototypical X-CLASS pointings. Since all count rates are equivalent to being on-axis cluster observations, we calculate the ECF for each respective observation only at the centre of each of the MOS and PN cameras.

A key step in the calculation of the ECF for a given observation is to create the ancillary response file (ARF) and redistribution matrix file (RMF). The observations were downloaded from the XMM Science archive¹ and the standard preliminary data reduction performed as detailed in the XMM data analysis manual including running the SAS tools `cifbuild` and `odfingest`, making use of the XMM calibration repository locally available at MPE. The data were then processed for the MOS1, MOS2 and PN chips individually, by running the tools `emproc` and `epproc` respectively to produce calibrated event lists. Light curves were then extracted and used to create good-time-intervals (GTIs) and these

¹<http://nxsa.esac.esa.int/nxsa-web/>

were used to remove periods heavily affected by proton and solar flares from the calibrated event lists. Finally, the SAS tools `rmfgen` and `arfgen` were used to create the RMF and ARF respectively.

Next, we used PyXspec (Arnaud 1996) to compute the energy conversion factors by simulating XMM observations of model galaxy clusters with a range of temperatures from $T = [0.3 - 10]$ keV, hydrogen column densities from $nH = [0.01 - 0.2] \times 10^{22} \text{ cm}^{-2}$ and redshifts from $z = [0.05 - 1.2]$. For each iteration, an observation was simulated using the PyXspec function `fakeit` making use of the RMF and ARF described above on each of the cameras individually, and using an exposure time of 10^7 s to limit the Poisson errors inherent in X-ray observations. The normalisation of the PyXspec model was chosen such that a cluster with $T = 1.0$ keV, metallicity $Z = 0.3 Z_{\odot}$ and redshift $z = 0.1$ would have a flux of $10^{-13} \text{ erg s}^{-1}$. We then selected the channels corresponding to the energy range of interest, i.e. $[0.5-2]$ keV, and computed the count rate in this energy band. This count rate was then compared with the model flux to give the necessary multiplicative factor to convert between the two quantities for each camera independently. These individual factors were then inverse summed giving the energy conversion factors on a grid of temperatures, hydrogen column densities and redshifts.

3.4.3 Physical parameter measurements

The physical parameters such as X-ray luminosities, temperatures, cluster masses and the radius at which the average density of a cluster is 500 times the critical density of the Universe, r_{500} are calculated using an iterative method, similar to that of Šuhada et al. (2012a). This method is summarised below with initial values of $T_{300kpc} = 2.5$ keV and $r_{500} = 0.5$ Mpc respectively.

1. The value r_{500} is converted from Mpc into arcseconds making use of the Astropy Cosmology module, which allows for straightforward cosmological calculations.
2. The count rate enclosed by this radius is extracted from growth curves, as presented Section 3.4.1.
3. We next convert this count rate to X-ray flux, making use of the relevant energy conversion factor as described in Section 3.4.2 depending on the cluster redshift, the hydrogen column density of the pointing and the current value of the temperature.
4. The X-ray luminosity $L_{500}^{[0.5-2]keV}$, in the $[0.5-2.0]$ keV band is then calculated along with the bolometric ($[0.05-100]$ keV) luminosity by making use of PyXspec, the Python implementation of XSPEC. To do this, we assume an absorbed APEC model (`phabs*apec`) with the following model parameters: hydrogen column density set to the value calculated at the position of the pointing; temperature set to the current T_{300kpc} value; metallic abundance $0.3Z_{\odot}$, redshift set to the spectroscopic redshift where available (i.e. redshift type: confirmed) or the photometric redshift calculated from the GROND observations as described in Section 3.3. The normalisation is

set such that the flux in the [0.5-2] keV band matches that calculated in step (iii) above. The function `calcLumin` is then used to determine the cluster luminosity in the [0.5-2] keV and [0.05-100] keV bands.

5. The scaling relations derived by the XXL (Pacaud et al. 2016; Giles et al. 2016; Lieu et al. 2016) are utilised to obtain the temperature within 300 kpc (T_{300kpc}) and M_{500} ,²

$$\frac{L_{500}^{[0.5-2]keV}}{3 \times 10^{43} \text{erg s}^{-1}} = 0.71 \left(\frac{T_{300kpc}}{3 \text{ keV}} \right)^{2.63} E(z)^{1.64}, \quad (3.4)$$

$$\frac{M_{500}}{2 \times 10^{14} M_{\odot}} = 1.16 \left(\frac{T_{300kpc}}{3 \text{ keV}} \right)^{1.67} E(z)^{-1}. \quad (3.5)$$

6. Finally, a new value for r_{500} is calculated from the relation,³

$$M_{500} = 500 \rho_c \times \frac{4\pi}{3} r_{500}^3. \quad (3.6)$$

7. Steps (i)-(vi) are the repeated with the updated values for T_{300kpc} and r_{500} until the calculated value for the temperature has converged to an accuracy of 0.01 keV.

For 3% of clusters with a reliable redshift, this method does not converge. These failures are either distant ($z > 1$) clusters or very nearby and contaminated by X-ray emission from the BCG, as discussed in Section 3.6.2.

3.4.4 Errors on X-ray derived properties

For the values calculated for the X-ray parameters in this chapter, we consider only errors introduced by the uncertainty in the measured count-rate in the [0.5-2] keV band, the error in the redshift assigned to the cluster and the scatter around the $L - T$ and $M - T$ scaling relations. We determine the uncertainty introduced by each of these parameters by offsetting their values, one-by-one, by 1σ for the count-rate and scaling relations and by the average error, $\Delta z = 0.02(1 + z)$, for the redshift in the iterative process described in the previous section. The uncertainties for all quantities calculated in the iterative process e.g. $L_{500}^{[0.5-2]keV}$, but here we discuss on the errors on the bolometric luminosity and temperature since these are the quantities which we compare with already existing measurements provided by the XMM-XXL and XMM-XCS catalogues.

We find that the dominant source of uncertainty in the calculated properties comes from the scatter on the $L - T$ relation, where we find that on average the calculated value for the bolometric luminosity is offset by $\sim 20\%$ and the temperature by $\sim 33\%$. The other parameters all influence the measurements by less than 10% apart from the redshift uncertainty which introduced an error of $\sim 14\%$. The final error bars shown in all plots

² $E(z)^2 = \Omega_M(1+z)^3 + \Omega_\Lambda$

³ $\rho_c = E(z)^2 3H_0^2 / 8\pi G$

Table 3.1: Average errors induced by offsetting the X-ray count-rate and redshift of the clusters and adjusting the scaling relations by their respective scatter and their effect on the bolometric luminosity and temperature obtained from the iterative method. The totals are calculated by adding the individual errors in quadrature.

Parameter	σ_L	σ_T
σ_{L-T}	20%	33%
σ_{M-T}	6%	2%
Count-rate	9%	3%
Δz	14%	3%
Total	27%	34 %

containing the X-ray properties calculated in this work are determined by summing the individual errors in quadrature. The results of the error calculations are summarised in Table 3.1.

3.5 Results

3.5.1 Spatial distribution of clusters

The selected XMM pointings are distributed throughout the high-Galactic latitude sky as illustrated by Figure 3.4. As such, cluster number densities and distributions in various parameter spaces should be only minimally affected by cosmic variance. In principle the density of detected clusters on the sky should continue to increase with future iterations of X-CLASS, for as long as XMM continues to function normally. Already a processing of new pointings up to January 2012 (Faccioli et al., in prep) has added an additional ~ 184 cluster candidates (72 of which already have redshifts), shown on Figure 3.4. So long as systematic followup of these new clusters is available, X-CLASS will remain a competitive cosmological sample for the near future and provide an excellent compliment to future surveys with eROSITA onboard SRG.

3.5.2 Redshift distribution of clusters

As stated earlier, the number density of clusters as a function of redshift depends strongly on the underlying cosmological model. The distribution of clusters with redshift as computed in this sample is displayed in Figure 3.5. For comparison, we also plot the distribution of clusters classified as ‘confirmed’ (spectroscopic) in the comparison with archival redshifts. We find good agreement between the two sets of redshifts.

We find that the median redshift for the X-CLASS sample is $z = 0.37$ when assigning

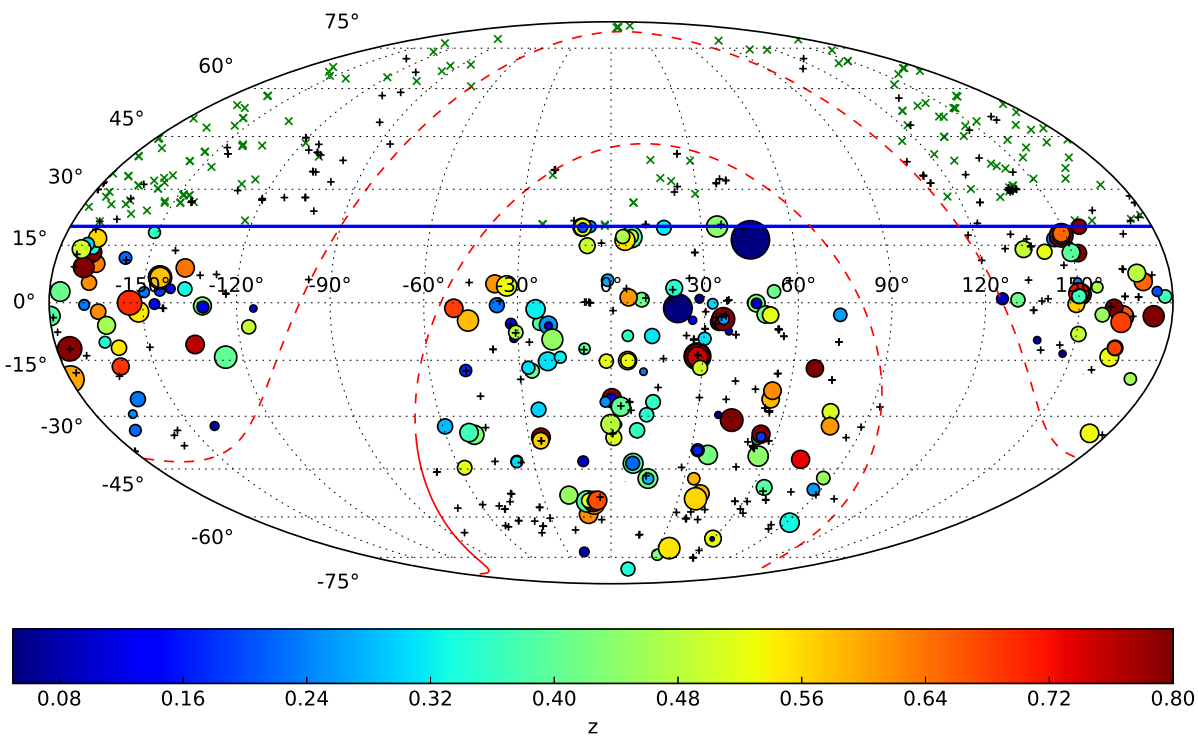


Figure 3.4: Distribution of clusters across the sky. X-CLASS clusters presented in this sample are described by coloured circles. The colour of the marker indicates the redshift on the cluster and size is proportional to the X-ray luminosity. The X-CLASS clusters further north than the limits of this survey are indicated by green x's and candidate clusters from a new processing of XMM data up to January 2012 are indicated by black +’s. The solid blue line shows the declination above which we do not observe and the red curves show Galactic latitudes $b = \pm 20^\circ$. Coordinates are given in the Equatorial J2000 system.

a lower limit of 0.85 to all clusters which were classified as being ‘too distant’ to obtain a redshift with a single 20 min OB, compared with $z = 0.33$ for XXL-100 and $z = 0.30$ for XCS-DR1. The difference with XXL-100 probably arises from the fact that their sample is based on a significantly higher flux limit than that inherent in our sample and thus a smaller fraction of distant clusters are included in their sample. The XCS-DR1 on the other hand, includes more XMM pointings, including those not included in this analysis due to insufficient exposure times. As such they detect more small, low-redshift groups, thus increasing their fraction of low redshift clusters.

The typical error on the redshift is found to be $\Delta z = 0.02(1 + z)$ and the outlier fraction, defined as having $|z_{ground} - z_{spec}| > 3\Delta z$ is 5%. In addition to providing redshift for 244 clusters of galaxies, we were able to provide lower limits on the redshifts of 18 distant cluster candidates. We consider a cluster to be “too distant” since the X-ray emission is clearly extended, by virtue of the C1⁺ classification but we do not find any appreciable red sequence consistent with it. It is possible that these cluster candidates are spurious detections and only the inspection of deep optical/IR imaging and/or deep Chandra observations could confirm the true nature of these objects. We discuss this further in Section 3.6.3. We also find 10 clusters with a redshift $z \leq 0.1$. These clusters represent an interesting subsample as it is difficult to measure their X-ray properties and we enter a more detailed discussion of this in Section 3.6.2.

3.5.3 X-ray properties of X-CLASS

An important characterisation of a sample of X-ray selected galaxy clusters is the relationship between the cluster redshifts and their luminosities as it gives an indication of the mass range represented by the sample. The distribution for this sample is shown in Figure 3.6. We also plot the expected cluster distribution from the full eROSITA all-sky survey (eRASS), with a selection function based on realistic eRASS simulations (Ramos Ceja 2016), and using the XXL scaling relations (Pacaud et al. 2016; Giles et al. 2016; Lieu et al. 2016), WMAP9 cosmology (Hinshaw et al. 2013) and the Tinker mass function (Tinker et al. 2008b). For reference we also show the distribution of the MCXC cluster sample which is based on the ROSAT All-sky survey and serendipitous cluster catalogues (Piffaretti et al. 2011). We notice that we detect fewer high luminosity clusters at low redshifts. The reason for this is two-fold. Firstly, the number of luminous clusters is limited at low redshifts due to the smaller volume which is probed compared to higher redshifts, and secondly, because very massive, nearby clusters have been deliberately excluded from the sample. From the right panel of Figure 3.6 we see that on average X-CLASS probes slightly higher redshifts and X-ray luminosities than expected from eROSITA.

It is also useful to see how this sample compares with other similar XMM surveys. In Figure 3.7 we show the X-CLASS luminosities as function of redshifts along with those from the XXL-100 and XCS-DR1 catalogues overlaid. The distribution of the X-ray bolometric luminosity of these three samples is displayed in Figure 3.8. These two plots illustrate some interesting differences between the samples. We notice the high number of bright nearby objects relative to our sample as expected from our removal of sources with high

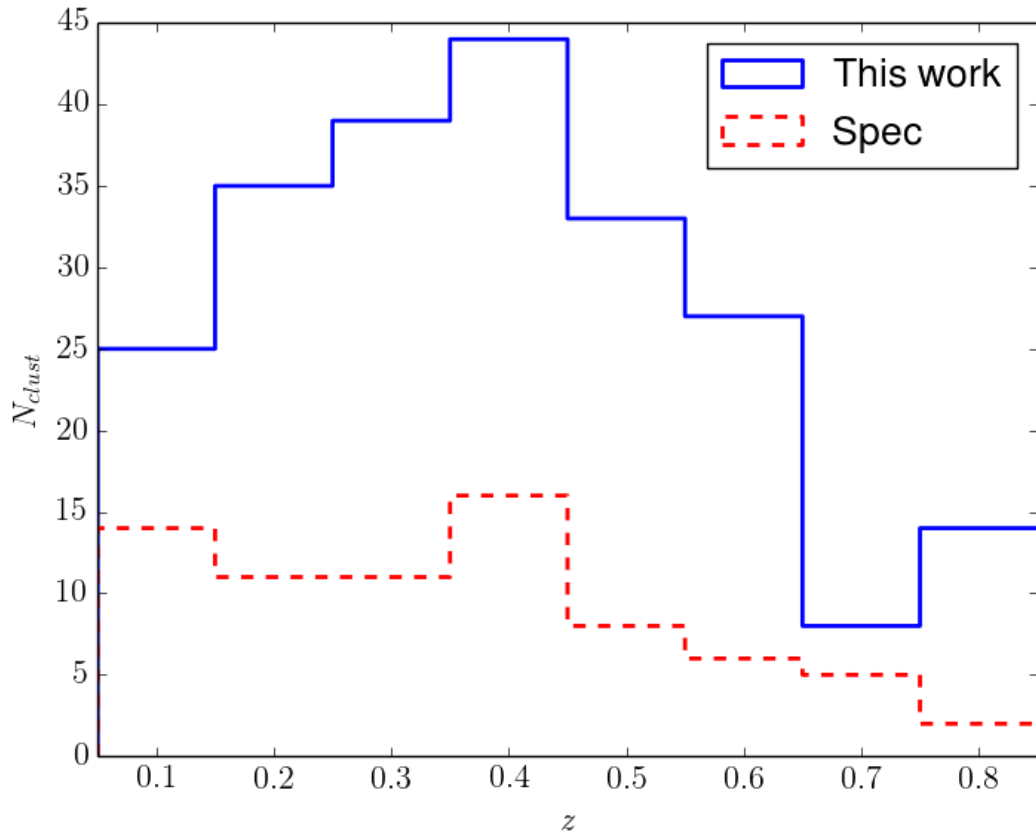


Figure 3.5: Distribution of X-CLASS clusters redshifts: GROND photometric redshifts for all clusters in the southern X-CLASS cosmological sample (solid-blue) and the spectroscopically confirmed subsample (dashed-red).

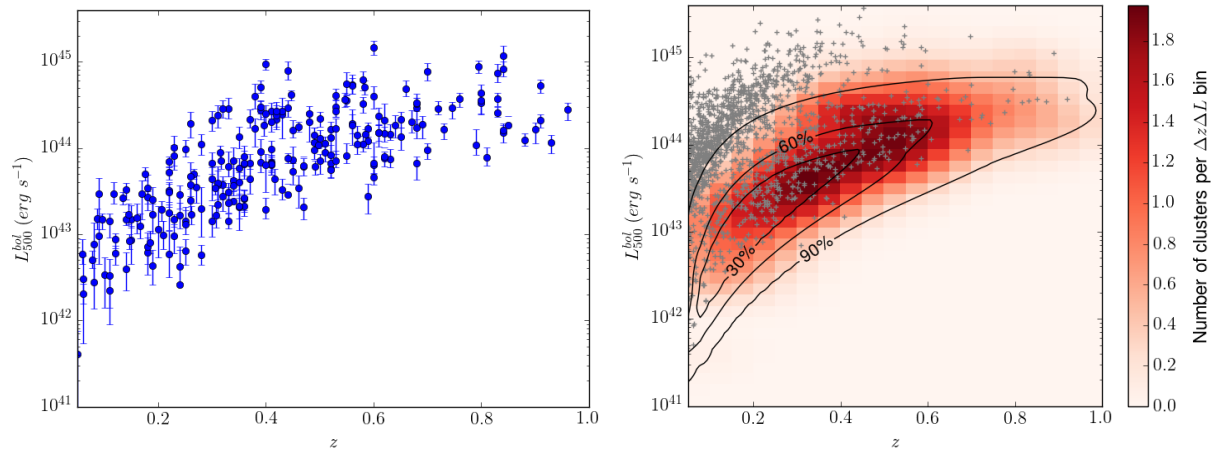


Figure 3.6: *Left*: The distribution of X-ray luminosity as a function of redshift for X-CLASS clusters. *Right*: The number density of X-CLASS clusters as a function of X-ray luminosities with redshift are indicated by the colour map, smoothed with a Gaussian filter. The contours indicate the expected distribution from the eROSITA 4 year all-sky survey under the assumptions discussed in the text and the grey +’s represent the ROSAT selected MCXC meta-catalogue (Piffaretti et al. 2011).

(> 0.5 cts/s) count rates. The lower flux limit of the XCS-DR1 is also clearly apparent. As expected we probe a significantly lower luminosity range than the XXL-100 although we would expect a more similar lower flux limit when compared to the entire XXL-C1 cluster sample consisting of 267 spectroscopically confirmed clusters which is yet to be released (Adami et al., in prep). The deficit in the number of high luminosity, high redshift clusters in the X-CLASS sample compared (in particular) to the XXL-100 is largely due to the fact that we do not have a secure redshift for many clusters with $z > 0.85$ and have relied on either photometric, or where available, spectroscopic redshifts already existing in the literature.

Ultimately, X-CLASS seems to be complementary to the XXL-100 and XCS-DR1 samples. Although not pushing to fluxes as low as the XCS-DR1, the decision to fix the exposure times to 10ks or 20ks greatly simplifies the selection function. Given that the (almost)-identical detection algorithm is used for the XXL and X-CLASS, we expect that the final XXL-C1 sample should have similar properties to the one presented here. While the XXL will not be affected by biases arising from including pointed observations of already known clusters, X-CLASS is assumed to be less affected by cosmic variance due to its scattered nature across the sky and has the potential to probe a significantly larger area of the sky. Much of the area covered by X-CLASS however lacks overlap with homogeneous and deep multi-wavelength surveys and followup, which this study partially addresses.

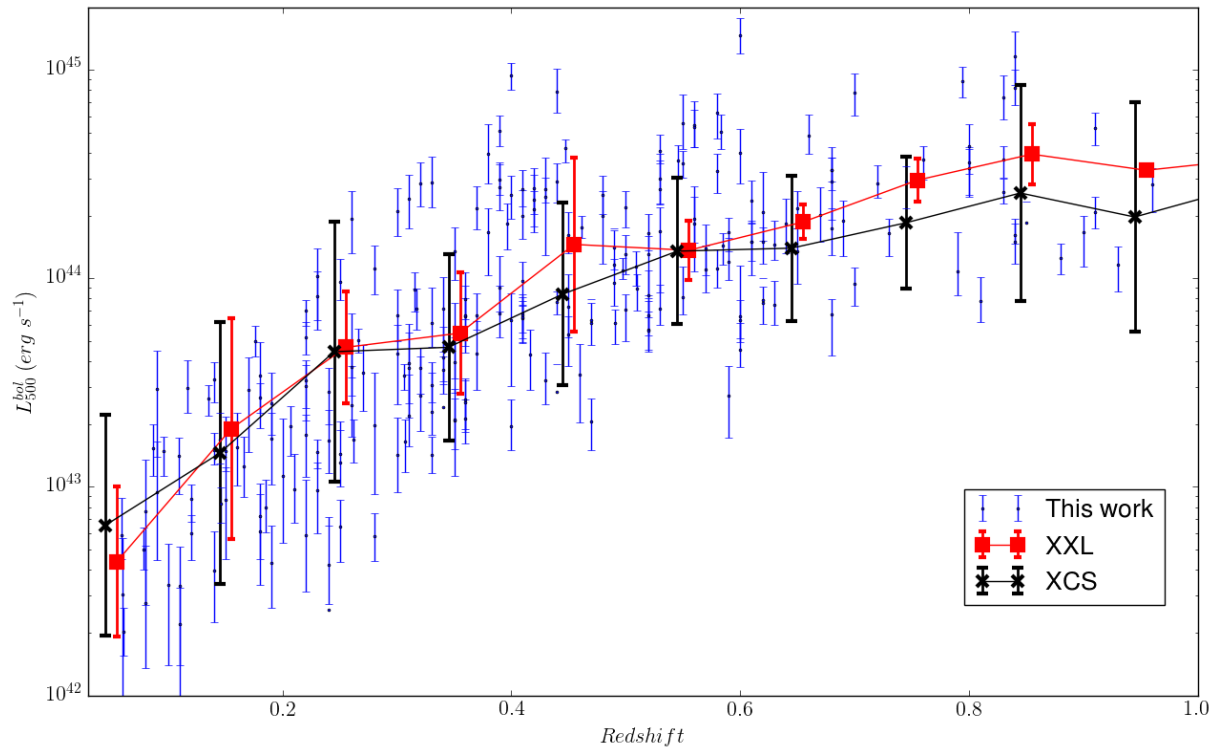


Figure 3.7: Distribution of X-ray luminosities as a function of redshift for X-CLASS clusters compared to the XCS-DR1 and XXL-100 catalogues. The XCS and XXL catalogues have been binned by to redshift slices of width $z = 0.1$ and the error bars represent the respective scatter about the median luminosity of each bin.

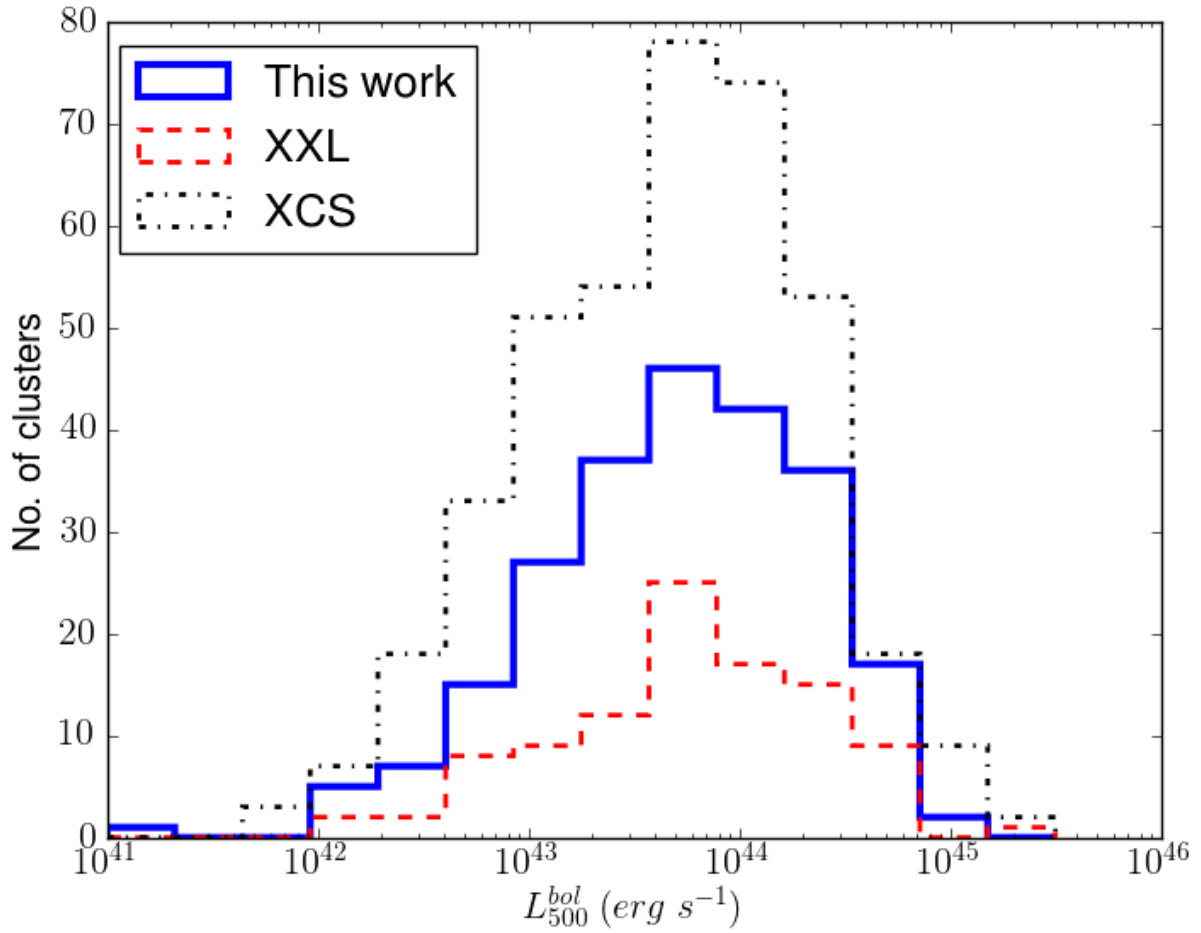


Figure 3.8: The number of clusters as a function of bolometric luminosity for the X-CLASS sample presented in this thesis (solid blue line), compared with the distributions of the XCS-DR1 (black, dashed-dot) and XXL-100 (red, dashed) samples respectively.

3.5.4 The X-CLASS/GROND cluster catalogue

We present the X-ray selected, X-CLASS/GROND cosmological catalogue in Table A.1 in Appendix A. Column 1 in Table A.1 is the X-CLASS catalogue ID. Columns 2 and 3 give the right ascension and declination of the X-ray centroid respectively. The photometric redshift, as derived from GROND observations is provided in Column 4. Where available, Columns 5 and 6 contain the redshift of the cluster as recovered by cross-matching the X-CLASS catalogue with various catalogues, such as XCS-DR1, redMaPPer and others in the NED, and the status flag of this redshift, as described in Section 3.3.1. Column 7 contains the count rate, given in units of counts per second, of the cluster in the [0.5-2 keV] band. Columns 8-10 contain various physical properties of the clusters calculated in Section 3.4, namely r_{500} , $L_{500}^{[0.5-2]keV}$, the luminosity in the [0.5-2 keV] band, measured in units of $10^{43} \text{erg s}^{-1}$ in an aperture out to r_{500} ; and finally the temperature of the cluster derived from the XXL scaling relations (Equations 3.4 and 3.5) in keV.

3.6 Discussion

3.6.1 Comparison of X-ray measurements with other XMM surveys

In order to ensure that we were able to accurately recover the X-ray properties of our sample, we compared the results of the analysis presented in Section 3.4 to the results obtained by the XXL and XCS teams. Since, the XCS-DR1 catalogue contains only bolometric luminosities we compare these, as opposed to luminosities in the [0.5-2] keV rest-frame luminosities. Due to the fact that our cluster temperatures are calculated from the $L - T$ scaling relation given by Pacaud et al. (2016), we expect that the quality of the fits of luminosity and temperature should be strongly correlated in the comparison with the XXL-100, i.e. a good agreement between the luminosities should provide good agreement between the temperatures. An important difference between the calculations presented here and those of the XXL-100/XCS-DR1 samples is that in the latter analyses, X-ray physical parameters were calculated through spectral template fitting directly to the X-ray data as opposed to the iterative method presented in Section 3.4.3. Spectral template fitting is considered to be the “gold standard” method for obtaining cluster temperature and luminosities and this forms the basis of a currently ongoing study (Molham Mostafa et al., in prep). For the purposes of this study, we deemed it sufficient to use the much faster iterative method, which as shown by Šuhada et al. (2012a) gives suitably accurate results and allows for a good characterisation of the overall sample.

The matching between X-CLASS and XXL-100/XCS-DR1 was done through the use of TOPCAT with a matching radius of $2'$. This radius was chosen because it was found to be large enough that it is able to account for the differing definition of the cluster centres given in the catalogue arising from the slightly different detection and measurement algorithms, and small enough that unrelated clusters were not matched to one another by chance. We

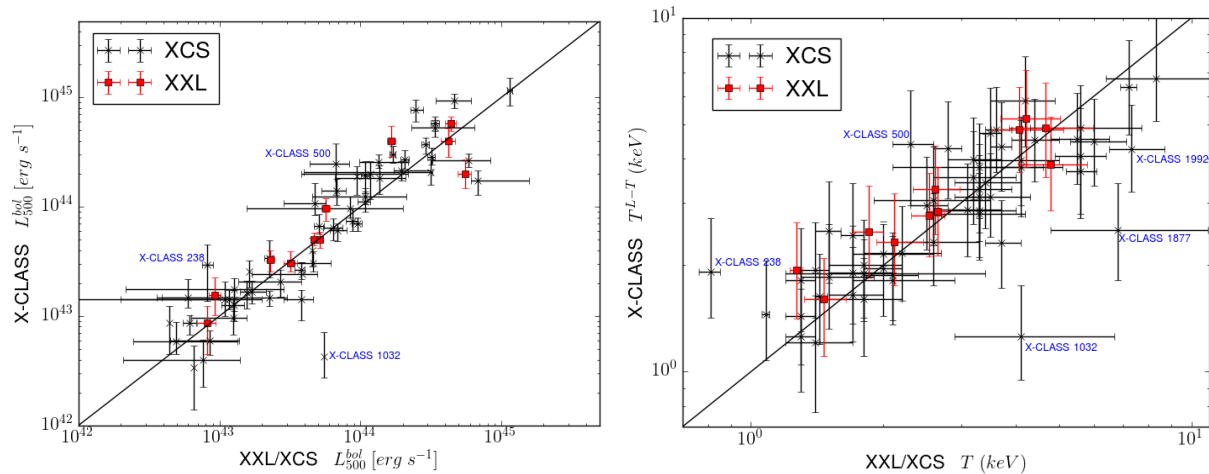


Figure 3.9: Comparison of X-CLASS bolometric [0.05-100 keV] X-ray luminosities within r_{500} of the cluster centre (left) and the X-ray temperatures (right) with the same quantities from the XCS and XXL catalogues.

found 11 and 64 clusters in common with the XXL-100 and XCS-DR1 catalogues covering a range of luminosities from $8 \times 10^{42} - 5 \times 10^{44} \text{ erg s}^{-1}$ and $2 \times 10^{42} - 10^{45} \text{ erg s}^{-1}$ respectively.

Figure 3.9 shows the good agreement between the values calculated for the bolometric luminosity and temperature respectively. The bias and standard deviation of the fit between the X-CLASS and XXL-100/XCS-DR1 calculated physical properties are summarised in Table 3.2. The good agreement with the XXL catalogue is somewhat unexpected given the similar nature of the processing, and that the luminosity and temperature measurements presented here are based on the XXL-100 scaling relations. The comparison with XCS-DR1 is a more reliable test of our measurements as they are computed by a completely independent team with different detection and measurement tools. We notice that the scatter around the one-to-one line is greater when comparing to XCS-DR1 than when compared to XXL-100. This is to be expected given that the XXL-100 measurements are performed on a significantly higher signal-to-noise sample, reflected in the size of the error bars.

The comparison with bolometric luminosities and more noticeably the temperature with XCS-DR1 highlight a number of clusters for which measurements are difficult for a variety of reasons. We performed further calculations based spectral fitting to resolve the tensions between the temperatures calculated in our analysis and those presented by XCS. We find that for X-CLASS 1032 (XMMXCS J0959.5+0526) the temperature recovered from our spectral analysis are in tension with those of XCS. For X-CLASS 1992 (XMMXCS J0959.6+0231) we find that our measurement is strongly affected by a high off-axis position on a pointing with a 20 ks exposure whereas the XCS measurement is performed on a pointing with the source more centralised but only 10 ks exposure. X-CLASS 1877 (XMMXCS J1000.4+0241) appears to be a rather complicated system and is likely affected by projection effects. It is originally detected at a similar redshift to the

Table 3.2: The bias and standard deviation of a comparison with other XMM cluster surveys.

Catalogue		L_{500}^{bol}	Temperature
XXL-100	Bias:	7%	10%
(11 clusters)	σ :	50%	18%
XCS-DR1	Bias:	2%	5%
(64 clusters)	σ :	55%	46%

one we calculate here ($z = 0.35$) in an XMM survey of the COSMOS field (Finoguenov et al. 2006). Subsequently, numerous large-scale structures have been reported within $1'$ at redshift $z \sim 0.7$ (Wen & Han 2011; Söchting et al. 2012) and so it is likely to be difficult to accurately measure the X-ray emission associated with the cluster at $z = 0.35$. The measurement of X-CLASS 238 (XMMXCS J0000.4-2512) is probably affected in our case by additional counts entering the calculations due to the presence of a nearby Abell cluster, A2690, which was the original target of the observation. Finally X-CLASS 500 (XMMXCS J0306.2-0005) is probably affected by a relatively high background in the pointing and nearby point sources.

3.6.2 Nearby groups

For the cosmological analysis for which this sample was constructed, the placing of an upper limit on the count-rate in the [0.5-2] keV band of 0.5 cts/s removed the majority of clusters below a redshift of 0.1. The remaining clusters that have an assigned redshift of $z < 0.1$ will most likely not be used in the cosmological analysis. The calculation of their X-ray properties highlighted some issues which seem to justify this decision. The cut in count-rate ensures that only very small groups are accepted into the original sample and as such they are extremely compact. This makes it difficult to disentangle any other possible sources of X-rays from either faint AGN, and/or occasionally the BCG of the cluster itself. These contribute to the 9% of sources for which the X-ray property computations did not converge and these are marked with “**” in Table A.1. In order to accurately measure the X-ray properties of these objects, one would need either deep XMM data to allow for spectral fitting or high resolution Chandra imaging to help with the removal of the contaminating point source or BCG.

3.6.3 Distant clusters

As mentioned in Section 3.5.2, we have a number of clusters for which we are unable to determine the redshift due to insufficient depth in the GROND data. Since the C1 selection of clusters is very pure, with only a minimal number of false detections, where we are unable

to find a significant red sequence we assume that the cluster is distant. This assumption is supported by a number of observations of clusters already with either spectroscopic or photometric redshifts in the redshift range $0.9 \leq z \leq 1.4$. Obtaining cluster photometric redshifts in this range has been shown to be feasible by [Pierini et al. \(2012\)](#), where they studied the galaxy population of a single X-ray selected cluster at $z = 1.1$ with data obtained from GROND. A separate program to obtain GROND photometric redshifts for some of these new detections lacking redshift information is currently underway with deeper observations and will form a useful sample for the study of high redshift clusters and their scaling relations in the future.

3.6.4 X-ray luminous clusters

From Figure 3.6, we are able to identify a subset of bright galaxy clusters with $L_{500}^{bol} > 5 \times 10^{44} \text{erg s}^{-1}$ at redshifts $z > 0.6$. The majority of these are already known and have been well studied and we find one new and potentially very interesting cluster. X-CLASS 2305, has no known counterpart in other cluster samples, including the Planck SZ cluster sample, despite having a luminosity $L_{500}^{bol} = 1.2 \times 10^{45} \text{erg s}^{-1}$. This cluster is subject of further study with Chandra and the Wide Field Imager (WFI), also on the MPG/ESO 2.2m telescope at La Silla ([Clerc et al 2016](#), in prep). The already known clusters are:

1. X-CLASS 228: This cluster is a part of XDCP with the alternate name XDCP J0954.2+1738 ([Nastasi et al. 2014](#)), where the bolometric luminosity is determined to be $L_{500}^{bol} = 6.70 \pm 0.75 \times 10^{44} \text{erg s}^{-1}$ in reasonable agreement with our value of $L_{500}^{bol} = 5.68 \times 10^{44} \text{erg s}^{-1}$. Our measurement is probably affected by the presence of X-CLASS 229 which is located $2'$ away.
2. X-CLASS 439/440: This is a very well studied cluster with alternate names XM-MXCS J015242.2-135746.8 and WARP J0152.7-1357 and it has been found in the ROSAT PSPC database by three independent groups ([Rosati et al. 1997](#); [Ebeling et al. 2000](#); [Romer et al. 2000](#)). This is a difficult system to measure as it consists of two major components at $z = 0.83$ and de-blending the emission from each of these components is difficult given that the separation of the two components are close together relative to the point-spread-function of XMM.
3. X-CLASS 505: Another well studied cluster at $z = 0.79$ also known as LCDCS 0504 ([Nelson et al. 2001](#); [Johnson et al. 2006](#)) and was the focus of a weak gravitational lensing analysis by [Guennou et al. \(2014\)](#).

3.7 Conclusions

In this chapter I presented the first systematic followup of X-ray selected galaxy clusters with GROND along with a new method of determining photometric redshifts based on both optical and X-ray data simultaneously. I was able to confirm and provide redshifts for 232

out of 265 cluster candidates. Of these, 88 clusters were already spectroscopically confirmed and these provided a valuable set of targets on which the redshift algorithm could be tested and calibrated. Of the remaining clusters, 66 already had a photometric redshift available in the literature and we find that the accuracy of our measurement supersedes that of many of the previously published catalogues. The remainder of the clusters were previously unconfirmed cluster candidates and I reported the first known redshifts for these objects. I found a median redshift of $z = 0.39$ for this sample and reported of photometric redshift accuracy of $\Delta z = 0.02(1 + z)$. I also presented X-ray luminosities and temperatures and found a median bolometric luminosity of $4.6 \times 10^{44} \text{erg s}^{-1}$ and a median temperature 2.6 keV. This sample of clusters is currently being used in a cosmological analysis following the z-CR-HR method (see Chapter 4). This survey can potentially carry on as long as XMM continues performing at its current levels and it is expected that an additional ~ 150 clusters will be detected per year, ~ 50 of which would pass the cosmological selection criteria. Already, a second iteration of the X-ray detection pipeline on archival data up to January 2012 has produced 184 new cluster candidates. The methods presented here will also be useful for future studies with eROSITA, particularly in fields not falling into the footprints of existing wide-field optical surveys such as DES where pointed observations similar to these will be necessary to confirm cluster candidates and to obtain photometric redshifts. The catalogue is available at <http://xmm-lss.in2p3.fr:8080/14sdb/>.

Chapter 4

Cosmological analysis of the X-CLASS/GROND catalogue

In this chapter I present the cosmological analysis of the X-CLASS/GROND cluster catalogue. This work will eventually form a publication which will be submitted as a companion paper of [Ridl et al. \(2017\)](#). The chapter is structured as follows. I begin with a broad overview of the current status of cluster cosmology, covering X-ray, Sunyaev-Zel'dovich (SZ) and optically selected samples of clusters with a focus on cosmological tests based on cluster number counts and measurements of the halo mass function. In Sections 4.2 and 4.3, I introduce the forward-modelling method that I utilised for my cosmological analysis: the z-CR-HR method. These sections are based on [Clerc et al. \(2012a\)](#), where this method was first presented. For this thesis, I used a Python translation of the original CR-HR code which was written in IDL. This translation did not allow for the inclusion of redshift information from the observed clusters and my main contribution to it was an extension to also include redshifts and testing the consistency of the two codes. In Section 4.4, I introduce parameter estimation by making use of the Cash likelihood and Markov Chain Monte Carlo (MCMC) methods and in Section 4.5, I discuss the validation and testing of our methods on simulated mock catalogues of clusters. For the work presented in these two sections, I was largely assisted by a visiting Masters student, Jonathan Sanner, who developed the interface between the z-CR-HR modelling and the MCMC sampler (`emcee`) and helped with the performance verification. Finally, in Section 4.6, I arrive at the final goal of my thesis, the analysis of the X-CLASS/GROND sample and find that the results are in tension with previous studies. I also present explanations for this tension and highlight some of the difficulties in working with a serendipitous cluster survey that includes pointed cluster observations.

4.1 Current status of cluster cosmology

The previous decade has seen the field of cluster cosmology develop substantially and great progress has been made in the development of methods to provide cosmological constraints

that are competitive with those derived from other observational probes such as CMB, BAO and SN. A major reason behind the improvement in results stems from a better understanding of cluster mass proxies and these are now better constrained, thanks in large part to accurate gravitational lensing methods that are able to provide masses accurate to the 10% level. Of crucial importance to any investigation of the cluster population is having a reliable knowledge of the probability that a given cluster would be detected in a survey, i.e. the selection function. Further, one requires robust scaling relations between observable mass proxies and total cluster masses. Indeed, in order to obtain reliable measures of cosmological parameters one should simultaneously fit for the scaling relations since these have a strong effect on the number of clusters that one is able to detect at a given mass and redshift. I summarise a few of the major cluster cosmology analyses performed in recent times here.

The main parameters derived from galaxy clusters are σ_8 , Ω_M and the dark energy equation of state, w . Many studies (Vikhlinin et al. 2009b; Mantz et al. 2010b, 2015) also include limits on the mass of light neutrinos, place constraints on the non-Gaussianity of primordial density fluctuations and provide tests to distinguish between various models of gravity. The measurement of σ_8 with cluster data has a rich history, in particular through the use of X-ray observed and selected clusters (Eke, Cole & Frenk 1996; Borgani et al. 2001; Reiprich & Bohringer 2002; Seljak 2002; Smith et al. 2003). This is because the predicted number density of clusters is very sensitive to σ_8 and the effects of sample selection typically introduce only a low level of uncertainty to calculations of this parameter. Uncertainties in the calibration of the absolute mass scale are more of a problem. It is normally difficult to constrain σ_8 independently due to a strong degeneracy with Ω_M and so most analyses seek to constrain this degeneracy and then insert a value for Ω_M (e.g., from baryon fraction measurements Allen et al. 2008; Mantz et al. 2014) from which it is possible to derive σ_8 . The reason for this degeneracy is that σ_8 determines the rms amplitude of the fluctuations at a given scale. Further, the corresponding length scale is also a function of Ω_M , with the implication that σ_8 then also depends on Ω_M . It is thus necessary to constrain these two parameters simultaneously.

The fraction of baryonic matter with respect to the total mass ($f_{gas} = M_{gas}/M_{total}$) of a galaxy cluster also provides a powerful probe of cosmology and is expected to be close to the cosmic baryon fraction $\Omega_b/\Omega_M = 0.156$ (Planck Collaboration XIII et al. 2015). The gas mass fraction of clusters should have a relatively low scatter between individual clusters and should not evolve much with redshift. Recent developments in hydrodynamical simulations of clusters such as EAGLE (Schaye et al. 2014) and ILLUSTRIS (Vogelsberger et al. 2014), which now include accurate modelling of the baryonic physics such as AGN feedback, means that they are better able to predict baryonic depletion in clusters which causes systematically lower baryonic fractions than the background universe. Thus reliable measurements of f_{gas} can provide good insights into the cosmic matter density. Some issues remain however and these simulations often produce too few galaxies in central regions of clusters and an excess around the outskirts compared to observations, indicating the presence of dynamical issues (Natarajan et al. 2017). Apart from allowing for robust constraints on Ω_M , Allen et al. (2004, 2008) also used f_{gas} measurements to constrain the

acceleration of the Universe providing an independent confirmation of the existence of dark energy.

X-ray cluster surveys

Vikhlinin et al. (2009b) derived cosmological constraints by making use of clusters detected by ROSAT. They used two samples, separated by redshift into low- z and high- z bins. This enabled the determination of evolutionary parameters such as w , along with Ω_M and σ_8 . The low- z sample was selected from RASS (Trümper 1993) and contains 49 clusters with $0.025 < z < 0.22$ whereas the high- z samples were selected from the 400d serendipitous survey (Burenin et al. 2007) and contains 36 clusters with $0.35 < z < 0.9$. All 85 clusters were followed up with Chandra. The calibration of the mass-observable relations was performed under the assumptions of hydrostatic equilibrium and the analysis includes constraints on the scaling relations. Corrections for the selection of clusters are also included. Three different mass proxies were used in this analysis, namely the average temperature T_X , the gas mass (M_{gas}) within r_{500} , and the product of these two $Y_X = T_X \times M_{gas}$. The details of their mass calibration are presented in Vikhlinin et al. (2009a). The derived masses from each of these proxies depend on the distance to the cluster and as such, one would expect that the high- z mass function would be modified if the background cosmological parameters are incorrect. This provides a useful consistency check for these results and thus enhances their reliability.

The parameters of interest, are those affecting the growth of structures and their power spectrum, as well as those affecting the distance-redshift relation. Since the measurements of the individual cluster specific quantities M_{gas} and Y_X depend on the distance to the cluster, it was necessary to recalculate these for each new combination of cosmological parameters. In addition to using only constraints derived from clusters, they also combined their analysis with a number of additional datasets, including CMB (WMAP5), BAOs and SNIa assuming Gaussian priors for each of these and included a prior on $h = 0.72 \pm 0.08$ from the HST Key Project (Freedman et al. 2001).

Based on the shape of the local mass function, they found $\Omega_M h = 0.184 \pm 0.035$ where the error includes both statistical errors and the systematic error arising from variations of the power-law slope of the $L - M$ relation. When combined with the HST prior on the Hubble constant, this provides a measurement of the matter density parameter $\Omega_M = 0.255 \pm 0.08$. From the normalisation of the local cluster mass function derived from the low- z sample, they find that the degeneracy between σ_8 and Ω_M is described by $\sigma_8 = 0.813(\Omega_M/0.25)^{-0.47}$. The inclusion of high- z clusters does not strongly affect the results giving $\sigma_8 = 0.803 \pm 0.011$ when $\Omega_M = 0.25$ compared to the result for the low- z only sample of $\sigma_8 = 0.813 \pm 0.012$. The constraints on Ω_M and σ_8 from the low redshift sample are found to be largely independent of the assumed dark energy model.

Based on the evolution of the mass function they determine that $\Omega_\Lambda > 0$ with a significance of 5σ , providing an independent confirmation of the existence of dark energy. Assuming a constant $w = w_0$ and a flat universe, the equation of state parameter for dark energy is found to be $w_0 = -1.14 \pm 0.21$ and this improves to $w_0 = -0.991 \pm 0.084$ when

fitting the clusters together with WMAP, BAO and SN observations.

Mantz et al. (2010c) studied a sample of 238 galaxy clusters drawn from various RASS selected sources (BCS, REFLEX and Bright MACS) and builds on a previous work by the same authors (Mantz et al. 2008). Due to the relatively shallow depth of RASS compared to ROSAT serendipitous or XMM selected clusters, this sample consists of only the largest clusters extending down in mass to $M_{500} > 2.7 \times 10^{14} M_{\odot}$ (a factor 2 larger than the limiting mass of Vikhlinin et al. (2009b)) and with a redshift range $0 < z < 0.5$. Ninety-four of these clusters were followed-up with Chandra and this allowed for the measurement of M_{gas} . The remaining 144 clusters had only a redshift and survey flux. This was the first work to present a method to place constraints on both cosmological parameters and cluster scaling relations simultaneously. A single likelihood function was applied to the full data set, including both the survey and followup observations, as well as combining the background cosmology with scaling relations. In their previous work (Mantz et al. 2008), the authors utilised hydrostatic mass estimates whereas here, the gas mass M_{gas} was used as a proxy for the total mass. The gas mass is measured more precisely than the temperature if clusters are relaxed and as shown by Allen et al. (2008) displays a relatively low scatter with the total mass in the mass range under study and the mass scale is set using the hydrostatic method.

Constraints for Ω_M and σ_8 , assuming a Λ CDM cosmology were obtained for each of the BCS, REFLEX, and Bright MACS individually before being combined. The combined results showed $\Omega_M = 0.23 \pm 0.04$ and $\sigma_8 = 0.82 \pm 0.05$, in good agreement with the constraints obtained by Vikhlinin et al. (2009b). When combining the cluster data with WMAP5 these results improve to $\Omega_M = 0.26 \pm 0.02$ and $\sigma_8 = 0.80 \pm 0.02$, a factor two reduction in the associated errors thus highlighting the power of combining multiple datasets.

When considering dark energy models with a constant equation of state, w , constraints on Ω_M , σ_8 and w are computed together. Based on cluster data alone, they find $w = -1.0 \pm 0.2$ while the constraints on Ω_M and σ_8 are almost identical to those from Λ CDM. For evolving w models and including all external datasets (WMAP5, BAO, SNIa and f_{gas}) they find $w_0 = -0.88 \pm 0.21$ and $w_{et} = -1.05^{+0.20}_{-0.36}$, where w_{et} is the equation of state at early times and this represents a Dark Energy Task Force (DETF) figure of merit of 15.5, representing a significant improvement over the constraints derived from just WMAP5, SNIa and BAO (Wang 2008) who had a figure of merit of 8.3.

Using this same sample of galaxy clusters as previously (although with a slightly higher flux cut than previously and after removing some clusters that appear to have their X-ray emission dominated by AGN), Mantz et al. (2015) added mass measurements from weak gravitational lensing, drawn from the *Weighing the Giants* (WtG) program (Von Der Linden et al. 2014; Applegate et al. 2014) allowing for the calibration of the absolute mass scale to a precision of 8%. The motivation for this was that previous constraints on σ_8 were limited due to uncertainties in the calibration of cluster mass measurements such that a 10% bias in the mass calibration leads to a shift of nearly 20% in σ_8 for a fixed Ω_M . Gravitational lensing provides a way to acquire a more accurate and less-biased mass calibration. The WtG catalogue used in this work consists of 50 massive galaxy clusters,

most of which were drawn from the previously described RASS samples and the lensing data was incorporated into cosmological tests based on the cluster mass function. The analysis used the same pipeline as Mantz et al. (2010c) and just included the WtG lensing data. Twenty-seven of the WtG clusters are members of the cosmological sample used in this work and could thus easily be included in the likelihood function to help constrain the $L - M$ relation. The remaining clusters could only be used to calibrate the relation between gas and total mass and it was verified that no biases were introduced by including the additional lensing data. The measurements of the gas mass fraction f_{gas} (Mantz et al. 2014, ; discussed below), were also included in this analysis to give additional constraints on dark energy parameters and to tighten the constraints on Ω_M by breaking the degeneracy with σ_8 .

Based purely on the cluster data they find $\Omega_M = 0.26 \pm 0.03$ and $\sigma_8 = 0.83 \pm 0.04$. The results were found to be very similar for flat and curved Λ CDM, flat constant and evolving- w models as well as for models with free neutrino mass. The gradual improvement of these constraints on Ω_M and σ_8 are illustrated in Figure 4.1. We see clearly how the areas of the confidence regions have decreased since Mantz et al. (2008), where hydrostatic mass estimates from Reiprich & Bohringer (2002) were used, to the use of gas mass as a proxy for the total mass in Mantz et al. (2010c) to the most recent results using weak gravitational lensing to calibrate the absolute mass scale.

The constraints derived for spatially-flat, constant- w modes are identical to those of the previous results in Mantz et al. (2010c) and we see that although the weak lensing data improves constraints on σ_8 , there is little contraction of the constraints for w . This is due to the low precision of individual cluster masses. These constraints are however competitive with those derived from other cosmological probes such as CMB, BAO or SNIa. The constraint derived from clusters only gives $w = -0.98 \pm 0.15$ while including external data sets results in a stronger constraint on $w = -0.99 \pm 0.06$. The constraints on cosmological parameters from various datasets are illustrated in Figure 4.1.

Mantz et al. (2014) followed a different approach to their previously discussed works in that they followed the work of Allen et al. (2004, 2008) and used measurements of the gas mass fraction f_{gas} to constrain cosmological parameters. Important requirements for studies such as this are to avoid systematic biases and to minimise the scatter in f_{gas} . To this end, their study was restricted to 40 hot ($k_B T \gtrsim 5$ keV), massive, dynamically relaxed galaxy clusters, extracted from the Chandra archive. Many of these clusters also have high-quality weak gravitational lensing data, providing accurate measurements of the total masses of those clusters. This restriction to dynamically relaxed clusters mitigates the biases arising from departures from hydrostatic equilibrium and the presence of sub-structure. Since the gravitational lensing data provides good estimates of the total cluster masses, this means that any residual biases can be well calibrated. The high quality of the Chandra data allowed for the intrinsic scatter in f_{gas} to be constrained for the first time and was measured in a spherical shell at radii $0.8-1.2r_{2500}$ as this is the region which was found to display the lowest intrinsic scatter. The scatter in this region was found to be $7.4 \pm 2.3\%$ and this is a large improvement of previous works.

By selecting a low redshift ($0.07 < z < 0.16$) sub-sample of 5 clusters constraints were

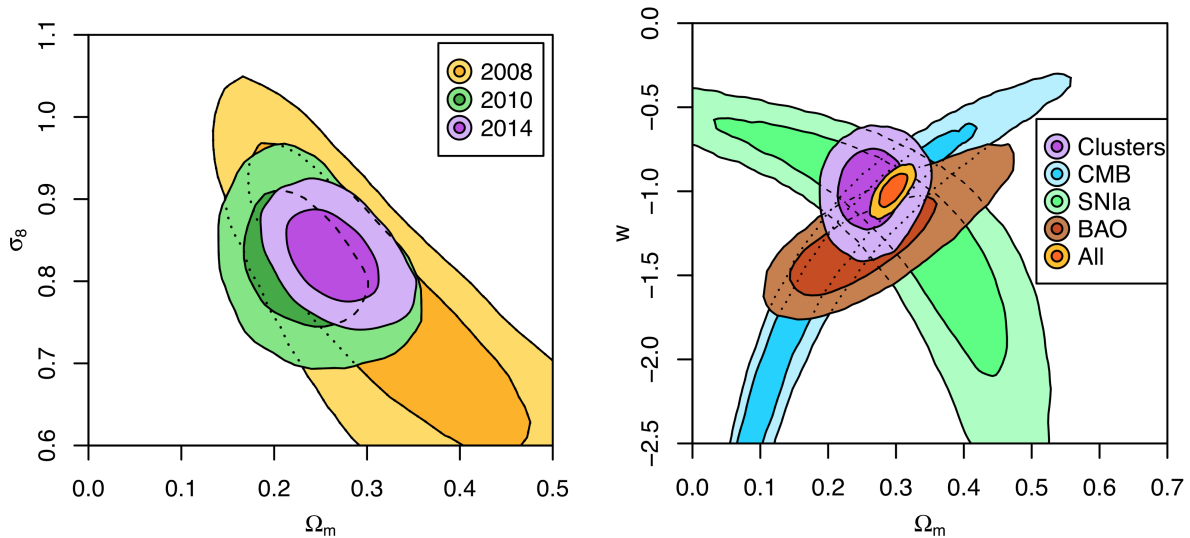


Figure 4.1: Constraints on various cosmological parameters coming from analyses based purely on clusters, and with combining with external datasets. The dark/light shading represent the 68.3% and 95.4% confidence regions. *Left*: Constraints on Ω_M and σ_8 from these papers by Mantz et al. (2008, 2010, 2015) showing the improvements achieved by increasing the accuracy of the calibration of the absolute mass scale and the associated scaling relations. *Right*: Constraints on w and Ω_M from various datasets along with the combination of all of them, highlighting the power of utilising multiple, independent datasets when trying to constrain cosmological parameters. Images courtesy of Mantz et al. (2015).

derived for Ω_M and h , since these parameters are only minimally affected by dark energy in the local Universe. Combining this data with constraints from WMAP, Planck and SNIa, they find $\Omega_M = 0.27 \pm 0.04$. Extending this sample to include all clusters, combining them with CMB, SNIa and BAO measurements, and considering a non-flat Λ CDM model, they find $\Omega_M = 0.296 \pm 0.011$, $\Omega_\Lambda = 0.706 \pm 0.013$ and $\Omega_k = -0.003 \pm 0.004$.

When considering spatially flat models with a constant equation of state parameter w , they find $w = -0.98 \pm 0.26$ and all models with evolving- w were found to be consistent with $w_0 = 1$, $w_a = 0$.

Böhringer, Chon & Collins (2014) measure the local luminosity function from the REFLEX II cluster catalogue, which is a RASS selected sample of 910 clusters, all of which have a known redshift. The sky coverage of this sample is the entire southern sky below declination $+2.5$ degrees and with galactic latitudes $b \geq 20$ degrees, covering a total area of nearly 14,000 square degrees. From this catalogue they were also able to constrain cosmological parameters. They find $\Omega_M = 0.29 \pm 0.04$ and $\sigma_8 = 0.77 \pm 0.07$ and the largest source of uncertainty are the slope and normalisation of the $L_X - M$ relation these parameters are marginalised to obtain the final results. They also investigate the redshift evolution of the luminosity function up to $z = 0.4$ and find no evidence for any evolution out to

this redshift. Other interesting results based on this survey include the construction of the first flux-limited catalogue of superclusters with a well defined selection function (Chon, Böhringer & Nowak 2013); and a study of the galaxy cluster power spectrum (Balaguera-Antolínez et al. 2011) which was found to be in good agreement with predictions from Λ CDM and compatible with a featureless power spectrum on scales $k > 0.01 h \text{ Mpc}^{-1}$, implying a lack of a significant BAO signal.

The works discussed up to now have all been based on ROSAT selected galaxy cluster samples as the RASS provides the widest field X-ray survey in existence allowing for the derivation of robust selection functions. Up until recently, there were no wide-field contiguous surveys performed with XMM-Newton but this has changed with the XMM-XXL program which covers 50 square degrees to a depth of 10 ks. This is a particularly interesting study in the context of this thesis as it makes use of similar X-ray data and analytical pipelines. The full cosmological analysis based on this sample is yet to be completed but early cosmological results based on cluster number counts, the X-ray luminosity function and spatial distribution of the 100 brightest clusters detected by the XXL are presented in Pacaud et al. (2016), and we summarise them here.

The mass function (assumed to be the one from Tinker et al. 2008a) combined with the total matter transfer function of Eisenstein & Hu (1999), is converted into a number density as a function of redshift, temperature and luminosity. Assuming a WMAP9 cosmology, and taking the scaling relations from XXL papers III (Giles et al. 2016) and IV (Lieu et al. 2016), the model predicts a total of 117 clusters; slightly more than the actually 100 detected. After accounting for Poisson noise and sample variance from cosmic density fluctuations however, the significance of this deficit falls below 1σ . The redshift distribution and number density of the detected clusters is also found to be in agreement with that which is expected from the fiducial WMAP9 cosmological model. When considering the Planck cosmological parameters the predicted number of clusters assuming the same scaling laws as above is 165 clusters, significantly more than the number detected and indeed such a tension between Planck CMB and cluster results have been well reported, including by the Planck team themselves (Planck Collaboration XXIV et al. 2016). Adjusting the $M - T$ relation of Lieu et al. (2016) to its 1σ upper-bound reduces the predicted number of clusters to 102, which is in good agreement with the 100 detected clusters and they conclude that tension between the two analysis is not significantly apparent.

The luminosity function was then used to place independent constraints on the $L - T$ relation of Giles et al. (2016). By making use of the raw number density in the $L_X - z$ plane and comparing it to different models they find that the slightly lower number of detected clusters than expected is better accounted for by increasing the slope of the scaling relation than by changing its normalisation. Finally, the spatial distribution is analysed through the use of the two-point angular correlation function and all estimators were found to show a positive correlation for scales lower than $6'$ with a slightly higher signal than expected from the WMAP9 cosmology. Further to this, 5 super-structures were detected and characterised. The XXL survey should in the future provide good constraints on cosmological parameters and a robust cosmological analysis is currently underway.

SZ cluster surveys

Apart from using the X-ray emission of the ICM to create well selected samples of galaxy clusters, recent developments mean that the SZ effect now also provides a useful tool for creating robust cosmological catalogues. The first competitive cosmological results based on SZ selected were obtained from two ground-based experiments namely, the Atacama Cosmology Telescope (ACT, Swetz et al. 2011) and the South Pole Telescope (SPT, Carlstrom et al. 2011). Both of these experiments published results incrementally as their respective survey areas have grown and the number of clusters increased and so we focus here mostly on the most recent results derived from the completed surveys.

The first SPT cosmological analyses were presented by Vanderlinde et al. (2010), with 21 SZ selected galaxy clusters extracted from 178 square degrees leading to an improvement in constraints derived from WMAP alone of around 50% for σ_8 and w . This was followed by Benson et al. (2013) making use of 18 clusters selected from the same 178 square degrees, 14 of which were also observed in X-rays with either XMM-Newton or Chandra, and Reichardt et al. (2013) who selected 100 optically confirmed clusters with $z > 0.3$ from 720 square degrees and were able to slightly improve the results of the previous study making use of the same methodology. The limiting factor in all these analyses was the calibration of the cluster mass scale. Bocquet et al. (2015) used the same sample of 100 clusters and combined them with velocity dispersion (σ_v) measurements for 63 clusters and X-ray, Y_X measurements for 16 clusters to calibrate the absolute mass scale. It was found that the σ_v and Y_X calibrations were consistent to 0.6σ and that the σ_v calibration favoured masses which were 16% higher. The cosmological analysis based on the completed SPT survey covering 2500 square degrees is presented by de Haan et al. (2016). They utilised 377 clusters with $z > 0.25$ and a sample purity of 95%. Additional constraints on the cluster masses were obtained from Chandra X-ray observations of 82 clusters (Vikhlinin et al. 2009b; McDonald et al. 2013) and a prior on the mass-observable relations taken from weak-lensing observations from Weighing the Giants (WtG, Von Der Linden et al. 2014; Applegate et al. 2014) and Canadian Cluster Comparison Project (CCCP, Hoekstra et al. 2015). For a Λ CDM cosmological model they find $\Omega_M = 0.289 \pm 0.042$ and $\sigma_8 = 0.784 \pm 0.039$ where a prior on $H_0 = 73.8 \pm 2.4 \text{ km s}^{-1} \text{ Mpc}^{-1}$ from Riess et al. (2011) is used. When considering more general models, they find constraints on the equation of state of dark energy to be $w = -1.023 \pm 0.042$, a 14% improvement on constraints obtained by combining only Planck CMB (Planck Collaboration XVI et al. 2014), H_0 , BAO (Anderson et al. 2014) and SNIa (Betoule et al. 2014) data.

ACT is a considerably smaller experiment than SPT. Sehgal et al. (2011) presented results obtained from nine optically confirmed high-mass clusters drawn from 455 square degrees and the latest cosmological results from ACT were presented by Hasselfield et al. (2013) where cosmological constraints are found based on 22 high signal-to-noise clusters with complete optical follow-up drawn from a 504 square degree field-of-view. When combining with priors from WMAP7, they find $\Omega_M = 0.292 \pm 0.025$ and $\sigma_8 = 0.829 \pm 0.024$. In an extension to Λ CDM, including non-zero neutrino mass density they find $\sum_\nu m_\nu < 0.29$ eV where the ACT data is additionally combined with BAO and H_0 priors.

With Planck, SZ-studies of galaxy clusters were launched into a new era. Planck performed an all-sky survey over 29 months covering a wide range of frequencies and produced the largest-SZ selected sample yet as well as the deepest systematic all-sky survey of galaxy clusters at any wavelength (Planck Collaboration XXVII et al. 2016). In total, 1653 cluster candidates were detected and of these 1203 were confirmed as clusters with the help of external datasets. The first cluster cosmology analysis (Planck Collaboration XX et al. 2014), associated to the 2013 data release from Planck, was performed on a subsample of 189 clusters, all but one of which had an optically confirmed redshift. In conjunction with the corresponding cosmological constraints derived from primary CMB anisotropies (Planck Collaboration XVI et al. 2014), this work generated a fair amount of controversy due to the disagreement between their respective constraints i.e., either a 40% bias in cluster masses or the inclusion of some process to suppress power in the CMB on small scales such as massive neutrinos is needed to reconcile the tension between the results. This remains an issue with the most recent cluster cosmology analysis (Planck Collaboration XXIV et al. 2016) which takes advantage of the completed survey and is performed on a sample of 439 clusters. In addition to this, they make use of weak gravitational lensing from WtG and CCCP to provide priors on the hydrostatic mass bias parameter $(1 - b)$. They also make use of a novel method using gravitational lensing of the CMB temperature fluctuations by the Planck clusters themselves to further constrain the bias. The combination of cluster and CMB constraints favours non-minimal neutrino masses and it is expected that improving mass calibrations from the 10% level which is to current status to $\sim 1\%$ would greatly enhance future analyses.

Other notable works

Many works e.g., Vikhlinin et al. (2009b), attempt to address the systematic uncertainties inherent in cluster abundance studies (i.e., uncertainty in the absolute cluster mass scale), by detailed observations of a small number of clusters. Another approach however is to use large samples combined with statistically mass-sensitive properties of clusters. One can then fit the cosmology and observable-mass relation of the cluster sample simultaneously. This idea forms the basis of the self-calibration approach where the clustering of clusters is combined with cluster number counts to constrain cosmological parameters with no knowledge of the observable-mass relation (e.g., Majumdar & Mohr 2004). One can also use observables that correlate with mass such as the cluster-shear cross-correlation function (Sheldon et al. 2009).

Although clusters are easily identified by the presence of an over-density in the galaxy distribution seen in optical wavebands, this has not been a popular method for selecting clusters for cosmological studies based on number counts. There is however a fairly large advantage in optical cluster surveys in that there are a number of wide-field surveys allowing for the detection of vast numbers of clusters such as SDSS. One such example of an optically selected sample of clusters is maxBCG (Koester et al. 2007) which contains $\sim 10,000$ clusters selected from ~ 7400 square degrees of SDSS imaging. Using the maxBCG sample Rozo et al. (2009) combined clusters with weak-lensing measurements (Johnston et al.

2007) to derive cosmological constraints that (for the first time using an optically selected sample) are comparable in accuracy to the more traditional approach using X-ray selected samples. To do this, they split the maxBCG sample into bins of similar richness for which masses were calculated in a statistical way from weak-gravitational lensing measurements by stacking clusters together. They also introduced a weak-lensing bias parameter β such that the observed mass $M_{obs} = \beta M_{true}$. This bias parameter was then included in the fitting of cosmological constraints. When combining their results with WMAP5 cosmology, they found $\Omega_M = 0.269 \pm 0.018$ and $\sigma_8 = 0.807 \pm 0.020$, along with a constraint on $\beta = 1.013 \pm 0.059$. All of these are in good agreement with the studies based on X-ray and SZ measurements described above and current and future surveys such as DES and LSST should only enhance the power of such methods.

In addition to these more common analyses making use of cluster number counts one can also use cluster observations to constrain a number of other cosmologically interesting parameters. One of these is placing constraints on primordial non-Gaussianity. For example [Mana et al. \(2013\)](#) studied the clustering of clusters to constrain models of the early universe. [Shandera et al. \(2013\)](#) found that by modifying the halo mass function to include non-Gaussianity, current levels of X-ray data can constrain one-parameter non-Gaussian models to a useful degree from studies of number counts. Various models of gravity can also be distinguished with the help of clusters. [Rapetti et al. \(2010\)](#) made use of the Mantz sample of clusters to perform a robust test on general relativity on cosmological scales and found no evidence for departures from either GR or the cosmological constant plus cold dark matter model of the universe. [Cataneo et al. \(2015, 2016\)](#) used clusters to place constraints on two popular models of $f(R)$ gravity from X-ray selected galaxy clusters and found that ongoing and upcoming surveys will soon be competitive with current Solar System tests of modified gravity. One can also use clusters to place constraints on the equation of state of dark matter as done by [Sartoris et al. \(2014\)](#) for a single cluster (MACS 1206) in the CLASH-VLT survey using a combination of exquisite gravitational lensing data from HST and a large number of galaxy velocities from VLT. They were able to confirm the hypothesis that dark matter is a pressureless fluid finding $w_{DM} = 0.00 \pm 0.15$ (stat) ± 0.08 (syst) with a plan to repeat this analysis on all 12 CLASH-VLT clusters in the future. By studying the galaxy cluster Abell 3827, [Massey et al. \(2015\)](#) found a slight offset between the dark matter halo of one of four massive central galaxies and its stars. Such an offset, shouldn't be seen in field galaxies, but can be predicted for galaxies falling into massive clusters if dark matter is allowed to self-interact, causing an extra dynamical friction. Interpreting the offset as arising purely from dark matter self-interaction they are able to put a lower limit on the interaction cross-section of dark matter. Comparing the amount of sub-structure seen in galaxy clusters to what is expected from simulations provides a good test of the hierarchical nature of structure formation. [Schwinn et al. \(2016\)](#) and [Jauzac et al. \(2016\)](#) studied substructures in Abell 2744 and found that the number of massive substructures represents a challenge to the cold dark matter paradigm since they find no similar structures in the Millennium simulation. Extreme value statistics imply a volume 10 times larger than the Millennium XXL is needed to find a single halo with a similar level of substructure to Abell 2744.

All of the results summarised here will be improved upon with future generation of experiments. For example, eROSITA will provide on the order of 100,000 X-ray selected galaxy clusters greatly improving the statistics from cosmological tests based on number counts, and its contiguous nature will allow for powerful studies of the clustering of clusters. Wide-field optical surveys such as DES and LSST will provide the deep optical information needed to confirm clusters and to obtain photometric redshifts while 4-MOST will provide spectroscopic redshifts for many thousands of clusters in the southern hemisphere. Further in the future, JWST, E-ELT and Athena will allow for the incredibly deep and detailed study of a small number of these clusters and allow us to probe the cluster mass function to the early-history of the Universe.

4.2 The z-CR-HR method

Up until now I have described the cosmological paradigm on which current models of the Universe are based; described the process of the formation of the most massive collapsed halos, galaxy clusters; and introduced the X-CLASS/GROND cosmological cluster sample. I now proceed with what is the crux of this thesis, the cosmological analysis of the X-CLASS/GROND sample by making use of a relatively new method of interpreting galaxy cluster number counts. In this method, the cosmological analysis is simplified by basing it purely on quantities that are directly observable in X-ray observations namely, the count-rate (CR) and the hardness ratio (HR) and using photometric redshift information derived from GROND optical observations. We refer to this from now on as the z-CR-HR method.

The z-CR-HR method was first presented by Clerc et al. (2012a) and is based on the premise that substantial information about the cluster redshift, temperature and luminosity is encoded in the raw X-ray data and that this information can be statistically extracted. In this method, the two X-ray based measurements (CR and HR) are plotted in a two-dimensional pseudo-color-magnitude diagram and compared to the diagram that is predicted from cosmological modelling. In the absence of individual cluster redshifts, the CR-HR method performs substantially better than traditional mass function analyses based on cluster counts. This method has been applied to a sample of X-ray selected clusters coming from the XMM database, X-CLASS, the catalogue from which the sample presented in Chapter 3 of this thesis was drawn (Clerc et al. 2012b). When redshifts are available, there is no significant improvement on the recovered cosmological parameters such as Ω_M and σ_8 by using the CR-HR method but parameters relating to the cluster scaling relations $L - T$ and $M - T$ as well as evolutionary parameters such as w are better constrained. Another significant advantage of the z-CR-HR method is that it is relatively simple and easily adaptable to large datasets such as those that will be coming from eROSITA. A particularly useful property of this method is that it bypasses the step of having to derive individual cluster masses from the X-ray measurements and that the scaling relations can be constrained simultaneously to the cosmological parameters. The tests that were performed on mock data in Clerc et al. (2012a) were done via a Fisher analysis whereas for the remainder of this work, all tests and analyses are performed through

Markov-Chain Monte-Carlo methods.

For the description of the z-CR-HR method, we assume a shallow X-ray survey, representative of existing surveys such as the XMM-XXL or X-CLASS, which have exposure times of ~ 10 ks allowing for a few hundred photons to be detected per cluster. This number of photons typically allows one to measure the average temperature of a cluster but it is not sufficient for the fitting of temperature profiles. Inherent in a survey such as this is that the selection function depends only on X-ray measured observables. It is thus easier to define than say, the selection function of an optically selected sample of clusters. Once a sample of clusters is selected, its count-rate is measured in 3 bands optimally chosen to maximise any potential cosmological signal. In our case we chose to measure the count rate in the [0.5-2] keV band which we refer to from now as the total count rate (CR). The two other bands that are measured are the [1 - 2] keV and [0.5 - 1] keV bands giving CR_1 and CR_2 so that $HR = CR_1/CR_2$. Once these values are measured, they are used to populate a grid of CR-HR for a number of slices in redshift giving a three-dimensional structure in observable space.

Once one has the observed and modelled distributions in hand, they then need to be compared through a likelihood analysis. The models are created over a range of cosmological parameters and each model is compared to the observed distribution to find the best fitting set of parameters to describe the observed distribution in the z-CR-HR space.

4.3 Modelling the z-CR-HR distribution

4.3.1 The halo mass function

In Chapter 1, we derived the halo mass function using the Press-Schechter formalism, under the assumption that the perturbations to the matter density field in the early Universe were Gaussian scale invariant i.e. that the shape of the primordial power spectrum is,

$$P(k) = Ak^{n_s}. \quad (4.1)$$

For our computation of the mass function, we use this as our starting point, with n_s depending on the fiducial cosmology, (e.g., from WMAP9, $n_s = 0.961$ Hinshaw et al. 2013). In order to transform the primordial power spectrum, to the one observed today at $z = 0$ we use the transfer function presented by Eisenstein et al. (1998). This transfer function is an analytic fitting formula that accounts for the amplitude and location of baryonic features in linear perturbation theory. The power spectrum is then normalised by σ_8 and evolved backwards in redshift by using the growth factor. Various options are available when performing the calculation of the growth factor as a function of the scale factor. These include an analytic formula, the integration of the Heath equation or, as we chose, through the numerical integration of the partial differential equation. We are now in a position to compute the halo mass function, which describes the differential comoving density of halos per mass interval dn for each mass $M + dM$ and redshift $z + dz$ bin,

$$\frac{dn}{dM} = f(\sigma) \frac{\bar{\rho}_m}{M} \frac{d \ln \sigma^{-1}}{dM}, \quad (4.2)$$

where the function $f(\sigma)$ is not expected to vary much with redshift, is only weakly dependent on the cosmology, and is parametrised as,

$$f(\sigma) = A \left[\left(\frac{\sigma}{b} \right)^{-a} + 1 \right] \exp \left(-\frac{c}{\sigma^2} \right). \quad (4.3)$$

The rms mass variance of the smoothed field is given by σ . In our derivation of the mass function, we introduced the concept of the filtered density field, where the density fluctuations are smoothed over spherical regions to create a series of halos such that each halo has a mass M enclosed by a radius $R = (3M/4\pi\rho_m)^{1/3}$. We apply such a smoothing to the power spectrum at each redshift slice, where the filter $W(kr)$ is of the form given in Equation 1.69.

The mass function is calculated in terms of the over-density relative to the background density. Specifically, we choose to calculate the mass function in terms of M_{200b} , the mass enclosed by a radius R_{200b} that has a mean density that is 200 times higher than the mean matter density of the Universe. The parameters of the function $f(\sigma)$ above have been fit based on a number of simulations and in our case, we have chosen to use the values derived by Tinker et al. (2008a). The mass function is then projected onto the sky so that we end up with number density per unit mass, redshift and solid angle, or $dn/(d\Omega dM_{200b} dz)$. In order to use the scaling relations to convert these masses into temperatures and luminosities, we first need to make a transformation so that the mass function are given in terms of the halo density relative to the critical density ρ_c , instead of the background density i.e. $M_{200b} \mapsto M_{200c}$. This is because the scaling relations are given in terms of M_{200} . To make this conversion, we use the fitting formula from Hu & Kravtsov (2003) and assume that the mass profile is represented by an NFW (Navarro, Frenk & White 1997) profile with the concentration model given by Bullock et al. (2001).

4.3.2 Scaling relations

Obtaining directly observable quantities such as CR and HR is not possible directly from the mass of a given cluster. Instead, we need an intermediate step to transform the number density of clusters as a function of mass into a function of X-ray temperature and bolometric luminosity. These two quantities, along with a weak dependence on the metallicity of the ICM describe the actual emissivity of a cluster. The relationships between the X-ray observable quantities and mass have been well studied along with the relationship between themselves e.g., the $L - T$ relation (Mitchell, Ives & Culhane 1977; Mitchell et al. 1979; Mushotzky 1984; Edge & Stewart 1991; Allen, Schmidt & Fabian 2001; Pratt et al. 2009; Clerc et al. 2014; Giles et al. 2016) and the $M - T$ relation (Finoguenov, Reiprich & Böhringer 2001; Arnaud, Pointecouteau & Pratt 2005; Mantz et al. 2010a; Lieu et al. 2016; Mantz et al. 2016). These relationships are all well described by power laws. How these scaling laws depend on redshift is still an open question given that it depends on a variety of physical effects such as gravitational heating, supernovae, AGN feedback and thermal pressure, and so we parametrise any potential evolution by a factor $(1+z)^\gamma$. The scaling

relations are then,

$$\frac{M_{200c}}{10^{14}h^{-1}M_{\odot}} = 10^{C_{MT}} \left(\frac{T}{T_{pivot}} \right)^{\alpha_{MT}} E(z)^{-1}(1+z)^{\gamma_{MT}}, \quad (4.4)$$

$$\frac{L_X}{10^{44}\text{erg s}^{-1}} = 10^{C_{LT}} \left(\frac{T}{T_{pivot}} \right)^{\alpha_{LT}} E(z)(1+z)^{\gamma_{LT}}. \quad (4.5)$$

In the above relations, T_{pivot} is the temperature of the pivot point from fitting a power-law to the observational data. Ideally its value should be around the midpoint of the sample being analysed. One must however take care to accurately compute the modified normalisation of these relations when changing the pivot point from scaling laws taken from literature. It is important to note that both of these relations contain a significant amount of intrinsic scatter. It is thus not sufficient to assign a single set of temperature and luminosity to each mass for a given redshift. We must rather introduce the parameters $\sigma_{\ln T|M}$ and $\sigma_{\ln L|T}$ which are the scatter in T and L_X for a given M_{200c} respectively. These are not expected to depend on either the mass or temperature, or to evolve with redshift.

The final parameter needed is the core radius r_c . To obtain this we assume that the surface brightness profile is described by a beta-model with $\beta = 2/3$. The core radius is left as a free parameter which depends on R_{500c} . The relationship between r_c and R_{500} is complex and depends very much on the physics in the ICM but we assume here that it can be modelled simply as $r_c \propto R_{500}$. In our modelling, we thus set a parameter $X_{C,0} = r_c/R_{500c}$ and do not allow for any evolution with redshift or a dependence directly on the mass.

4.3.3 Instrumental model for XMM-Newton

The X-ray emission of a galaxy cluster is generally well characterised by a single temperature its and luminosity. In order to calculate the expected CR and HR of a given cluster it is necessary to simulate an observation taking into account a number of considerations. In our analysis we assume that the HR is constant across the entire spatial distribution of the cluster which is reasonable for shallow surveys such as the ones considered here since the PSF of the instrument is fairly large compared to the extent of the clusters on the sky prohibiting the resolution of substructures in the clusters. For significantly deeper surveys where temperature gradients are more easily resolved, this assumption would break down. We thus model the emission as a single temperature plasma. Further, this should not affect any scaling related quantities as these have been fitted under the same assumption when fitting models to the various cluster spectra.

For our simulations, we used the APEC model to describe the spectrum of the cluster and used an average metallicity $Z = 0.3Z_{\odot}$. The equivalent column density of hydrogen, N_H , in the line of sight accounts for Galactic extinction and is set according to the pointing (Kalberla et al. 2005) which we are attempting to simulate and the overall spectrum is normalised to give the correct integrated luminosity. Using XSPEC, in conjunction with photon redistribution matrices for the EPIC sensors, and accounting for the filter (we only use the THIN1 filter and correct the observed count rates for any differences as described

in Section 3.4) one can derive the number of photons that would be detected by the EPIC sensors per second in each energy channel for a cluster of a given temperature and luminosity. We then measure the count rates in each of the three bands described earlier by integrating over the respective energy ranges.

Coming back to the discussion of HR, we notice that since it is a ratio of the integrated counts in two given bands for a given temperature, it does not depend on L_X , since the luminosity just serves to scale the amplitude of the entire spectrum, thus conserving its shape. We would thus expect that for an emission spectrum consisting entirely of thermal bremsstrahlung HR would exhibit a degeneracy with $T/(1+z)$ but since we include a non-zero metallicity, the emission lines introduce changes to the observed count rates in each energy band as the emission lines enter them at varying redshifts. As discussed earlier, these effects are more prominent for clusters at low temperatures because of the relatively greater importance of the line emission.

4.3.4 The effect of varying cosmological parameters and scaling relations

It is instructive to investigate the impact that the variation of cosmological parameters would have on the recovered z-CR-HR distributions. To do this, we first consider a fiducial WMAP9 (Hinshaw et al. 2013) cosmological model and utilise the scaling relations presented by the XXL collaboration (Pacaud et al. 2016; Giles et al. 2016; Lieu et al. 2016) and plot the recovered distribution in the CR-HR space for three redshift intervals ($0.05 < z < 0.3$, $0.3 < z < 0.6$ and $0.6 < z < 1.3$). We then adjust the input cosmological parameters one-by-one in order to highlight the impact that the parameter in question has on the resultant CR-HR distribution as well as the number of clusters one would expect to detect. We illustrate these effects in Figures 4.2, 4.3 and 4.4.

In all figures, the black-dashed curves represent a fiducial WMAP9 cosmology with both the $L - T$ and $M - T$ scaling relations coming from the XXL collaboration. The solid-red curves represent the distribution after a single cosmological parameter is adjusted. The text at the top of the left-most panels indicates the parameter that has been adjusted with black text on the right being the value for the fiducial model and the red text on the left for the modified model. The numbers in the bottom corners indicate the number of clusters expected in that redshift interval.

Cosmological parameters

The results of this testing are shown in Figure 4.2 for Ω_M , σ_8 and w_0 . For Ω_M which was adjusted to an unrealistically high value ($\Omega_M = 0.38$), we notice that the shape and position of the CR-HR distributions are only marginally altered, with the greatest effect being seen in the highest redshift interval where clusters are on average shifted to slightly lower hardness ratio and higher count rates. By far the larger impact that this parameter has is on the number of clusters expected to be detected, increasing by a factor of ~ 1.85 in the low redshift interval and 2.5 in the highest redshift bin. This is somewhat unsurprising

as a high matter density results in the formation of clusters earlier in the history of the Universe and allows for their rapid growth so that they are already massive enough that they can be detected, even at high redshifts. Adjusting σ_8 has a similar effect to that of Ω_M , in that a higher value (in our case $\sigma_8 = 1.1$), also greatly increases the number clusters although σ_8 is comparatively more impactful at high redshifts. We also notice that for an increased value of σ_8 , clusters are shifted to higher HR at low redshifts while the position of the CR-HR distribution is largely unchanged at high redshifts. The similarities in effects introduced by these two parameters is to be expected, given that they are highly degenerate. Typically, if one fits a higher value for Ω_M a lower value of σ_8 is needed in order to maintain a constant number of detected clusters. The normalisation of the degeneracy between these two parameters is governed by the calibration of the absolute mass scale since, as we see in the top panel of Figure 4.4, an increase in the absolute mass scale results in the detection of fewer clusters which needs to be compensated for by Ω_M and σ_8 . The effect of increasing w_0 is more apparent in the position of the CR-HR distributions where clusters are shifted downwards in HR while maintaining roughly similar CR. The number of clusters expected to be detected is however less dramatically affected compared to Ω_M and σ_8 , indicating that perhaps there could be difficulties constraining this parameter based on the total number of clusters alone.

Scaling relations

Accurate calibration of the scaling laws relating cluster observable properties such as luminosity and temperature to mass is crucially important to a study of this nature, as evidenced by Figures 4.3 and 4.4. The impact that the normalisation of these relations have on the number of detected clusters is fairly straightforward. An increase in the normalisation of the $L - T$ relation, C_{LT} , for instance implies that for a given temperature, the average luminosity of a cluster also increases. Since the cluster luminosity has a direct impact on the resultant count-rate one would expect that more luminous clusters are easier to detect. The effect on the position of the distribution in the CR-HR space is slightly more subtle in that, instead of simply shifting towards higher CR, the density peak rather shifts downwards in HR. This is because, we expect to detect all clusters above a certain luminosity in a given redshift range the high-luminosity end of the luminosity function does not benefit much from the increase in luminosity (we would have detected those clusters anyway). Instead, we add clusters to the detected sample from the region of the luminosity function which lies around the detection limit i.e. low luminosities, with typically lower masses and temperatures. These clusters would normally have then also a lower HR and so the CR-HR distribution becomes increasingly populated with smaller, low luminosity clusters as the normalisation of the scaling relation increases. We see a similar effect in the bottom panel of Figure 4.3, which illustrates the effects of the evolution of the $L - T$ relation. In this case, the evolution γ_{LT} is negative, corresponding to a decrease in the normalisation of the scaling relation with redshift, going as $(1+z)^{\gamma_{LT}}$. We obviously then see little effect in the low redshift interval but as the redshift increases we see that the distribution shifts upwards in HR (with converse reasoning from the discussion on C_{LT}).

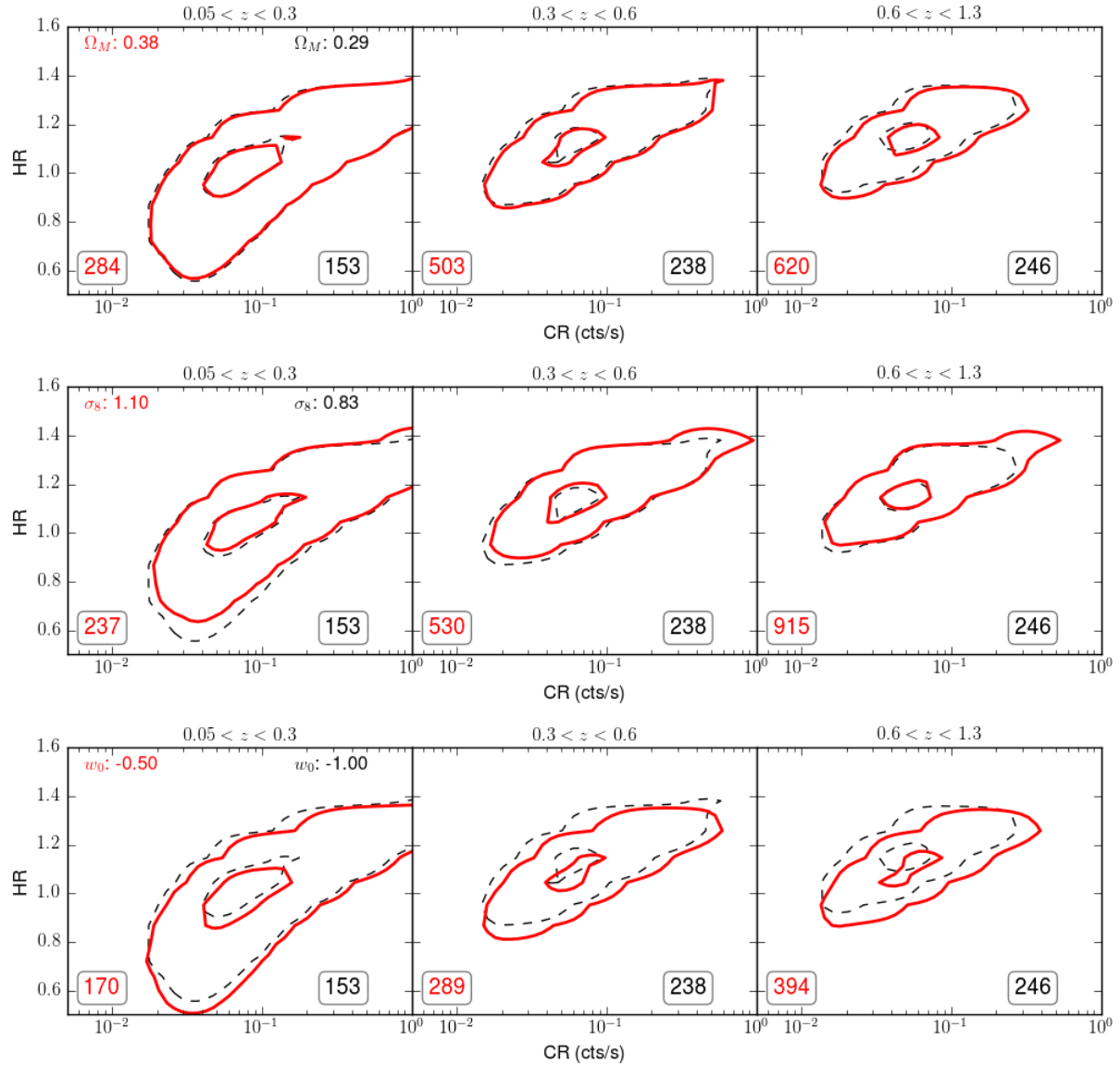


Figure 4.2: The impact of varying cosmological parameters on the number of clusters detected of a given redshift, count rate and hardness ratio. The contour levels contain 30 and 90 percent of the clusters. Illustrated here are a fiducial WMAP9+XXL cosmology (dashed-black) and the effect of varying Ω_M (top), σ_8 (middle) and w_0 (bottom) represented by the solid-red curves. The numbers at the bottom of the panels indicate the expected number of clusters in that redshift interval for each of the fiducial (black) and modified (red) models.

The power-law slope of the $L - T$ relation strongly influences the number of low mass systems that are detected relative to high mass systems. If one assumes a pivot point at ~ 3 keV, as we do for this study, then one would expect that with a lower power-law slope the luminosity of clusters with a temperature below 3 keV would be enhanced while the luminosity of hotter clusters is relatively diminished. Since the number density of clusters is dominated by the low mass end of the mass function, we would thus expect to see an increase in the number of clusters detected. We thus also see a corresponding broadening and shift of the distribution in CR-HR space towards lower HR, which is greater at lower redshifts due to the high abundance of low mass systems that would cross the detectability threshold.

The effects of adjusting the parameters relating to the $M - T$ relation are similar to those of the $L - T$ relation, although, in the opposite direction. That is, an increase in the normalisation of the $M - T$ relation leads to a decrease in the number of detected clusters since this would mean the clusters of a given mass have a lower temperature, implying a lower luminosity and detectability.

4.3.5 Accounting for pointed observations of known clusters

Galaxy clusters are particularly interesting sources to observe and study. Therefore, in general, any serendipitous survey of clusters will naturally include telescope pointings where the object of study was itself a cluster. This may bias the number of clusters that you would detect compared to that if one searched for them in all observations performed with a given instrument. This is often accounted for by simply removing clusters which were the target of the observation from the sample and subtracting the region on the sky in which they are detected from the survey area. This is often assumed not to affect the cluster population statistically.

When dealing with XMM observations however, a substantial fraction, ($\sim 13\%$) of pointings are directed specifically towards clusters and in the full X-CLASS C1+ catalogue of 347 clusters, there are 92 which lie within $3'$ of the pointing centre. This is almost double the number that would be expected based purely on the target information in the XMM observation files. We thus cannot simply remove all pointed cluster observations from the sample as the selection function for the removed clusters is very subjective, and the high fraction of clusters would significantly alter the statistics of the overall population. For example, at high redshifts, pointed observations would be mostly of the most massive clusters, as these are the type of objects that might appear in a shallow wide-field survey such as RASS, or as optical clusters from SDSS. Removing these objects would result in an under-representation of massive clusters at high redshifts, strongly influencing cosmological constraints, especially those that affect the evolution of the cluster mass function. Similarly, including them with corrections would introduce the opposite bias.

The bias introduced by these pointed observations is non-trivial to quantify and we base our modelling on the assumption that targeted clusters will, in general, lie at the centre of the pointing. An additional complication to this modelling then relates to the fact the sensitivity of XMM increases significantly towards the centre of the CCDs, while diminish-

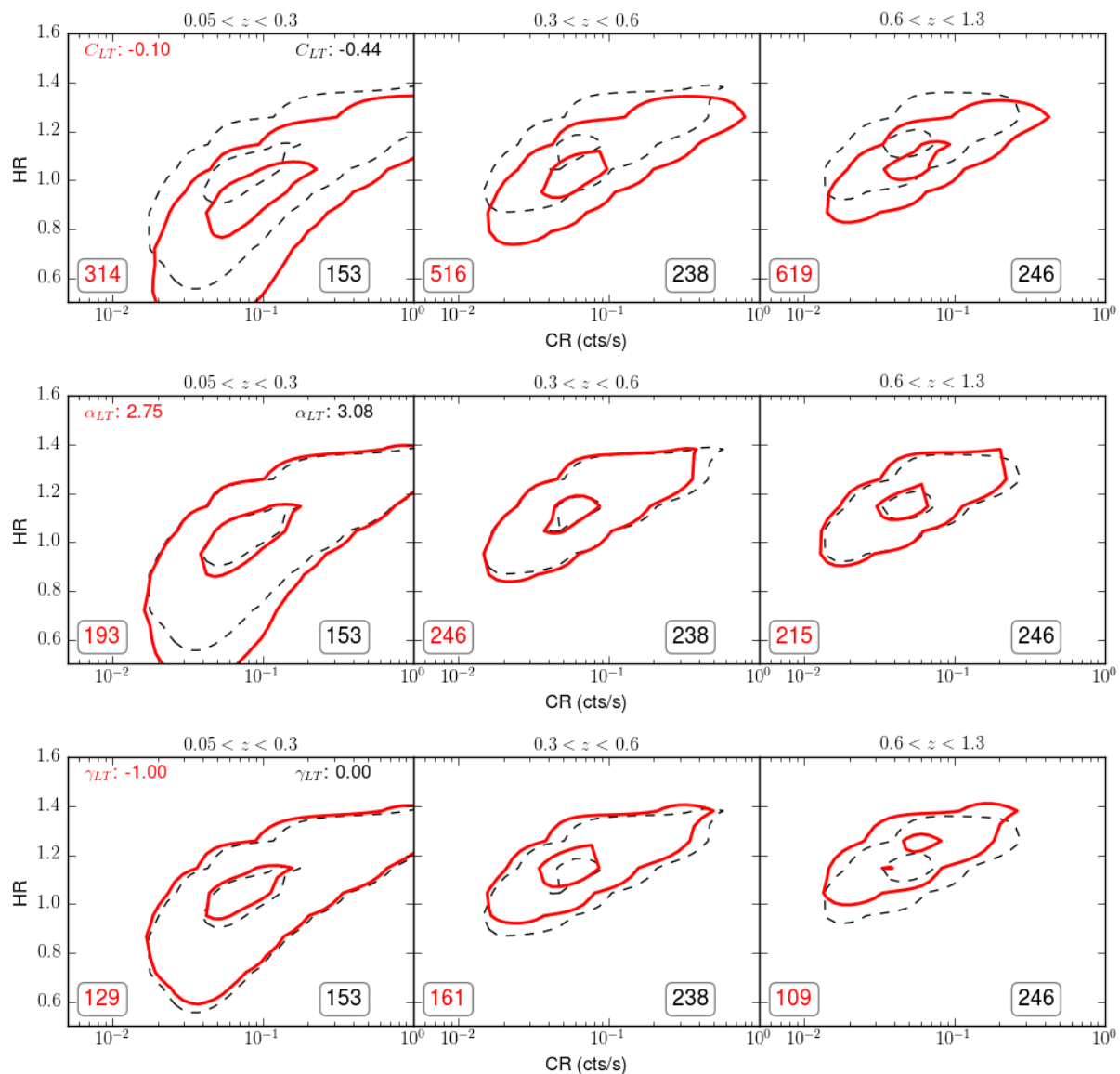


Figure 4.3: The impact of varying the normalisation, slope and evolution of the $L - T$ relation as parameterised in Equation 4.5 with $T_{pivot} = 4$ keV, on the number of clusters detected of a given redshift, count rate and hardness ratio. The contour levels contain 30 and 90 percent of the clusters. Illustrated here are a fiducial WMAP9+XXL cosmology (dashed-black) and the effect of varying C_{LT} , α_{LT} and γ_{LT} (solid-red). The number at the bottom of the panels indicate the expected number of clusters in that redshift interval.

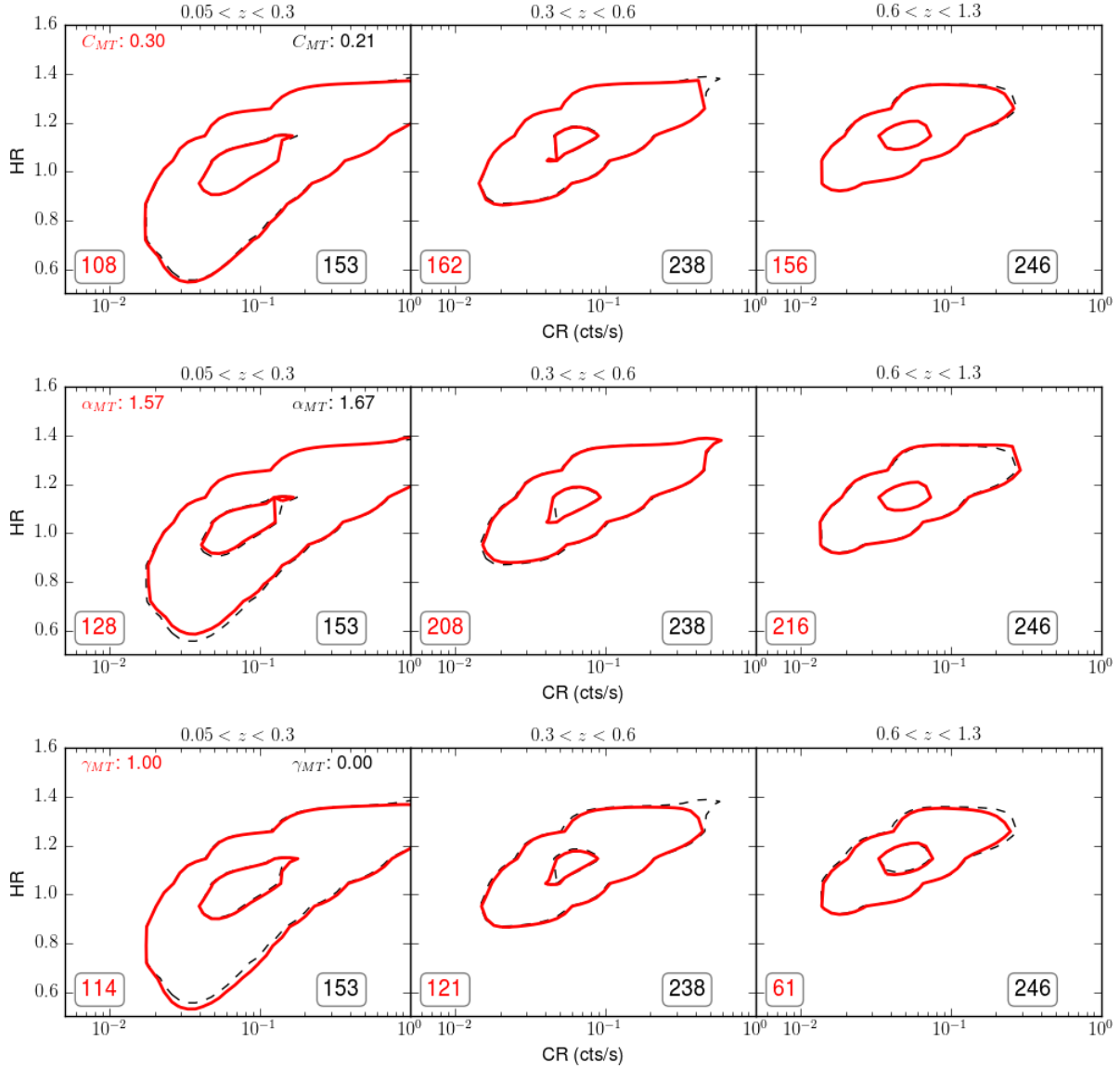


Figure 4.4: The impact of varying the normalisation, slope and evolution of the $M - T$ relation as parameterised in Equation 4.4 with $T_{pivot} = 4$ keV, on the number of clusters detected of a given redshift, count rate and hardness ratio. The contour levels contain 30 and 90 percent of the clusters. Illustrated here are a fiducial WMAP9+XXL cosmology (dashed-black) and the effect of varying C_{MT} , α_{MT} and γ_{MT} (solid-red). The number at the bottom of the panels indicate the expected number of clusters in that redshift interval.

ing greatly towards the outskirts. This is due firstly to vignetting, resulting in a decrease in the effective area off-axis, and secondly, because the PSF of the instrument becomes distorted at high off-axis values causing the appearance of objects to be distorted and the flux diluted. We must thus account for this when determining the over-concentration of clusters towards the centre of pointings on average.

To model the bias, we split the clusters into two populations, one within $5'$ of the pointing centre (assuming that all pointed clusters are within $5'$) and the other between $5'$ and $13'$. Clerc et al. (2012b) showed that the number of clusters with a given CR in each of these populations shows an excess of clusters in the inner regions even after accounting for the different sizes of the areas covered and the lower sensitivity in the outer regions. We thus model the bias as a function of CR and make the assumption that it does not depend on HR. We derive a single multiplicative factor as a function of CR and use this to make a correction to the expected CR-HR diagram derived for a set of cosmological parameters.

In the previous analysis with X-CLASS, no redshift information was taken into account. The main advance in our work however, is in including photometric redshifts for our sample and using this to strengthen constraints on evolutionary parameters. Since the selection function of XMM targets is probably dependent on the redshift interval in question (e.g., the discussion about pointed observations of high redshift clusters at the beginning of this section) we compute the bias for each redshift slice in which we perform the cosmological modelling. This introduces a limiting factor to the size of the redshift bins that we can use, as it is necessary to have enough clusters in each bin to accurately model the bias. As much as possible we try to ensure that the bias factor can be computed for each CR interval at each redshift. By definition, the bias factor is always greater than or equal to 1. When this is not possible, we assume a bias factor of 1, since if there are no clusters with a given CR and z , there should be no pointed observations at such clusters and therefore these regions of parameter-space are unbiased. The pointing bias recovered for each redshift slice in the binning scheme used in the work is shown in Figure 4.5. Once the bias is calculated as a function of CR, it is used to multiply the CR-HR diagram in each redshift interval. The effect it has is shown in the bottom panel of Figure 4.5 where we see that the most notable impact is of increasing the number of clusters expected to be observed. This is especially the case for the high-redshift interval where we also notice a shift towards higher CR.

4.3.6 Selection function

In our discussion so far we have derived a theoretical expectation for the number of clusters per unit solid angle, redshift, CR and HR, i.e. $dn/(d\Omega dCR dHR dz)$. In order to compare this to an observed data set, it is necessary to then derive the probability of detection for each cluster in our distribution. This is typically a difficult task and is one of the limiting factors for many cosmological analyses. For X-ray surveys, this task is somewhat easier than for cluster surveys performed at other wavelengths as it is based on X-ray derived parameters entirely. In Chapter 3, we described how clusters are detected in a typical XMM pointing. The basic ideas behind this method are fairly standard across surveys and instruments. That is: one normally detects clusters using a filtered image and

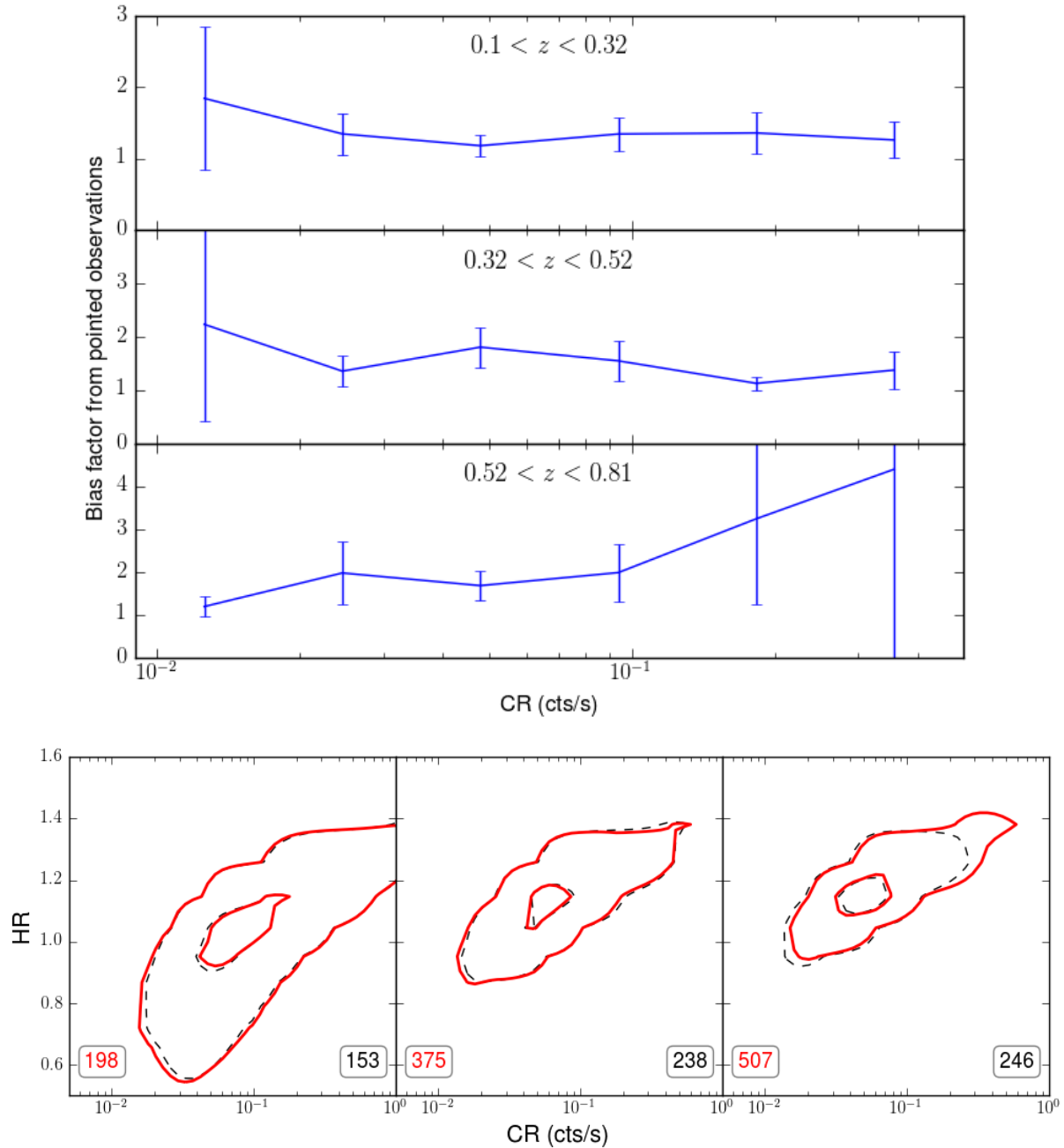


Figure 4.5: *Top:* The bias factor in three redshift intervals as a function of CR arising due to the presence of pointed observations in the sample. The values here take the sensitivity and area weighted ratio between the number of clusters in the inner and outer populations into account. *Bottom:* The effect that the bias has on the recovered CR-HR distribution for each redshift interval. The main impact is simply one of increasing the number of clusters expected, particularly at high redshifts, where we also notice a broadening of the distribution towards higher CR. This makes sense as these would be massive, high redshift clusters, which are currently objects attracting a lot of attention from astronomers studying them across the electromagnetic spectrum.

then proceeds by fitting a cluster emission model to the raw photon image. Of course, the Poissonian nature of X-ray data must also be accounted for. The efficiency of these algorithms in terms of the completeness and purity must be well understood if one wishes to perform a robust cosmological analysis with a catalogue constructed from such sources. This is typically done through extensive simulations where the source detection algorithm is run on simulated X-ray images to determine the probability that a given source is detected. These images are simulated in the same manner as was described previously in this chapter. For more details on the selection of clusters, refer to Section 3.2 in the chapter about the X-CLASS/GROND catalogue.

Since the selection function depends on the sensitivity of the instrument, one would expect to have the nature of the detected clusters to vary statistically depending on which areas of the XMM cameras are used for the detection and characterisation of clusters. For instance, Clerc et al. (2012b) only used the inner 10' of selected XMM pointings for their cosmological analysis whereas, for the X-CLASS/GROND sample considered here, we include clusters detected out to 13'. This results in a net increase in the total area on the sky which is included in the survey with the compromise of a lower average sensitivity due to vignetting effects and PSF degradation towards the edges of the XMM field-of-view. To see how this affects the overall number of clusters and their position in the CR-HR plane, we compute CR-HR distributions for equal area (100deg²) surveys with each respective selection function applied. In practice, this would require more XMM pointings to be included for the 10' study, which if comparing to Clerc et al. (2012b) is actually the case since their sample extended across the whole sky, as opposed to just the sky south of +20° in declination for the X-CLASS/GROND sample. We show this in Figure 4.6 where we notice that the shape and position of the resultant cluster distributions are roughly similar but as expected, a greater number of clusters are detected per square degree for the survey containing only the inner 10' (and thus higher sensitivity part) of the XMM cameras.

4.3.7 The effects of measurement errors

The modelling of the distribution of clusters in CR-HR space makes a prediction based on the expected number of counts to be detected for each cluster in each energy band, namely CR_{tot} ([0.5-2] keV), CR_1 ([1-2] keV), and CR_2 ([0.5-1] keV). Due to the Poisson nature of X-ray observations, particularly in the low-count regime in which we are operating, the number of actually detected photons will vary from the expected number. This is coupled with the effect of measuring cluster emission against an X-ray background, which limits the detection of photons coming from the outskirts of clusters as well as the impact that PSF distortion has on the shape and flux distribution of any detected sources. All of these factors contribute to the uncertainty in the CR and HR measured by the XMM cameras and it must thus be robustly modelled in order to provide an accurate description of the actually observed CR-HR distributions created from cluster observations.

For the work presented in this thesis, we utilise the error model of Clerc et al. (2012a,b),

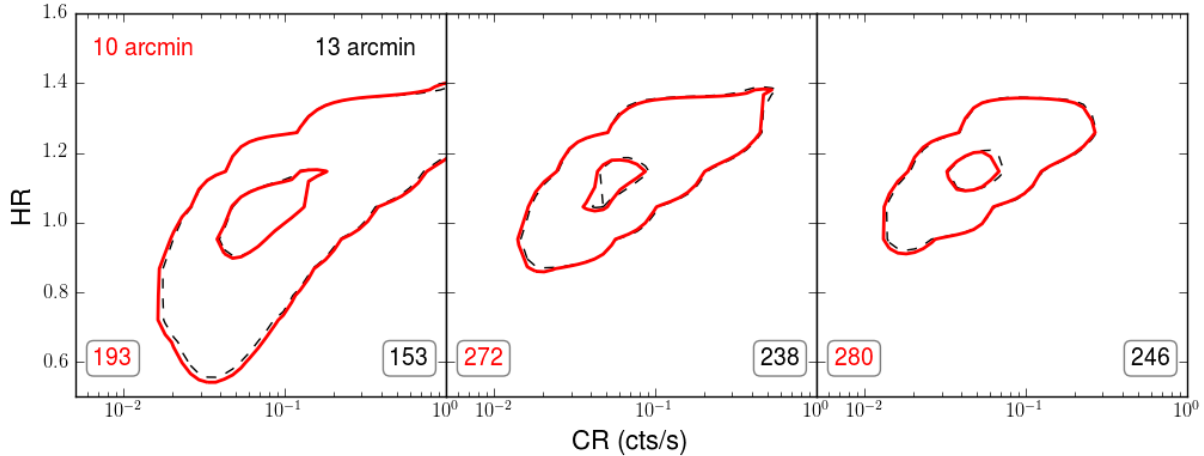


Figure 4.6: The effect of implementing two different selection functions. The dashed-black curves show the 30 and 90 percent contours for a selection function based on a maximum XMM off-axis position of 13' while the solid-red curves represent a selection function where the maximum off-axis position is 10'. It is important to recall here that the CR and HR measurements of all clusters are corrected for vignetting effects and for the aperture in which they are measured.

which assumed an unbiased, Gaussian error model with a scatter given by,

$$\sigma_{\text{CR}|\widehat{\text{CR}}} = \sigma_0 \left(\frac{T_{\text{exp}}}{10\text{ks}} \right)^{-1/2} \left(\frac{\widehat{\text{CR}}}{\widehat{\text{CR}}_0 \text{ cts s}^{-1}} \right), \quad (4.6)$$

where CR is the measured count rate, $\widehat{\text{CR}}$ is the ‘true’ count rate, $\widehat{\text{CR}}_0 = 0.03\text{cts s}^{-1}$ and $\sigma_0 = 0.003 \text{ cts s}^{-1}$. These values thus imply a 10 percent scatter for an object with 300 counts in a 10 ks observation and we see that the uncertainty on the number of photons is proportional to \sqrt{N} . Clerc et al. (2012a) validated this model against clusters selected from the XMM-LSS survey (Pacaud et al. 2007).

The hardness ratio depends on two measurements of the count rate in different energy bands. The errors are thus more challenging to model and so the uncertainties are estimated from simulations of many clusters with realistic spectra on a grid of redshifts, temperatures and luminosities. From these simulations, the true count rate in each band is extracted and using these values in Equation 4.6 we calculate the errors on the measured quantities. We can then calculate the uncertainties on CR and HR for a given $\widehat{\text{HR}}$ from these simulated values. The effect of including this in our cosmological code is to spread the number of clusters in each CR-HR bin over a larger area in parameter space. It is performed independently for each redshift interval where the redshift intervals are large enough to account for the redshift uncertainty. The impact of the error modelling on the resultant CR-HR distribution for each redshift interval is illustrated in Figure 4.7.

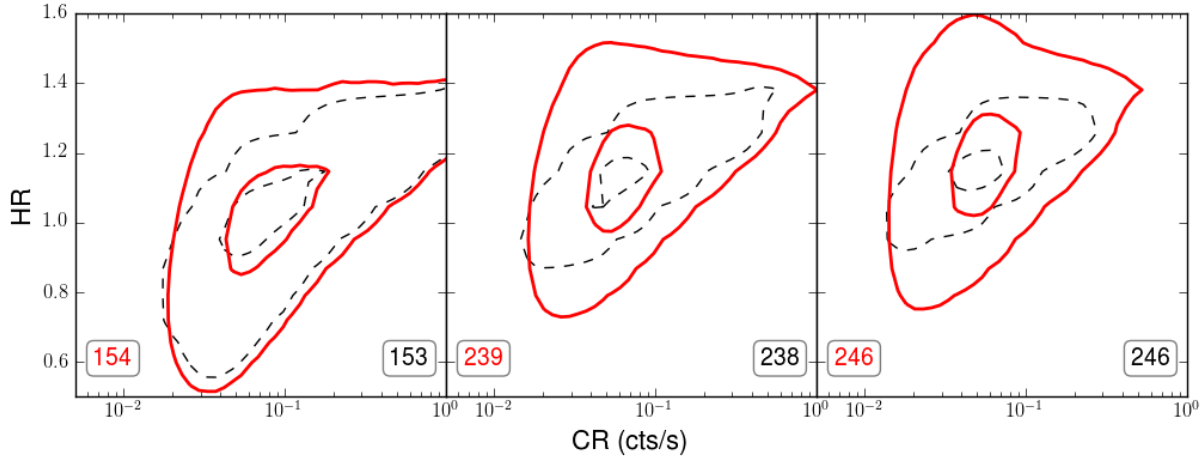


Figure 4.7: The impact of uncertainties in the measurement in CR and HR. The introduction of measurement errors induces a significant smoothing of the resultant CR-HR distributions. As expected, the total number of clusters remains almost identical.

4.4 Parameter estimation

A major motivation for the work presented in the thesis is to constrain a number of cosmological parameters. More specifically, we would like to know which set of cosmological parameters, along with those describing the scaling relations best describe the expected number density of clusters as a function of z , CR and HR. We also wish to understand the uncertainties on each of the constrained parameters. In order to obtain the most accurate constraints we employ a maximum likelihood method.

4.4.1 Cash likelihood

The first requirement to use the maximum likelihood method, is a description of the likelihood. To do this we make use of the Cash C-statistic (Cash 1979) which, in the case of low number counts, provides a useful way of determining how well a given set of data fits the expected distribution. In the original paper by Cash, the statistic was presented in an application for photon counting experiments, such as in the X-ray experiments of the time. This provides a nice symmetry between our data and cosmological analysis given that we are also dealing with X-ray data in the low count regime. We show the details of this statistic here. To begin with one must first write down the Poisson probability distribution function,

$$P = \prod_{i=1}^N \frac{m_i^{n_i} e^{-m_i}}{n_i!}, \quad (4.7)$$

where m_i is the expected number counts in a given bin i , and n_i is the observed number count in that bin. In general, the parameters that maximise the value for P are not the true set of parameters since the maximum likelihood is just a statistic. It is thus more

useful to generate the confidence intervals before one can interpret the results. To do this, Cash defined the statistic,

$$C = -2 \ln P = -2 \sum_{i=1}^N (n_i \ln m_i - m_i - \ln n_i!). \quad (4.8)$$

Since the confidence interval will involve a subtraction of two implementations of the above statistic with different parameters, we can drop the last term $\ln n_i!$, since it is independent of the parameters. Now, writing $M = \sum m_i$ as the overall expected model we arrive at,

$$C = 2 \left(M - \sum_{i=1}^N n_i \ln m_i \right). \quad (4.9)$$

In our case, we are dealing with a relatively small number of clusters with a strong, centralised peak in the number density and tailing off steeply around the edges of the CR-HR parameter space. It is thus likely that with a uniform (or even logarithmic) binning of the CR-HR space, there will be many empty bins. It would not make sense to use a very coarse binning to ensure that there were counts in each bin as this would result in the loss of a lot of information and make the task of parameter estimation far more difficult. Instead, since the bins can be picked in an almost arbitrary manner, one can in principle take a very fine binning such that n_i is either zero or one. In this case, the Cash statistic becomes,

$$C = 2 \left(M - \sum_{i=1}^N \ln I_i \right), \quad (4.10)$$

where we have replaced $m_i = I(\mathbf{x}_i)d\mathbf{x}$ for an arbitrary parameter system $\mathbf{x} = (x_1, x_2, x_3, \dots)$ and resultant the terms involving dx vanish exactly when calculating the confidence interval ΔC since they are independent of the parameters. The summation is now only over all measured counts.

In our case we have binned our observable distribution into CR and HR and thus obtain,

$$\ln \mathcal{L} = \sum_i \ln \left(\frac{dn}{dCRdHR}(\text{CR}_i, \text{HR}_i) \right) - \int_{\text{CR}_{\min}}^{\text{CR}_{\max}} \int_{\text{HR}_{\min}}^{\text{HR}_{\max}} \frac{dn}{dCRdHR} dCRdHR, \quad (4.11)$$

The sum in the above equation runs over all selected clusters and the integral (calculated over the $C1^+$ selection criteria i.e., with $0.009 < \text{CR} < 0.5$ and $0.05 < \text{HR} < 2.0$) gives the number of clusters expected to be within the CR-HR region. These distributions in CR-HR space should include the effects of the pointing bias and the modelling of measurement errors.

4.4.2 Markov Chain Monte Carlo sampling

In a typical cosmological study, such as the one presented in this thesis, one is interested in fitting a number of parameters simultaneously. The parameters that one could think

of fitting include the six base parameters describing a Λ CDM model, along with those describing the scaling relations and their evolution. In order to recover the maximum likelihood set of parameters, one could naively break up the parameter space into a large N -dimensional grid, where N is the number of parameters, and then determine the likelihood at each point on the grid. If it is computationally expensive to calculate the likelihood, the number of times it would need to be calculated becomes prohibitively large. This is because the number of grid points scales as D^N where D is the number of bins for each parameter. So even if the time to calculate the likelihood is 1s, it would take ~ 37 computing days to finish the sampling of 6 parameters with moderate resolution of 20 bins. For our study, calculating the likelihood for a given set of parameters takes around 120s so this would clearly not be feasible. The problem with this naive sampling method is that all parts in the parameter space are uniformly sampled, including those that have an incredibly low likelihood of being the ‘true’ set of parameters we are seeking. A more effective way to sample the parameter space is to distribute samples over regions of high likelihood rather than spending any time in the low likelihood regions. In this way, one can greatly diminish the number of samples needed. One of the ways in which this is usually done is through Markov Chain Monte Carlo (MCMC) sampling.

MCMC algorithms are designed to sample the posterior probability distribution function (PDF) to provide an approximate sampling distribution, even in high dimensional parameter spaces. Such sampling analyses have been useful to numerous studies in astronomy and cosmology, perhaps most notably in deriving cosmological constraints from CMB observations. An important advantage that Bayesian methods of data analysis have is that one can marginalise over nuisance parameters, i.e parameters which we are not interested in constraining but which affect the model that generates the data. By doing this, we are able to integrate over all possible values of the nuisance parameter and thus include the effects of its uncertainty in the results obtained for the parameters of interest. An MCMC generated set of samples of the model and nuisance parameters automatically provides sampling values of the model from the marginalised PDF. Since our likelihood calculation is rather computationally expensive, it is crucially important to have an efficient mechanism for sampling the posterior PDF so that it does not take too many functional evaluations before a statistically independent sample is selected.

In an MCMC algorithm, the goal is to sample the posterior probability density,

$$p(\Theta|D) = \frac{p(\Theta)p(D|\Theta)}{p(D)}, \quad (4.12)$$

where $p(\Theta)$ is the prior distribution, $p(D|\Theta)$ is the likelihood function and $p(D)$ is the normalisation. Here, Θ are the parameters affecting the probability distribution and D are the observed data points. The prior distribution includes any information already known about the parameters in question. For example one could include priors on Ω_M from an independent CMB analysis in a cosmological analysis based on galaxy clusters. One can also use uninformative priors which do not really contain any information on the parameters but serve to ensure that the sampler does not enter unphysical areas of the parameter space which would waste time and possibly even prevent the chain from

converging to the correct location. The likelihood function should be relatively easy to calculate although this is where the bulk of the time in an MCMC run is spent. The normalisation, $P(D)$, is independent of the parameters Θ and so it is not necessary to calculate it which is a tremendous boon as it is generally computationally very expensive.

Constraints on a given parameter can be approximated by creating a histogram of the samples in the subspace spanned by that parameter and the expectation value can be found by averaging over all accepted samples. In general, it is a non-trivial process to generate samples. A MCMC sampler creates a random walk through the parameter space and over a significant number of steps draws a representative set of samples. In particular, each step in the walk depends only on the position of the previous step.

Metropolis-Hastings method

The most common MCMC algorithms used to date have been based on the Metropolis-Hastings method. This algorithm works by calculating the likelihood \mathcal{L} at the current point in the parameter space and then performing a second calculation \mathcal{L}' at a prospective next step. The sampler moves to the next position if the ratio $R = \mathcal{L}'/\mathcal{L}$ is larger than a randomly drawn number $r \in [0, 1]$. So we see that we always move to a point that has a higher likelihood and there is a chance to either move or stay at the same position depending on R and r .

After some time the chain will have converged to a region of high likelihood and the points that have been accepted represent a statistically independent sampling of the posterior PDF. The term ‘converge’ is perhaps misleading, and often used incorrectly, in that, it is not the chain itself which converges to a single value, since even once it is at the most likely position there is always a chance that it can step to a point of lower likelihood. Instead, it is the mean of the samples that converges to a final value or rather, the distribution of samples converges to the final posterior probability distribution function.

One of the drawbacks of this method is the fact that even though after a substantial number of steps the samples follow the posterior PDF correctly, a set of nearby samples might be correlated and not reflect the distribution. In this case, the samples must be ‘thinned’ by selecting only every n -th sample. Another problem is that even if the sample set finally converges to the correct distribution, it can take some time to reach the area of high likelihood and the first samples may follow a very different distribution. It is thus necessary to drop the first samples during what is called a ‘burn-in’ period. Both of these issues lead to the throwing away of samples which required a significant computational investment and represents a large amount of real-world computing time. This is often an unacceptable compromise.

Affine invariant ensemble sampler

Ordinary MCMC algorithms such as the Metropolis-Hastings method have a variety of tuning parameters that need to be adjusted depending on the problem at hand. One such parameter is the step size between the current position of the MCMC chain and the next

proposed point. There is no one-size-fits-all step which would be applicable to all distributions of interest. For instance, consider a probability density $\pi(x)$. The step size which works for this distribution would likely not work particularly well for the scaled probability density $\pi_\lambda(s) = \lambda^{-n}\pi(\lambda x)$ if λ is very large or very small. Christen & Fox (2007) introduced a method for sampling the probability density independently of the scale or aspect ratio of anisotropic distributions by making use of an affine transformation. An affine transformation maps variables x to y through the invertible transformation $y = Ax + b$. This implies that if X has a probability density $\pi(x)$, then Y has a probability density $\pi_{A,b}(y) = \pi_{A,b}(Ax + b)$. Later, Goodman & Weare (2010) proposed an affine invariant ensemble sampling algorithm whereby a large ensemble of ‘walkers’ is evolved simultaneously. This algorithm outperforms the Metropolis-Hastings algorithm significantly. The proposal distribution for each walker then depends on the position of all of the other walkers. The process of updating a given walker X_k is performed by selecting another walker X_j from the ensemble at random. The new position is then,

$$X_k \mapsto Y = X_j + Z[X_k - X_j], \quad (4.13)$$

where Z is a random variable. Effectively what we have done is selected a point somewhere along the vector connecting X_k and X_j , where the distance to the new point is scaled by the random variable Z , which itself depends on a scaling parameter that needs to be set initially. This is called the ‘stretch move’ and is illustrated in Figure 4.8. This process can be easily parallelized, greatly increasing its real-time computational efficiency. One cannot however evolve all walkers simultaneously but rather the walkers must be split into two complementary ensembles. We can then evolve all of the walkers in the first ensemble relative to those in the second ensemble and thereafter, use the newly updated position of the first set to evolve the second. For our study, we used this method, as implemented by the publicly available Python package `emcee` (Foreman-Mackey et al. 2012). This is an excellent implementation of the above described algorithm and allows for the use of hundreds of walkers and CPU cores in parallel. We illustrate the simultaneous evolution of these walkers in Figure 4.9.

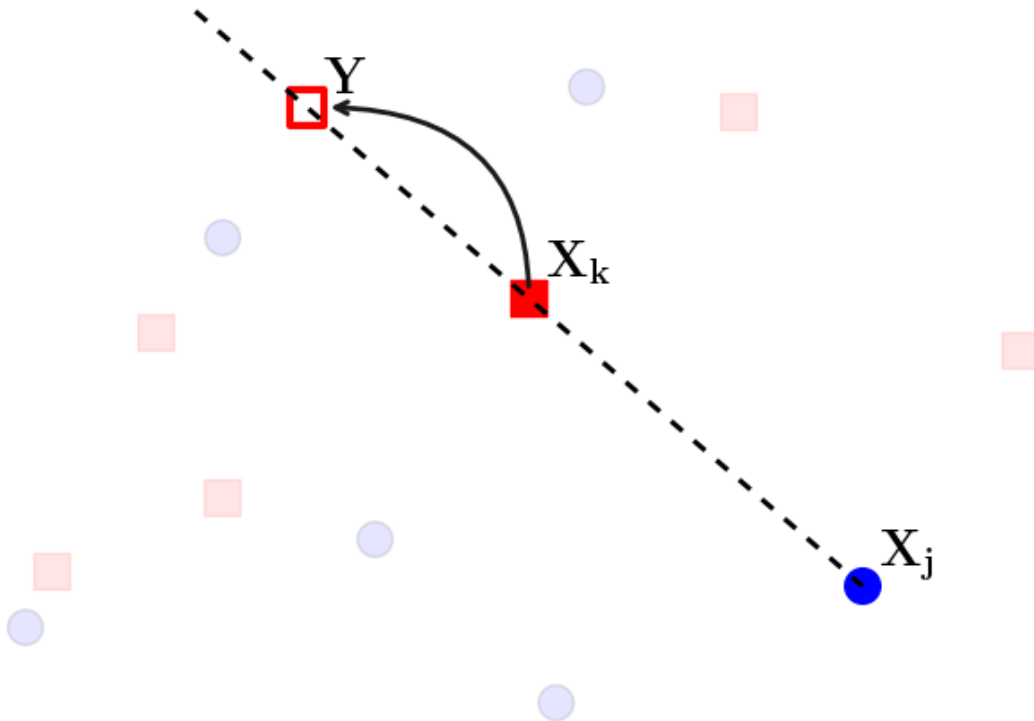


Figure 4.8: An illustration of the ‘stretch’ move. Here, the blue circles and red squares represent two population ensembles of walkers as implemented by `emcee`. A walker from the first population X_k is moved to a new position Y , which lies along the straight line connecting X_k and X_j , a randomly selected walker from the second population represented by blue circles, i.e., $Y = X_j + Z[X_k - X_j]$. In principle, Z can be either greater or less than one and so it is also possible that X_k moves towards X_j . Once all walkers in the population of red squares have been stepped forward, the blue circles are evolved based on their new positions.

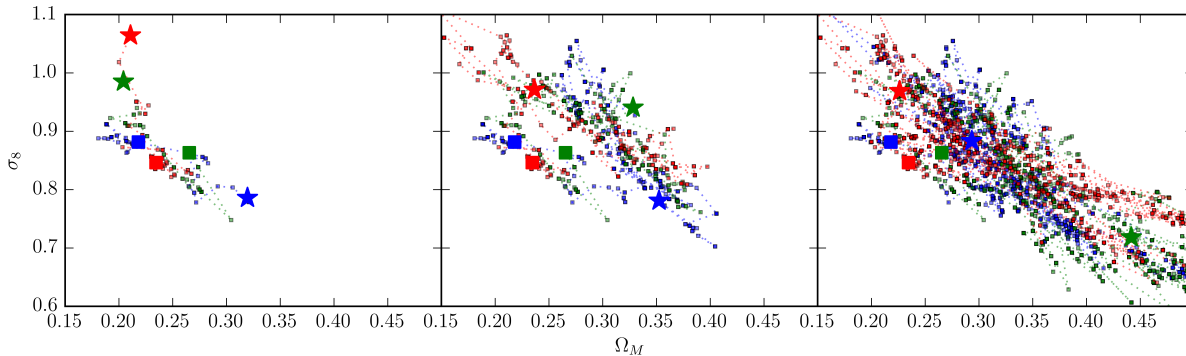


Figure 4.9: An illustration of the walkers making up the ensemble in a MCMC run with `emcee` when fitting Ω_M and σ_8 . The three colour-coded walkers, start their journeys at the points marked by the large squares. Small squares indicated the position of the walker at each successive step and the large stars mark the position of the walkers after 50 (left), 250, (middle) and at the end of the run after some 850 steps (right). We see that although the walkers have not ended up at the same location, they have ended up with similar sampling distributions, each representative of the posterior distribution of the parameters in question

4.5 Verification and testing

In order to verify that we are able to accurately recover a given cosmological model from our data, we test the full chain of our analysis pipeline. We do this by running our code on mock data sets. As much as possible we attempted to keep this testing as blind as possible, i.e. with as little interaction between the person creating the simulated data and the person running the analysis. Here, we describe the process of the mock creation and show the results of our testing.

4.5.1 Mock creation

All mocks were created based on a single, hypothetical XMM 10 ks pointing characterised by a hydrogen column density of $n_H = 3.0 \times 10^{20} \text{ cm}^{-2}$, a background of 2.0 cts s^{-1} and the THIN1 filter on each detector. Our cosmological code calculates the number of clusters per square degree and then multiplies it by the relevant area for that pointing. We can thus freely specify the area to any value we choose without affecting the statistical distribution of mock clusters. Preliminary testing was performed assuming an area of either 100 or 10,000 square degrees. The larger area survey ensures that the resulting cosmological fits are not dominated by Poisson noise thus giving a good indication that the input cosmological parameters were recovered. We began by assuming a hypothetical cosmology and the parameters that were to be tested kept hidden from the person running the MCMC. This ensures that the results are not biased by some prior knowledge of the cosmological parameters.

The chosen cosmological parameters were used to model the expected z-CR-HR distri-

bution of clusters as discussed in Section 4.3. Since a large amount of the computational time of this calculation is spent in pointing dependent process, we simplified our mocks to be drawn from a single, hypothetical pointing and adjusted the area depending on the type of experiment we wished to simulate. This z-CR-HR structure is then broken down into a number of redshift slices and each slice is treated independently. Integrating the resulting CR-HR distribution for each redshift slice gives the number of clusters of a given redshift that would be expected from the given cosmology and selection function. For each redshift slice we then randomly extracted a Poisson realised number of samples from the resulting CR-HR probability distribution to create a mock catalogue where each sample had a redshift, count-rate and hardness ratio. We tested multiple sampling algorithms to extract the mock catalogue and ultimately chose to use `Pandas`, a Python implemented numerical package developed for statistical analyses of large datasets.

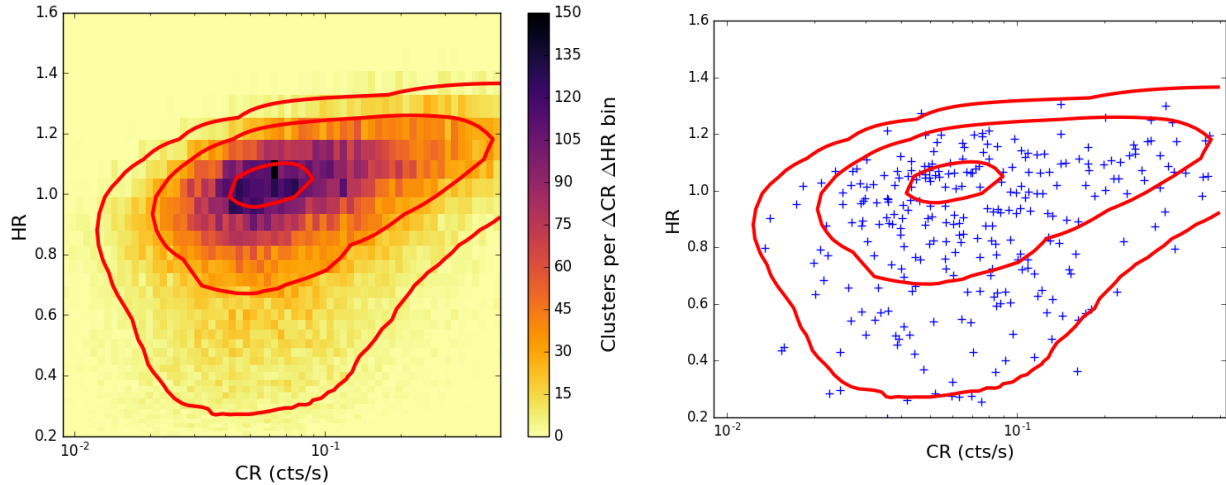


Figure 4.10: The distribution of ‘fake’ clusters drawn from a model z-CR-HR diagram for a 10,000 square degree survey (*left*) and a 100 square degree survey (*right*). The contours are drawn from the model distribution and represent the expected 10, 68 and 95 percent enclosing regions.

4.5.2 Testing the MCMC algorithm on mocks

Multiple realisations of the same fiducial cosmology for a given pointing were created and tested simultaneously to ensure that the input cosmological model was consistently recovered accurately and not just by chance. Although rather time-consuming in both real and computational time, this testing helped to uncover numerous bugs in the code and assisted in the resolution of a number of numerical issues introduced by inaccurate interpolators or integrators.

We focused on two kinds of hypothetical X-ray surveys in our testing. The first type of experiment we considered was representative of the analysis we had planned on real data,

that is, deriving cosmological constraints from the X-CLASS/GROND cosmological cluster sample. For these tests we assumed an area of 100 square degrees to a depth of 10 ks with XMM-Newton (roughly equivalent to our catalogue). After some preliminary testing we found that there was a significant statistical variation in the recovered parameters. This variation was not significant enough that it was more than the variation one could expect from a Poisson point process. However, since we wished to ensure that our algorithm would converge very precisely to the correct input cosmology we decided that attempts to reduce the statistical errors by increasing the survey size.

To this end, we considered a second type of experiment covering 10,000 square degrees. The reason for this is that we wanted to have a large enough number of mock clusters that we would not be dominated by Poissonian fluctuations and could thus thoroughly test the internal mechanisms of our analysis pipeline and the internal consistency of our testing processes.

The initial testing process involved two people, myself and a visiting Masters student, Jonathan Sanner from Ecole Polytechnique. The creation of mock catalogues was performed by me, and these were then handed on to Jonathan without any indication of the actual values of the cosmological parameters that we were trying to constrain. All values not under testing were kept to their fiducial values. He would then run the MCMC until it had converged to some result and only then were the input cosmological parameters unveiled. This ensured that the MCMC code could not be developed with a specific result in mind and should thus perform well in general.

The results from a test performed on a mock X-CLASS like survey covering 100 square degrees are shown in Figure 4.11. For this test we assumed the cosmological parameters derived by Clerc et al. (2012b) and attempted to recover those same parameters. Due to the relatively low number of clusters in such a sample (~ 250 clusters), we decided on relatively thick redshift slices to ensure a good sampling of each respective CR-HR distribution. For future surveys, both with an extended X-CLASS covering the full extra-galactic sky and all recent XMM pointings; and eROSITA, which will detect $\sim 100,000$ galaxy clusters, a considerably finer binning scheme could be envisaged. Clerc et al. (2012a) showed that the constraining power of the z -CR-HR method peaks with clusters binned into redshift bins of size $\Delta z = 0.01$. Such an accuracy can be expected for photometric redshifts derived from large optical surveys such as SDSS and DES.

The results obtained from this test are all consistent to within 1σ with the input cosmology. For σ_8 , γ_{MT} and $X_{C,0}$ the improvements from adding redshift information is small. The constraints the remaining parameters are however more significantly tightened, particularly those obtained for γ_{LT} . This is consistent with the results of Clerc et al. (2012a) who performed a similar test with a Fisher matrix analysis and pushing to finer redshift binning schemes.

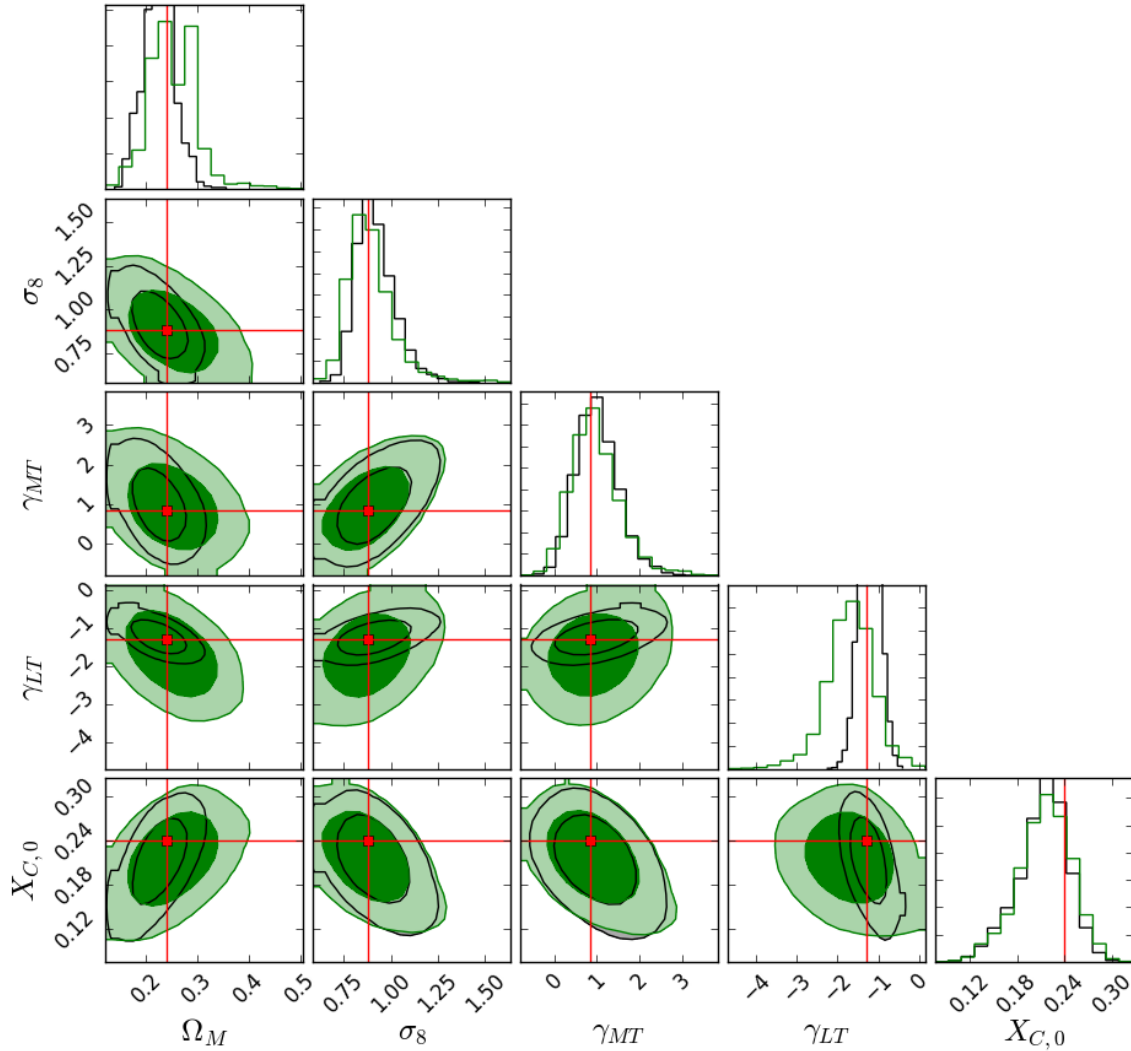


Figure 4.11: The recovered posterior distributions for a run of the MCMC code on a mock catalogue. The green contours indicate the case where redshift information was not considered. The overlaid-black contours represent the distribution recovered when binning clusters by redshift into 3 bins ($0.05 \leq z < 0.32$, $0.32 \leq z < 0.53$ and $0.53 \leq z < 1.32$). The input values are indicated by the red lines. Most parameters show minor improvements with this binning scheme however, clear improvements are already seen in the constraints on Ω_M and γ_{LT} .

4.6 Cosmological analysis of the X-CLASS/GROND catalogue

The ultimate goal of this thesis was to derive cosmological constraints from a sample of X-ray selected galaxy clusters; specifically, to improve on the results of Clerc et al. (2012b) by taking advantage of the photometric redshifts obtained with GROND.

4.6.1 Consistency test with the full X-CLASS C1⁺ sample

The first data on which we tested our cosmological code was the entire X-CLASS C1⁺ catalogue, extending over the whole sky. This is the identical sample to that was used in the previous study and so provides a useful reference to ensure the consistency of our results. Our MCMC algorithm was designed from the outset to run on observable files i.e., those containing all of the relevant information about the clusters in the sample such as z , CR and HR, as well as the bias from pointed observations; and so it was easy to adapt the configuration to move from running on mock data to real data.

The analysis of Clerc et al. (2012b) started with an assumption that the local scaling laws are known *a priori*. There are a number of possible expressions for these scaling laws to be found in various sources of literature and ultimately it was decided to use the scaling relation of Pratt et al. (2009), from now referred to as P09 for the $L-T$ relation and Arnaud, Pointecouteau & Pratt (2005) for the $M-T$ relation (A05). In particular, the P09 relation was chosen because after fixing the cosmological parameters to their values derived from WMAP5, this relation was best able to reproduce the observed number density of clusters as a function of their flux, with data drawn from the REFLEX, 160d, 400d and RDCS cluster surveys when allowing for evolution different from the self-similar expectation. Two scaling laws from P09 were considered, one derived from all clusters in their sample (ALL) and one derived from clusters classified to be **not** cool-core clusters (NCC). A critically important parameter to the number of observed clusters is the scatter on the $L-T$ relation and some liberties were taken in the choice of this value in that scatter measured for each of the two samples were applied freely to the other relation. It turns out that the best-fitting model required the normalisation and power-law slope from the NCC relation and the scatter from the ALL relation.

Once the local scaling law was chosen, the focus shifted to constraining the cosmological parameters. This included Ω_M and σ_8 along with the evolution of the $L-T$ and $M-T$ scaling relations and the parameter $X_{C,0} = r_c/R_{500c}$. This parameter relates the core radius to the radius at which the average density of the matter enclosed is 500 times the critical density of the universe. It is critically important since the core radius of the clusters strongly influences the selection function. Many previous studies assume a fixed physical size for the core radius while we allow it to be a free parameter. The results of our MCMC analysis are shown in Figure 4.12 as green contours. We used this analysis as our starting point for testing on real data with the same set of cosmological parameters and scaling relations to perform our own MCMC analysis. The results we obtained are shown

Table 4.1: The results obtained by Clerc et al. (2012b) compared to the results obtained for the MCMC analysis performed for this thesis. Values quoted are the median values of the MCMC chains and the errors are such that they contain 68 percent of the samples obtained by the MCMC algorithm.

Parameter	Clerc+12	Ridl+17
Ω_M	$0.24^{+0.04}_{-0.09}$	$0.23^{+0.05}_{-0.04}$
σ_8	$0.88^{+0.10}_{-0.13}$	$0.87^{+0.08}_{-0.07}$
γ_{MT}	$0.83^{+0.45}_{-0.56}$	0.77 ± 0.35
γ_{LT}	$-1.3^{+1.3}_{-0.7}$	$-0.99^{+0.6}_{-0.7}$
$X_{C,0}$	0.24 ± 0.04	0.25 ± 0.03

alongside the contours derived by Clerc et al. (2012b) and we notice an excellent overlap in the obtained constraints, summarised in Table 4.1.

Interestingly the 68 and 95 percent confidence interval for our more recent analysis are considerably smaller than those obtained by the prior work. This could be due to an insufficient number of steps taken by our MCMC simulation to accurately fill the wings of the posterior distributions or could be a feature of the different Monte-Carlo samplers that were utilised in this analysis. We have found that the likelihood calculations between the IDL code used by C12 and the Python code used here are accurate to within ~ 0.6 percent when dealing with a single pointing and to within ~ 2.7 percent when running on the compressed list of 60 pseudo-pointings so it is unlikely that this influences the results to the level seen in Figure 4.12.

We notice that there is a strong degeneracy between many of the parameters, indicated by highly elliptical contours, most noticeably in the relationships of all parameters with σ_8 . We see that this introduces some complications later on in our analysis of the X-CLASS/GROND sample.

4.6.2 Analysis of the X-CLASS/GROND sample

The next step in our analysis was to recover the same set of cosmological parameters from the X-CLASS/GROND catalogue, a slightly smaller sample of 265 galaxy clusters (compared with 347 used previously), with as similar input parameters as possible. Our sample potentially has a less secure selection function due to the fact that for the analysis of C12, only the inner 10' of each XMM pointing was utilised for the detection of sources whereas our sample extends this to 13' where the sensitivity of XMM decreases considerably. This means that fewer clusters are detected per square degree and sources detected in the outskirts of the XMM pointing are less well characterised due to the smaller number of detected photons and the distortion of the shape due to the degraded PSF. The reduced number of clusters also affects the bias that is introduced from pointed observations as the statistics in each CR bin in which it is calculated. The lower sensitivity of the 13'

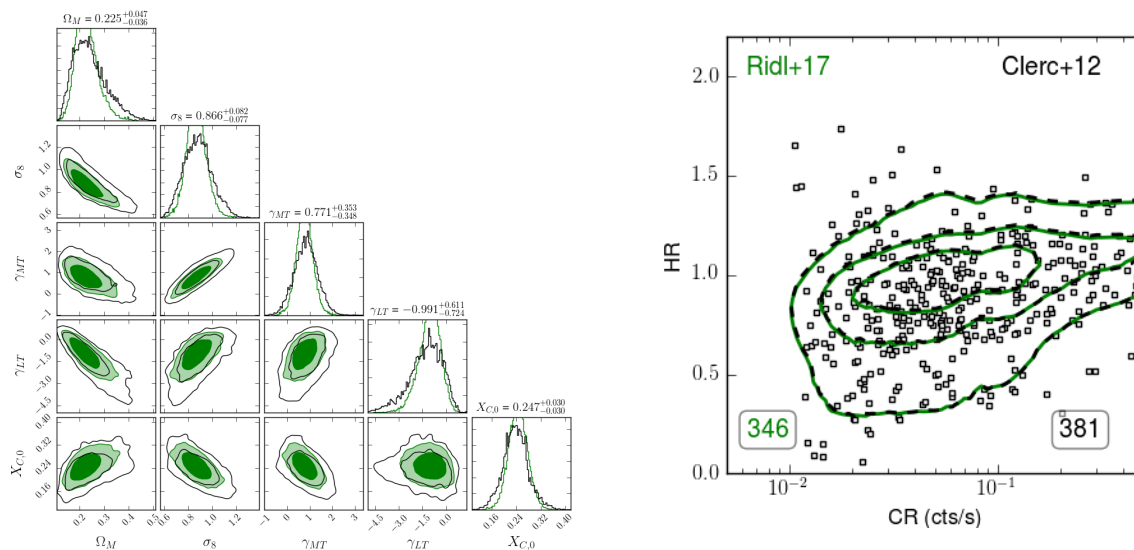


Figure 4.12: *Left*: The black contours indicate the 68 and 95 percent confidence intervals derived from the output MCMC chains of C12, making use of the entire X-CLASS C1⁺ cosmological sample of 347 galaxy clusters. The green, filled regions indicate the sample confidence intervals derived from the analysis presented in this thesis. We notice a very good agreement between the best-fit values with the new confidence intervals overlapping completely with those of C12, although with considerably smaller scatter. *Right*: The predicted distribution of clusters with CR-HR derived and the total number of clusters expected from the C12 (black) best-fit parameters and those derived from our analysis (green). We notice the good agreement of both sets of parameters with the number of clusters, shown for each set of parameters in the bottom right and left respectively.

survey (from now called the ‘full survey’) also impacts the bias and as we will see, it likely influences the results that are obtained.

To make a better comparison with the C12 analysis, we consider a reduced survey based only on the inner 10’ of the XMM pointings (from now referred to as the ‘inner survey’) and we are thus able to use the same selection function and remove the effects of its variation from our comparison. This sample consists of 211 clusters. We did introduce a small change into the analysis in that we made use of the photometric redshifts acquired from GROND to select only clusters with $0.1 < z < 0.81$. This was done to remove very nearby clusters whose X-ray emission is often contaminated by emission from the BCG, as discussed in Chapter 3.

Single redshift bin

As a first step, we consider all clusters to be in a single redshift bin ranging from $0.1 < z < 0.81$ to ensure that firstly, we are able to recover the similar constraints as to those obtained for the C12 sample and secondly, in order to quantify the value that having redshift information adds to strengthening our constraints. The results that we obtained from an analysis of the samples of the posterior distribution extracted by our MCMC algorithm are shown in Figure 4.13 where we have considered both the inner and full surveys.

We notice that there is significant tension between the constraints derived for both surveys when compared to the analysis of C12 and our own analysis of their sample. This is somewhat concerning as one would naively expect to find similar results given that there are not a lot of differences in either the samples used or the methods of analysis. In fact, our method remained completely unchanged when moving from the C12 sample to the X-CLASS/GROND catalogue. The biggest difference introduced for the more recent analyses was in the modelling of the bias factor. It is particularly illustrative to compare the recent results with a test that was performed prior to the recalibration of the bias whereby only clusters with $0.1 < z < 0.81$ were selected but the bias model of C12 was used when making the predictions for the number of expected clusters in each CR-HR bin. These results are shown in Figure 4.14, alongside an illustration of the changes in the bias model for the various samples. Interestingly, we note that these constraints agree considerably better with the C12 results than the ones described in Figure 4.13. This indicates that there could be an issue with the latest bias models and this will require further investigation. Also, the differences between the bias models are particularly striking at high-CR where most of it disappears in the X-CLASS/GROND surveys with the cut in the redshift range having the largest influence. I note that no test has yet been performed on the 10’ survey with all clusters selected which is the catalogue with the most similar bias model to that of C12.

A possible explanation for the influence of this changed bias has on the derived constraints in Figure 4.13 could be as follows. The lower expected number density of high-CR clusters can be accounted for by adjusting the normalisation of the $M - T$ relation upwards. The parameter that can be responsible for this in our analysis is the evolution of

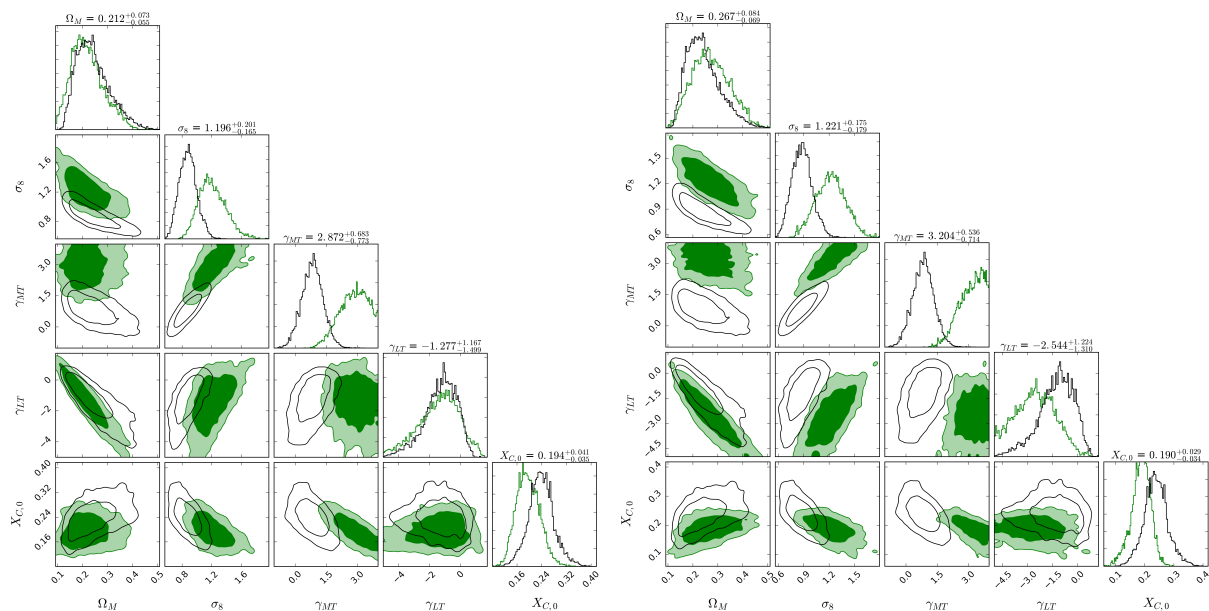


Figure 4.13: The recovered posterior distributions based on an MCMC analysis of the inner (left) and full (right) surveys. The results obtained in our analysis are shown as the green contours and the results of C12 are indicated by the black contours. We see no significant difference between the results obtained for the two surveys although there is tension between both surveys and the results obtained by both C12 and our analysis of that sample. The tension is slightly smaller for the inner survey, which could be explained by the greater similarity between this data and that of C12. The most significant tension comes from constraints for σ_8 and γ_{MT} . These two parameters are highly degenerate with each other. This is because a high value for σ_8 causes the number of clusters forming in the Universe to be greater, particularly at high redshifts. This necessitates a high value of γ_{MT} as it reduces the number of objects that fall into the range of detection dictated by the selection function. This is illustrated in Figures 4.2 and 4.4.

the $M - T$ relation and so it is driven to values exceeding those of C12.

This is due the steepness of the halo mass function at high masses where clusters have typically higher CR. An increase in the normalisation of the $M - T$ relation has the effect of lowering the measured CR for a given cluster. Since there are relatively few clusters with CR higher than the limit of our sample, only very few clusters are shifted into our detection window. Conversely, many clusters with lower masses would have their CR shifted to values outside our detection limits. Since there are many more of these low-mass clusters, the overall number of clusters decreases. To compensate for this decrement in the number of clusters, one needs to increase σ_8 , which disproportionally adds clusters at high redshifts. To offset this, the other three parameters are more marginally adjusted in order to give an expected number density of clusters that matches what we have observed and included in our catalogue.

More investigation is needed to fully understand the processes affecting our results. Nevertheless, the constraints derived thus far (although in significant tension with cosmological constraints presented from various studies such as CMB, BAO or other cluster related works) are a promising start to the cosmological analysis of the X-CLASS/GROND sample.

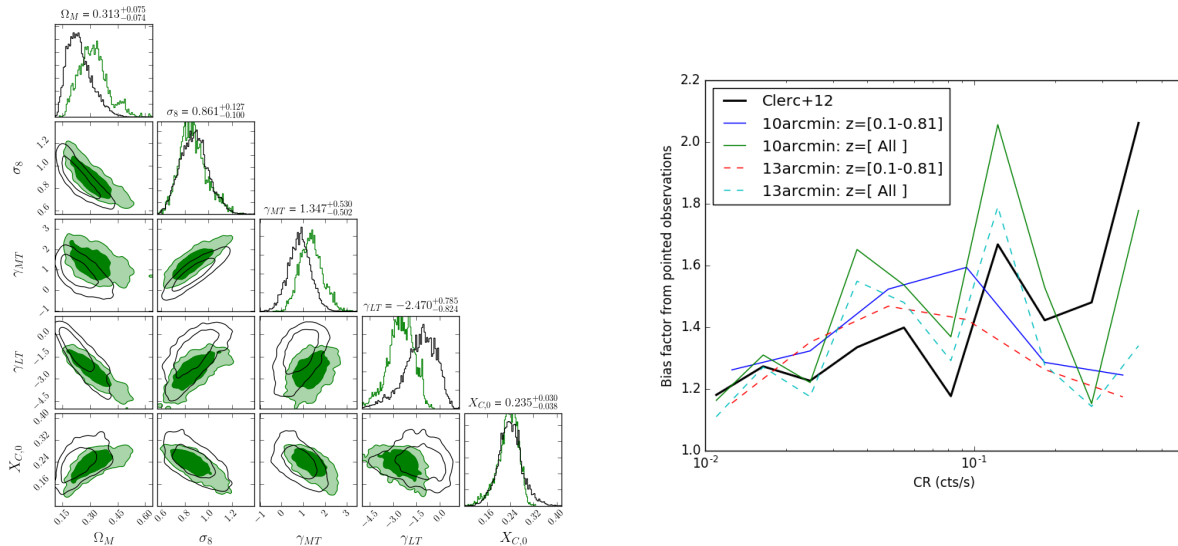


Figure 4.14: *Left*: The constraints obtain by combining the redshift selection $0.1 < z < 0.81$ with the bias model used by C12 and in our analysis of their sample. These constraints are not in tension with the results based on the previous sample, providing an indication that there might be an issue with the bias modelling for the more recent work. *Right*: The bias factor for a variety of surveys. Shown here are the bias factor from C12, and for the X-CLASS/GROND sample containing the entire sample and only those with $0.1 < z < 0.81$; and for both the inner and full surveys. I highlight the high-CR regions where all subsequent samples have considerably lower bias values that the C12 values.

Three redshift bins

By performing a Fisher analysis based on a hypothetical XMM survey, Clerc et al. (2012a) showed that having knowledge of cluster redshifts can add significantly to the constraining power of the z -CR-HR method. The impact on the cosmological parameters Ω_M and σ_8 is low with only marginal improvements expected in the constraints derived since these parameters depend mostly on the local cluster abundance and are already well constrained without redshift information. For the dark energy equation of state w_0 however, the constraints were shown to improve dramatically (by a factor 5) with measured redshifts of a high enough precision to allow a binning width of $\Delta z = 0.1$. Further the constraints on the evolution of scaling laws also showed large improvements, particularly for the $L - T$ parameter which improves by a factor 3 with the same redshift binning.

To this end we launched an investigation into how well we could further constrain the five parameters included in the case of a single redshift bin. Probably the biggest challenge to the introduction of cluster redshifts is to accurately calibrate the pointing bias due to the reduced number of clusters from which the bias is calculated. One would naively expect that this bias would depend on redshift and as we saw in Figure 4.5 this is indeed the case. In particular, the uncertainty on the bias in the low-CR regime of the two low-redshift intervals is high, indicating that this value is poorly constrained while in the high-redshift interval, we have a comparatively large bias and uncertainty. The value computed for the bias in this regime is particularly concerning since it boosts the number of expected high redshift clusters dramatically and this could strongly influence the constraints derived for the evolution of the scaling laws in particular.

We decided on a redshift binning scheme so that there were roughly an equal number of clusters in each bin, and the number of bins was chosen to ensure that the bias factor from pointed observations could be calculated for each bin with at least 6 CR intervals. The binning scheme finally decided on was $0.1 \leq z < 0.32$, $0.32 \leq z < 0.52$ and $0.52 \leq z < 0.81$, containing 75, 79 and 67 clusters respectively.

The predicted CR-HR distributions are then calculated for each redshift interval independently and these are compared to the observed cluster distribution. The computation of the likelihood is performed in the same way as previously for each redshift bin. This includes the introduction of the error model (which we assume to be independent of redshift), and taking into account the pointing bias, which is predetermined for each redshift slice. The log-likelihood's for each redshift slice are then added to one another to give the total likelihood for the set of parameters in question.

The results of the z -CR-HR analysis for the same five parameters considered throughout this chapter are shown in 4.15. As with the case involving no redshift information, we notice a significant level of tension with the results obtained by C12.

4.6.3 Looking forward

There is still a substantial amount of work to be completed before our efforts are able to produce reliable results consistent with the prevailing model of our times Λ CDM. Apart

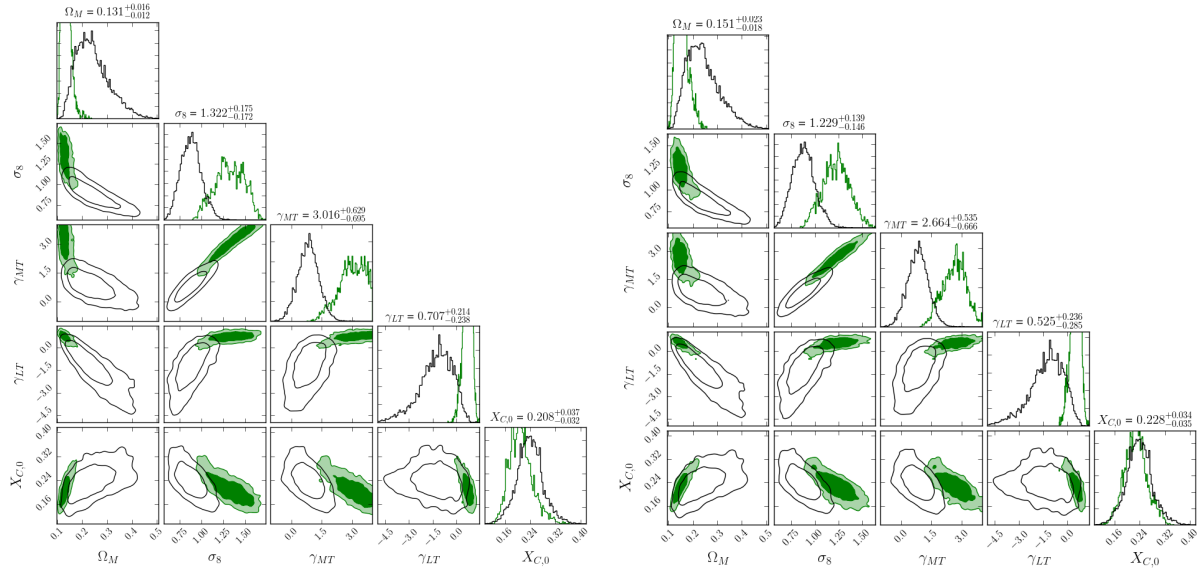


Figure 4.15: The recovered posterior distributions based on an MCMC analysis of the inner (left) and full (right) surveys when including information about the cluster redshifts. Both the inner and full surveys display similar levels on tension with the previous analyses.

from working to improve our modelling of the pointing bias, which appears to be a limiting factor in the current analysis, there are numerous ways in which our results can be improved.

As a starting point, it would be logical to utilise the more modern and recently published $L - T$ and $M - T$ scaling relations derived from the XXL collaboration (Giles et al. 2016; Lieu et al. 2016). These scaling relations should more accurately represent the X-CLASS cluster catalogue due to the similar depth, and detection and analysis pipelines used for source characterisation. As discussed earlier, the introduction of new scaling relations into our cosmological code can be somewhat non-trivial as a significant amount of testing is needed to ensure that they accurately represent the sample on which the cosmological tests are being performed and to ensure that a sensible value of the scatter is implemented. To do this, one would ideally leave the scatter as a further free parameter and try to constrain its best-fit value along with the normalisation, power-law slope and evolution of the scaling relation. Also, since the XXL $L - T$ relation already contains constraints for its evolution, this would allow for a deeper analysis of the $M - T$ relation. Of particular interest could be a study focused on constraining the normalisation of this relation with a deviation from the expected value hinting at a possible mass bias, such as that introduced by the assumption of hydrostatic equilibrium. Such a mass bias is required to partially resolve the tension between the constraints derived from the Planck CMB and clusters and our methods could provide an independent avenue in which this critically important issue can be investigated.

Another interesting study would be to try to remove the impact of the pointing bias by considering only an annulus between $5'$ and $13'$ of the XMM pointings. This of course could introduce a bias of its own, in that the sample of clusters lying within this annulus

would not necessarily represent the overall cluster distribution since large classes of objects such as distant clusters would lose a disproportionate number of objects.

Another currently existing survey in which the pointing bias will be nullified is the XMM-XXL, which covers 50 square degrees in two contiguous extragalactic regions of 25 square degrees each. Further in the future, eROSITA will provide a contiguous survey across the entire sky in which the pointing bias will be completely nullified. Once the all-sky survey is complete, eROSITA will also perform a few years of pointed observations. One could thus also envisage a serendipitous cluster search in these deeper fields, as was done with ROSAT and XMM-Newton, where the pointing bias would once more play an important role in our understanding of the selection function. It is thus important for future work that we are able to accurately quantify this bias and properly account for it.

4.6.4 Summary and conclusions

In this chapter I focused on describing the cosmological analysis that we are currently performing on the X-CLASS/GROND cluster catalogue. After ‘setting the scene’ for cluster cosmology with an extensive review of recent results, I detailed the steps that make up the forward modelling approach that we use to predict the distribution of galaxy clusters as a function of redshift, count-rate and hardness ratio: the z-CR-HR method. I then explained the statistical framework based on Bayesian statistics and Markov Chain Monte Carlo methods that we utilised to obtain the best-fitting cosmological parameters that describe the observed data. Thereafter I proceeded with what is the main goal of this entire thesis: constraining cosmological parameters with galaxy clusters. I demonstrated that with our method and its new Python implementation, we are able to recover the results of [Clerc et al. \(2012b\)](#), providing a useful validation of our processes and MCMC sampling technique. I then attempted to derive constraints based on the X-CLASS/GROND sample considering the cases where redshift information was available and when it was not. This was done with limited success but there are many positive signs indicating that robust cosmological constraints should be possible in the near future. I investigated possible causes of the tension noticed when comparing our results to those from various other studies and experiments and highlighted possible ways in which our analysis could be improved through the use of more up-to-date scaling relations from XXL and by considering a truly serendipitous XMM survey based on only the outskirts of the XMM pointings existing in the XMM data archive.

Chapter 5

Concluding remarks

5.1 Summary and conclusions

The principle goal of the work presented in this thesis was to use X-ray selected galaxy clusters to obtain constraints on cosmological parameters. The sample of galaxy clusters that was chosen for this purpose was X-CLASS, a serendipitous search for clusters in archival XMM observations. Most of these clusters lacked any kind of prior redshift followup. However, in order to obtain strong constraints on dark energy parameters or the evolutionary parameters of the cluster scaling relations, redshifts are needed (Clerc et al. 2012a). To this end, we conducted a large observational program with GROND, a seven-channel simultaneous imager on the MPG 2.2m telescope at the ESO La Silla observatory. We were able to use the data from these observations to derive redshifts for all but a few of the X-CLASS sample which further allowed for the determination of the X-ray bolometric luminosities and temperatures of these clusters. With the redshifts in hand, we undertook a cosmological analysis based on the z-CR-HR method and despite being unable to obtain reliable constraints on cosmology or the evolution of the scaling relations we showed that, once a few issues are resolved, this method will provide a powerful tool for cluster cosmology analyses. A detailed summary of the work presented in each chapter is given below.

Chapter 1

In this introductory chapter I laid the theoretical foundations on which the work presented in this thesis is built. I begun with an overview of general relativity - Einstein's theory of gravity - and from this showed how it naturally describes a dynamic and expanding universe when applied on cosmological scales. I then explained the cosmological principle, whereby the Universe is considered to be spatially homogeneous and isotropic, and used this to derive the Robertson-Walker metric which describes the (curved) four-dimensional space-time in which our Universe exists. Combining this with the Einstein field equations, I derived the Friedmann equation, which describes the rate of expansion of the Universe, quantified by the Hubble parameter. From these equations I described the cosmic evolution in matter,

radiation and dark energy dominated scenarios, all of which have been prominent at various points in the thermal history of the Universe. I went on to present the observational evidence for an expanding universe, as measured by Hubble in 1929, and introduced the concept of redshift, a topic of great importance in the context of this thesis. To conclude this theoretical background, I discussed the process of structure formation in the Universe and described how all structures that we see in the Universe today grow from small, random density fluctuations in the early Universe. These fluctuations begin to evolve under the influence of gravity and eventually collapse to form the planets, stars, galaxies, clusters of galaxies and even the large-scale structure of the cosmic web that we observe today. I showed how the density fluctuations can be characterised by the mass function and how this can be used to investigate the underlying cosmological model.

Throughout my thesis, studies of clusters across the electromagnetic spectrum have played an important role. I presented an observationally driven summary of how clusters are detected and characterized at various wavelengths with a focus on X-ray detection and measurements and optical cluster confirmation. I presented the physics behind the X-ray emission from the intra-cluster medium (ICM), the hot gas making up most of the baryonic mass of galaxy clusters. The ICM can also be detected due to the effect that it imprints on the background CMB, as photons stream through clusters lying along the line-of-sight. I further discussed how we can use an important optical property of galaxy clusters, namely the red sequence, to derive the redshift of clusters. In addition to the work presented in this thesis, I was fortunate to be the third author on a paper (de Gasperin et al. 2016) which presented one of the first galaxy clusters detected due to its radio emission and it turns out to be the third least massive cluster hosting a radio relic. My contribution to this work was the optical confirmation of the cluster, along with providing the photometric redshift ($z = 0.20 \pm 0.02$), which turned out to match well with the redshift of a well known, nearby cluster, Abell 3527, with a spectroscopic redshift of $z = 0.1983$, meaning that the distance between these two objects is ~ 4 Mpc. Obtaining total cluster masses, including both the baryonic and dark matter components remains a challenge for cosmological cluster analyses and I presented a brief overview of one of the techniques used to do this: gravitational lensing. Gravitational lensing makes use of the distortion and magnification effects that a massive object has on the shape and size of background galaxies, to map the distribution of the total mass. In the case of a cluster, most of this mass consists of dark matter.

To conclude this chapter, I introduced various methods used for constraining cosmological parameters with galaxy clusters. I focused mostly on galaxy cluster number counts and the halo mass function, as these are the most relevant methods to my thesis. I showed how the number of galaxy clusters as a function of mass and redshift varies depending on the parameters of the underlying cosmological model and showed how we can use clusters to differentiate between different models. I also touched on methods involving the spatial clustering of clusters and measurements of the baryon fraction of clusters. Finally, I discussed an interesting concept whereby clusters can be used as standard candles to calibrate the absolute distance scale by making use of a combination of X-ray and SZ observable quantities. I concluded this chapter with a discussion on the systematic errors that enter cluster cosmological analyses, with a focus on observational errors and selection effects.

Chapter 2

I presented the data analysis techniques needed to convert raw GROND data into science quality images from which it was possible to extract well calibrated photometric catalogues of galaxies. This chapter was based mostly on work presented in [Ridl et al. \(2017\)](#). I began the chapter with an overview of the GROND instrument and its technical details such as the *grizJHK* filter system, the pixel scale and the field-of-view of the detectors. I introduced the standard GROND observing blocks and discussed the choices that were made in exposure times, dithering positions and readout modes. Ultimately we decided on four dithering positions with exposure times of 459.6 s or 1476.0 s in the optical bands depending on a rough classification of the cluster redshift based on DSS optical imaging. Preliminary data analysis including bias and dark subtraction, flat-fielding and the removal of fringing effects were performed with the standard GROND data reduction pipeline available at MPE. This is based on the tools of *IRAF/PyRAF*. This pipeline produces astrometrized co-added images and photometric measurements idealised for point sources. Since I was interested in observations of galaxies, which are not point sources, I developed my own tools based on *Swarp*, *Scamp* and *SExtractor*. One of the difficulties of observing with GROND (and indeed any optical instrument with a small field-of-view) is obtaining an accurate calibration of the photometric zeropoints. I finally decided that the most reliable option was, for a given night, to use the photometric calibration of all fields falling within the footprint of SDSS to obtain a master zeropoint for that night and apply this to all observed fields uniformly. Once these zeropoints were available, I created photometric catalogues of galaxies that could be used to derive photometric redshifts based on the red sequence technique. All data was inspected in terms of its quality to ensure that it met the standard required to obtain robust photometric redshifts.

Chapter 3

This chapter was based entirely on [Ridl et al. \(2017\)](#) and has been published in MNRAS with just parts of that paper being discussed in Chapter 2 instead of here. The work presented in this chapter constituted the vast majority of my the time spent during my doctorate. The chapter began with an introduction to cluster surveys with a particular emphasis on XMM surveys such as the XMM-LSS, XMM-XXL and XMM-XCS. I further introduced the red sequence method, used for obtaining cluster photometric redshifts, and described the context of this work: the creation of a cosmological sample of galaxy clusters from archival XMM data.

I presented an overview of the XMM Cluster Archive Super Survey (X-CLASS). Much of this overview was drawn from [Clerc et al. \(C12, 2012b\)](#). I detailed the methods used for the processing of raw XMM data to create wavelet filtered, co-added X-ray images from which sources were detected and classified as either point-like or extended based on a maximum likelihood profile fitting procedure called *XAMIN*. I then discussed the selection criteria used for the construction of the X-CLASS cosmological sample, from which our targets for followup observations with GROND were selected. In total, the X-CLASS/GROND

sample consists of 265 X-ray selected galaxy clusters with a well defined selection function. This sample will be useful for cosmological studies.

I presented the methods of the redshift followup, starting by matching our clusters to already existing redshift information based on a variety of catalogues. Eighty-eight clusters were found to already have a spectroscopic redshift available while sixty-six had a photometric redshift. These already existing redshifts would provide a useful sample of the testing and calibration of the photometric redshifts acquired from the GROND data. The relatively small field-of-view of the GROND optical CCD's ($5' \times 5'$ means that a characterisation of the local background galaxy distribution is not possible based on a single cluster observation. This means that we were unable to use techniques relying on a knowledge of the background galaxy distribution to obtain photometric redshifts. I thus had to develop a new method specifically for these observations, maximising the available information. I pursued a red sequence method with the inclusion of information from the X-ray detection of the cluster, namely its position and extent. I modelled the expected colour of a typical red sequence galaxy based on the spectral energy distribution templates of Polletta et al. (2007) and calibrated it against CFHTLS photometry for galaxy clusters selected from the XXL-100 brightest clusters sample. Galaxies were then assigned a probability of being a cluster red sequence member based on a comparison of their measured colour to the expected colour. This probability was then weighted based on the distance to the X-ray centre of the cluster with a β -model profile and taking the measured X-ray extent into account.

The results from the photometric redshift pipeline were inspected visually by three astronomers, to pick up any obvious errors that the pipeline had made due to contamination from galaxies that were clearly not cluster members. This process was facilitated through an online tool which I developed specifically for this purpose. Among these contaminants were distant star-forming galaxies lying along the same line-of-sight as the galaxy cluster which got a high weight from the red sequence model for a much lower redshift and, due to the close proximity on the sky, a high weight from the β -model. Another class of contaminant was foreground, early-type galaxies which had colours in multiple bands fitting well to a red sequence and obtained a high β -model weight based on their position on the sky. In these cases, there was usually a visually clear red sequence of more distant galaxies which were more likely to be associated with the detected X-ray emission.

Ultimately, we were able to obtain a redshift for 232 out of 265 galaxy clusters and highlighted a further 24 cluster candidates that are potentially more distant than $z = 0.8$. The median redshift of our sample is $z = 0.39$. The results of our redshift calculations were compared to a sample of spectroscopically confirmed clusters and we found that our results were accurate to $\Delta z = 0.02(1 + z)$. This accuracy was deemed to be sufficient for the purposes of our cosmological analysis.

We also wished to characterise our sample in terms of its X-ray properties. To do this, I calculated the X-ray bolometric luminosity and temperature of each cluster. I used an iterative method which started by assuming a temperature of $T = 2.5$ keV and radius $r_{500} = 0.5$ Mpc. The count-rate of the cluster was measured within this radius and this was converted to a flux through the use of pre-computed energy conversion factors. I then

used XSPEC to compute the cluster luminosity and the scaling relations derived by the XXL collaboration to obtain a new temperature, mass and r_{500} . This process was repeated with the new value for the temperature and r_{500} until it converged to a final value of the temperature.

The results from the X-ray property calculations were compared with the results from two similar surveys, namely the XMM-XXL and the XMM-XCS. There was good agreement with both samples and we found a scatter in the luminosity of ~ 50 percent in the comparison with each of these samples. The median luminosity of the sample is 7.2×10^{43} erg s $^{-1}$, and the median temperature is 2.9 keV.

Chapter 4

In this fourth chapter, I finally got to the cosmological analysis of the X-CLASS/GROND cluster catalogue. Before detailing my analysis with the z-CR-HR method, I presented a thorough overview of the current status of cluster cosmology. This discussion was focused on cosmological tests based on the halo mass function and I highlighted the improvements made in recent years thanks to better constrained observable-mass relations with gravitational lensing.

I then introduced the z-CR-HR method, a relatively new, forward-modelling technique where comparisons between observations and theoretical predictions are made with directly observed quantities, namely the count-rate and hardness ratio. After first deriving the halo mass function, we determine the number density of clusters as a function of the X-ray temperature and luminosity through the use of cluster scaling relations. These temperatures and luminosities can then be converted into the observable space of count-rates and hardness ratios. The selection function is then applied directly in this space providing a robust and clean selection of clusters. The effects of observational errors as well as the bias from having included pointed cluster observations in this serendipitous survey are also included.

The estimation of cosmological parameters and the evolution of the $L - T$ and $M - T$ scaling relations was performed through the use of a maximum likelihood method. To do this, I used the Cash C-statistic which, in the case of low number counts, allows one to determine how well a given dataset fits its expected distribution. In order to sample the posterior probability distribution function, I used an affine-invariant Markov Chain Monte Carlo sampler, as implemented through the publicly available Python package `emcee`. This sampler was tested and verified through extensive testing on mock cluster catalogues.

This thesis was concluded with a cosmological analysis of the the X-CLASS/GROND catalogue. I first performed a consistency check by re-computing the results obtained by C12 where no redshift information was used and all clusters in the X-CLASS sample were used. The cosmological constraints that I attempted to constrain were Ω_M and σ_8 , along with the evolution of the $L - T$ and $M - T$ scaling relations and $X_{C,0}$, the ratio of the cluster core radius and r_{500} . I found a good agreement between the two sets of results providing the necessary validation of our methods. I then proceeded to with the analysis of the X-CLASS/GROND sample, which differs from the C12 sample in that it includes 13'

of each XMM pointing, compared with $10'$ and only covers areas of the sky with declination $\delta < 20^\circ$. The results that I obtained are somewhat in tension with those of C12, and those derived from other types of experiments such CMB, BAO or SN1a, as well as other cluster analyses. The likely cause of this that it is difficult to accurately account for the pointing bias but a lot of progress is being made in this regard and it shouldn't prevent the ultimate success of this project.

5.2 Future prospects

The sample that has been presented in this thesis contains all XMM pointings up to May 2010. Since then, nearly 7 years (accounting ~ 40 percent of its operations) have passed, in which XMM has continued to observe new regions in the sky. The prospects for enlarging our sample of XMM selected clusters are thus very good and already 184 new cluster candidates have been identified in XMM data up to January 2012. Most of these have already been observed with GROND and thus present an excellent opportunity for a continuation of our work with an enlarged sample. If XMM continues to perform at its current levels, we expect an additional 150 clusters to be detected each year of which about 50 would pass the cosmological C1⁺ selection criteria presented in Chapter 3.

In the GROND analysis presented in this thesis, I completely neglected the near-IR data obtained in the *JHK* bands. Including this data will allow for a more detailed study of the cluster members in terms of stellar mass and evolution. It would also be interesting to study their properties in the context of the cluster environment. The inclusion of these bands could also help to improve the recovered photometric redshift by adding three additional points to the observed spectral energy distribution.

As discussed in Chapter 3, we have identified 24 candidates to be distant $z > 0.8$ clusters. Most of these have been followed up as a part of a program to identify and observe distant clusters with GROND. Once photometric redshifts are in hand, we will be able to extend our cosmological analysis to higher redshifts and we could also make use of the full GROND data *grizJHK* to study the evolution of the optical and near-IR properties of cluster galaxies in the $z \sim 1$ regime. This sample would be a useful and interesting complement to another sample of clusters, drawn from the XDCP, for which there are also data from deep GROND observations, currently sitting unexplored in the GROND archive. These clusters are all spectroscopically confirmed and would also provide an incredibly useful calibration set for the distant X-CLASS clusters.

As stated in Chapter 4, there is still much work to be done before the cosmological results from the current X-CLASS/GROND catalogue are finalised. This includes a more accurate modelling of the pointing bias and the utilisation of the more recent and relevant scaling relations from the XMM-XXL collaboration. Another interesting study which will be performed will be based on only an annulus from $5'$ to $13'$ on each XMM pointing. This will remove the necessity of computing the pointing bias. However, some correction may be needed to account for certain classes of clusters which are preferentially observed by XMM, such as ROSAT serendipitous, or distant clusters. Comparing the analyses of these

various cluster selections will provide a useful self-verification and probe the robustness of our results.

Looking further to the future with the expected launch of eROSITA in 2018, a new window for cluster cosmology will be opened. We will move orders of magnitude upwards from samples of a few hundreds of X-ray selected clusters to a cluster catalogue consisting of 50,000-100,000 clusters. This unique set of data will allow us to not only deeply probe cosmological constraints such as Ω_M and σ_8 but also to provide strong constraints of the observable-mass scaling relations. The main goal of eROSITA cluster cosmology studies will be to obtain the strongest constraints to-date on the parameters relating to dark energy, helping us to uncover the nature of this mysterious force which is driving the accelerated expansion of the Universe. Since eROSITA will observe the entire extragalactic sky, the pointing bias inherent to our serendipitous survey will be nullified, greatly simplifying our analysis. The biggest changes that would need to be made to our current cosmological pipeline would be to derive a new selection function for eROSITA clusters which would require extensive simulations to accurately calibrate the efficiency of the cluster detection pipeline. Observational errors would also need to be quantified. With such a large data set, one can envisage the simultaneous fitting of both cosmological parameters and scaling relations, removing the necessity for an extremely precise mass calibration from external probes.

The ability of our cosmological analysis to operate without the need for cluster redshifts means that we will be able to obtain strong constraints, particularly on Ω_M and σ_8 without the need for photometric and spectroscopic follow-up observations. Of course, such followup is necessary to achieve eROSITA's primary science goal of constraining dark energy models, and extensive plans for this are already scheduled or underway with SPIDERS (with SDSS in the north) and 4MOST (on the VISTA telescope in the south) providing spectroscopic redshifts for a large number of clusters. The techniques developed for obtaining photometric redshifts with GROND will also be useful for the followup of clusters not falling within currently existing wide-field surveys such as SDSS and DES. Combining all of this data with other future experiments such as Euclid, Gaia and LSST will drive our understanding of dark energy to new highs.

Appendix A

The X-CLASS/GROND catalogue

Table A.1: The X-CLASS/GROND catalogue.

ID	RA J2000	DEC J2000	z	z_{lit}	z -Type	Count rate	r_{500}	$L_{500}^{[0.5-2]keV}$	T_{L-T}
X-CLASS	(degrees)	(degrees)	GROND	Literature	Literature	(cts/s)	(Mpc)	($10^{43} erg/s$)	(keV)
(1)	(2)	(3)	(4)	(5)	(6)	(7)	(8)	(9)	(10)
20	193.438	10.195	0.63			0.034	0.7 ± 0.2	5.6 ± 0.8	3.5 ± 0.8
35	196.274	-10.279	0.34	0.330	phot	0.031	0.7 ± 0.9	1.2 ± 1.7	2.1 ± 3.0
39	36.499	-2.828	0.27	0.280	conf	0.014	0.5 ± 0.1	0.3 ± 0.1	1.4 ± 0.3
40	35.189	-3.434	0.32	0.330	conf	0.037	0.7 ± 0.2	1.4 ± 0.2	2.3 ± 0.6
44	202.449	11.685	0.22			0.088	0.7 ± 0.2	1.4 ± 0.3	2.4 ± 0.6
50	172.813	-19.934	0.46			0.014	0.6 ± 0.2	1.6 ± 0.6	2.3 ± 0.7
51	177.616	1.758	F			0.032	*	*	*
54	145.938	16.738	0.16	0.180	conf	0.101	0.7 ± 0.2	1.2 ± 0.2	2.3 ± 0.7
56	145.886	16.667	0.25	0.250	conf	0.187	0.9 ± 0.2	3.7 ± 0.3	3.4 ± 0.9
57	145.995	16.688	0.32	0.250	conf	0.028	0.6 ± 0.2	0.7 ± 0.1	1.9 ± 0.5
59	31.958	2.157	D			0.117	*	*	*
65	339.252	-15.273	0.31	0.300	phot	0.262	1.0 ± 0.3	8.0 ± 1.6	4.5 ± 1.2
82	39.493	-52.394	0.13	0.135	conf	0.215	0.8 ± 0.2	1.2 ± 0.1	2.3 ± 0.6
86	348.766	-58.935	0.44			0.020	0.6 ± 0.9	1.4 ± 2.0	2.2 ± 3.1
87	349.095	-59.076	0.62			0.048	0.8 ± 0.2	7.5 ± 1.4	4.0 ± 1.1
88	183.395	2.896	0.36	0.410	conf	0.160	1.0 ± 0.3	8.9 ± 0.7	4.5 ± 1.1
102	28.314	1.038	0.05	0.059	conf	0.354	0.6 ± 0.1	0.3 ± 0.1	1.4 ± 0.4
135	300.803	-32.798	0.28	0.260	phot	0.123	0.9 ± 0.2	4.2 ± 0.9	3.6 ± 0.9
180	359.069	-34.695	D			0.056	*	*	*
205	314.089	-4.630	0.54	0.583	conf	0.111	0.9 ± 0.2	15.4 ± 1.3	5.3 ± 1.3

In column 4: the flag ‘F’ indicates that we were unable to obtain a secure redshift from the GROND observations as discussed in Section 3.3.4 and ‘D’ that the cluster has been classified as distant.

In columns 8-10: * indicates that we were unable to compute X-ray properties due to the lack of a secure redshift and ** that the X-ray processing pipeline failed to converge on a reasonable value.

ID	RA J2000	DEC J2000	z	z_{lit}	z -Type	Count rate	r_{500}	$L_{500}^{[0.5-2]keV}$	T_{L-T}
X-CLASS	(degrees)	(degrees)	GROND	Literature	Literature	(cts/s)	(Mpc)	($10^{43} erg/s$)	(keV)
(1)	(2)	(3)	(4)	(5)	(6)	(7)	(8)	(9)	(10)
208	243.512	-6.276	0.49			0.026	0.8±1.1	4.5±6.5	3.4±4.8
219	190.801	13.220	0.80	0.791	phot	0.046	0.7±0.2	11.6±2.0	4.4±1.1
224	36.377	-4.240	0.13	0.140	conf	0.243	0.8±0.2	1.4±0.2	2.5±0.7
228	148.572	17.634	0.83	0.828	phot	0.084	0.8±0.2	22.3±3.0	5.5±1.4
229	148.582	17.597	0.40	0.380	conf	0.127	0.9±0.3	6.0±1.6	4.0±1.2
233	10.729	-18.011	0.24			0.015	0.5±0.7	0.2±0.2	1.1±1.5
237	0.270	-25.066	D	0.910	phot	0.021	0.6±0.2	8.0±1.4	3.6±0.8
238	0.125	-25.203	0.13	0.150	conf	0.107	0.7±0.2	0.7±0.1	1.9±0.5
244	21.394	-1.279	0.59	0.490	phot	0.030	0.7±0.2	4.7±0.7	3.4±0.8
245	21.402	-1.431	0.14	0.019	conf	0.151	**	**	**
263	213.741	-0.349	0.12	0.140	conf	0.149	0.7±0.2	0.7±0.1	1.9±0.5
270	353.083	19.917	0.26			0.033	0.7±0.2	1.2±0.3	2.2±0.6
287	358.069	-26.093	0.25	0.275	tent	0.044	0.6±0.6	0.7±0.7	1.8±1.8
300	53.620	-36.238	0.33			0.034	0.7±0.2	1.1±0.2	2.1±0.5
314	56.257	-41.213	0.44			0.144	1.0±0.2	9.5±1.6	4.6±1.1
335	35.287	19.968	0.44	0.450	phot	0.223	1.1±0.3	21.6±3.1	6.3±1.6
372	45.526	-0.001	0.68	0.340	tent	0.030	0.7±0.2	6.6±1.2	3.7±1.0
374	177.549	1.646	0.37	0.450	phot	0.049	0.7±0.2	1.9±0.5	2.6±0.7
377	6.648	17.159	0.34	0.390	conf	0.289	1.1±0.3	15.1±0.8	5.6±1.4
378	6.708	17.325	0.47	0.491	conf	0.025	0.7±0.2	2.6±0.4	2.8±0.7
382	180.204	-3.458	0.39	0.396	phot	0.179	1.0±0.3	9.0±1.4	4.6±1.2
386	193.143	-29.417	0.25			0.018	0.5±0.1	0.4±0.1	1.4±0.3
387	193.227	-29.456	D	1.240	conf	0.030	**	**	**
399	170.958	5.496	0.62	0.650	conf	0.045	0.8±0.2	7.8±0.8	4.0±1.0

ID	RA J2000	DEC J2000	z	z_{lit}	z -Type	Count rate	r_{500}	$L_{500}^{[0.5-2]keV}$	T_{L-T}
X-CLASS	(degrees)	(degrees)	GROND	Literature	Literature	(cts/s)	(Mpc)	($10^{43} erg/s$)	(keV)
(1)	(2)	(3)	(4)	(5)	(6)	(7)	(8)	(9)	(10)
407	208.943	18.382	0.36	0.290	phot	0.026	0.7±0.2	1.2±0.2	2.2±0.6
408	59.354	1.300	0.23	0.130	phot	0.096	**	**	**
412	164.104	-3.589	0.66	0.630	phot	0.086	0.9±0.2	15.2±1.8	5.1±1.2
414	210.317	2.752	0.24	0.238	phot	0.044	0.7±0.2	0.8±0.2	1.9±0.5
417	39.136	-52.392	0.60			0.018	0.6±0.2	2.8±0.5	2.7±0.7
418	39.022	-52.421	0.59			0.045	0.8±0.2	6.2±1.0	3.7±0.9
419	337.096	-5.342	0.39	0.350	phot	0.046	0.8±0.2	2.8±0.5	3.0±0.8
420	155.739	19.886	0.81			0.011	0.6±0.1	3.4±0.7	2.7±0.6
424	333.903	-17.760	0.41	0.400	phot	0.049	0.8±0.2	2.8±0.6	2.9±0.8
430	54.438	-25.378	0.53	0.585	conf	0.040	0.8±0.2	5.5±0.6	3.5±0.9
435	156.003	4.038	0.47	0.480	phot	0.012	0.6±0.2	1.0±0.2	2.0±0.5
439	28.187	-13.953	0.84	0.831	phot	0.182	0.9±0.3	32.3±5.4	6.4±1.7
440	28.166	-13.975	0.84	0.831	phot	0.085	0.8±0.2	24.2±2.4	5.7±1.4
441	28.090	-14.087	0.32			0.052	0.7±0.2	1.7±0.4	2.5±0.6
442	28.241	-14.114	0.67	0.745	conf	0.048	0.8±0.2	10.2±1.6	4.2±1.1
453	191.230	-0.445	0.23	0.220	tent	0.031	0.6±0.2	0.5±0.2	1.6±0.5
454	191.225	-0.559	0.22	0.230	conf	0.045	0.6±0.2	0.7±0.1	1.9±0.5
459	4.572	16.294	0.55	0.550	conf	0.098	0.9±0.2	11.5±0.7	4.8±1.2
462	76.332	-28.815	0.46	0.509	conf	0.050	0.8±0.2	4.5±0.5	3.4±0.9
469	202.662	-1.643	D	0.660	tent	0.013	**	**	**
470	208.572	-2.366	0.53	0.546	conf	0.100	0.9±0.2	11.8±1.0	4.8±1.2
476	36.859	-4.538	0.32	0.307	conf	0.021	0.6±0.2	0.8±0.2	1.9±0.5
477	36.353	-4.680	0.29	0.266	conf	0.091	0.8±0.2	2.1±0.2	2.8±0.7
478	173.116	-34.568	0.60			0.011	0.6±0.2	2.1±0.3	2.5±0.6

ID	RA J2000	DEC J2000	z	z_{lit}	z -Type	Count rate	r_{500}	$L_{500}^{[0.5-2]keV}$	T_{L-T}
X-CLASS	(degrees)	(degrees)	GROND	Literature	Literature	(cts/s)	(Mpc)	($10^{43} erg/s$)	(keV)
(1)	(2)	(3)	(4)	(5)	(6)	(7)	(8)	(9)	(10)
479	173.133	-34.731	0.53			0.084	0.9±0.2	10.1±1.7	4.6±1.2
485	161.182	-1.332	D	0.750	tent	0.016	0.6±0.1	6.6±2.0	3.4±0.8
495	151.960	12.972	D	1.082	conf	0.010	0.5±0.1	6.4±1.3	3.2±0.6
499	65.073	-50.532	0.39			0.066	0.8±0.2	3.6±0.5	3.2±0.8
500	46.561	-0.095	0.36	0.430	conf	0.261	0.9±0.3	8.3±2.9	4.4±1.4
501	46.573	-0.141	0.12	0.109	conf	0.195	0.7±0.2	0.7±0.2	1.9±0.5
502	184.169	-12.074	0.68	0.790	tent	0.085	0.8±0.2	10.1±2.4	4.3±1.2
503	184.109	-11.962	0.60			0.016	0.7±0.2	2.9±0.6	2.8±0.7
505	184.190	-12.022	D	0.794	conf	0.101	0.9±0.2	25.6±2.0	5.9±1.5
507	1.000	-35.948	0.51			0.041	0.7±0.2	3.6±0.7	3.1±0.8
510	17.010	-80.311	0.34			0.066	0.8±0.2	2.9±0.8	3.0±0.9
514	42.529	-31.067	D	0.910	conf	0.047	0.7±0.2	17.2±1.8	4.9±1.2
517	351.397	-11.994	0.40			0.019	0.6±0.1	1.0±0.2	2.0±0.5
527	222.539	9.075	0.58	0.640	conf	0.031	0.8±0.2	6.8±1.3	3.8±1.0
528	73.587	-53.259	0.43			0.029	**	**	**
530	73.779	-53.399	0.41	0.410	conf	0.060	**	**	**
531	8.949	-43.379	0.62	0.630	conf	0.017	0.7±0.2	3.2±0.4	2.9±0.7
533	8.616	-43.316	0.42	0.390	conf	0.196	1.0±0.3	9.7±0.5	4.7±1.2
534	8.443	-43.292	0.22	0.220	conf	0.149	0.8±0.2	2.2±0.2	2.8±0.7
536	339.853	-5.788	0.26	0.242	phot	0.317	1.0±0.3	6.6±1.5	4.3±1.2
538	339.892	-6.006	0.10	0.173	phot	0.055	0.5±0.2	0.2±0.1	1.2±0.4
540	341.195	-72.736	0.19			0.028	0.5±0.1	0.3±0.1	1.3±0.3
541	341.492	-72.748	0.09			0.203	0.6±0.2	0.5±0.2	1.7±0.5
542	223.322	3.578	0.33	0.346	phot	0.056	0.8±0.2	2.5±0.4	2.9±0.8

ID	RA J2000	DEC J2000	z	z_{lit}	z -Type	Count rate	r_{500}	$L_{500}^{[0.5-2]keV}$	T_{L-T}
X-CLASS	(degrees)	(degrees)	GROND	Literature	Literature	(cts/s)	(Mpc)	($10^{43} erg/s$)	(keV)
(1)	(2)	(3)	(4)	(5)	(6)	(7)	(8)	(9)	(10)
551	5.619	-48.726	D			0.023	*	*	*
553	198.731	-16.642	0.69	0.610	phot	0.034	0.7±0.2	7.1±1.6	3.8±1.1
560	195.647	-2.309	D	0.620	tent	0.012	0.7±0.7	3.2±3.4	2.9±3.0
562	229.102	-0.832	0.42	0.380	tent	0.103	0.9±0.2	7.4±1.2	4.2±1.1
567	229.243	-1.111	0.12	0.117	conf	0.226	0.8±0.2	1.3±0.2	2.4±0.7
569	312.031	-17.699	0.17			0.101	0.8±0.2	1.3±0.5	2.4±0.8
634	49.572	-3.035	0.41	0.370	phot	0.107	0.9±0.2	7.0±1.2	4.1±1.0
872	156.213	-18.563	D			0.061	*	*	*
890	20.273	3.802	0.35	0.340	phot	0.113	0.9±0.2	5.0±1.0	3.7±1.0
911	78.082	-32.747	0.61			0.039	0.7±0.2	5.7±1.2	3.6±1.0
924	45.813	16.438	0.04	0.032	tent	0.042	**	**	**
927	12.418	-29.588	0.35	0.108	tent	0.043	0.8±0.2	2.5±0.9	2.9±0.9
955	2.206	-32.264	0.18	0.267	tent	0.029	0.6±0.2	0.3±0.1	1.4±0.4
964	234.184	-14.173	0.40	0.400	conf	0.312	1.2±0.3	24.8±2.0	6.7±1.6
967	310.411	-35.147	0.41	0.430	conf	0.125	0.9±0.2	8.9±1.0	4.5±1.1
996	195.731	-15.677	F			0.020	*	*	*
997	195.715	-15.701	F			0.044	*	*	*
998	195.582	-15.718	F			0.014	*	*	*
1014	30.240	-9.354	0.31	0.338	tent	0.032	0.7±0.2	1.7±0.6	2.5±0.8
1030	3.368	-27.379	0.40			0.157	1.0±0.2	8.4±1.4	4.5±1.1
1032	149.887	5.428	0.24	0.250	phot	0.011	0.5±0.1	0.3±0.1	1.3±0.3
1059	358.902	5.855	0.27	0.280	phot	0.050	0.7±0.2	1.6±0.4	2.5±0.7
1117	40.097	-23.289	D			0.016	*	*	*
1125	162.402	-13.968	0.36			0.050	0.8±0.2	2.7±0.6	3.0±0.8

ID	RA J2000	DEC J2000	z	z_{lit}	z -Type	Count rate	r_{500}	$L_{500}^{[0.5-2]keV}$	T_{L-T}
X-CLASS	(degrees)	(degrees)	GROND	Literature	Literature	(cts/s)	(Mpc)	($10^{43} erg/s$)	(keV)
(1)	(2)	(3)	(4)	(5)	(6)	(7)	(8)	(9)	(10)
1126	162.698	-14.172	0.53			0.087	0.9±0.2	9.1±1.0	4.4±1.1
1146	335.062	-28.044	0.36	0.165	tent	0.029	0.7±0.2	1.2±0.3	2.2±0.6
1195	323.419	-0.643	0.23	0.211	tent	0.172	0.9±0.2	3.2±0.8	3.3±0.9
1218	37.440	-29.631	0.06	0.061	conf	0.143	0.5±0.1	0.1±0.0	1.0±0.3
1219	174.013	-3.497	0.80			0.054	0.8±0.2	14.3±2.5	4.7±1.2
1239	218.691	-32.686	0.08	0.087	tent	0.166	0.6±0.2	0.4±0.2	1.6±0.6
1296	92.046	-61.896	0.24			0.068	0.7±0.2	1.3±0.3	2.3±0.6
1297	91.901	-61.928	0.33			0.242	1.0±0.3	9.3±1.5	4.8±1.2
1345	125.398	1.042	0.09	0.130	phot	0.353	0.8±0.2	1.3±0.6	2.4±0.8
1352	51.157	-3.190	0.52			0.047	0.8±0.2	5.0±1.7	3.5±1.0
1386	17.576	19.638	0.32	0.317	conf	0.081	0.8±0.2	2.9±0.4	3.1±0.8
1400	63.674	14.447	F			0.047	*	*	*
1424	215.314	3.130	0.19	0.310	phot	0.069	0.7±0.2	0.8±0.3	2.0±0.6
1425	322.662	4.919	0.61			0.051	0.8±0.2	8.3±1.3	4.1±1.0
1449	13.250	-8.661	0.32	0.315	conf	0.073	0.8±0.2	3.5±0.5	3.3±0.8
1478	352.180	-55.567	0.60	0.830	phot	0.085	0.9±0.2	12.9±2.3	4.9±1.3
1480	349.822	-55.326	0.16	0.180	phot	0.103	0.7±0.2	0.8±0.2	1.9±0.5
1482	349.222	-54.906	0.38	0.440	phot	0.255	1.0±0.3	12.2±2.2	5.2±1.4
1483	351.639	-55.022	0.41	0.320	phot	0.064	0.8±0.2	3.8±0.6	3.3±0.8
1485	352.008	-54.929	D	0.960	phot	0.025	0.6±0.2	10.4±2.3	4.0±1.0
1486	349.934	-54.640	0.52	0.550	phot	0.019	0.7±0.2	2.5±0.4	2.7±0.7
1487	351.396	-54.723	0.15	0.169	phot	0.064	0.6±0.2	0.5±0.2	1.6±0.5
1488	352.502	-54.619	0.18	0.176	conf	0.229	0.8±0.2	2.1±0.2	2.8±0.7
1489	352.418	-54.790	0.15	0.139	phot	0.021	0.0±0.4	0.0±0.1	0.0±0.8

ID	RA J2000	DEC J2000	z	z_{lit}	z -Type	Count rate	r_{500}	$L_{500}^{[0.5-2]keV}$	T_{L-T}
X-CLASS	(degrees)	(degrees)	GROND	Literature	Literature	(cts/s)	(Mpc)	($10^{43} erg/s$)	(keV)
(1)	(2)	(3)	(4)	(5)	(6)	(7)	(8)	(9)	(10)
1490	353.884	-54.588	D	0.670	phot	0.030	0.8±0.2	7.4±1.3	3.9±1.0
1581	148.809	18.208	0.42	0.416	conf	0.018	0.7±0.2	1.9±0.5	2.5±0.7
1582	148.814	18.062	0.65			0.024	0.7±0.2	5.3±1.2	3.4±0.9
1620	86.796	-51.202	0.26			0.072	0.7±0.2	1.7±0.3	2.5±0.7
1688	26.205	-4.550	0.14	0.170	phot	0.037	0.5±0.2	0.2±0.1	1.3±0.4
1691	60.056	-67.599	0.52			0.054	0.8±0.2	6.1±0.8	3.8±0.9
1693	59.765	-67.727	0.05	0.070	tent	0.030	0.4±0.1	0.0±0.0	0.6±0.2
1705	34.636	-5.016	D	0.880	conf	0.014	0.6±0.2	5.2±0.7	3.1±0.7
1706	34.938	-4.891	0.35	0.330	conf	0.019	0.6±0.2	0.7±0.1	1.8±0.5
1773	341.460	-52.912	0.45			0.091	0.9±0.2	5.9±0.9	3.8±0.9
1801	332.777	-16.950	0.31			0.045	0.7±0.2	1.7±0.5	2.5±0.7
1809	302.081	-44.595	0.52			0.023	0.7±0.2	2.8±0.5	2.8±0.7
1811	36.870	-40.852	0.42	0.400	tent	0.136	0.9±0.2	8.0±1.4	4.4±1.1
1814	5.404	-8.604	0.36			0.022	0.6±0.2	1.0±0.2	2.0±0.5
1818	37.959	-7.477	0.11	0.179	phot	0.029	0.5±0.2	0.1±0.1	1.0±0.4
1819	32.553	-0.247	0.30	0.280	phot	0.020	0.6±0.2	0.7±0.2	1.8±0.5
1821	52.263	2.940	0.35	0.410	conf	0.040	0.7±0.2	2.8±0.3	2.9±0.7
1827	9.368	-33.890	0.36	0.348	tent	0.072	0.8±0.2	3.2±0.5	3.1±0.8
1837	163.600	-11.774	0.55	0.700	conf	0.018	0.6±0.2	3.9±0.6	3.0±0.8
1838	163.488	-11.816	0.68			0.014	0.6±0.2	3.0±0.8	2.7±0.8
1845	334.410	-35.867	0.85			0.026	0.7±0.7	7.2±7.3	3.6±3.6
1851	33.473	-73.921	0.43			0.015	0.6±0.2	1.5±0.3	2.3±0.6
1853	350.358	19.753	0.30	0.400	phot	0.239	1.0±0.2	7.1±1.3	4.3±1.1
1854	350.535	19.730	0.53	0.500	phot	0.065	0.8±0.3	6.2±2.3	3.8±1.3

ID	RA J2000	DEC J2000	z	z_{lit}	z -Type	Count rate	r_{500}	$L_{500}^{[0.5-2]keV}$	T_{L-T}
X-CLASS	(degrees)	(degrees)	GROND	Literature	Literature	(cts/s)	(Mpc)	($10^{43} erg/s$)	(keV)
(1)	(2)	(3)	(4)	(5)	(6)	(7)	(8)	(9)	(10)
1855	350.588	19.647	0.21	0.230	phot	0.038	0.6±0.2	0.5±0.1	1.6±0.4
1856	3.862	17.290	0.47			0.030	0.7±0.2	2.6±0.5	2.8±0.7
1858	205.771	-0.015	0.70	0.600	phot	0.124	0.9±0.2	22.6±3.0	5.8±1.5
1862	190.793	14.340	0.37	0.340	conf	0.037	0.7±0.2	1.8±0.3	2.6±0.7
1864	130.351	0.774	0.41	0.410	conf	0.043	0.7±0.2	2.7±0.4	2.9±0.8
1868	358.469	-15.217	0.52			0.025	0.7±0.2	2.5±0.4	2.7±0.6
1874	150.423	2.425	0.13	0.120	conf	0.115	0.6±0.2	0.5±0.1	1.6±0.4
1876	150.507	2.226	0.84	0.830	conf	0.044	0.7±0.2	12.7±1.3	4.5±1.1
1877	150.125	2.696	0.35	0.350	phot	0.039	0.7±0.2	1.8±0.3	2.5±0.7
1879	150.058	2.379	0.32	0.350	conf	0.027	0.6±0.2	1.0±0.3	2.0±0.7
1880	150.093	2.391	0.23	0.220	conf	0.013	0.6±0.2	0.3±0.1	1.4±0.4
1882	150.196	1.658	0.22	0.220	conf	0.189	0.9±0.2	2.8±0.2	3.1±0.8
1883	150.182	1.768	0.34	0.350	conf	0.021	0.6±0.2	1.0±0.2	2.0±0.6
1886	150.030	2.209	D	0.930	conf	0.010	0.6±0.2	5.0±1.1	3.0±0.8
1888	149.600	2.820	0.35	0.340	conf	0.036	0.7±0.2	1.6±0.3	2.5±0.7
1889	134.606	13.958	0.49	0.488	phot	0.057	0.8±0.2	5.3±0.8	3.6±0.9
1892	5.416	-15.075	0.56			0.064	0.8±0.2	7.0±1.0	3.9±1.0
1893	5.559	-15.098	0.53			0.028	0.7±0.2	3.0±0.4	2.9±0.7
1896	169.360	7.727	0.48	0.480	conf	0.086	0.9±0.3	7.1±2.0	4.1±1.3
1900	9.843	0.802	0.36	0.410	conf	0.041	0.7±0.2	2.7±0.4	2.9±0.8
1903	67.148	-17.146	0.84			0.020	0.6±0.2	6.0±0.8	3.4±0.9
1906	328.656	-9.261	0.08	0.078	conf	0.170	0.6±0.1	0.3±0.0	1.4±0.3
1908	37.778	-54.064	0.56			0.154	1.0±0.3	16.4±2.1	5.4±1.4
1928	73.502	-3.143	0.26	0.260	tent	0.081	0.8±0.2	2.0±0.5	2.7±0.7

ID	RA J2000	DEC J2000	z	z_{lit}	z -Type	Count rate	r_{500}	$L_{500}^{[0.5-2]keV}$	T_{L-T}
X-CLASS	(degrees)	(degrees)	GROND	Literature	Literature	(cts/s)	(Mpc)	($10^{43} erg/s$)	(keV)
(1)	(2)	(3)	(4)	(5)	(6)	(7)	(8)	(9)	(10)
1943	149.162	-0.360	0.03	0.087	conf	0.348	0.7±0.2	0.7±0.1	2.0±0.5
1944	149.044	-0.365	0.57	0.580	phot	0.039	0.8±0.2	5.3±1.0	3.5±0.9
1954	54.353	-34.955	D	0.840	conf	0.021	0.6±0.2	6.3±0.4	3.4±0.8
1955	36.017	-4.226	0.24	1.050	conf	0.039	0.7±0.2	19.1±1.6	4.8±1.2
1956	36.146	-4.249	0.24	0.262	conf	0.038	0.6±0.2	0.8±0.1	1.9±0.5
1992	149.921	2.521	0.83	0.720	conf	0.048	0.8±0.2	10.0±0.8	4.2±1.0
1993	334.939	-27.917	0.20	0.207	conf	0.070	0.7±0.2	0.9±0.2	2.1±0.6
1994	334.900	-28.167	0.30			0.093	0.8±0.2	2.7±0.5	3.0±0.8
1995	334.966	-28.175	F			0.019	*	*	*
1999	150.655	-8.148	0.49	0.500	phot	0.039	0.8±0.2	3.8±0.6	3.2±0.8
2002	359.900	-32.187	F	0.480	phot	0.109	0.9±0.2	8.6±1.2	4.4±1.1
2003	326.523	4.383	0.52	0.530	conf	0.115	0.9±0.2	12.8±0.7	5.0±1.2
2005	191.013	16.866	0.54	0.560	conf	0.093	0.8±0.2	6.7±2.0	3.9±1.2
2006	197.843	-5.781	0.18	0.172	tent	0.030	0.6±0.2	0.4±0.1	1.5±0.4
2012	188.998	-33.883	0.22	0.082	tent	0.057	0.7±0.2	1.4±0.4	2.4±0.7
2020	214.847	6.643	0.56	0.570	phot	0.144	1.0±0.2	16.1±2.1	5.4±1.3
2021	214.973	6.568	0.58	0.560	phot	0.156	1.0±0.3	18.3±2.7	5.6±1.5
2022	215.001	6.581	0.58	0.570	phot	0.087	0.9±0.2	10.8±1.6	4.6±1.2
2023	163.898	-4.990	0.58	0.610	phot	0.032	0.7±0.2	4.4±0.6	3.3±0.8
2025	163.796	-5.071	0.66	0.680	conf	0.061	0.8±0.2	11.2±0.8	4.5±1.1
2031	54.656	-35.690	0.20	0.185	conf	0.053	0.6±0.1	0.4±0.1	1.6±0.4
2045	175.063	2.941	0.20			0.022	0.6±0.2	0.6±0.2	1.7±0.6
2046	218.702	3.631	0.13	0.146	conf	0.083	0.6±0.2	0.4±0.1	1.6±0.4
2048	54.547	-22.941	0.18	0.173	phot	0.154	0.8±0.2	1.5±0.4	2.5±0.7

ID	RA J2000	DEC J2000	z	z_{lit}	z -Type	Count rate	r_{500}	$L_{500}^{[0.5-2]keV}$	T_{L-T}
X-CLASS	(degrees)	(degrees)	GROND	Literature	Literature	(cts/s)	(Mpc)	($10^{43} erg/s$)	(keV)
(1)	(2)	(3)	(4)	(5)	(6)	(7)	(8)	(9)	(10)
2049	54.461	-23.074	0.62			0.038	0.7±0.2	5.7±1.1	3.6±0.9
2057	187.696	11.189	D			0.022	*	*	*
2062	338.836	-25.962	D	1.393	phot	0.024	**	**	**
2063	147.072	-13.279	0.06			0.039	0.5±0.2	0.2±0.1	1.2±0.6
2078	32.608	-39.494	F	0.306	conf	0.050	0.7±0.2	1.6±0.1	2.4±0.6
2079	32.556	-39.549	0.17	0.166	conf	0.075	0.7±0.2	0.6±0.1	1.8±0.5
2093	335.812	-1.661	0.32	0.297	phot	0.265	1.0±0.3	9.2±1.7	4.8±1.1
2094	200.323	-11.741	0.55			0.029	0.7±0.2	3.4±0.4	3.0±0.7
2099	323.423	-42.729	0.19			0.103	0.7±0.2	1.2±0.3	2.3±0.6
2100	323.395	-42.902	0.31			0.040	0.7±0.2	1.1±0.2	2.1±0.6
2115	188.598	15.316	0.30	0.308	phot	0.048	0.7±0.2	1.9±0.6	2.6±0.8
2118	327.847	-5.448	0.16	0.145	conf	0.135	0.7±0.2	0.8±0.1	2.0±0.5
2122	308.703	-34.530	0.37			0.164	0.9±0.2	7.4±1.1	4.3±1.1
2128	157.532	-3.111	0.45	0.430	phot	0.047	0.7±0.2	3.0±0.6	3.0±0.8
2130	329.308	-7.712	0.47	0.450	phot	0.034	0.7±0.7	2.7±2.7	2.8±2.9
2161	34.009	-47.876	0.59			0.011	0.6±0.1	1.3±0.5	2.1±0.5
2162	149.853	1.772	0.12	0.120	conf	0.079	0.6±0.2	0.3±0.1	1.4±0.4
2163	149.965	1.680	0.33	0.370	conf	0.056	0.8±0.2	2.8±0.2	3.0±0.8
2166	349.197	-42.711	0.11	0.096	conf	0.278	0.7±0.2	0.7±0.1	1.9±0.5
2169	198.667	-25.340	0.23	0.250	tent	0.189	0.9±0.3	3.8±1.1	3.5±1.1
2187	197.876	-5.869	0.45	0.461	conf	0.086	0.9±0.2	6.3±0.4	3.9±0.9
2189	352.216	14.882	0.47	0.497	conf	0.044	0.8±0.2	4.3±0.2	3.3±0.8
2199	309.625	-1.424	0.81	0.680	conf	0.051	0.8±0.2	11.2±1.3	4.5±1.1
2203	341.053	-9.575	0.44	0.447	conf	0.184	1.0±0.2	13.0±1.4	5.2±1.2

ID	RA J2000	DEC J2000	z	z_{lit}	z -Type	Count rate	r_{500}	$L_{500}^{[0.5-2]keV}$	T_{L-T}
X-CLASS	(degrees)	(degrees)	GROND	Literature	Literature	(cts/s)	(Mpc)	($10^{43} erg/s$)	(keV)
(1)	(2)	(3)	(4)	(5)	(6)	(7)	(8)	(9)	(10)
2207	192.362	5.208	0.62			0.020	0.7±0.2	3.3±0.7	2.9±0.7
2209	149.769	13.089	0.36	0.396	conf	0.118	0.9±0.2	6.4±0.9	4.0±1.1
2212	189.708	9.254	0.80			0.042	0.8±0.2	12.2±3.0	4.5±1.2
2225	14.396	-26.112	0.36			0.063	0.8±0.2	2.7±0.7	3.0±0.8
2254	38.264	-71.275	0.55			0.172	1.0±0.3	16.7±2.4	5.5±1.4
2255	225.214	-10.861	0.40			0.025	0.7±0.2	2.7±1.1	2.9±1.0
2256	225.275	-10.876	0.76			0.042	0.8±0.2	12.4±1.9	4.6±1.1
2257	334.149	-36.799	0.57			0.033	0.7±0.2	4.4±0.7	3.3±0.8
2260	187.211	13.995	0.50			0.085	0.9±0.2	7.7±1.2	4.2±1.0
2265	343.444	-14.208	0.32			0.034	0.7±0.2	1.3±0.3	2.2±0.6
2294	5.622	1.383	0.61	0.620	tent	0.038	0.7±0.2	5.7±0.8	3.6±0.9
2297	15.127	-47.823	0.42			0.154	1.0±0.3	9.0±1.4	4.5±1.2
2298	15.239	-47.860	0.28			0.062	0.7±0.2	1.0±0.4	2.0±0.7
2299	86.974	-47.651	0.45			0.026	0.7±0.2	2.3±0.6	2.7±0.7
2303	73.126	-42.153	0.73			0.029	0.7±0.2	6.3±1.4	3.6±0.8
2304	179.895	-19.862	D			0.069	*	*	*
2305	180.059	-20.047	0.60			0.279	1.1±0.3	37.2±4.4	7.3±1.8
2307	29.323	-16.991	0.50			0.032	0.7±0.2	3.0±0.6	2.9±0.8
2311	141.282	13.450	F			0.048	*	*	*
2312	141.206	13.293	D	0.520	phot	0.031	0.7±0.2	3.4±0.5	3.0±0.8
2313	53.003	-27.724	D			0.012	*	*	*
2321	137.723	-9.738	0.08	0.092	tent	0.080	0.5±0.1	0.2±0.1	1.1±0.4
2323	245.403	-1.491	0.11	0.106	tent	0.049	0.5±0.1	0.2±0.1	1.2±0.4
3075	28.173	-13.649	D	0.830	conf	0.032	0.7±0.2	9.4±0.9	4.0±0.9

ID	RA J2000	DEC J2000	z	z_{lit}	z -Type	Count rate	r_{500}	$L_{500}^{[0.5-2]keV}$	T_{L-T}
X-CLASS	(degrees)	(degrees)	GROND	Literature	Literature	(cts/s)	(Mpc)	($10^{43}erg/s$)	(keV)
(1)	(2)	(3)	(4)	(5)	(6)	(7)	(8)	(9)	(10)
3104	327.673	-5.685	0.36	0.440	conf	0.045	0.8 ± 0.2	3.1 ± 0.3	3.0 ± 0.7
3170	184.205	-12.137	0.79	0.480	phot	0.014	0.6 ± 0.2	4.5 ± 0.8	3.1 ± 0.8
3281	3.386	-27.188	0.50			0.054	0.8 ± 0.2	5.0 ± 0.7	3.5 ± 0.9
3283	146.378	9.776	0.21	0.220	conf	0.047	0.7 ± 0.2	0.9 ± 0.2	2.0 ± 0.6
3485	351.361	-12.068	0.08	0.085	conf	0.154	**	**	**

Bibliography

- Abazajian K. N. et al., 2009, , 182, 543 *cited on pages 61*
- Abell G. O., 1958, *Astrophys. J. Suppl. Ser.*, 3, 211, ☞ *cited on pages 34, 74, and 77*
- Adam R. et al., 2017, *Astron. Astrophys.*, 598, A115, ☞ *cited on pages 36*
- Allen S., Schmidt R., Fabian A., 2001, *Mon. Not. R. Astron. Soc.*, 328, L37, ☞
cited on pages 113
- Allen S. W., Evrard A. E., Mantz A. B., 2011, *Annu. Rev. Astron. Astrophys.*, 49, 409, ☞
cited on pages 74
- Allen S. W., Rapetti D. A., Schmidt R. W., Ebeling H., Morris R. G., Fabian A. C., 2008,
Mon. Not. R. Astron. Soc., 383, 879, ☞ *cited on pages 102, 104, and 105*
- Allen S. W., Schmidt R. W., Ebeling H., Fabian A. C., van Speybroeck L., 2004, *Mon.*
Not. R. Astron. Soc., 353, 457, ☞ *cited on pages 102 and 105*
- Anderson L. et al., 2014, *MNRAS*, 441, 24 *cited on pages 108*
- Applegate D. E. et al., 2014, *Mon. Not. R. Astron. Soc.*, 439, 48, ☞
cited on pages 104 and 108
- Arnaud K. A., 1996, in *Astronomical Society of the Pacific Conference Series*, Vol. 101,
Astronomical Data Analysis Software and Systems V, Jacoby G. H., Barnes J., eds.,
p. 17 *cited on pages 87*
- Arnaud M., Pointecouteau E., Pratt G. W., 2005, *Astron. Astrophys.*, 441, 893, ☞
cited on pages 113 and 135
- Arnouts S., Cristiani S., Moscardini L., Matarrese S., Lucchin F., Fontana A., Giallongo
E., 1999, *Monthly Notices of the Royal Astronomical Society*, 310, 540
cited on pages 79
- Astropy Collaboration et al., 2013, , 558, A33 *cited on pages 179*
- Balaguera-Antolínez A., Sánchez A. G., Böhringer H., Collins C., Guzzo L., Phleps S.,
2011, *Mon. Not. R. Astron. Soc.*, 413, 386, ☞ *cited on pages 107*

- Baldry I. K., Glazebrook K., Brinkmann J., Ivezić Z., Lupton R. H., Nichol R. C., Szalay a. S., 2004, *Astrophys. J.*, 681, ☞ *cited on pages 32*
- Banerji M. et al., 2010, *Mon. Not. R. Astron. Soc.*, 406, 342, ☞ *cited on pages 32*
- Barcons X. et al., 2007, , 476, 1191 *cited on pages 83*
- Barkhouse W. A. et al., 2006, *Astrophys. J.*, 645, 64, ☞ *cited on pages 29 and 74*
- Barré H., Nye H., Janin G., 1999, *ESA Bull.*, ☞ *cited on pages 22*
- Baum W. A., 1959, *Publ. Astron. Soc. Pacific*, 71, 106, ☞ *cited on pages 74*
- Benson B. A. et al., 2013, *Astrophys. J.*, 763, 147, ☞ *cited on pages 108*
- Bertin E., 2006, in *Astronomical Society of the Pacific Conference Series*, Vol. 351, *Astronomical Data Analysis Software and Systems XV*, Gabriel C., Arviset C., Ponz D., Enrique S., eds., p. 112 *cited on pages 61*
- Bertin E., 2011, in *Astronomical Society of the Pacific Conference Series*, Vol. 442, *Astronomical Data Analysis Software and Systems XX*, Evans I. N., Accomazzi A., Mink D. J., Rots A. H., eds., p. 435 *cited on pages 62*
- Bertin E., Arnouts S., 1996, *Astron. Astrophys. Suppl. Ser.*, 117, 393, ☞ *cited on pages 62 and 76*
- Bertin E., Mellier Y., Radovich M., Missonnier G., Didelon P., Morin B., 2002, in *Astronomical Society of the Pacific Conference Series*, Vol. 281, *Astronomical Data Analysis Software and Systems XI*, Bohlender D. A., Durand D., Handley T. H., eds., p. 228 *cited on pages 61*
- Betoule M. et al., 2014, *Astron. Astrophys.*, 568, A22, ☞ *cited on pages 108*
- Bleem L. E. et al., 2015, *The Astrophysical Journal Supplement Series*, 216, 27, ☞ *cited on pages 77*
- Bocquet S., 2015 *cited on pages 42*
- Bocquet S., Saro A., Dolag K., Mohr J. J., 2016, *Mon. Not. R. Astron. Soc.*, 456, 2361, ☞ *cited on pages xi, 20, and 21*
- Bocquet S. et al., 2015, *Astrophys. J.*, 799, 214, ☞ *cited on pages 45 and 108*
- Boehringer H. et al., 2000, *Astron. Astrophys.* v.369, p.826-850, 369, 826, ☞ *cited on pages 74*
- Böhringer H., Chon G., Collins C. A., 2014, *Astron. Astrophys.*, 570, A31, ☞ *cited on pages 106*

- Bonamente M., Joy M. K., LaRoque S. J., Carlstrom J. E., Reese E. D., Dawson K. S., 2006, *Astrophys. J.*, 647, 25, ☞ *cited on pages 48*
- Borgani S., Guzzo L., 2001, *Nature*, 409, 39, ☞ *cited on pages xiv, 42, and 44*
- Borgani S. et al., 2001, *Astrophys. J.*, 561, 13, ☞ *cited on pages 102*
- Bower R. G., Lucey J. R., Ellis R. S., 1992, *Mon. Not. R. Astron. Soc.*, 254, 589
cited on pages 32
- Bower R. G., Terlevich A., Kodama T., Caldwell N., 1998, ☞ *cited on pages xii and 33*
- Branduardi-Raymont G., Kellett B., Fabian A., McGlynn T., Manzo G., Peacock A., 1985, *Adv. Sp. Res.*, 5, 133, ☞ *cited on pages 29*
- Bruzual G., Charlot S., 2003, *Mon. Not. R. Astron. Soc.*, 344, 1000
cited on pages 78 and 81
- Bullock J. S., Kolatt T. S., Sigad Y., Somerville R. S., Kravtsov A. V., Klypin A. A., Primack J. R., Dekel A., 2001, *Mon. Not. R. Astron. Soc.*, 321, 559, ☞
cited on pages 113
- Burenin R. A., Vikhlinin A., Hornstrup A., Ebeling H., Quintana H., Mescheryakov A., 2007, *Astrophys. J. Suppl. Ser.*, 172, 561, ☞ *cited on pages 103*
- Carlstrom J. E. et al., 2011, *Publ. Astron. Soc. Pacific*, 123, 568, ☞
cited on pages 36 and 108
- Carlstrom J. E., Holder G. P., Reese E. D., 2002, *Annu. Rev. Astron. Astrophys.*, 40, 643,
☞ *cited on pages xiii, 35, and 48*
- Cash W., 1979, *Astrophys. J.*, 228, 939, ☞ *cited on pages 125*
- Cataneo M., Rapetti D., Lombriser L., Li B., 2016, *J. Cosmol. Astropart. Phys.*, 2016, 024,
☞ *cited on pages 110*
- Cataneo M. et al., 2015, *Phys. Rev. D*, 92, 044009 *cited on pages 110*
- Chon G., Böhringer H., Nowak N., 2013, *MNRAS*, 429, 3272 *cited on pages 107*
- Christen J. A., Fox C., 2007 *cited on pages 129*
- Clerc N. et al., 2014, *Mon. Not. R. Astron. Soc.*, 444, 2723 *cited on pages 29, 74, and 113*
- Clerc N. et al., 2016, *Mon. Not. R. Astron. Soc.*, 463, 4490, ☞ *cited on pages 45*
- Clerc N., Pierre M., Pacaud F., Sadibekova T., 2012a, *Mon. Not. R. Astron. Soc.*, 423,
3545, ☞ *cited on pages 73, 77, 84, 101, 111, 123, 124, 133, 141, and 145*

- Clerc N., Sadibekova T., Pierre M., Pacaud F., Le Fevre J. P., Adami C., Altieri B., Valtchanov I., 2012b, *Mon. Not. R. Astron. Soc.*, 423, 3561
cited on pages xxi, 2, 29, 74, 75, 77, 86, 111, 121, 123, 133, 135, 136, 143, and 147
- Collins C. A. et al., 2000, *Mon. Not. R. Astron. Soc.*, 319, 939, ☞ *cited on pages 47*
- de Gasperin F. et al., 2016, ☞ *cited on pages xiii, 39, and 146*
- de Haan T. et al., 2016, *Astrophys. J.*, 832 *cited on pages 36 and 108*
- E. Kellogg, H. Gursky, H. Tananbaum R. G., 1972, *ApJ*, 178, 309 *cited on pages 22 and 28*
- Ebeling H. et al., 2000, *The Astrophysical Journal*, 534, 133 *cited on pages 99*
- Eckert D., Jauzac M., Vazza F., Owers M. S., Kneib J.-P., Tchernin C., Intema H., Knowles K., 2016, *Mon. Not. R. Astron. Soc.*, 461, 1302, ☞ *cited on pages 37*
- Edge A. C., Stewart G. C., 1991, *Mon. Not. R. Astron. Soc.*, 252, 428, ☞
cited on pages 113
- Eisenstein D. J., Hu W., 1999, *Astrophys. J.*, 511, 5 *cited on pages 107*
- Eisenstein D. J. et al., 1998, *Astrophys. J.*, 496, 605, ☞ *cited on pages 112*
- Eisenstein D. J. et al., 2011, *Astron. J.*, 142, 72, ☞ *cited on pages 13*
- Eke V. R., Cole S., Frenk C. S., 1996, *Mon. Not. R. Astron. Soc.*, 282, 263, ☞
cited on pages 102
- Feretti L., Giovannini G., Govoni F., Murgia M., 2012, *Astron. Astrophys. Rev.*, 20, 1
cited on pages 37
- Finoguenov A. et al., 2006, *Astrophys. J. Suppl. Ser. Vol. 172, Issue 1, pp. 182-195.*, 172, 182, ☞ *cited on pages 29, 74, and 98*
- Finoguenov A., Reiprich T. H., Böhringer H., 2001, *Astron. Astrophys.*, 368, 749, ☞
cited on pages 113
- Foreman-Mackey D., Hogg D. W., Lang D., Goodman J., 2012, ☞ *cited on pages 129*
- Forman W., Jones C., Cominsky L., Julien P., Murray S., Peters G., Tananbaum H., Giacconi R., 1978, *Astrophys. J. Suppl. Ser.*, 38, 357 *cited on pages 22*
- Freedman W. L. et al., 2001, *Astrophys. J.*, 553, 47, ☞ *cited on pages 103*
- Giles P. A. et al., 2016, *Astron. Astrophys.*, 592, A3, ☞
cited on pages 77, 88, 91, 107, 113, 115, and 142
- Gladders M. D., Yee H. K. C., 2000, *Astron. J.*, 120, 2148, ☞ *cited on pages 74 and 75*

- Goodman J., Weare J., 2010, Commun. Appl. Math. Comput. Sci., 5, 65, [↗](#)
cited on pages 129
- Greiner J. et al., 2008, Publ. Astron. Soc. Pacific, 120, 405, [↗](#) *cited on pages 51 and 54*
- Greiner J. et al., 2009, The Astrophysical Journal, 693, 1610 *cited on pages 53*
- Greiner J. et al., 2011, Astronomy & Astrophysics, 526, A30 *cited on pages 53*
- Greiner J. et al., 2015, Nature, 523, 189 *cited on pages 53*
- Guennou L. et al., 2014, , 561, A112 *cited on pages 84*
- Guennou L. et al., 2014, Astronomy & Astrophysics, 566, A149 *cited on pages 99*
- Hand N. et al., 2012, Phys. Rev. Lett., 109, 041101, [↗](#) *cited on pages 36*
- Hasselfield M. et al., 2013, J. Cosmol. Astropart. Phys., 2013, 008, [↗](#)
cited on pages 36 and 108
- Hinshaw G. et al., 2013, , 208, 19 *cited on pages 75 and 91*
- Hinshaw G. et al., 2013, Astrophys. J. Suppl. Ser., 208, 19, [↗](#) *cited on pages 112 and 115*
- Hoeft M., Bruggen M., 2007, Mon. Not. R. Astron. Soc., 375, 77, [↗](#) *cited on pages 37*
- Hoekstra H., Herbonnet R., Muzzin A., Babul A., Mahdavi A., Viola M., Cacciato M.,
2015, Mon. Not. R. Astron. Soc., 449, 685, [↗](#) *cited on pages 108*
- Hofmann F., Sanders J. S., Nandra K., Clerc N., Gaspari M., 2016, Astron. Astrophys.,
585, A130, [↗](#) *cited on pages xii, 27, 28, and 47*
- Hu W., Kravtsov A. V., 2003, Astrophys. J., 584, 702, [↗](#) *cited on pages 113*
- Ilbert O. et al., 2006, Astronomy & Astrophysics, 457, 841 *cited on pages 79*
- Jauzac M. et al., 2016, Mon. Not. R. Astron. Soc., 463, 3876, [↗](#) *cited on pages 110*
- Jauzac M. et al., 2014, Mon. Not. R. Astron. Soc., 446, 4132, [↗](#) *cited on pages 45*
- Jauzac M. et al., 2015, Mon. Not. R. Astron. Soc., 452, 1437, [↗](#) *cited on pages 45*
- Jha S., 2002, PhD thesis, HARVARD UNIVERSITY *cited on pages xi and 11*
- Johnson O. et al., 2006, Mon. Not. R. Astron. Soc., 371, 1777 *cited on pages 99*
- Johnston D. E. et al., 2007, [↗](#) *cited on pages 109*
- Kalberla P. M. W., Burton W. B., Hartmann D., Arnal E. M., Bajaja E., Morras R.,
Pöppel W. G. L., 2005, Astron. Astrophys., 440, 775, [↗](#) *cited on pages 114*

- King I. R., 1966, *Astron. J.*, 71, 64, ☞ *cited on pages 27*
- Kodama T., Tanaka I., Kajisawa M., Kurk J., Venemans B., De Breuck C., Vernet J., Lidman C., 2007, *Mon. Not. R. Astron. Soc.*, 377, 1717, ☞ *cited on pages 32*
- Koester B. P. et al., 2007, *Astrophys. J.*, 660, 221, ☞ *cited on pages 34, 75, and 109*
- Krühler T. et al., 2008, *Astrophys. J.*, 685, 376, ☞ *cited on pages 51 and 58*
- Küpcü Yoldaş A., Krühler T., Greiner J., Yoldaş A., Clemens C., Szokoly G., Primak N., Klose S., 2008in , AIP Publishing, pp. 227–231 *cited on pages 51 and 58*
- L. Danese, Zotti G. D., di Tullio G., 1980, *Astron. Astrophys.*, 82, 322, ☞ *cited on pages 45*
- Lieu M. et al., 2016, *Astron. Astrophys.*, 592, A4, ☞ *cited on pages 88, 91, 107, 113, 115, and 142*
- Limousin M. et al., 2007, *Astrophys. J.*, 668, 643, ☞ *cited on pages 45*
- Lintott C. J. et al., 2008, *Mon. Not. R. Astron. Soc.*, 389, 1179, ☞ *cited on pages 31*
- Lloyd-Davies E. J. et al., 2011a, *Mon. Not. R. Astron. Soc.*, 418, 14 *cited on pages 29*
- Lloyd-Davies E. J. et al., 2011b, *Mon. Not. R. Astron. Soc.*, 418, 14 *cited on pages 74*
- Majumdar S., Mohr J. J., 2004, *Astrophys. J.*, 613, 41, ☞ *cited on pages 109*
- Mana A., Giannantonio T., Weller J., Hoyle B., Hütsi G., Sartoris B., 2013, *MNRAS*, 434, 684 *cited on pages 47 and 110*
- Mancone C. L., Gonzalez A. H., 2012, *Publ. Astron. Soc. Pacific*, 124, 606 *cited on pages 81*
- Mantz A., Allen S. W., Ebeling H., Rapetti D., 2008, *Mon. Not. R. Astron. Soc.*, 387, 1179 *cited on pages 104 and 105*
- Mantz A., Allen S. W., Ebeling H., Rapetti D., Drlica-Wagner A., 2010a, *Mon. Not. R. Astron. Soc.*, 406, 1773 *cited on pages 113*
- Mantz A. et al., 2010b, *Mon. Not. R. Astron. Soc.*, 406, no, ☞ *cited on pages 102*
- Mantz A., Allen S. W., Rapetti D., Ebeling H., 2010c, *Mon. Not. R. Astron. Soc.*, 406, 1759 *cited on pages 104 and 105*
- Mantz A. B., Allen S. W., Morris R. G., Rapetti D. A., Applegate D. E., Kelly P. L., von der Linden A., Schmidt R. W., 2014, *Mon. Not. R. Astron. Soc.*, 440, 2077, ☞ *cited on pages 102 and 105*

- Mantz A. B. et al., 2016, [☞](#) *cited on pages 113*
- Mantz A. B. et al., 2015, MNRAS, 446, 2205 *cited on pages xvii, 47, 102, 104, and 106*
- Maraston C., Strömbäck G., Thomas D., Wake D. A., Nichol R. C., 2009, Mon. Not. R. Astron. Soc. Lett., 394, 107 *cited on pages 78*
- Martinez H. J., O’Mill A. L., Lambas D. G., 2006, Mon. Not. R. Astron. Soc., 372, 253, [☞](#) *cited on pages 32*
- Martinez Aviles G. et al., 2016, Astron. Astrophys., 595, A116, [☞](#) *cited on pages xiii and 39*
- Massey R. et al., 2015, Mon. Not. R. Astron. Soc., 449, 3393, [☞](#) *cited on pages 110*
- McDonald M. et al., 2013, Astrophys. J., 774, 23, [☞](#) *cited on pages 108*
- McHardy I. M., Lawrence A., Pye J. P., Pounds K. A., 1981, Mon. Not. R. Astron. Soc., 197, 893, [☞](#) *cited on pages 29*
- McNamara B. R., Kazemzadeh F., Rafferty D. A., Bîrzan L., Nulsen P. E. J., Kirkpatrick C. C., Wise M. W., 2009, Astrophys. J., 698, 594, [☞](#) *cited on pages xiii and 38*
- Mehrtens N. et al., 2012, Mon. Not. R. Astron. Soc., 423, 1024 *cited on pages 29, 74, and 77*
- Mei S. et al., 2009, Astrophys. J., 690, 42, [☞](#) *cited on pages 33*
- Mei S. et al., 2006, Astrophys. J., 644, 759, [☞](#) *cited on pages 32*
- Merloni A. et al., 2012, eprint arXiv:1209.3114, 84, [☞](#) *cited on pages 22*
- Mirkazemi M. et al., 2015, Astrophys. J., 799, 60, [☞](#) *cited on pages 78 and 81*
- Mitchell R. J., Dickens R. J., Burnell S. J. B., Culhane J. L., 1979, Mon. Not. R. Astron. Soc., 189, 329, [☞](#) *cited on pages 113*
- Mitchell R. J., Ives J. C., Culhane J. L., 1977, Mon. Not. R. Astron. Soc., 181, 25P, [☞](#) *cited on pages 113*
- Monet D. et al., 1998, The USNO-A2.0 Catalogue. U.S. Naval Observatory, Washington DC *cited on pages 61*
- Mushotzky R. F., 1984, Phys. Scr., T7, 157, [☞](#) *cited on pages 113*
- Nastasi A. et al., 2014, Astronomy & Astrophysics, 564, A17 *cited on pages 84 and 99*
- Natarajan P. et al., 2017, [☞](#) *cited on pages 102*

- Navarro J. F., Frenk C. S., White S. D. M., 1997, *Astrophys. J.*, 490, 493, [↗](#)
cited on pages 113
- Nelson A. E., Gonzalez A. H., Zaritsky D., Dalcanton J. J., 2001, , 563, 629
cited on pages 99
- Pacaud F. et al., 2016, 2, 1 *cited on pages 29, 47, 74, 77, 78, 88, 91, 96, 107, and 115*
- Pacaud F. et al., 2007, *Mon. Not. R. Astron. Soc.*, 382, 1289
cited on pages 29, 74, and 124
- Pacaud F. et al., 2006, *Mon. Not. R. Astron. Soc. Vol. 372, Issue 2*, pp. 578-590., 372, 578,
[↗](#) *cited on pages 75, 76, and 77*
- Perlmutter S. et al., 1999, *Astrophys. J.*, 517, 565, [↗](#) *cited on pages 9*
- Pierini D. et al., 2012, *Astron. Astrophys.*, 540, A45, [↗](#) *cited on pages 99*
- Pierre M. et al., 2007, *Mon. Not. R. Astron. Soc.*, 382, 279, [↗](#) *cited on pages 29, 74, and 75*
- Pierre M. et al., 2016, *Astron. Astrophys.*, 592, A1, [↗](#) *cited on pages 29 and 74*
- Pierre M., Pacaud F., Juin J. B., Melin J. B., Clerc N., Corasaniti P. S., Corasaniti P. S.,
2011, *Mon. Not. R. Astron. Soc. Vol. 414, Issue 2*, pp. 1732-1746., 414, 1732, [↗](#)
cited on pages 75
- Piffaretti R., Arnaud M., Pratt G., Pointecouteau E., Melin J.-B., 2011, *Astronomy &
Astrophysics*, 534, A109 *cited on pages xvi, 29, 91, and 93*
- Planck Collaboration XIII et al., 2015, *A&A*, 571, A29, [↗](#) *cited on pages 102*
- Planck Collaboration XVI et al., 2014, *Astron. Astrophys.*, 571, A16, [↗](#)
cited on pages 18, 108, and 109
- Planck Collaboration XX et al., 2014, *Astron. Astrophys.*, 571, A20, [↗](#) *cited on pages 109*
- Planck Collaboration XXIV et al., 2016, *Astron. Astrophys.*, 594, A24, [↗](#)
cited on pages 107 and 109
- Planck Collaboration XXIX, 2014 *cited on pages 77*
- Planck Collaboration XXVII et al., 2016, *Astron. Astrophys.*, 594, A27, [↗](#)
cited on pages 36 and 109
- Planck Collaboration XXXII et al., 2015, *Astronomy & Astrophysics*, 581, A14
cited on pages 77
- Polletta M. et al., 2007, , 663, 81 *cited on pages 78 and 148*

- Popesso P., Bhringer H., Romaniello M., Voges W., 2005, *Astron. Astrophys.*, 433, 415, ☞
cited on pages 31
- Pratt G. W., Croston J. H., Arnaud M., Böhringer H., 2009, *Astron. Astrophys.*, 498, 361,
☞ *cited on pages 113 and 135*
- Ramos Ceja M., 2016, PhD thesis *cited on pages 91*
- Rapetti D., Allen S. W., Mantz A., Ebeling H., 2010, *Mon. Not. R. Astron. Soc.*, 406, 1796
cited on pages 110
- Reichardt C. L. et al., 2013, *Astrophys. J.*, 763, 127, ☞ *cited on pages 36 and 108*
- Reiprich T. H., Böhringer H., 2002, *Astrophys. J.*, 567, 716, ☞ *cited on pages 102 and 105*
- Richard J. et al., 2014, *Mon. Not. R. Astron. Soc. Lett.*, 446, L16, ☞ *cited on pages 45*
- Ridl J. et al., 2017, *MNRAS*, 468, 662, ☞ *cited on pages 51, 73, 101, and 147*
- Riess A. G. et al., 1998, *Astron. J.*, 116, 1009, ☞ *cited on pages 9*
- Riess A. G. et al., 2011, *Astrophys. J.*, 730, 119, ☞ *cited on pages 108*
- Romer A. et al., 2000, *The Astrophysical Journal Supplement Series*, 126, 209
cited on pages 99
- Romer A. K., Viana P. T. P., Liddle A. R., Mann R. G., 2001, *Astrophys. J.*, 547, 594, ☞
cited on pages 29 and 74
- Rosati P., Della Ceca R., Norman C., Giacconi R., 1997, *The Astrophysical Journal Letters*,
492, L21 *cited on pages 99*
- Rozo E. et al., 2009, *Astrophys. J.*, 708, 645 *cited on pages 109*
- Rykoff E. S. et al., 2012, *Astrophys. J.*, 746, 178, ☞ *cited on pages 47 and 81*
- Rykoff E. S. et al., 2014, *Astrophys. J.*, 785, 104, ☞ *cited on pages 34, 74, 75, and 78*
- Sadibekova T., Pierre M., Clerc N., Faccioli L., Gastaud R., Le Fevre J.-P., Rozo E.,
Rykoff E., 2014, *Astron. Astrophys.*, 571, A87, ☞ *cited on pages 29, 50, and 74*
- Salpeter E. E., 1955, , 121, 161 *cited on pages 81*
- Sandage A., Visvanathan N., 1978, *Astrophys. J.*, 223, 707 *cited on pages 32*
- Sanders J. S., Fabian A. C., Russell H. R., Walker S. A., Blundell K. M., 2016, 000, ☞
cited on pages xii, 27, and 28
- Sartoris B. et al., 2014, *Astrophys. J. Lett.*, 783 *cited on pages 110*

- Sayers J. et al., 2013, *Astrophys. J.*, 778, 52, [↗](#) *cited on pages 36*
- Schaye J. et al., 2014, *Mon. Not. R. Astron. Soc.*, 446, 521, [↗](#) *cited on pages 102*
- Schechter P., 1976, *Astrophys. J.*, 203, 297, [↗](#) *cited on pages 31*
- Schlegel D. J., Finkbeiner D. P., Davis M., 1998, , 500, 525 *cited on pages 63*
- Schwinn J., Jauzac M., Baugh C. M., Bartelmann M., Eckert D., Harvey D., Natarajan P., Massey R., 2016, [↗](#) *cited on pages 110*
- Scoville N. et al., 2007, *Astrophys. J. Suppl. Ser.*, 172, 150, [↗](#) *cited on pages 29 and 74*
- Sehgal N. et al., 2011, *Astrophys. J.*, 732, 44, [↗](#) *cited on pages 36 and 108*
- Seljak U., 2002, *Mon. Not. R. Astron. Soc.*, 337, 769, [↗](#) *cited on pages 102*
- Shandera S., Mantz A., Rapetti D., Allen S. W., 2013, *J. Cosmol. Astropart. Phys.*, 2013, 004, [↗](#) *cited on pages 110*
- Sheldon E. S. et al., 2009, *Astrophys. J.*, 703, 2217, [↗](#) *cited on pages 109*
- Silva L., Granato G. L., Bressan A., Danese L., 1998, , 509, 103 *cited on pages 78*
- Skrutskie M. F. et al., 2006, , 131, 1163 *cited on pages 61*
- Smith G. P., Edge A. C., Eke V. R., Nichol R. C., Smail I., Kneib J.-P., 2003, *Astrophys. J.*, 590, L79, [↗](#) *cited on pages 102*
- Söchting I. K., Coldwell G. V., Clowes R. G., Campusano L. E., Graham M. J., 2012, , 423, 2436 *cited on pages 98*
- Springel V. et al., 2005, *Nature*, 435, 629, [↗](#) *cited on pages xi and 13*
- Starck J.-L., Murtagh F. D., Bijaoui A., 1998, *Image processing and data analysis: the multiscale approach*. Cambridge University Press *cited on pages 76*
- Šuhada R. et al., 2012a, *Astronomy & Astrophysics*, 537, A39 *cited on pages 74, 87, and 96*
- Šuhada R. et al., 2012b, *Astron. Astrophys.*, 537, A39, [↗](#) *cited on pages 29*
- Sunyaev R. A., Zeldovich Y. B., 1970, *Astrophys. Sp. Sci. Vol. 7, Issue 1*, pp.3-19, 7, 3 *cited on pages 74*
- Swetz D. S. et al., 2011, *Astrophys. J. Suppl. Ser.*, 194, 41, [↗](#) *cited on pages 36 and 108*
- Tinker J., Kravtsov A. V., Klypin A., Abazajian K., Warren M., Yepes G., Gottlöber S., Holz D. E., 2008a, *Astrophys. J.*, 688, 709, [↗](#) *cited on pages 20, 107, and 113*

- Tinker J., Kravtsov A. V., Klypin A., Abazajian K., Warren M., Yepes G., Gottlöber S., Holz D. E., 2008b, *The Astrophysical Journal*, 688, 709 *cited on pages 91*
- Trümper J., 1993, *Science* (80-.), 260 *cited on pages 22 and 103*
- Valtchanov I., Pierre M., Gastaud R., 2001, *Astronomy & Astrophysics*, 370, 689 *cited on pages 76*
- Vanderlinde K. et al., 2010, *Astrophys. J.*, 722, 1180, ☞ *cited on pages 36 and 108*
- Verlinde E. P., 2016, ☞ *cited on pages xiv and 41*
- Vikhlinin A. et al., 2009a, *Astrophys. J.*, 692, 1033, ☞ *cited on pages 103*
- Vikhlinin A. et al., 2009b, *Astrophys. J.*, 692, 1060, ☞ *cited on pages 45, 49, 73, 102, 103, 104, 108, and 109*
- Vikhlinin A., McNamara B. R., Forman W., Jones C., Quintana H., Hornstrup A., 1998, *Astrophys. J.*, 502, 558, ☞ *cited on pages 74*
- Visvanathan N., Sandage A., 1977, *Astrophys. J.*, 216, 214 *cited on pages 32*
- Vogelsberger M. et al., 2014, *Mon. Not. R. Astron. Soc.*, 444, 1518, ☞ *cited on pages 102*
- Von Der Linden A. et al., 2014, *MNRAS*, 439, 2 *cited on pages 104 and 108*
- Wang Y., 2008, *Phys. Rev. D*, 77, 123525, ☞ *cited on pages 104*
- Weisskopf M. C., Tananbaum H. D., Van Speybroeck L. P., O'Dell S. L., 2000, *Chandra X-Ray Observatory (CXO):Overview* *cited on pages 22*
- Wen Z. L., Han J. L., 2011, , 734, 68 *cited on pages 98*
- Wen Z. L., Han J. L., 2015, *Astrophys. J.*, 807, 178, ☞ *cited on pages 34 and 75*
- Wen Z. L., Han J. L., Liu F. S., 2012, *Astrophys. J. Suppl. Ser.*, 199, 34, ☞ *cited on pages 34 and 75*
- Wood K. S. et al., 1984, , 56, 507 *cited on pages 29*
- Zwicky F., 1937, *Astrophys. J.*, 86, 217 *cited on pages 45*

Acknowledgements

I have been immensely privileged to have received the outstanding supervision of Dr Nicolas Clerc. I am thankful for the consistent insights, ideas and wisdom of the last 3.5 years. The impact of his consistent support, encouragement and advice on helping to bring this thesis to completion cannot be overstated and for this I am deeply grateful. I also thank my official supervisor, Prof. Dr. Kirpal Nandra, for allowing me the opportunity to work on this project and for the provision of valuable resources for performing observations, travelling to conferences and meetings, and for funding my research through MPE. I also thank the remaining members of my thesis committee Dr. Jeremy Sanders and Prof. Dr. Joe Mohr for their constructive comments and advice. Numerous other members of the MPE High Energy Group have also contributed ideas and useful comments including Dr. Mara Salvato, Dr. Jochen Greiner, Dr. Andrea Merloni, Dr. Antonis Georgakakis, Dr. Arne Rau and Dr. Tom Dwelly. Thanks must also be extended for the world-class technical and IT support provided by Harald Baumgartner, Joachim Paul, and Achim Bohnet.

I thank my X-CLASS collaborators Dr. Marguerite Pierre, Dr. Tatyana Sadibekova, Dr. Lorenzo Faccioli, Mona Molham Mostafa and Rene Gastaud for their contributions.

Thank you to Dr. Mathilde Jauzac for encouraging me firstly to pursue a PhD abroad and pushing me to always be the best that I can be. I will always be grateful for the sustained friendship, encouragement and advice you have given and for the detailed comments on my thesis which was a great help in getting to the final product.

I acknowledge the use of the following contributions, funding, data and programs: Thanks to F. Hofmann, M. Bernhardt, G. Vasilopoulos and T. Schweyer and the support astronomers, A. Hempel, M. Rabus, R. Lachaume and I. Lacerna for helping with the GROND observations. Thanks also to G. Erfanianfar, M. Mirkazemi, M. Klein, M. Jauzac and D. Pierini for useful discussions and J. Sanner for help with the visual inspection of photometric redshift results. This research made use of APLpy, an open-source plotting package for Python hosted at <http://aplpy.github.com> and Astropy, a community-developed core Python package for Astronomy ([Astropy Collaboration et al. 2013](#)). This research has made use of the NASA/IPAC Extragalactic Database (NED) which is operated by the Jet Propulsion Laboratory, California Institute of Technology, under contract with the National Aeronautics and Space Administration. Part of the funding for GROND (both hardware as well as personnel) was generously granted from the Leibniz-Prize to Prof. G. Hasinger (DFG grant HA 1850/28-1). I acknowledge funding of this thesis by the Max Planck Institute for extraterrestrial Physics in Garching.

Moving to a new country with a foreign language would have been difficult without the wonderful friendships that have been forged in the fire that is a PhD program. Thanks to everyone for the friendship, support and encouragement. I have been fortunate here in Munich to have found a true gem in the world of rugby at Studentenstadt Rugby München. It has been an immense privilege to pull on the black jersey and the friendships that have been made will undoubtedly last far into the future. *Einmal Stusta, immer Stusta.*

I thank my girlfriend Corina for the financial support and encouragement over the final periods of my thesis and for ensuring that I remembered that there was more to life than Astrophysics. Finally, I thank my family for everything that they have done, for the sacrifices that have been made to help me get to this point and for the consistent supply of support, motivation and inspiration.